R U H R - U N I V E R S I T Ä T B O C H U M
I n s t i t u t f ü r M e c h a n i k

Seismic Reconnaissance in a Tunnel Environment using Full Waveform Inversion

Mitteilungen aus dem Institut für Mechanik Nr. 170

Herausgeber (Publisher):

Institut für Mechanik
— Schriftenreihe —
Ruhr-Universität Bochum
D-44780 Bochum

ISBN 978-3-935892-48-3

Printed in Germany

Tag der mündlichen Prüfung (thesis defense): 24. Juni 2016

Erster Referent (first referee):	Prof. Dr. rer. nat Klaus Hackl
Zweiter Referent (second referee):	Prof. Dr. Wolfgang Friederich
Dritter Referent (third referee):	Prof. Dr.-Ing. Matthias Baitsch
Fachfremder Referent (fourth referee):	Prof. Dr. rer. nat. habil. Andreas H. Schumann
Vorsitzender (committee chair):	Prof. Dr.-Ing. habil. Tom Schanz

Acknowledgements

I would like to sincerely thank Prof. Dr. rer. nat. Klaus Hackl for providing me the research opportunity in his research group. I gratefully acknowledge him for the supervision and crucial contributions to the project.

I owe my special gratitude to Prof. Dr.-Ing. Matthias Baitsch for his supervision, advice and guidance. His contributions were always vital for the project.

Furthermore, I would like to thank Prof. Dr. Wolfgang Friederich for his contributions to the project. I would also like to thank my colleagues for their support in different ways. My family deserves special mention for their continuous mental support and encouragement.

Finally, financial support was provided by the German Research Foundation (DFG) in the framework of project A2 of the Collaborative Research Center SFB 837. This support is gratefully acknowledged.

Kurzfassung

In dieser Arbeit wird die Anwendung der Full-Waveform Inversion (FWI) in einer Tunnelumgebung untersucht. Genauer gesagt wird versucht, Objekte zu erkennen, die unter Verwendung der FWI unterschiedliche mechanische Materialeigenschaften aufweisen als der Rest der Tunnelumgebung.

Die Vorhersage der geologischen Struktur vor einem Tunnel erfolgt in der Regel durch die Lauf der ersten reflektierten Wellen, die aufgrund von geologischen Veränderungen zurückprallen. FWI verlässt sich nicht nur auf die ersten angekommenen reflektierten Wellen, sondern auf alle auftreffenden Wellen aller Amplituden. Um ein FWI Problem zu lösen, wird der Unterschied zwischen den berechneten und realen Modellen minimiert. Die Minimierung wird durch Ausführen einer großen Anzahl von Vorwärts-Simulationen erzielt. Aus diesem Grund ist es sehr wichtig, ein präzises Vorwärtsmodell aufzustellen. Reflektierende Ränder sind eines der Hindernisse, die in einem Tunnelmodell näher angegangen werden müssen. Wir verwenden die Technik der Perfectly Matched Layers (PML), die eine sehr beliebte Technik für absorbierende Ränder ist und in unserem Modell sehr effektiv scheint. Die Vorwärts-Modelle werden mit Hilfe der Finite-Elemente-Methode höherer Ordnung gelöst. Dabei sind Polynome höherer Ordnung erforderlich, um die Wellen präzise modellieren zu können.

Um die Vorwärtsmodelle zu testen, wird die numerische Lösung mit einem analytischen Modell und mit Modellen aus einem allgemein anerkannten Programm der Geophysik-Community verglichen. Zur Vereinfachung wird zunächst mit der akustischen Wellengleichung begonnen, die lediglich Druckwellen berücksichtigt. Als nächstes werden realistischere Komponenten wie beispielsweise inhomogene Dämpfung- und Dichteverteilungen zum Vorwärtsmodell hinzugefügt. Darüber hinaus wird die elastische Wellengleichung in Betracht gezogen, weil sie Druck-, und Scher- und Oberflächenwellen beinhaltet, die für den Grundbau realistischer sind.

Die Wellengleichung wird im Frequenzbereich gelöst. Diskrete Fourier-Transformationstechniken werden eingesetzt, um die Wellenformen im Zeitbereich zu erkennen. Auf diese Weise kann festgestellt werden, wie stark die Störreflektion aus den absorbierenden Randbedingungen ist. Die Modellierung von Wellen im Frequenzbereich hat beim Lösen des Vorwärtsmodells einen Rechennachteil im Vergleich zu einigen Methoden im Zeitbereich. Allerdings bietet die Modellierung im Frequenzbereich Flexibilität, um die Antwort eines Systems bei einer bestimmten diskreten Frequenz zu betrachten. Diese Flexibilität vereinfacht das inverse Problem und infolgedessen kann ein besseres Inversionsergebnis erzielt werden.

Meist wird das CG-Verfahren verwendet, um die Zielfunktion zu minimieren, welche die Differenz zwischen dem berechneten und realen Model beschreibt. Allerdings wird sowohl die Methode des steilsten Abstiegs als auch das PCG-Verfahren in dieser Arbeit verwendet. Beim Aufstellen des inversen Problems müssen zunächst wichtige Faktoren, wie der Frequenz-Satz und die Quelle-Empfänger-Konfiguration abgearbeitet werden. Es wird versucht, optimale und praktische Optionen auszuwählen und gleichzeitig ein gut gestelltes inverses Problem zu erhalten. Die Positionen der Quelle-Empfänger-Standpunkte müssen mit Bedacht ausgewählt werden. Sie müssen an erreichbaren Orten platziert werden. Obwohl sie in einem Computermodell an jedem beliebigen Ort platziert werden können, werden sie nur an bestimmten Stellen gesetzt, um die Feldarbeit praktischer und kostengünstiger zu gestalten. Auf diese Weise kann auf zusätzliche Bohrungen verzichtet werden. Die Standorte und die Anzahl der Empfänger sind entscheidend für die Wohlgestelltheit des inversen Problems. Sie müssen an jenen Orten

angebracht werden, an denen sie ausreichend Reflexionen der geologischen Veränderungen anfangen können. Sonst hätte die Systemantwort nicht genügend Informationen über die geologische Gegebenheit und das inverse Problem wäre inkorrekt gestellt. In dieser Arbeit werden die Standorte und die Anzahl der Quelle-Empfänger-Standpunkte untersucht. Ferner wird versucht, die Standpunkte so zugänglich wie möglich und deren Anzahl so gering wie möglich zu halten, und damit das bestmögliche Ergebnis mit dem geringsten Aufwand zu erziehen.

Summary

In this work, we investigate the application of full waveform inversion (FWI) in a tunnel environment. More precisely, we try to detect objects which have different mechanical material properties than the rest of the tunnel domain by using FWI. Predicting the geological structure ahead of a tunnel is done usually by the traveltimes of the first reflected waves bounced back from the geological changes. FWI relies on not only first arrivals of the reflected waves, but all arrivals and amplitudes of all waves.

To solve an FWI problem, the difference between the computer and real models has to be minimized. The minimization task is carried out by performing many forward simulations. For this reason, it is very crucial to have a precise forward model. Reflecting boundaries are one of the obstacles which must be tackled in a tunnel model. We use perfectly matched layers (PML) technique which is recently very popular absorbing boundary technique and they turn out to be very effective in our model. The forward models are solved by higher-order finite element method because high order polynomials are required to model the waves precisely.

To test the forward models, we compared the numerical solutions with the analytical models and the models in a well-accepted program in the geophysics community. For the sake of simplicity, we start with the acoustic wave equation which accounts only for pressure waves. Next, more realistic elements, such as inhomogeneous attenuation and density fields, are added to the forward model. Furthermore, the elastic wave equation is taken into consideration because it accounts for pressure, shear, and surface waves which are more realistic for soils.

We solve the wave equation in the frequency domain. Discrete Fourier transformation techniques are deployed to see the waveforms in the time domain. This way, it can be observed how much spurious reflection is bounced back from the absorbing boundaries. Frequency domain modelling of waves has a computational drawback in solving the forward model compared to the time domain modelling. However, it provides flexibility to observe the response of a system at a specific discrete frequency. Moreover, in an inversion simulation, this flexibility plays an important role as the inverse model can be inverted over a specific set of discrete frequencies. This flexibility makes the simplification of the inverse problem easier and as a result, a better inversion result can be obtained.

We mostly use the conjugate gradient method to minimize the penalty function which describes the difference between the computer and real models. However, steepest descent and preconditioned conjugate gradient methods are also used throughout this work. There are certain issues which must be done precisely while setting up the inverse problem such as frequency set and source/receiver configuration. We try to choose optimal and practical options and at the same time, to have a well-posed inverse problem. The locations of the source/receiver points must be carefully chosen; they must be placed at reachable locations. Although they can be placed anywhere in a computer model, they can only be at certain locations to make the field work more practical and less expensive such that there is no need to make a borehole. Their locations and numbers are decisive on well-posedness of the inverse problem. They have to be at such locations that the receivers can catch enough reflection from the geological changes. Otherwise, the system response would not have enough information about the geology of the domain and the inverse problem would become ill-posed. We investigate the locations and numbers of source/receiver points and try to keep them as practical and as few as possible and try to produce the best possible result at the same time.

Abbildungsverzeichnis

Tabellenverzeichnis

Inhaltsverzeichnis

1 Introduction

This work is a part of the project SFB 837 whose aim is to research on various aspects of tunneling process. This project has a few millions euro budget and dozens of employees who carry out investigation on a variety of issues in tunneling. SFB 837 is divided into several subprojects and this work is done under umbrella of subproject A2. The main goal of this subproject is to use full waveform inversion to detect anomalies and obstacles ahead of a tunnel. These anomalies can be fracture zones, erratic rocks, cavities, faults, or other geological structures.

Since the mankind started civilizing, they have been building different structures to support the daily life. Very surprisingly, they even built tunnels thousands of years ago which can be called an engineering miracle considering the fact that not much technology was available in those days. An example of such an ancient tunnel was found beneath the ancient city Teotihuacan in Mexico.

Nowadays, technology is growing very fast in all branches and we can see its effect also in tunneling. With growing population of countries, governments try to find optimal solutions to traffic and transportation. Big cities are becoming so condense that solution above the ground is not an option in some cases. For this reason, finding the solution under the ground becomes more attractive solution especially in urban areas. This is a common practice in the world, especially in developed countries. As an example, Karlsruhe, Germany, can be mentioned. The city is designed to handle more traffic with underground transportation and it is done smoothly in the city center by not blocking the traffic flow.

Tunnels are not implemented only to resolve traffic problems in big cities. They are implemented also when the landscape blocks the traffic. Mountain can be an example for such a landscape, and tunnels, in some cases, are the best option to create a traffic connection between the areas divided by the mountain. Such a solution saves a lot of energy because vehicles consume a lot more fuel going up a hill and a tunnel can connect two points with a straight line with almost no altitude difference. Furthermore, such shortcuts decrease accident risks, especially in bad weather conditions, and make the journey shorter and painless. Mont Cenis Tunnel is one of many tunnels in the Alps which can be mentioned as an example to the tunnels in mountains.

Another landscape which can block the land traffic is water. Underwater tunnels unite the land traffic of two pieces of lands separated by water. For example, there is a long tunnel from France to United Kingdom which combines the European continent with the British Isles, and eases traffic and transportation problems significantly. The dimensions of the tunnel and the depth of water above it says a lot about how enormous the engineering structure is; it is about 50 km long and it is about 100 meters below the water surface.

With the growing technology, tunneling process has been becoming easier, especially over few decades. Previously, the only option to build tunnels was conventional methods. The method has been improved enormously by time and still protects its validity. This method consists of drilling and blasting with explosives. Low cost prior to construction, possibility to replace failing equipments easily, variable response to fracture zone are advantages of the conventional

tunnel construction. However, the drawbacks are low safety, slow tunneling progress and intensive effort in lining. Apart from this, this method cannot be applied in all types of soil; it can be used in hard rocks, whereas it is almost impossible to use it in soft soil.

In some cases, the conventional methods are replaced by mechanical tunneling which is very new method and which takes advantage of growing technology a lot. Very sophisticated tunnel boring machines (TBM) are produced which eases and speeds up the whole process of tunnel excavation and construction. Each TBM is designed to a single tunnel diameter and a specific geological structure, which are drawbacks of TBMs. High cost prior to the tunneling, high maintenance costs, and the fact that damage to the TBM stops the whole construction process are other disadvantages of TBMs. Despite the disadvantages, it has big preferable advantages such as high safety, fast progress in construction, low lining effort, low construction costs in the construction of long tunnels, and ability to deal with difficult geological structures including both soft and hard rocks, [Jetschny, 2010].

In case of long tunnels, with big diameters mechanical, or automated, tunneling is a very attractive choice when other advantages of this process are also taken into account. Since sudden changes in the geological structure of the ground, such as fault zones and caverns, during excavation can damage the TBMs, it becomes very crucial to figure out the ahead of the tunnel. Damage to TBM causes a delay in the construction. Any delay in the process costs money and time, as tunnel boring machine is very expensive and as it is important to keep the machine functional during its stay at the construction site. In other words, if the work delays at the construction site, the money spent for the machines and employees in the meantime is loss of the company. Once an anomaly is detected few dozens of meters ahead of tunnel, a measure can be taken before reaching that area, which, in return, will prevent money and time loss. Furthermore, some anomalies in the ground may cause big settlements on the surface which can damage structures on the ground. Thus, detecting anomalies ahead of tunnel is very important not only in terms of money and time, but also in terms of safety of people and structures. It again prevents big money loss along with human lives and health which are more important than money. Searching for anomalies can also be important in the case of conventional tunneling. For example, several seismic survey were performed during the construction of the Centovalli railway tunnel, [Sattel et al., 1992]. The tunnel was excavated through gneiss rock mass which is overlain by unconsolidated moraine deposits. If the tunnel intersected the moraine deposit suddenly at a low angle, the mining work and the tunnel could have been hazarded. Moreover, the city area of Locarno could have been imposed to high settlements.

If the geological structure is known, the solution to the wave propagation is unique; this is a direct or a forward problem. On the other hand, the problem is called an inverse problem if the wave response of the system is known and the geological structure is sought. In contrast to forward problems, inverse problems usually suffer non-unique solutions; there can be several possible solutions to an inverse problem. Seismic surveying is important in tunneling to localize the anomalies ahead of tunnel. To do so, sources and receivers are required. Sources are points where the vibrations are triggered and the seismograms are read by geophones which we call receiver points. Source can be triggered by a small explosion, a sledgehammer, or by TBM itself. In theory, source and receiving geophones can be places in any location. Nevertheless, it is only practical to place those points at certain locations. For example, in some applications, geophone array is placed in a borehole whose cost is high. In some cases, it is even not practical to make boreholes when a tunnel is constructed in urban areas such as crowded city centers. It becomes difficult to place geophones at locations deep below the surface. When it comes to sources, it is not always practical to excite vibration by explosion, especially in urban places.

In other words, in real world application, we have restrictions over the locations of source and receiver geophones.

The waves start propagating in the ground as soon as the source is fired. They propagate in form of pressure and shear waves. At the boundaries of different materials, some of the energy is reflected back and some are refracted. The refracted waves continue moving forward. Some energy is even transformed into surface waves. The seismograms become chaotic by all kinds of reflected and refracted waves which are superposed in a single seismogram. The chaos is even bigger with higher degree of heterogeneity of the medium.

To do so, efficient geophysical techniques are used in the industry. Some very interesting methods and results are presented in [Ashida, 2001], [Kneib et al., 2000], [Jetschny et al., 2011] and [Yamamoto et al., 2011], which all rely on the seismic surveying. Furthermore, [Miro, 2012] use the static displacement response at the surface to identify the ground model in the case of some special ground model scenarios. Mostly, in tunneling applications, seismic migration techniques, which rely mainly on traveltimes of reflected and refracted waves, are used. The restrictions over the locations of the sources and the receiver geophones increase the ambiguity of the inverse problem even more. The idea of this work is based on to reduce the ambiguity of seismic inverse problems in tunneling applications. We aim to do it by having an input which contains more than traveltime information. We plan to achieve it with the help of full waveform (FWI) technique.

Full waveform inversion is the seismic inversion technique that we utilize throughout this work. From 1980s, Tarantola [Tarantola, 1984], [Tarantola, 1987] is one of the main pioneers of FWI. [Nguyen, 2016] investigates the application of FWI in a tunnel model in the case of some specific ground model scenarios. The goal of FWI is to fit the computer seismograms and observed seismograms in a rigorous sense. In contrast to migration techniques, FWI tries to fit not only traveltimes, but also amplitudes of seismograms thru an iterative process which runs till the defined convergence criteria is satisfied. Although computational cost of FWI is high, it takes advantage of full waveforms that carry a lot more information than only traveltimes. This fact brings advantages as well as drawbacks. A lot of information can end up with a more precise geological image. However, the advantage comes with a price and the abundance of the information increases the nonlinearity of the inverse problem. According to [Ajo-Franklin, 2005], inversion in frequency domain may decrease the non-linearity of the problem. There are several groups of discrete frequencies that are sorted in increasing order. The inverse problem is inverted over the frequency groups starting from the smallest group up to the highest group. The results of lower frequencies are used as an initial model of higher frequencies. The non-linearity of the inverse problem in high frequencies is tackled by an initial model which is closer to the global solution. This fact is our main motivation to solve the inverse problem in the frequency domain.

An inverse process is nothing else but a big bunch of forward processes. That is why the first step of a feasible and successful inversion is a right forward model. We start with the simplest case and improve the forward model by integrating real-world effects into the model. We investigate acoustic waves in 2 dimensional space and later, extend it to 3D. We add viscosity effect to the acoustic equation to make the model more realistic as no material is attenuation free. Only for some models, such as small scale model consisting of hard rock, the effect of attenuation is negligible. Since we work in the frequency domain, we use Kolsky-Futterman model, [Kolsky, 1956], [Futterman, 1962], which replaces velocity field with a complex velocity. In this case we also take the effect of inhomogeneity of density field. In this case, we search

not only for velocity field, but also for density field simultaneously. The inverse problem becomes more complicated as number of sought fields increase. We try to search for 2 and 3 fields simultaneously by using FWI.

It is important to mention that acoustic waves accounts for only P-waves. This is completely true for fluids. However, ground is solid and it has P-waves and S-waves. It even has surface, Rayleigh and Love, waves at the surface and at the interface of different layers. Acoustic waves are a good start and it can be applied to real world problems if P-waves are extracted from the seismograms. However, elastic wave equation describes the response of the earth a lot more precise. For this purpose, after obtaining successful acoustic model, we also investigate the elastic wave equation in the tunnel domain and try to model elastic waves appropriately. Furthermore, we run inverse simulation to search for Lamé parameters as well as density field. The inverse problem becomes complicated here too since the number of sought fields is more than one.

To model the waves correctly, we need to introduce absorbing boundaries. Since the numerical model is only a slice from the ground, we have artificial reflecting boundaries which do not exist in the real model and reflect all waves into the domain. In real world, those boundaries do not exist and no waves are reflected from them. To avoid it, we use perfectly matched layer [Berenger, 1994] whose popularity is increasing recently. It is proved that this method is very effective in tackling spurious reflections from the artificial boundaries. For acoustic waves, we use standard PMLs. However for elastic waves, when the model is shallow, the surface waves touch the artificial boundary at the bottom of the model and they are transformed into body waves which pollutes the solution [Festa and Nielsen, 2003]. We use convolutional PML to overcome possible pollutions because of the surface waves, [Festa et al. 2005], [Festa and Vilotte, 2005].

There are several numerical methods used to solve partial differential equations, such as finite-difference method, finite element method, boundary element method and so on. There are also several derivations of every method. Each of them can be preferable in solving some specific problems. For example, spectral element method is a derivation of finite element method and it provides a diagonal mass matrix which decreases the computational cost significantly by using a correct time integration scheme. Other derivations of finite element method are discontinuous Galerkin method, extended finite element method and so on. Higher-order finite element method is the numerical method we deploy to solve forward problems. High order polynomials play an important role in modelling the waves precisely. Mesh size has to be smaller than the wave length in order to avoid numerical instability and make the numerical results precise. Higher order method makes it possible to model higher frequency waves just by increasing the polynomial degree. Since we work in the frequency domain, we can use lower degree polynomial for lower frequencies and higher degree polynomials for higher frequencies with the same mesh. It means, higher-order method gives us flexibility besides its role in modelling the waves.

We need to utilize an appropriate computer tool to solve our numerical problem. Specfem [Komatitsch and Vilotte, 1998], [Tromp et al., 2008], [Vai et al., 1999], [Lee et al., 2008], [Komatitsch and Tromp, 1999], [Komatitsch et al., 2004] is one of very popular tools for geophysical applications is which is developed by a group at Princeton University. The software solves the wave equations with the spectral element method, which is a special kind of high-order finite element method. It is very robust and efficient, and is widely used by geophysicists all over the world. This program solves the wave problems in the time domain though and we solve the wave equations in the frequency domain. This is the reason why we choose a different tool to solve our problems. There are other programs available out there which solves the wave equations in the frequency domain and which are free for academic use. Nevertheless, it

is not always practical to use a tool which is not familiar and which is not well documented. At some points, they can block the flexibility of users. For these reasons, we developed our tool to solve the wave problems in frequency domain and perform full waveform inversion analysis. The tool to solve the forward problem is built upon a Java-based higher-order finite element program developed by Prof. Dr. Matthias Baitsch. Being platform independent is a big advantage of java-based programs. Nevertheless, java-based programs are slower than native libraries. Linear algebraic operations are usually most expensive part of the simulations. However, this tool takes advantage of robustness of native libraries, which do linear algebraic operations, such as PARDISO [Kuzmin et al., 2013], [Schenk and Gaertner, 2004], LAPACK [LAPACK Users' Guide], BLAS [Lawson et al., 1979], [Dongarra et al., 1988],
[Dongarra et al., 1989], NAG [NAG1], [NAG2] and so on. Apart from this, this program is designed in such a way that it can be extended very easily in many aspects; different derivations of finite element method can be implemented, different material models and different element types can be added without any difficulty. Using the flexibility of this program, the wave equations were added to the list of partial differential equations solved by the program. While developing the inversion tool, the aim was to make it extendable too. This tool is also not for one scenario and it can be extended according to the wish of the user. For example, a new partial differential equation used for the FWI problem can easily be added to the list of equations which the tool can solve. This provides an opportunity to carry out further research on different issues of full waveform inversion problems.

To validate the code and models, we test our numerical solutions of 2D and 3D acoustic halfspace forward problems to the analytical solutions. Apart from this, we compare the numerical results of 2D acoustic and elastic models to the numerical results of Specfem which is a very credible well-known program used by a lot of geophysicists. To verify our inverse models, we use synthetic models. In one case, we make a blind test in cooperation with the geophysics institute at Ruhr University Bochum. They make a synthetic model and calculate the system response of their model in Specfem. By using the system response in our inversion, we try to figure out the model.

2 Waves

2.1 Waves in earth

Earth can show both elastic and inelastic behavior depending on the rate of strain it is subjected to. Nothing in nature is perfectly elastic and permanent deformations can be formed in the structure of the earth when it is subjected to a strong earthquake. The Canterbury earthquake is one of those strong earthquakes which struck New Zealand in 2010 and it caused permanent deformations in earth at certain locations. One can refer to the photos taken by Malcolm Teasdale at the webpage of KiwiRail to see distorted railways due to the permanent deformations in the earth caused by the Canterbury earthquake.

However, in some cases, we can precisely predict the oscillations in the earth with an elastic theory. Small-scale earthquakes which do not create permanent deformations in the earth can be modelled with the elastic theory. One of the main goals of this work is to model the waves precisely so that they can be used for non-destructive ahead of tunnel prediction. This test does not form any permanent deformation in the ground and small amplitude vibrations are triggered usually using the tunnel boring machine or some acoustic signal. For such a non-destructive test, we can stay within the limits of small strains to simulate the waves with the elastic theory.

2.1.1 Linear elastic theory and Hooke's law

It can be assumed that every material has its elastic range. For very small strains, behavior of elastic earth material can be approximated by Hooke's Law which is based on a linear stress-strain relation. In Figure 2.1, one can see the schematic representation of linear elastic range in both ductile and brittle materials.

Hooke's Law is used to describe a linear, elastic and isotropic material model mathematically. In general, two elastic material parameters are enough to predict the stress-strain relation of the material: the Lamé parameters λ and μ. However, there are several elastic material parameters, such as elasticity modulus E, shear modulus G, Poisson ratio ν, and compression modulus K, which are also used frequently. In this work, the Lamé parameters λ and μ are used as elastic parameters. When it comes to other elastic parameters, any of them can be thought as a function of λ and μ. The following equations

$$G = \mu \tag{2.1}$$

$$E = \frac{\mu(3\lambda + 2\mu)}{\lambda + \mu} \tag{2.2}$$

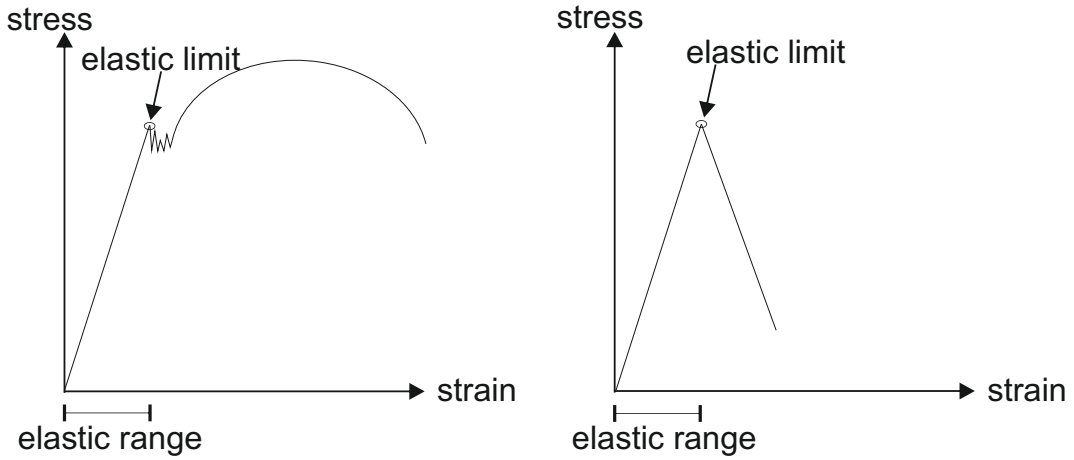

(a) Ductile materials (b) Brittle materials

Figure 2.1: Stress/strain relationship in brittle and ductile materials

Schematic representation

$$\nu = \frac{\lambda}{2(\lambda + \mu)} \tag{2.3}$$

$$K = \lambda + \frac{2}{3}\mu \tag{2.4}$$

show how parameters G, E, ν, and K are related with Lamé parameters.

The potential energy $W(\boldsymbol{\varepsilon})$ of the linear, elastic and isotropic material described by Hooke's Law is

$$W(\boldsymbol{\varepsilon}) = \mu\boldsymbol{\varepsilon} : \boldsymbol{\varepsilon} + \frac{1}{2}\lambda(tr(\boldsymbol{\varepsilon}))^2, \tag{2.5}$$

where

$$tr(\boldsymbol{\varepsilon}) = \varepsilon_{11} + \varepsilon_{22} + \varepsilon_{33} \tag{2.6}$$

is the trace of the strain tensor $\boldsymbol{\varepsilon}$. The stress tensor $\boldsymbol{\sigma}$ can be derived by differentiating the potential function $W(\boldsymbol{\varepsilon})$ by the strain tensor $\boldsymbol{\varepsilon}$

$$\sigma_{ij} = \frac{\partial W(\boldsymbol{\varepsilon})}{\partial \varepsilon_{ij}} = 2\mu\varepsilon_{ij} + \lambda\varepsilon_{kk}\delta_{ij}. \tag{2.7}$$

The fourth order constitutive tensor $\boldsymbol{C}$ is derived by

$$C_{ijkl} = \frac{\partial W}{\partial \varepsilon_{ij}\partial \varepsilon_{kl}} = \mu(\delta_{il}\delta_{jk} + \delta_{ik}\delta_{jl}) + \lambda\delta_{ij}\delta_{kl}. \tag{2.8}$$

The relation between the stress tensor $\boldsymbol{\sigma}$ and $\boldsymbol{\varepsilon}$ is described by

$$\boldsymbol{\sigma} = \boldsymbol{C} : \boldsymbol{\varepsilon}. \tag{2.9}$$

Again, for small strains, we skip the geometrical non-linearity, and take linear strain measure into account. In this case,

$$\boldsymbol{\varepsilon} = \frac{1}{2}\left[\nabla \boldsymbol{u} + \nabla^T \boldsymbol{u}\right] \tag{2.10}$$

where

$$\nabla \boldsymbol{u} = \frac{\partial u_i}{\partial x_j} \boldsymbol{e}_i \boldsymbol{e}_j. \tag{2.11}$$

2.2 Categorization of waves

The equations above suffice to model linear elastic waves mathematically. However, the physics of the problem is as much interesting as the mathematics behind it. The solution of the elastic partial differential equation is usually a superposition of waves with different physics. Waves are categorized according to the relation between their propagation direction and the kind of deformation it causes. They are divided mainly into two categories: body waves (P-wave and S-wave) and surface waves (Love waves and Rayleigh waves).

2.2.1 Body waves

P-wave and S-wave are two types of body waves. P-wave stands for primary waves since it travels with the highest speed in the ground compared to other waves. Its speed in isotropic homogeneous environment is

$$v_p = \sqrt{\frac{\lambda + 2\mu}{\rho}} \tag{2.12}$$

which depends on the elastic parameters and the density. P-wave is also referred to as longitudinal waves since its propagation direction is also the direction of the vibration of particles in the ground.

S-wave is also called as shear wave, secondary wave, or transverse wave. Its speed of propagation is smaller than the speed of P-waves and this is a reason why it is called secondary wave. Its propagation speed is

$$v_s = \sqrt{\frac{\mu}{\rho}} \tag{2.13}$$

which, as the speed of P-wave, is a function of the elastic parameters. The propagation direction of the S-waves is perpendicular to the direction of the vibration of particles in the ground.

As in [Achenbach, 1984], plane harmonic body waves in an elastic homogeneous medium are described as

$$\boldsymbol{u}(\boldsymbol{x}) = A\boldsymbol{d}\exp([ik(\boldsymbol{x}\cdot\boldsymbol{g} - ct)]), \tag{2.14}$$

where k and c are wavenumber and wave velocity, respectively. Here, $\boldsymbol{g}$ is the unit propagation vector, $\boldsymbol{d}$ is the unit direction vector of particle motions.

If the body wave is a longitudinal P-wave, the unit vector $\boldsymbol{d}$ equals to the unit vector $\boldsymbol{g}$ ($\boldsymbol{d} = \boldsymbol{g}$) and $c = v_p$. In other words, as mentioned before, the direction of particle motion is same as the wave propagation direction. If the wave is a transverse S-wave, the wave propagation direction is perpendicular to the particle motion which is interpreted mathematically as $\boldsymbol{d} \cdot \boldsymbol{g} = 0$ and $c = v_s$. The shear wave itself is divided into two categories: SV-wave with $\boldsymbol{d} = \boldsymbol{z} \wedge \boldsymbol{g}$ and $c = v_s$, and SH-wave with $\boldsymbol{d} = \boldsymbol{z}$ and $c = v_s$. The direction z is perpendicular to the 2-dimensional plane in which the wave propagates. This categorization is again associated with the relation between the propagation of the waves and the direction of the vibration in the particles. Particles move in a vertical direction in SV-wave, whereas they move in horizontal direction in SH-wave. Nevertheless, in both cases, the vibration direction is perpendicular to the wave propagation direction.

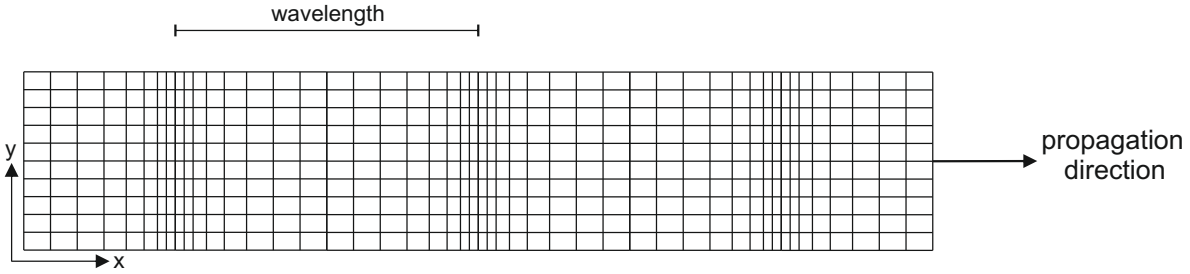

(a) P-wave

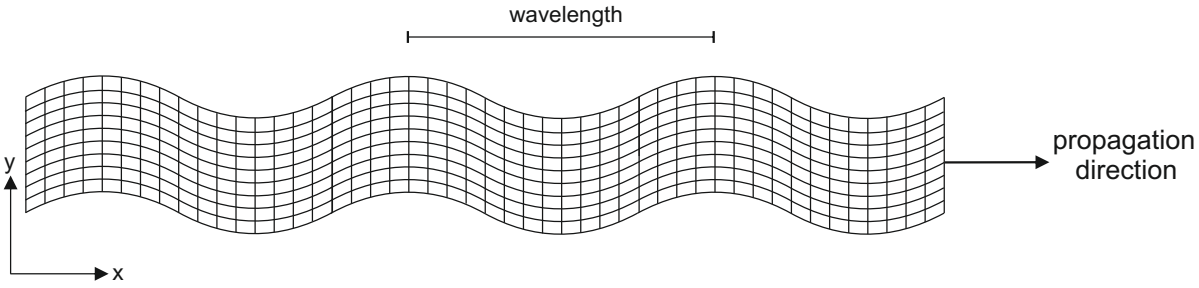

(b) SV-wave

Figure 2.2: Body waves

2.2.2 Surface waves

There are two types of surface waves, Love wave and Rayleigh wave, which are named after the scientists who first discovered them. When waves hit a free surface, some energy is reflected back and some is refracted thru the next layer, whereas the rest of the energy is transmitted to surface waves. P- and SV-waves transmitted at a free surface may trigger Rayleigh surface waves travelling at a lower speed than P- and S-waves. While Rayleigh wave propagates, the particle motion is elliptical as shown in Figure 2.3. During an earthquake, the vertical displacement on the surface caused by Rayleigh wave is significantly bigger than the one caused by body waves. Thus, Rayleigh waves are more destructive than body waves in an earthquake. However, Rayleigh waves are only effective in regions close to the free surface and they decay

exponentially with depth. When it comes to Love waves, they are also formed at the surfaces. Repeated reflections of SH waves at the surface form Love waves which are slower than body waves, but slightly faster than Rayleigh waves. In Figure 2.3, it can be seen that the surface is subject to a torsion whose direction changes continuously in the horizontal plane.

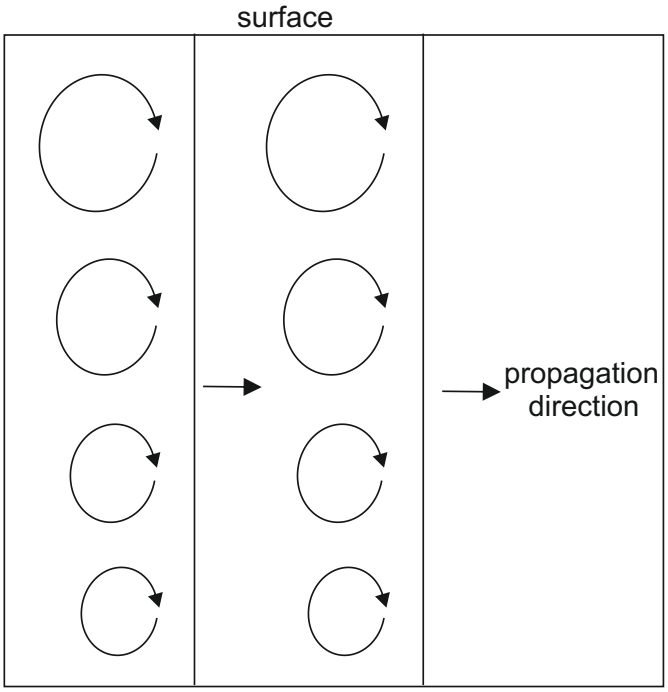

(a) Rayleigh wave

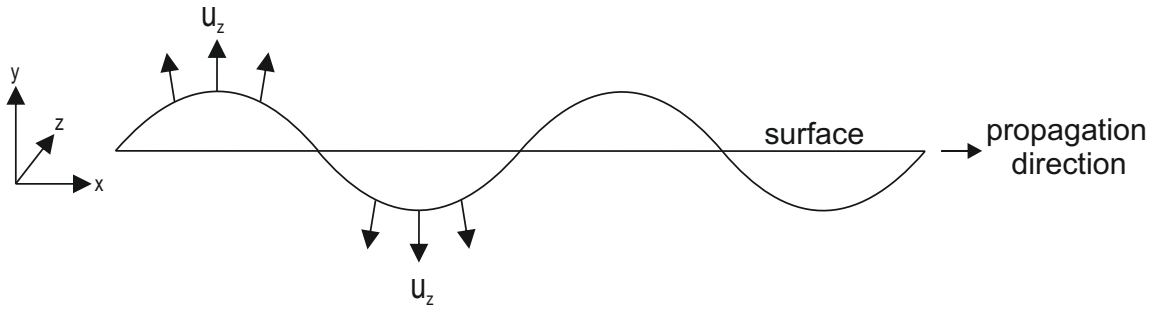

(b) Love wave

Figure 2.3: Surface waves

2.2.3 Reflection and refraction of waves at free boundaries

As already mentioned in the previous section, although some part of the energy of the incoming wave is converted to surface waves at the free surface, the rest of it is either reflected back to the domain where the incident waves are coming from, or continue moving forward to the next layer, but with refraction. On the other hand, if the incident wave is P- or SV- wave, 4 waves are

formed at the boundary different from surface waves: a reflected P-wave, a reflected SV-wave, a refracted P-wave, and a refracted SV-wave. For the sake of simplicity, we assume a solid-solid interface as in Figure 2.4. As incident wave is moving in layer A towards layer B. At the boundary, some part of the wave is reflected back and some moves forward with a refraction. Some part of the energy may be converted to a different kind of wave at a boundary; some part of P-wave energy is converted to SV-wave and the opposite is also true.

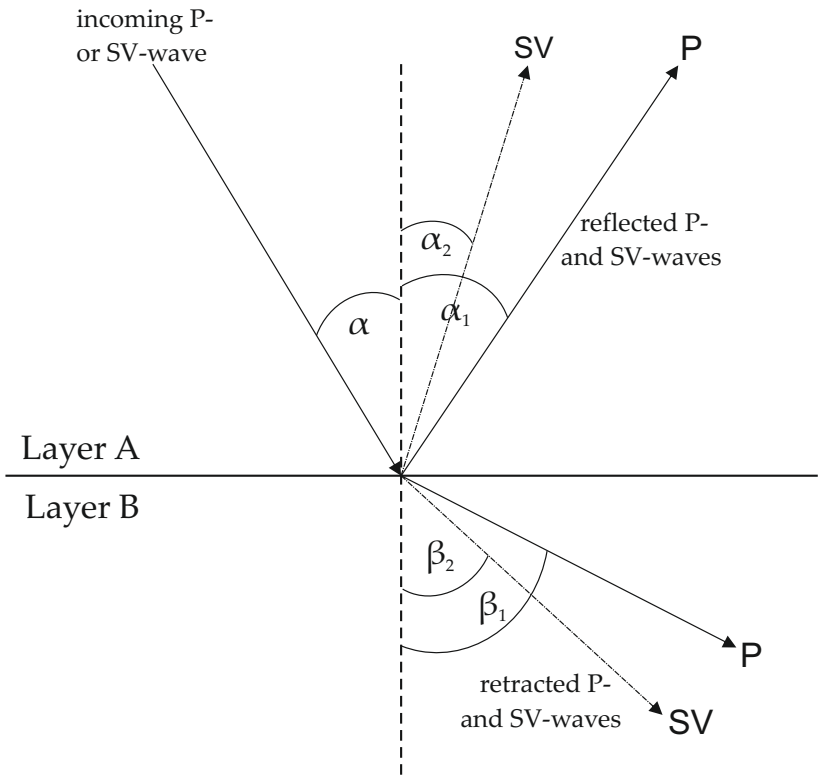

Figure 2.4: P- and SV-waves at solid-solid interface

Incident, reflected and refracted waves [Achenbach, 1984]

2.3 Wave equations

Wave equations, which are partial differential equations, are used to model the propagation of waves. In this section, we focus on two wave equations: elastic and acoustic. Acoustic wave equation is a special form of the elastic equation where the shear modulus μ is zero. The equations are solved in the frequency domain. For a single frequency, the equations show time harmonic response of the structure. However, transient response by solving the equation for discrete frequencies which covers the effective frequency range of the source function and by performing the inverse Fourier transformation of the time harmonic responses.

The inhomogeneous partial differential equations which are solved in each iteration of the inverse process do not have analytical solutions. We are using higher-order finite element method

to solve the equations precisely.

2.3.1 Elastic wave equation

The elastic wave equation describes the dynamic response of solids because it accounts for P-wave, S-wave, and surface waves at free boundaries. We do not consider permanent deformations and we solve the wave equation for isotropic and linear elastic materials. As mentioned before, small deformations suit our problem very well because the intention of this work is to perform a non-destructive inversion with the wave response of the earth. The elastic wave equation

$$\rho(\boldsymbol{x})\ddot{\widetilde{\boldsymbol{u}}}(\boldsymbol{x},t) - \boldsymbol{\nabla}\cdot\widetilde{\boldsymbol{\sigma}}(\boldsymbol{x},t) = \widetilde{\boldsymbol{f}}(\boldsymbol{x},t), \quad \boldsymbol{x}\in\mathbb{R}^3, \quad t\in[t_0,\infty] \tag{2.15}$$

can be derived by the balance of momentum with continuum mechanics as shown for example in [Marsden and Hughes, 1983]. In case of a non-dissipative, isotropic, and linear elastic medium, the constitutive relation is formulated as

$$\widetilde{\boldsymbol{\sigma}}(\boldsymbol{x},t) = \boldsymbol{C} : \boldsymbol{\nabla}\widetilde{\boldsymbol{u}}(\boldsymbol{x},t). \tag{2.16}$$

Since the domain we aim to solve the wave equations in the frequency domain, we assume a harmonic excitation $\widetilde{\boldsymbol{f}}(\boldsymbol{x},t) = \boldsymbol{f}(\boldsymbol{x})e^{i\omega t}$ of the angular frequency ω to obtain the time harmonic equation

$$-\rho(\boldsymbol{x})\omega^2\boldsymbol{u}(\boldsymbol{x},\omega) - \boldsymbol{\nabla}\cdot\boldsymbol{\sigma}(\boldsymbol{x},\omega) = \boldsymbol{f}(\boldsymbol{x},\omega), \quad \boldsymbol{x}\in\mathbb{R}^3, \quad \omega\in[-\infty,\infty], \tag{2.17}$$

$$\boldsymbol{\sigma}(\boldsymbol{x},\omega) = \boldsymbol{C} : \boldsymbol{\nabla}\boldsymbol{u}(\boldsymbol{x},\omega) \tag{2.18}$$

which is the elastic wave equation in the frequency domain.

2.3.2 Acoustic wave equation

The acoustic wave equation describes the propagation of waves in fluid medium which can be either liquid or gas. In such a medium, the shear modulus μ is zero. As in [Fichtner, 2011], if we consider $\mu = 0$ in the isotropic constitutive relation with linear strain

$$\boldsymbol{\sigma} = \boldsymbol{C} : \boldsymbol{\varepsilon} = \boldsymbol{C} : \boldsymbol{\nabla}\boldsymbol{u}, \tag{2.19}$$

we obtain

$$\sigma_{ij} = \lambda\delta_{ij}\boldsymbol{\nabla}\cdot\boldsymbol{u}. \tag{2.20}$$

Scalar pressure field $p = -\lambda\nabla\boldsymbol{u}$ is inserted in the elastic wave equation which yields

$$\rho\ddot{\boldsymbol{u}} + \boldsymbol{\nabla}p = \boldsymbol{f}. \tag{2.21}$$

After $-\lambda\nabla\boldsymbol{u}$ is replaced by p, the last equation is divided by ρ, divergence of both sides are taken, and λ is replaced by $c^2\rho$,

$$\frac{1}{c^2\rho}\ddot{p} - \boldsymbol{\nabla}\cdot\left[\frac{1}{\rho}\boldsymbol{\nabla}p\right] = -\boldsymbol{\nabla}\cdot(\frac{1}{\rho}\boldsymbol{f}) \tag{2.22}$$

is obtained. This is the acoustic wave equation with inhomogeneous density. If inhomogeneity of ρ is negligible, we can obtain

$$\Delta p - \frac{1}{c^2}\ddot{p} = \boldsymbol{\nabla}\cdot\boldsymbol{f}. \tag{2.23}$$

To be more precise, we can rewrite the acoustic wave equation in the time domain with a constant density field as

$$\triangle\widetilde{p}(\boldsymbol{x},t) - \frac{1}{c^2(\boldsymbol{x})}\frac{\partial^2\widetilde{p}(\boldsymbol{x},t)}{\partial t^2} = \widetilde{f}(\boldsymbol{x},t), \quad \widetilde{p}:\Omega\times[t_0,\infty]\to\mathbb{R}, \tag{2.24}$$

where $\widetilde{p}(\boldsymbol{x},t)$ is the pressure field in time domain, $c(\boldsymbol{x})$ is the velocity field, and $\widetilde{f}(\boldsymbol{x},t)$ is the source function in the time domain. We assume a harmonic excitation $\widetilde{f}(\boldsymbol{x},t) = f(\boldsymbol{x})e^{i\omega t}$ of the angular frequency ω in the equation (2.24) to obtain the time harmonic equation

$$\triangle p(\boldsymbol{x},\omega) + \frac{\omega^2}{c^2(\boldsymbol{x},\omega)}p(\boldsymbol{x},\omega) = f(\boldsymbol{x},\omega), \quad p:\Omega\to\mathbb{R}, \tag{2.25}$$

which is the frequency domain acoustic equation. This equation is also referred as scalar-valued Helmholtz equation in literatures.

2.3.3 Viscoacoustic waves

We did not consider the attenuation effect in the acoustic wave equation in the previous section. However, in reality, there is no material without the attenuation effect. Some materials, such as rocks, have so low attenuation that the waves are barely damped in a small domain. At the same time, there are materials with high attenuation. In a domain with such a material, the attenuation has to be taken into account in order to model waves properly. In this section, attenuation is considered in the acoustic wave equation in the frequency domain. Apart from attenuation, inhomogeneous density effect is also considered in the acoustic wave equation. Mainly, the acoustic equation with a constant density field is referred to in many studies. In many cases, it may suffice to model waves with a constant density field unless there is significant density gradient. However, for a domain with high density gradient, the equation with an inhomogeneous density field is

$$\boldsymbol{\nabla}\cdot\left[\frac{1}{\rho(\boldsymbol{x})}\boldsymbol{\nabla}p_\omega\right] + \frac{\omega^2}{\rho(\boldsymbol{x})c^2(\boldsymbol{x})}p_\omega = f_\omega. \tag{2.26}$$

In this study, attenuation effect is integrated into acoustic equation by using Kolsky-Futterman model, [Kolsky, 1956], [Futterman, 1962], which replaces the velocity field c with a complex-valued field

$$\bar{c} = c\left[\left(1 + \frac{1}{\pi Q}|log(\frac{\omega}{\omega_r})|\right) + i\frac{sgn(\omega))}{2Q}\right]^{-1}. \tag{2.27}$$

in the frequency domain with Q and ω_r denoting the attenuation factor and the reference frequency, respectively. In this case, besides being complex-valued, the velocity field $\bar{c}$ also becomes dependent on the angular frequency ω.

2.4 Boundaries

The domain over which the wave equation is solved makes the problem unique. The aim of this work is to solve the acoustic and elastic wave equations in a tunnel environment. To do so, few boundaries have to be taken into account as well as the main equations to describe the problem properly. There are two very important boundaries: reflecting boundaries, and absorbing boundaries which do not exist physically.

2.4.1 Reflecting boundaries

The boundaries of a physical model are reflective in nature. Mathematically speaking, the reflecting boundaries can be categorized in two groups: Dirichlet and Neumann boundary conditions. Dirichlet boundary condition prescribes pressure and displacement at the region Γ_u in the acoustic and elastic equations, respectively. In other words,

$$p(\boldsymbol{x}, t) = p^*(\boldsymbol{x}, t) \quad \forall \boldsymbol{x} \in \Gamma_u \tag{2.28}$$

in the acoustic equation, and

$$\boldsymbol{u}(\boldsymbol{x}, t) = \boldsymbol{u}^*(\boldsymbol{x}, t) \quad \forall \boldsymbol{x} \in \Gamma_u \tag{2.29}$$

in the elastic equation. Throughout this work, we consider homogeneous Dirichlet boundary condition in which $p^*(\boldsymbol{x}, t)$ and $\boldsymbol{u}^*(\boldsymbol{x}, t)$ are zero. The homogeneous Neumann boundary condition is

$$\boldsymbol{\nabla} p \cdot \boldsymbol{n} = \boldsymbol{0} \quad \forall \boldsymbol{x} \in \Gamma_\sigma \tag{2.30}$$

in the acoustic equation, and

$$\boldsymbol{\sigma} \cdot \boldsymbol{n} = 0 \quad \forall \boldsymbol{x} \in \Gamma_\sigma \tag{2.31}$$

in the elastic equation. Although modelling reflecting boundary conditions can be a tricky task in case of the finite difference method, finite element method copes with them in a straightforward way.

Free surface represents the air-soil interface in our models. In a tunnel model, air-soil interfaces are the upper surface and all of the inner tunnel edges. In mathematical terms, the pressure is zero at a free surface. This is a Dirichlet boundary condition in the acoustic wave equation, whereas Neumann boundary condition in the elastic wave equation.

2.4.2 Absorbing boundaries

The domain of a tunnel is so big that it is considered as infinite in theory. However, it is interesting to know the solution only in a small portion of the whole domain. Furthermore, it is desired to have not a big numerical model in order to have inexpensive computation. These factors play decisive role in having a smaller numerical model than the real model. Smaller domain imposes artificial edges which pollute the solution in the numerical model. We describe the artificial boundary technique we used in our model in the next section.

3 Absorbing boundaries

As mentioned in the previous section, the numerical models are usually chosen much smaller than the real models in order to minimize the computational cost. This results in artificial boundaries in the numerical model and they cause pollutions in the solution of the waves; the waves are reflected back from the artificial boundaries and the domain is polluted with spurious reflected waves. To model the waves precisely, we need to avoid the pollution by spurious waves by using absorbing boundary techniques. This is a crucial step in having a precise forward model.

Several absorbing boundary techniques to tackle artificial boundaries have been investigated and developed by researchers. Paraxial approximation of waves is one technique used to suppress the spurious reflected waves. Low-order paraxial approximations suppress the waves with very low incidence angles quite well, [Engquist and Majda, 1977], [Clayton et al. 1980]. However, waves with big incidence angles are not handled precisely. High-order approximations, [Keys, 1985], [Higdon, 1991], cope with this problem better, although it is not perfect. We describe this method in a separate section because paraxial approximation is a conventional absorbing boundary technique.

Another method to deal with artificial boundaries is a sponge absorbing method
[Cerjan et al. 1985] whose implementation in wave equations is very simple. The idea of this method is to represent artificial boundary with a damping zone within which the wave is multiplied with a Gaussian function which decays exponentially and forces the waves to be attenuated inside the absorbing layer such that the waves are not reflected back. This method is practical and precise. It can handle waves with big incidence angles as well as small incidence angles efficiently. However, the damping zone must be thick to damp the spurious waves. Because of the thick damping zone, the computational cost increases significantly, especially in 3D simulations.

Perfectly matched layers (PML) is recently very widely used as an absorbing boundary technique. It was first introduced by Berenger [Berenger, 1994] to overcome artificial boundaries in Maxwell's equation. The robustness, efficiency and practicality of this method were noticed by researchers. It has been applied in other wave equations too and several derivations of this technique have been developed. It has been also applied to acoustic [Harari et al. 2000] and elastic wave equations ([Collina and Tsogka, 2001], [Komatitsch and Tromp, 2003],
[Festa and Vilotte, 2005], [Festa et al. 2005] and it is significantly successful to cope with artificial layers not only in terms of body waves, but also surface waves. The method reminds of sponge absorbing method as they both have a damping zone and the waves are forced to decay exponentially to zero. However, PML tackles the reflections in a more efficient way; very thin PML layers can absorb the spurious reflections from the artificial layers very effectively.

The choice of absorbing boundary method is very important in modelling the waves in an unbounded domain. In case a method does not absorb the incident waves properly in the time domain, the domain can be chosen much bigger than necessary and the simulation can be stopped before the reflected waves pollute the domain of interest. However, this increases the computational time and cost significantly. In a highly viscous medium, there is no need to make the

domain too big because the waves are damped till they reach the artificial layers. Nevertheless, we try to keep the computational cost minimum and to have good absorption of both body and surface waves at the absorbing layers. Moreover, we try to choose such a method that has a simple implementation in the wave equations.

3.1 Paraxial approximations

As in [Fichtner, 2011], we consider the acoustic equation in the time domain (equation 2.24) in a homogeneous and source-free ($\widetilde{f} = 0$) acoustic medium. Since the wave solution is a linear combination of plane waves, we substitute

$$p = \exp(i(\boldsymbol{k} \cdot \boldsymbol{x} - \omega t)) \tag{3.1}$$

plane waves in the wave equation and obtain

$$\frac{\omega^2}{c^2} - k_x^2 - k_y^2 - k_z^2 = 0 \tag{3.2}$$

where $\boldsymbol{k} = (k_x, k_y, k_z)$ is the wave number vector. As a result, one can obtain k_z as

$$k_z = \pm\frac{\omega}{c}\sqrt{1 - \frac{c^2}{\omega^2}(k_x^2 + k_y^2)} \tag{3.3}$$

The spurious waves reflected at a artificial boundary propagates in opposite direction to the incident wave. According to this fact, the aim of paraxial approximations technique is to suppress $k_z < 0$ which account for the reflected waves in negative z direction and to allow only $k_z > 0$ which accounts for the waves propagating in positive z direction. In other words, only positive k_z is taken into account

$$k_z = \frac{\omega}{c}\sqrt{1 - \frac{c^2}{\omega^2}(k_x^2 + k_y^2)}. \tag{3.4}$$

The partial derivative of the plane wave in the equation 3.1 with respect to z

$$\partial_z p = \partial_z \exp(i(\boldsymbol{k} \cdot \boldsymbol{x} - \omega t)) = ik_z \exp(i(\boldsymbol{k} \cdot \boldsymbol{x} - \omega t)) \tag{3.5}$$

leads to the equation

$$\left[\partial_z - i\frac{c}{\omega}\sqrt{1 - \frac{c^2}{\omega^2}(k_x^2 + k_y^2)}\right] p(k_x, k_y, z, \omega) = 0. \tag{3.6}$$

The square root is expanded by truncated Taylor series

$$\frac{ck_z}{\omega} = 1 + O\left(\left|\frac{c^2}{\omega^2}(k_x^2 + k_y^2)\right|\right), \tag{3.7}$$

$$\frac{ck_z}{\omega} = 1 - \frac{1}{2}\left[\frac{c^2}{\omega^2}(k_x^2 + k_y^2)\right] + O\left(\left|\frac{c^2}{\omega^2}(k_x^2 + k_y^2)\right|^2\right) \tag{3.8}$$

which are called A1 and A2 paraxial approximations, respectively. The equations are transformed into the time domain and the following wave equations

$$\dot{p} + c\partial_z p = 0, \tag{3.9}$$

$$\ddot{p} + c\partial_z \dot{p} - \frac{1}{2}c^2(\partial_x^2 + \partial_y^2)p = 0 \tag{3.10}$$

are formed. The square root can be approximated in other ways to have a better absorption at the artificial layers, which can lead to other wave equations ([Claerbout, 1979], [Zhang, 1985]). To investigate the effectiveness of A1 and A2 paraxial approximations, again as in [Fichtner, 2011], we split the plane wave into the plane wave propagating in positive z direction, p^+, and the reflected plane wave moving in negative z direction, u-

$$p = p^+ + Rp^- \tag{3.11}$$

with

$$p^+ = e^{i(k_x x + k_y y + k_z z - \omega t)}, \tag{3.12}$$

and

$$p^- = e^{i(k_x x + k_y y - k_z z - \omega t)} \tag{3.13}$$

where R defines the amplitude of the spurious waves. The angle between $\boldsymbol{k}$ and the x-axis, and the angle between $\boldsymbol{k}$ and the z-axis are denoted by ϕ and θ, respectively. Then $\boldsymbol{k}$ can be mathematically represented as

$$\boldsymbol{k} = \begin{pmatrix} \cos\phi \, \sin\theta \\ \sin\phi \, \sin\theta \\ \cos\theta \end{pmatrix}. \tag{3.14}$$

In case of a perfect absorption, the equality

$$R = 0 \tag{3.15}$$

has to be fulfilled. We assume that the artificial layer is at the position $z = 0$. Inserting 3.11 in the paraxial approximations A1 and A2, R is calculated as

$$R = -\frac{1 - \cos\theta}{1 + \cos\theta} \tag{3.16}$$

in A1 condition, and

$$R = -\frac{(1 - \cos\theta)^2}{(1 + \cos\theta)^2} \tag{3.17}$$

in A2 condition. In both cases, R is a function of the incident angle θ. It is clearly seen that R is smaller in case of A2 because it is higher order than A1. If the incident angle is small enough, the amplitudes of the spurious waves are also very small. However, for little bigger angles the spurious waves become big. As θ approaches to π, the reflected waves becomes significantly big. Higher-order approximation can reduce the amplitudes of the spurious waves, [Higdon, 1990], [Keys, 1985], [Clayton et al. 1980]. Nevertheless, higher-order approximations

end up with wave equations which contain higher-order spatial derivatives which are computationally very expensive and which are not trivial to implement.

The paraxial approximation method is not only applied to acoustic wave equation, but it can also be used in case of the elastic wave equation, [Fichtner, 2011]. However, in some cases, the numerical problem is associated with instability problems, [Emerman and Stephen, 1983], [Mahrer, 1986], [Mahrer, 1990], [Simone and Hestmolm, 1998].

This method has been widely used and investigated by researchers for many years. They have improved the method with different higher-order approximations and applied it to different wave equations. However, there are always some errors due to spurious waves reflected from the artificial layers. Apart from the body waves, in case of shallow models, the reflection of surface waves from the artificial bottom boundary is another problem this method cannot handle well.

When it comes to implementation of paraxial approximations technique, there are two wave equations which have to be solved on the artificial layers which may make it less practical to implement.

3.2 Perfectly-matched layers

PML is computationally cheap and only very thin damping zone is enough to absorb the incident ways and prevent the reflections from the artificial layers regardless of the frequency and the incidence angle. The first PML application was based on the field splitting; each field component in Maxwell's equation was split in two in a two-dimensional space. This ends up in more variables, especially in the three-dimensional case as the field components are then split into three. Moreover, applying split-field formulation to numerical methods is not very practical. After Berenger's work, noticing the practicality and efficiency of PML technique, researchers conducted more investigations on it and developed the method further. Stretching complex coordinate [Chew and Weedon, 1994] is not of the important discoveries to make the PML formulation easier and better understandable. Furthermore, anisotropic PML in Maxwell's equation [Sacks et al., 1995] showed that it was possible to avoid field-splitting. This, in turn, brought a lot of flexibility to implement numerical models with finite element and finite difference methods.

In contrast to paraxial approximations, there are no numerical instability issues in application of PML technique to the elastic wave equation. Furthermore, PML can be implemented such that it can also absorb the Rayleigh surface waves, but not only body waves [Festa et al. 2005]. Anisotropic PML in elastic wave equation [Zheng and Huang, 2002] eases the implementation of the method without requiring field-splitting which increases the variables in the damping zone.

The basic idea of PML is to introduce a damping zone around the area of interest which is supposed to absorb the energy of waves reaching the artificial boundaries as shown in Figure 3.1.

First we consider the case where the domain is infinite in x-direction. The same approach is applied to the y-direction. In this study, we follow the complex coordinate stretching approach [Chew and Weedon, 1994], [Chew and Liu, 1996]. Inside the damping zone, a complex coordi-

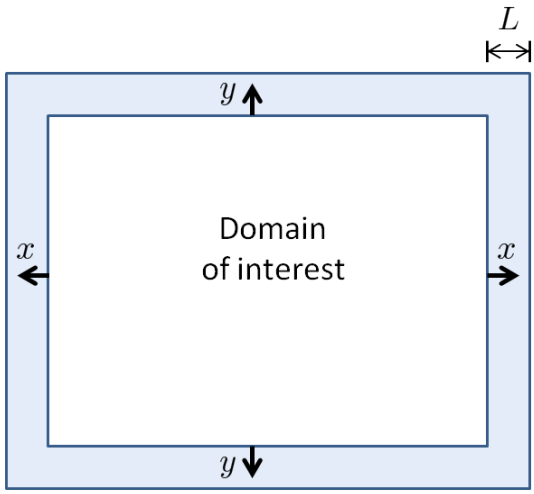

Figure 3.1: Perfectly-matched layer (PML)

nate

$$\widetilde{x} = x^0 + \int_{x^0}^{x} \varepsilon_x(x')dx', \tag{3.18}$$

is introduced instead of the real coordinate. Here, ε_x is a complex function of the local variable x (see Fig. 3.1). We show in following subsections how the complex coordinate is substituted in the wave equations to which some mathematical tricks are applied to have a convenient formulation in the end.

In this work, we appeal to two types of PML: standard PML and convolutional PML. The complex function ε_x defines whether PML is standard or convolutional. Standard PML is represented by

$$\varepsilon_x(x) = 1 + i\gamma_x(x)/\omega \tag{3.19}$$

where γ_x represents PML damping behavior and it is zero outside the PML region. The γ function we use throughout this study is

$$\gamma_x(x) = c_{\text{pml}}(1 - \cos(\frac{\pi}{2}\frac{x}{L})), \quad x \in [0, L] \tag{3.20}$$

where L is the width of the PML layer and c_{pml} is a parameter which has to be chosen correctly. $x = 0$ is the point where the PML region starts, whereas $x = L$ is the point where the PML region ends. Since $\gamma_x(x = 0) = 0$ and $\gamma_x(x = L) = c_{\text{pml}}$, γ_x increases from zero to c_{pml} from the beginning till the end of the PML layer.

To see how effective standard PML is in damping the incident body waves at absorbing layers, we consider plane body waves in equation (2.14). As in [Festa et al. 2005], the complex coordinate $\tilde{x}$ in (3.18) can be rewritten as

$$\tilde{x} = x + \frac{\kappa(x)}{i\omega} \tag{3.21}$$

where $\kappa(x)$ is a function of x starting from zero at the interface of PML and the domain and growing to its maximum at the end of PML layer. We substitute the complex coordinate in the plane body waves

$$\boldsymbol{u} = \boldsymbol{A}e^{i(\omega t - k_x x - k_y y)} \tag{3.22}$$

in PML which leads to

$$\tilde{\boldsymbol{u}} = \boldsymbol{u} e^{-\frac{k_x}{\omega}\kappa}. \tag{3.23}$$

Since $\frac{k_x}{\omega} = c$ is constant, the body waves in PML become independent of frequency and decay exponentially. We can conclude that with a right choice of the function γ_x a standard PML layer can prevent the reflection of body waves on a artificial layer very well. However, this fact does not guarantee that a standard PML layer can also absorb surface Rayleigh waves well. Plane Rayleigh waves are mathematically described in [Achenbach, 1984] and [Aki and Richards, 2011]. As in [Festa et al. 2005], we use this description to see what happens to Rayleigh waves in a standard PML absorbing layer. In [Achenbach, 1984], the two horizontal and vertical components of plane Rayleigh waves in a two-dimensional plane is given by

$$u_x = \left[A_1 e^{-b_1 y} + A_2 e^{-b_2 y}\right] e^{[ik(x-ct)]} \tag{3.24}$$

$$u_y = \left[-\frac{b1}{ik} A_1 e^{-b_1 y} + \frac{ik}{b_2} A_2 e^{-b_2 y}\right] e^{[ik(x-ct)]} \tag{3.25}$$

with

$$b_1 = k(1 - \frac{c^2}{v_p^2})^{\frac{1}{2}} = \omega d_1, \qquad b_2 = k(1 - \frac{c^2}{v_s^2})^{\frac{1}{2}} = \omega d_2 \tag{3.26}$$

where v_p, v_s and c are pressure, shear and Rayleigh wave speeds, respectively. The surface waves decays exponentially in vertical direction as it can also be seen from the equations above. These waves still hit the bottom of the model which is not x direction, but y direction. We replace the y coordinate by its complex counterpart to investigate what happens to surface waves in PML layers in y direction. As a result, u_x and u_y turn out to be

$$u_x = \left[A_1 e^{-\omega y d_1} e^{-i d_1 \kappa} + A_2 e^{-\omega y d_2} e^{-i d_2 \kappa}\right] e^{[ik(x-ct)]} \tag{3.27}$$

$$u_y = \left[-\frac{b1}{ik} A_1 e^{-\omega y d_1} e^{-i d_2 \kappa} + \frac{ik}{b_2} A_2 e^{-\omega y d_2} e^{-i d_2 \kappa}\right] e^{[ik(x-ct)]} \tag{3.28}$$

in PML layers in the vertical direction. The term $e^{-id_2\kappa}$ is a sinusoidal term independent of the frequency where κ ranges from zero to its maximum value in the PML layer. On the other hand, if ωy is very small and tends to be very close to zero, the terms $e^{-\omega y d_1}$ and $e^{-\omega y d_2}$ approach to one; in other words, u_x and u_y surface waves are converted into body waves in PML layer in y direction if ωy is small enough. Standard PML do not handle surface waves well in vertical PML layer for very low frequencies and very shallow profiles. In contrast to standard PML, convolutional PML copes very well with the surface waves [Festa et al. 2005].

As mentioned before, the basic idea of PML is to stretch the coordinate in the complex plane. The differences between standard and convolutional PMLs are the stretching functions. In convolutional PML this function is

$$\varepsilon_x(x) = 1 + \frac{\gamma_x(x)}{\omega_c + i\omega}. \tag{3.29}$$

Through the equation (3.18), the complex coordinate in PML region becomes

$$\varepsilon_x(x) = x + \frac{\kappa(x)}{\omega_c + i\omega}. \tag{3.30}$$

Again, we replace the real coordinate x_2 by its complex counterpart to investigate what happens to body and surface waves in the PML layers. First, we replace x coordinate by its complex coordinate $\tilde{x}$ in body waves which reduces down to

$$\tilde{\boldsymbol{u}} = \boldsymbol{u} e^{-ik_x\kappa\frac{\omega_c}{\omega^2+\omega_c^2}} e^{-k_x\kappa\frac{\omega}{\omega^2+\omega_c^2}}. \tag{3.31}$$

The term $\frac{\omega}{\omega^2+\omega_c^2}$ can be forced to be greater than some positive constant with a right selection of ω_c and as a result, an exponential decay is imposed on the waves with increasing κ. However, this time, the decay is frequency dependent in contrast to the standard PML. Fortunately, this dependency can be controlled by the right choice for ω_c.

Next, to see what happens to surface waves in PML layers in y direction we apply the complex stretched coordinate to the plane surface waves where the decay terms $e^{[-\omega y d_j]}$ reduce down to

$$e^{-\kappa\frac{\omega\omega_c}{\omega^2+\omega_c^2}d_j} e^{-i\kappa\frac{\omega^2}{\omega^2+\omega_c^2}d_j} \tag{3.32}$$

where the exponential decay term going to zero with order $\frac{\omega}{\omega_c}$ ([Festa et al. 2005]). Thus, convolutional PMLs are successful in handling both body and surface waves even at very low frequencies and in shallow domains if the constant ω_c and the function γ are chosen right. Standard PML is also very effective in absorbing body waves under any circumstance. The surface waves are also absorbed effectively either if the frequency is high enough or if the model is not shallow. In case of a shallow model and low frequency, convolutional PML are preferred.

3.2.1 Perfectly-Matched Layers (PML) in Acoustic Wave Equation

By using chain rule and the relation between the complex coordinate $\widetilde{x}$ and x, the differential operator

$$\frac{\partial}{\partial\widetilde{x}} = \frac{\partial x}{\partial\widetilde{x}}\frac{\partial}{\partial x} = \frac{1}{\varepsilon_x}\frac{\partial}{\partial x} \tag{3.33}$$

is introduced.

Inside the PML region, coordinates and the differential operators are replaced by their complex counterparts in the acoustic equation (2.25). ε_x and ε_y are complex numbers and their imaginary parts account for absorption of waves in PMLs. After inserting the differential operators for the x and y-directions by their complex counterparts (3.33), the acoustic equation becomes

$$\frac{\omega^2}{c^2}p_\omega + \frac{1}{\varepsilon_x(x)}\frac{\partial}{\partial x}\frac{1}{\varepsilon_x(x)}\frac{\partial p_\omega}{\partial x} + \frac{1}{\varepsilon_y(y)}\frac{\partial}{\partial y}\frac{1}{\varepsilon_y(y)}\frac{\partial p_\omega}{\partial y} = 0 \tag{3.34}$$

in PML region where at least one of ε_x and ε_y is different from one. Applying the product rule, equation (3.34) is reformulated as

$$\frac{\omega^2}{c^2}\varepsilon_x\varepsilon_y p_\omega + \nabla\cdot(\mathbf{D}\nabla p_\omega) = 0 \tag{3.35}$$

where

$$\mathbf{D} = \begin{bmatrix} \frac{\varepsilon_y}{\varepsilon_x} & 0 \\ 0 & \frac{\varepsilon_x}{\varepsilon_y} \end{bmatrix} \tag{3.36}$$

in 2D and

$$\mathbf{D} = \begin{bmatrix} \frac{\varepsilon_y \varepsilon_z}{\varepsilon_x} & 0 & 0 \\ 0 & \frac{\varepsilon_x \varepsilon_z}{\varepsilon_y} & 0 \\ 0 & 0 & \frac{\varepsilon_x \varepsilon_y}{\varepsilon_z} \end{bmatrix} \tag{3.37}$$

in 3D [Zheng and Huang, 2002].

3.2.2 Perfectly-Matched Layers (PML) in Elastic Wave Equation

Field-splitting makes implementation of PML inconvenient and increases the computational cost because every field component is divided into subcomponents. Anisotropic PML [Zheng and Huang, 2002] does not require field-splitting; it can be used to make the implementation of PML in the elastic wave equation simple and to have no need to split the components.

We use convolutional PML in the case of the elastic waves to prevent the transformation of surface waves to body waves in the bottom PML layer if the domain is shallow.

By applying complex coordinate (3.18) to the elastic wave equation (2.17) and considering the fact that source function $f(\mathbf{x}, \omega)$ is zero in the PML region, the wave equation in the PML layer takes the form

$$-\rho\omega^2 \mathbf{u} = \nabla_\xi \cdot \sigma \tag{3.38}$$

where $\nabla_\xi = \frac{1}{\xi_{x_i}} \frac{\partial}{\partial x_i} e_i$. For the sake of simplicity, x_i represents x, y, and z for $i = 1, 2, 3$, respectively. A new tensor $\widetilde{\sigma} = \frac{\varepsilon_x \varepsilon_y \varepsilon_z}{\varepsilon_{x_i}} \sigma_{ij} e_i e_j$ is introduced so that (3.38) can take the form

$$-\rho\omega^2 \varepsilon_x \varepsilon_y \varepsilon_z \mathbf{u} = \nabla \cdot \widetilde{\sigma}. \tag{3.39}$$

$\widetilde{\mathbf{C}}$ is introduced whose entries are

$$\widetilde{C}_{ijkl} = C_{ijkl} \frac{\varepsilon_x \varepsilon_y \varepsilon_z}{\varepsilon_{x_i} \varepsilon_{x_k}}. \tag{3.40}$$

This is where the anisotropy comes into play in the PML region. (3.39) can be rewritten as

$$-\rho\omega^2 \varepsilon_x \varepsilon_y \varepsilon_z \mathbf{u} = \nabla \cdot (\widetilde{\mathbf{C}} : \nabla \mathbf{u}). \tag{3.41}$$

4 Fourier transformation

Fourier transformation [Williams, 1999] is an important part of this work since we need to go back and forth between time and frequency domains all the time. We solve the forward problem in the frequency domain. However, to have a better understanding of the seismograms, it is necessary to transform the data to the time domain by inverse Fourier transformation. Apart from this, in real world, or in blind test such as in the inversion results section, the data is first in time domain. To perform inversion in frequency domain, it is inevitable to use forward Fourier transformation and obtain data in frequency domain. The forward Fourier transformation is associated with the integral

$$F(\omega) = \int_{-\infty}^{\infty} f(t) e^{-i\omega t} dt, \tag{4.1}$$

whereas the inverse Fourier transformation is

$$f(t) = \frac{1}{2\pi} \int_{-\infty}^{\infty} F(\omega) e^{i\omega t} d\omega. \tag{4.2}$$

In this work, we solve the wave equation in the frequency domain; in other words, we solve time harmonic wave equation. Nevertheless, it is not possible to generate harmonic waves in a real life application such as in a tunnel environment. However, the generated waves can be approximated as the superposition of the time harmonic waves. We can write the acoustic and elastic wave equations in general form

$$\left(\frac{\partial^2}{\partial t^2} + L_{\boldsymbol{x}} \right) \tilde{\boldsymbol{u}}(\boldsymbol{x}, t) = \boldsymbol{f}(\boldsymbol{x}, t) \tag{4.3}$$

where $L_{\boldsymbol{x}}$ is a linear differential operator. $\boldsymbol{u}$ is scalar and vector in the case of acoustic and elastic equations, respectively. We can separate the dependency of the source function $f(\boldsymbol{x}, t)$ on time and space by

$$\boldsymbol{f}(\boldsymbol{x}, t) = \tilde{f}_t(t) \boldsymbol{f}_{\boldsymbol{x}}(\boldsymbol{x}) \tag{4.4}$$

where $\tilde{f}_t$ and $\boldsymbol{f}_{\boldsymbol{x}}$ depend only on time and space, respectively. We now multiply both sides of (4.3) with $e^{-i\omega t}$ and integrate over $(-\infty, \infty)$:

$$\int_{-\infty}^{\infty} \frac{\partial^2 \tilde{\boldsymbol{u}}(\boldsymbol{x}, t)}{\partial t^2} e^{-i\omega t} dt + \int_{-\infty}^{\infty} L_{\boldsymbol{x}} \tilde{\boldsymbol{u}}(\boldsymbol{x}, t) e^{-i\omega t} dt = \int_{-\infty}^{\infty} \tilde{f}_t(t) f_{\boldsymbol{x}}(\boldsymbol{x}) e^{-i\omega t} dt. \tag{4.5}$$

The second term on the left hand side and the term on the right hand side are easily suited to Fourier transformation integral:

$$\int_{-\infty}^{\infty} L_{\boldsymbol{x}} \tilde{\boldsymbol{u}}(\boldsymbol{x}, t) e^{-i\omega t} dt = L_{\boldsymbol{x}} \int_{-\infty}^{\infty} \tilde{\boldsymbol{u}}(\boldsymbol{x}, t) e^{-i\omega t} dt = L_{\boldsymbol{x}} \boldsymbol{u}(\boldsymbol{x}, \omega), \tag{4.6}$$

$$\int_{-\infty}^{\infty} \tilde{f}_t(t) f_{\boldsymbol{x}}(\boldsymbol{x}) e^{-i\omega t} dt = f_{\boldsymbol{x}}(\boldsymbol{x}) \int_{-\infty}^{\infty} \tilde{f}_t(t) e^{-i\omega t} dt = f_{\boldsymbol{x}}(\boldsymbol{x}) f_\omega(\omega). \tag{4.7}$$

The first term can also be derived with Fourier transformation integral. We derive the relation between the Fourier transformation of the second derivative of a function and the Fourier transformation of the function itself by the inverse transformation:

$$\tilde{\boldsymbol{u}}(\boldsymbol{x}, t) = \frac{1}{2\pi} \int_{-\infty}^{\infty} \boldsymbol{u}(\boldsymbol{x}, \omega) e^{i\omega t} d\omega. \tag{4.8}$$

The second derivative of $\tilde{\boldsymbol{u}}(\boldsymbol{x}, t)$ with respect to t turns out to be

$$\begin{aligned} \frac{\partial^2 \tilde{\boldsymbol{u}}(\boldsymbol{x}, t)}{\partial t^2} = \frac{\partial^2}{\partial t^2} \left(\frac{1}{2\pi} \int_{-\infty}^{\infty} \boldsymbol{u}(\boldsymbol{x}, \omega) e^{i\omega t} d\omega \right) &= \frac{1}{2\pi} \int_{-\infty}^{\infty} (i\omega)^2 \boldsymbol{u}(\boldsymbol{x}, \omega) e^{i\omega t} d\omega \\ &= \frac{1}{2\pi} \int_{-\infty}^{\infty} -\omega^2 \boldsymbol{u}(\boldsymbol{x}, \omega) e^{i\omega t} d\omega \end{aligned} \tag{4.9}$$

which implies that

$$\int_{-\infty}^{\infty} \frac{\partial^2 \tilde{\boldsymbol{u}}(\boldsymbol{x}, t)}{\partial t^2} e^{-i\omega t} dt = -\omega^2 \boldsymbol{u}(\boldsymbol{x}, \omega). \tag{4.10}$$

the equation (4.7) can be rewritten as

$$\left(-\omega^2 + L_{\boldsymbol{x}}\right) \boldsymbol{u}(\boldsymbol{x}, \omega) = f_\omega(\omega) \boldsymbol{f}_{\boldsymbol{x}}(\boldsymbol{x}). \tag{4.11}$$

This equation is the time harmonic wave equation. In this study, we usually choose a nodal space dependent source term. For the sake of simplicity, we replace $\boldsymbol{f}_{\boldsymbol{x}}(\boldsymbol{x})$ with a vector $\boldsymbol{\delta}_k(\boldsymbol{x} - \boldsymbol{s})$ whose component k is a Dirac delta function $\delta(\boldsymbol{x} - \boldsymbol{s})$ where $\boldsymbol{s}$ is the source point. We can obtain the Green's function by dividing both sides by $f_\omega(\omega)$ which is nothing else but a scalar value for a single frequency:

$$\left(-\omega^2 + L_{\boldsymbol{x}}\right) \boldsymbol{G}(\boldsymbol{x}, \omega) = \boldsymbol{\delta}_k(\boldsymbol{x} - \boldsymbol{s}) \tag{4.12}$$

$\boldsymbol{u}(\omega)$ can be calculated by

$$\boldsymbol{u}(\boldsymbol{x}, \omega) = f_\omega(\omega) \boldsymbol{G}(\boldsymbol{x}, \omega) \tag{4.13}$$

The time domain seismograms are calculated by inverse Fourier transformation as

$$\boldsymbol{u}(\boldsymbol{x}, t) = \frac{1}{2\pi} \int_{-\infty}^{\infty} \boldsymbol{u}(\boldsymbol{x}, \omega) e^{i\omega t} = \frac{1}{2\pi} \int_{-\infty}^{\infty} \boldsymbol{f}_\omega(\omega) G(\boldsymbol{x}, \omega) e^{i\omega t} \tag{4.14}$$

Reversing the process, we can obtain frequency domain data from the seismograms in the time domain by using Fourier transformation.

We use Ricker function, which is the second derivative of a Gaussian function, as the source functions $f_\omega(\omega)$. It is

$$f_r(t) = \left(1 - 2(\pi f_p [t - d_r])^2\right) e^{-(\pi f_p [t - d_r])^2} \tag{4.15}$$

in the time domain, and

$$F_r(\omega) = -\frac{2}{f_p\sqrt{\pi}}\left(\frac{\omega}{2\pi f_p}\right)^2 e^{\left(-id_r\omega-[\frac{\omega}{2\pi f_p}]^2\right)} \tag{4.16}$$

in the frequency domain where f_p is the peak frequency and d_r is the temporal delay. The Ricker wavelet $d_r = 0.5$ sec and $f_p = 50$ Hz is illustrated in Figures 4.1 and 4.2. It can be seen that the functions in both time and frequency domains decreases very rapidly towards zero outside the effective range of time and frequency, respectively; the time and frequency outside this range do not really contribute to the integral. This fact helps to convert the forward and inverse Fourier integrals over an infinite domain to an integral over a finite domain.

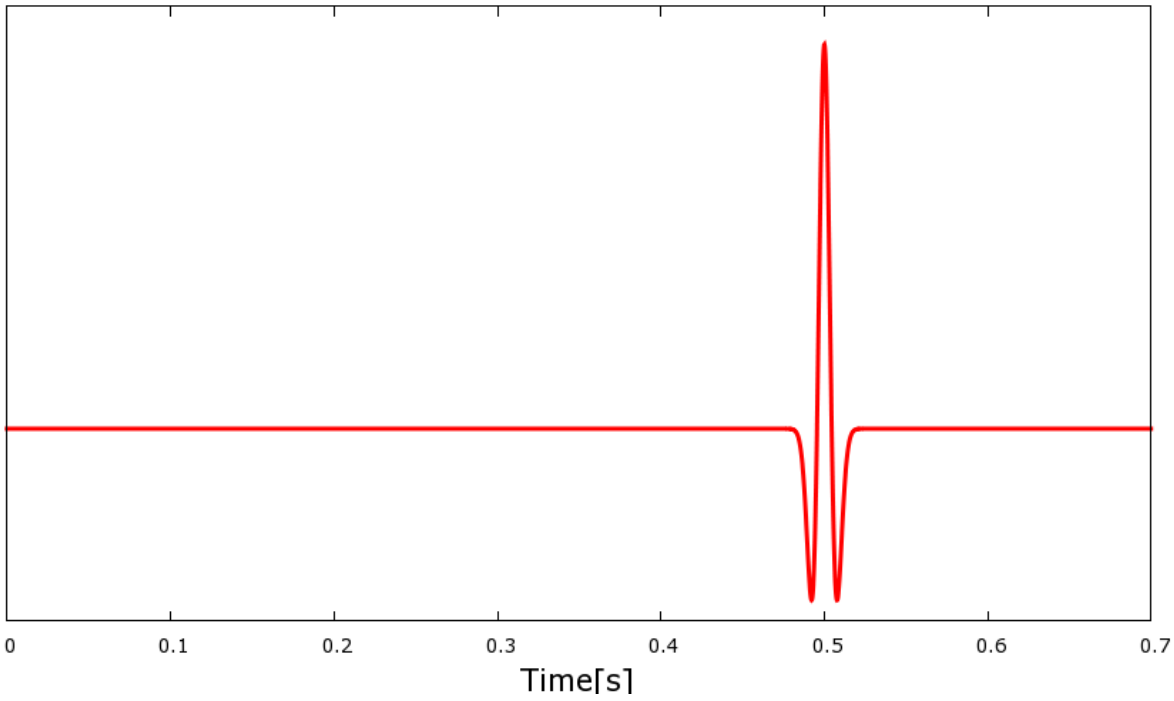

Figure 4.1: Ricker function in the time domain

$d_r = 0.5$ sec, $f_p = 50$ Hz

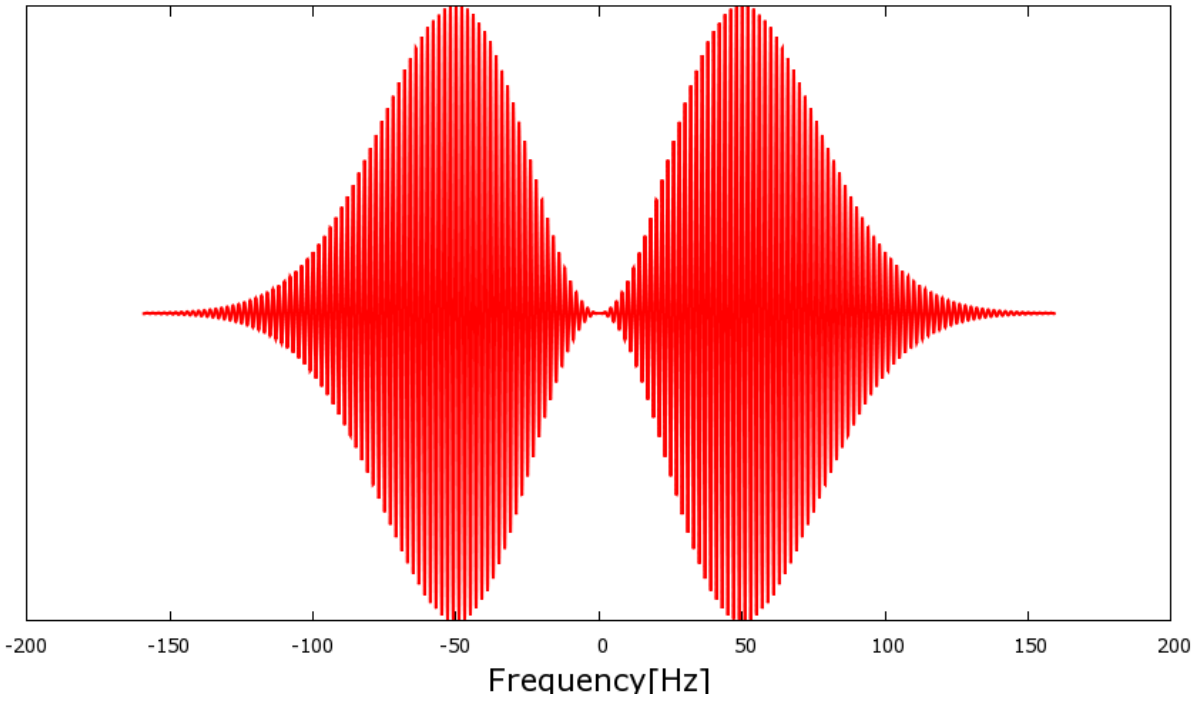

(a) Real part

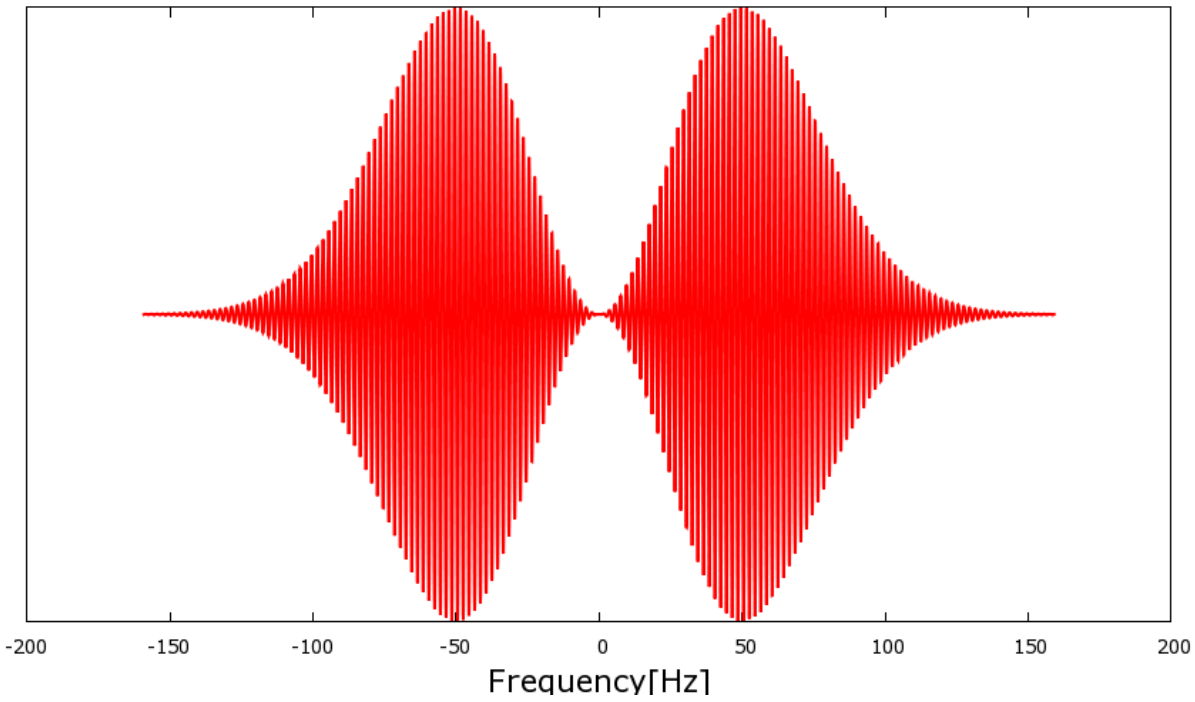

(b) Imaginary part

Figure 4.2: Ricker function in the frequency domain

$d_r = 0.5$ sec, $f_p = 50$ Hz

4.1 Fourier Series

We assume a periodic function $f(t)$ with period T, which implies $f(t+T) = f(t)$. Then, $f(t)$ can be represented by a Fourier series

$$f(t) = \frac{1}{2}a_0 + \sum_{n=1}^{\infty}\left[a_n \cos(\frac{2\pi nt}{T} + b_n \sin(\frac{2\pi nt}{T})\right]. \tag{4.17}$$

The conditions that this series converges to $f(t)$ is fulfilled if $f(t)$ and its first derivatives are piecewise continuous within each period [Achenbach, 1984]. The speed of the convergence of the Fourier series to the function $f(t)$ depends on the smoothness of $f(t)$; the series converges faster to smoother functions. To find coefficients a_n, we multiply both sides of (4.17) by $\cos(mx)$ and integrate over $[-T/2, T/2]$. Similarly, to find coefficients b_n, we multiply both sides by $\sin(nx)$ and integrate. By using orthogonality relations of $\sin$ and $\cos$ functions

$$\int_{-T/2}^{T/2} \cos(\frac{2\pi nt}{T})\ \cos(\frac{2\pi mt}{T})dt = \frac{1}{2}\,T\,\delta_{nm} \tag{4.18}$$

$$\int_{-T/2}^{T/2} \sin(\frac{2\pi nt}{T})\ \sin(\frac{2\pi mt}{T})\,dt = \frac{1}{2}\,T\,\delta_{nm} \tag{4.19}$$

$$\int_{-T/2}^{T/2} \cos(\frac{2\pi nt}{T})\ \sin(\frac{2\pi mt}{T})\,dt = 0, \tag{4.20}$$

where δ_{nm} is Kronecker delta

$$\delta_{mn} = \begin{cases} 1 \text{ if } m = n \\ 0 \text{ if } m \neq n. \end{cases} \tag{4.21}$$

The coefficients a_n and b_n are calculated as

$$a_n = \frac{2}{T}\int_{-T/2}^{T/2} f(t)\ \cos(\frac{2\pi nt}{T})\,dt, \tag{4.22}$$

$$b_n = \frac{2}{T}\int_{-T/2}^{T/2} f(t)\ \sin(\frac{2\pi nt}{T})\,dt, \tag{4.23}$$

$$a_0 = \frac{2}{T}\int_{-T/2}^{T/2} f(t)\,dt. \tag{4.24}$$

4.2 Discretization of the Fourier Transform

For our problems, the infinite integral of the Fourier transformation can be precisely approximated by the finite integral

$$F(\omega) = \int_{-\infty}^{\infty} f(t)\, e^{-i\omega t} dt \approx \int_{-L/2}^{L/2-\Delta t} f(t)\, e^{-i\omega t}\, dt \tag{4.25}$$

To convert the continuous Fourier transformation to discrete Fourier transformation, rectangular integration rule is applied. First, we need to discretize the functions $f(t)$ and $F(\omega)$ by N evenly spaced samples

$$\Delta x = \frac{L}{N} \tag{4.26}$$

$$x = q\Delta x, \quad q = -N/2, -N/2+1, ..., N/2-1 \tag{4.27}$$

To obtain a DFT formulation, we set

$$\Delta\omega = 2\pi/L. \tag{4.28}$$

$$\omega = q\Delta\omega, \quad q = -N/2, -N/2+1, ..., N/2-1. \tag{4.29}$$

After applying rectangular integration rule, equation (4.25) is transformed to discontinuous equation

$$F(m\Delta\omega) \approx \sum_{q=-N/2}^{N/2-1} f(q\Delta t)\, e^{-imq\Delta t\Delta\omega}\, \Delta t = \frac{L}{N} \sum_{q=-N/2}^{N/2-1} f(q\Delta t)\, e^{-i2\pi mq/N}. \tag{4.30}$$

4.3 Discretization of the Inverse Fourier Transform

To convert the continuous Fourier transformation to discrete inverse Fourier transformation, we assume that the infinite integral can be represented accurately by a finite integral

$$f(t) = \frac{1}{2\pi} \int_{-\infty}^{\infty} F(\omega)\, e^{i\omega t} d\omega \approx \frac{1}{2\pi} \int_{-L/2}^{L/2-\Delta\omega} F(\omega)\, e^{i\omega t}\, d\omega \tag{4.31}$$

Discretizing the functions $f(t)$ and $F(\omega)$ as in the previous section and applying rectangular integration, the equation for discrete inverse Fourier transformation

$$f(m\Delta t) = \frac{1}{2\pi} \sum_{q=-N/2}^{N/2-1} F(q\Delta\omega)\, e^{imq\Delta\omega\Delta t}\, \Delta\omega = \frac{1}{L} \sum_{q=-N/2}^{N/2-1} F(q\Delta\omega)\, e^{i2\pi mq} \tag{4.32}$$

is obtained.

4.4 Discussion

To transform the data in the frequency domain to the time domain, the effective frequency range has to be taken into account. To narrow frequency range results in a wrong interpretation of data in the time domain. On the other hand, too wide range makes the computational expensive because the frequencies outside the effective range do not really contribute to the overall integral. An optimal frequency step size is also very important in the transformation; too big step size makes the calculations wrong, whereas too small step size makes it computationally expensive.

Numerical simulations generate seismograms which cover only a limited time range. For the sake of not to have a very long simulation time, the seismograms are plotted only till some defined time. In real wave simulations in a domain such as a tunnel domain, the waves normally do not disappear for a very long time range for which numerical simulations cannot be run because of the computational cost. The seismograms stop fluctuating and drop to zero very rapidly at the last point in time of the simulation duration (Figure 4.3).

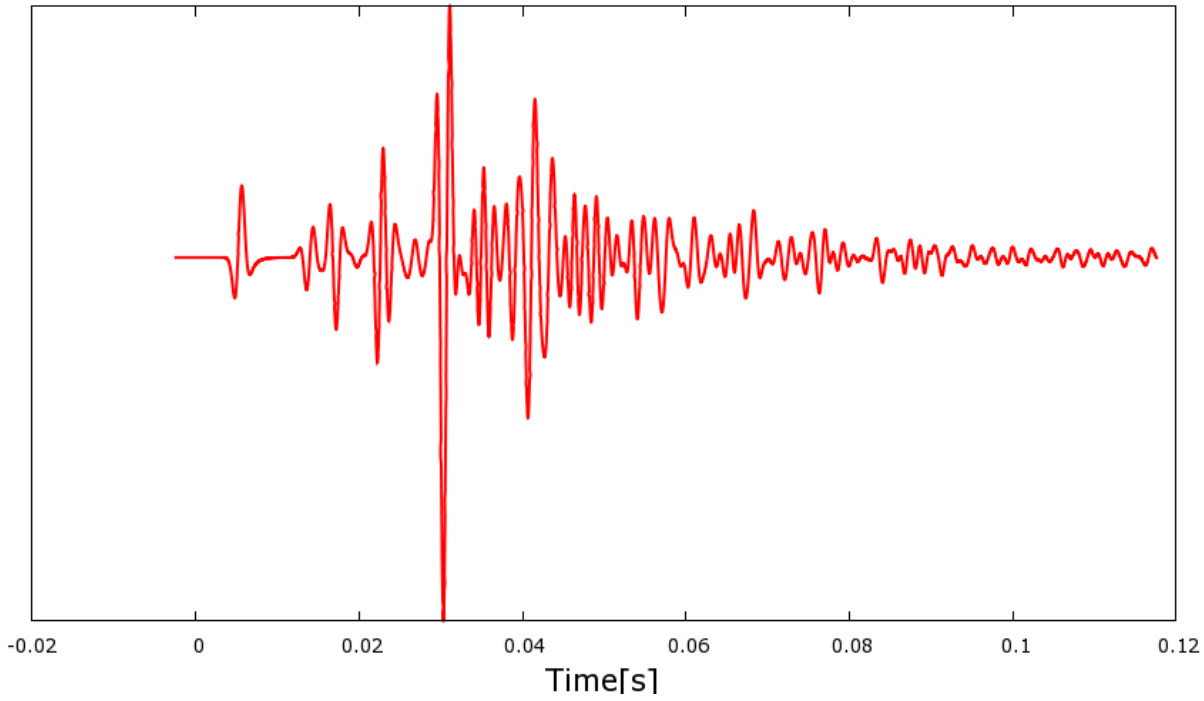

Figure 4.3: Seismogram with a rapid stop

This rapid drop changes the frequency content of the seismograms significantly. This is avoided by using a window function. In this work, we use a window function which is a constant function of value 1 in the first 90% of the time and $\cos$ function whose angle ranges linearly at the interval $[0, \pi/2]$ over the rest of the time (Figure 4.4).

Multiplying a seismogram with such a window function, it approaches to zero very smoothly at the very end of the seismogram rather than dropping to zero instantly (Figure 4.5). This, in turn, saves the frequency content of the seismogram from being polluted by a sudden drop in it.

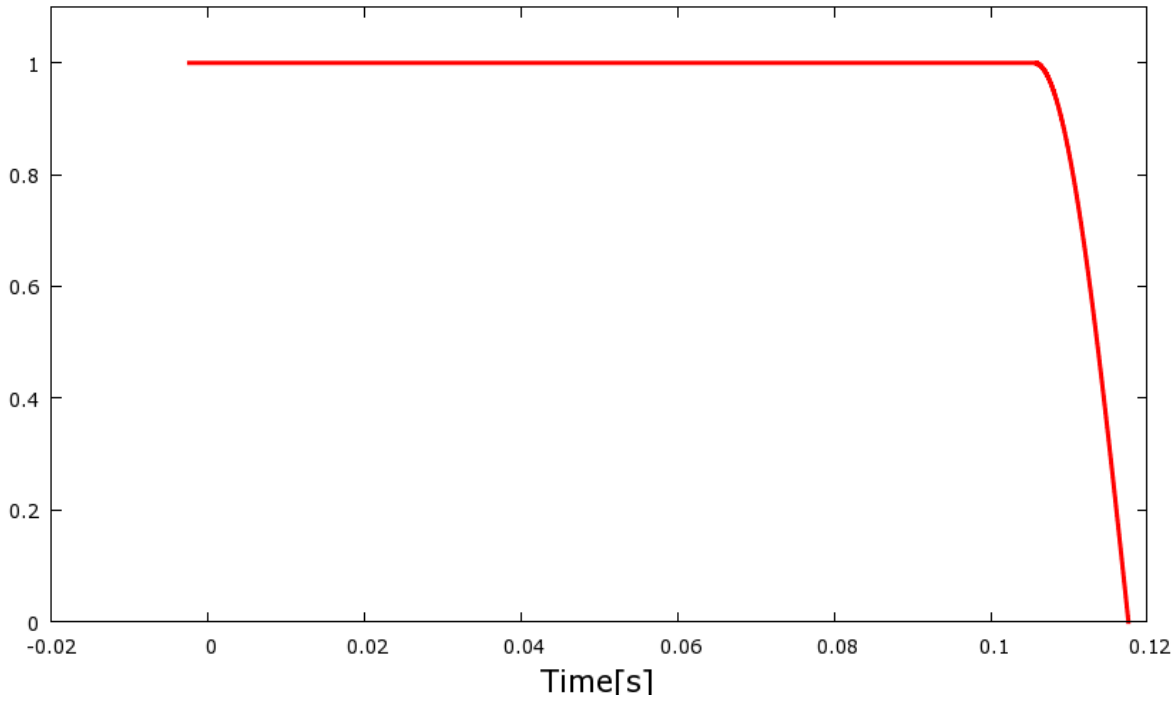

Figure 4.4: Sample window function

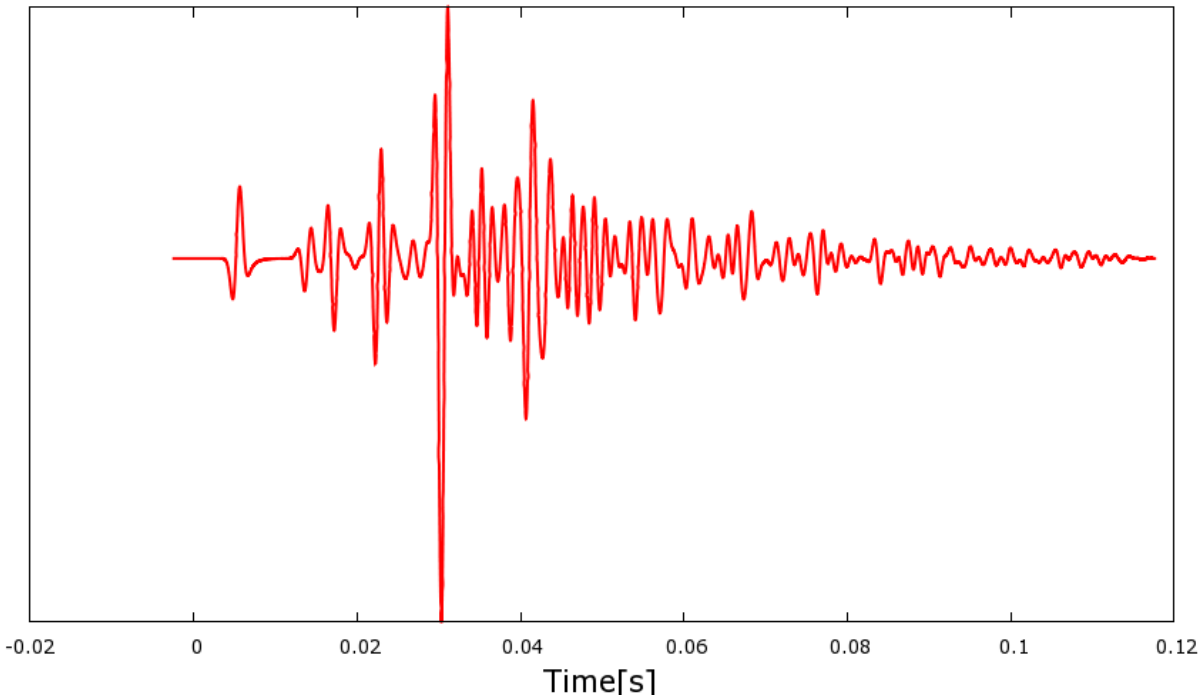

Figure 4.5: Seismogram multiplied with the window function

5 Numerical methods for wave equations

Analytical solutions of the wave equations are available only for some special cases; for example, the solutions are known for full-space, half-space and some bounded domains with a homogeneous material and materials with some regular heterogeneity. In the inverse simulations of our tunnel models, the forward model solved in each iteration is a randomly heterogeneous model. However, for an arbitrary domain with a random heterogeneity, numerical methods are required to solve the wave equations since the analytical solutions are not available. Finite difference and finite element methods are the numerical methods which are used the most frequently to model the propagation of waves by solving the wave equations. Both of the methods solve the equations by discretizing them.

Finite difference method is very frequently used in modelling the propagation of waves. The method is integrated very well into wave propagation problems, [Alterman and Karal, 1968], [Madariaga, 1967], [Virieux, 1984], [Dablain, 1986], [Kristek et al., 2002], [Moczo et al., 2002], [Wang et al., 2008].

5.1 Finite element method (FEM)

Higher-order finite element method, [Szabó and Babuška, 2011], is the numerical method used to model the waves throughout this work. It is a well-known numerical technique which is very often referred to by mathematicians, natural scientists and engineers both for real world and research problems. Mathematically speaking, it is a very effective technique to solve partial differential equations. When it comes to its application in real world problems, it has a wide range of application fields such as structural engineering, mechanical engineering, physics, geophysics, electrical engineering, aeronautical engineering and so on. After being researched by many scientists, several types of FE- such as spectral element method, discontinuous Galerkin method, extended finite element method, etc.- have been developed each of which is effective for some specific problems. However, we will mention only spectral element method and discontinuous Galerkin method because they are of interest in seismology.

The spectral element method, [Seriani and Priolo, 1994], [Priolo et al., 1994],
[Chaljub et al., 2007], [Komatitsch and Vilotte, 1998], is one of the most popular methods in seismology. The fame of this method underlies the fact that it provides diagonal mass matrix. Diagonal mass matrix is obtained by using Lagrange shape functions and Gauss-Lobatto-Legendre integration rule which makes all non-diagonal terms of the mass matrix zero. Using a right time integration scheme, the most time consuming part- solving system of linear equations- becomes computationally very cheap because a diagonal matrix stands on the left hand side which does not require any direct or indirect solver. Thus, the computation becomes significantly cheaper, which is very important especially in case of big scale problems which are very often encountered in the field of seismology. However, the method has its restrictions too; the chosen quadrature rule requires quadrangle meshes in 2D and hexahedral meshes in 3D. In some cases, triangular meshes in 2D and tetrahedral meshes in 3D are more convenient to

use. This is the motivation for using discontinuous Galerkin (DG), [Dumbser and Kaser, 2006], [Lambrecht and Friederich, 2013], method in seismology. Moreover, the neighboring elements are related with each other only by numerical fluxes at their boundaries. This fact provides flexibility to refine an element locally. Furthermore, this fact makes it very practical to implement the parallelized form of the method.

In this study, we use higher-order finite element method to solve the wave equations in the frequency domain; we use hierarchical shape functions which are not same as the shape functions of the spectral element method which offers very low computational cost in the time domain. However, in the frequency domain, there is a need for a direct or indirect solver to solve the system of linear equations because a time integration scheme is not used in the frequency domain. Thus, we do not expect much difference between using spectral element method and a normal higher-order finite element method in the frequency domain. High orders are important to model the waves correctly and it provides flexibility working with low and high frequencies using the same mesh only by changing the degree of FE polynomials. FE is a very general method and can be applied to solve many partial differential equations. The equations we solve are frequency acoustic and elastic wave equation. Application of FE starts with generating weak forms of equations from their strong form. Generation of weak forms of the wave equations and shape functions are described in the following sections.

Numerical methods transform partial differential equations into a system of linear equations

$$\boldsymbol{K}\boldsymbol{u} = \boldsymbol{f} \tag{5.1}$$

whose solution is computationally expensive especially for large systems. Here, $\boldsymbol{K}$ is a matrix which represents the system properties, $\boldsymbol{u}$ is a sought vector which represents the response of the system, and $\boldsymbol{f}$ is a vector which represents the source. In our inversion problems, the forward problem is solved for each of several source functions separately. In other words, the system of the linear equations has to be solved several times for the same system. In such a case, it is better to use direct methods; a direct method decomposes the matrix only once, and the system is solved for each source separately. The decomposition of a matrix is computationally much more expensive than solving a decomposed system, especially for large systems. We use sparse direct solvers as mentioned in the introduction.

5.1.1 Weak Formulation of the Acoustic Equation

In this section, the application of FE method to the acoustic wave equation is described in detail from mathematical point of view. We split the whole numerical domain Ω into domain of interest Ω_{doi} and absorbing domain Ω_{pml}. The numerical domain is surrounded by edges of PML layers Γ_{pml}, free surface which is Dirichlet boundary Γ_u, and Neumann boundary Γ_σ. In this case, $\partial\Omega = \Gamma_{\mathrm{pml}} \cup \Gamma_u \cup \Gamma_\sigma$ where $\partial\Omega$ is the border of the whole numerical domain. We apply Neumann boundary at Γ_{pml} too. First of all, we write down acoustic equation with all

boundary conditions as

$$\begin{cases} \boldsymbol{\nabla}(\boldsymbol{D}\boldsymbol{\nabla}p) + k^2\varepsilon_x\varepsilon_y p - f = 0 & \forall \boldsymbol{x} \in \Omega \\ \frac{\partial p}{\partial \tilde{\mathbf{n}}} = \tilde{\nabla}p \cdot \tilde{\mathbf{n}} = 0 & \forall \boldsymbol{x} \in \Gamma_{pml} \\ \frac{\partial p}{\partial \mathbf{n}} = \nabla p \cdot \mathbf{n} = 0 & \forall \boldsymbol{x} \in \Gamma_{\sigma} \\ p = 0 & \forall \boldsymbol{x} \in \Gamma_{u}. \end{cases} \tag{5.2}$$

Here, $\boldsymbol{D}$ is the matrix defined in the equations (3.36) and (3.37). For simplicity we replace $\frac{\omega}{c}$ by wavenumber k. Here, f = 0 in Ω_{pml} as we do not trigger the waves from the domain which is only responsible to absorb the coming waves properly. Inside the domain of interest, we have only real coordinate system, which implies that $\gamma_x = \gamma_y = 0$ and $\varepsilon_x = \varepsilon_y = 1$ in Ω_{doi}. The complex coordinate and complex norm vector $\tilde{\mathbf{n}} = \frac{\nabla\tilde{\Gamma}_\sigma}{\|\tilde{\nabla}\Gamma_\sigma\|}$ can be represented by their real counterparts with the help of the chain rule. Using the relation $\frac{\partial}{\partial\tilde{x}_i} = \frac{1}{\varepsilon_i}\frac{\partial}{\partial x_i}$ which is derived by the chain rule

$$(\tilde{\nabla}p)_i = \frac{\partial p}{\partial \tilde{x}_i} = \frac{1}{\varepsilon_i}\frac{\partial p}{\partial x_i} \tag{5.3}$$

$$(\tilde{\nabla}\Gamma_\sigma)_i = \frac{\partial \Gamma_\sigma}{\partial \tilde{x}_i} = \frac{1}{\varepsilon_i}\frac{\partial \Gamma_\sigma}{\partial x_i} \tag{5.4}$$

and the Neumann boundary condition at Γ_{pml} takes the form

$$\begin{aligned} &\frac{1}{(\varepsilon_x)^2}\frac{\partial p}{\partial x}\frac{\partial \Gamma_{pml}}{\partial x}\frac{1}{\|\nabla\Gamma_{pml}\|} + \frac{1}{(\varepsilon_y)^2}\frac{\partial p}{\partial y}\frac{\partial \Gamma_{pml}}{\partial y}\frac{1}{\|\nabla\Gamma_{pml}\|} = 0 \\ &\Leftrightarrow \frac{\varepsilon_y}{\varepsilon_x}\frac{\partial p}{\partial x}n_1 + \frac{\varepsilon_x}{\varepsilon_y}\frac{\partial p}{\partial y}n_2 = 0 \\ &\Longrightarrow \frac{\partial p}{\partial \tilde{n}} = \mathbf{D}\nabla p \cdot \mathbf{n} = 0. \end{aligned} \tag{5.5}$$

Now, test function $w : \Omega_{\text{doi}} \to \mathbb{C}$ is chosen and it has the following properties:

- w satisfies the geometrical boundary conditions $w = 0 \ \forall \ \boldsymbol{x} \in \Gamma_u$
- w is infinitesimal
- w is arbitrary

To obtain the weak form of the equation, the strong form is multiplied with w and integrated over the whole domain Ω

$$\int_\Omega w\left[\nabla \cdot (\mathbf{D}\nabla p) + k^2\varepsilon_x\varepsilon_y p - f\right] d\Omega = 0 \tag{5.6}$$

$$\Leftrightarrow \int_\Omega w\left[\nabla \cdot (\mathbf{D}\nabla p)+\right] d\Omega + \int_\Omega k^2\varepsilon_x\varepsilon_y p = \int_\Omega w f d\Omega. \tag{5.7}$$

After applying the product rule

$$\nabla \cdot [w\mathbf{D}\nabla p] = w\left[\nabla \cdot (\mathbf{D}\nabla p)\right] + \nabla w \cdot [\mathbf{D}\nabla p] \tag{5.8}$$

the equation takes the form

$$\Leftrightarrow \int_\Omega \nabla \cdot [w\mathbf{D}\nabla p]\, d\Omega - \int_\Omega \nabla w \cdot [\mathbf{D}\nabla p]\, d\Omega + \int_\Omega w k^2 \varepsilon_x \varepsilon_y \, d\Omega = \int_\Omega w f \, d\Omega. \tag{5.9}$$

Gauss theorem is used to convert the integral over the domain to an integral over the boundary

$$\int_\Omega \nabla \cdot [w\mathbf{D}\nabla p]\, d\Omega = \int_\Gamma w\mathbf{D}\nabla p \cdot n \, d\Gamma$$

$$= \int_{\Gamma_u} w\mathbf{D}\nabla p \cdot n \, d\Gamma_u + \int_{\Gamma_{\text{pml}}} w\mathbf{D}\nabla p \cdot \mathbf{n} \, d\Gamma_{\text{pml}} + \int_{\Gamma_\sigma} w\mathbf{D}\nabla p \cdot \mathbf{n} \, d\Gamma_\sigma. \tag{5.10}$$

Since $w = 0$ on Γ_u according to the definition of the test function,

$$\int_{\Gamma_u} w\mathbf{D}\nabla p \cdot n \, d\Gamma_u = 0. \tag{5.11}$$

According to equation (5.5),

$$\int_{\Gamma_{\text{pml}}} w\mathbf{D}\nabla p \cdot \mathbf{n} \, d\Gamma_{\text{pml}} = 0. \tag{5.12}$$

Outside the absorbing domain, $\mathbf{D} = \begin{bmatrix} 1 & 0 \\ 0 & 1 \end{bmatrix}$ and according to equation (5.2),

$$\int_{\Gamma_\sigma} w\mathbf{D}\nabla p \cdot \mathbf{n} \, d\Gamma_\sigma = 0. \tag{5.13}$$

And we obtain the simplified form of the weak form as

$$-\int_\Omega \nabla w \cdot [\mathbf{D}\nabla p]\, d\Omega + \int_\Omega w \frac{\omega^2}{c^2} \varepsilon_x \varepsilon_y \, d\Omega = \int_\Omega w f \, d\Omega. \tag{5.14}$$

The next step is to discretize the test function w and pressure field p. They are approximated as linear combinations of element shape functions $N(\mathbf{x})$

$$w(\mathbf{x}) \approx \sum_{i=1}^{NS} N_i(\mathbf{x}) w_i \tag{5.15}$$

$$p(\mathbf{x}) \approx \sum_{i=1}^{NS} N_i(\mathbf{x}) p_i, \tag{5.16}$$

where NS is the size of the basis. By substituting discretized functions in equation (5.14), we can write the equation in matrix and vector form as

$$\mathbf{Kp} + \omega^2 \mathbf{Mp} = \mathbf{f}, \tag{5.17}$$

where entries of the matrices **K**, **M** and vector **f** can be calculated as

$$K_{ij} = \int_\Omega -\nabla N_i(\mathbf{x}) \cdot (\mathbf{D} \nabla N_j(\mathbf{x})) d\Omega, \tag{5.18}$$

$$M_{ij} = \int_\Omega \varepsilon_x \varepsilon_y \frac{1}{c^2} N_i(\mathbf{x}) N_j(\mathbf{x}) d\Omega, \tag{5.19}$$

$$f_i = \int_\Omega N_i(\mathbf{x}) f(\mathbf{x}) d\Omega. \tag{5.20}$$

These integrals are calculated by splitting the domain into small elements $\Omega = \bigcup_{e=1}^{NE} \Omega_e$ where NE is the number of all elements. To make the geometry $\boldsymbol{x}$ a function of the natural coordinate of a single element, The geometry is approximated by the ansatz functions $N^i \xi$ and element positions $\boldsymbol{x}^e$ in an element in physical coordinates:

$$x_i(\boldsymbol{\xi}) \approx \sum x^{ei} N^i(\xi). \tag{5.21}$$

In case of straight element edges, the geometry can be perfectly approximated with only linear ansatz functions. The curved elements can be also precisely approximated with higher degree functions. It can be written in a more general form as

$$\begin{bmatrix} x_1(\xi) \\ x_2(\xi) \\ x_3(\xi) \end{bmatrix} \approx \begin{bmatrix} N_1(\xi) & 0 & 0 & N_2(\xi) & 0 & 0 & \dots \\ 0 & N_1(\xi) & 0 & 0 & N_2(\xi) & 0 & \dots \\ 0 & 0 & N_1 & 0 & 0 & N_3(\xi) & \dots \end{bmatrix} \begin{bmatrix} x_1^{e1} \\ x_2^{e1} \\ x_3^{e1} \\ x_1^{e2} \\ x_2^{e2} \\ x_3^{e2} \\ \cdot \\ \cdot \\ \cdot \end{bmatrix}. \tag{5.22}$$

The derivatives with respect to physical coordinates $\boldsymbol{x}$ is transformed to the derivatives with respect to the natural coordinates ξ with the help of the Jacobi matrix which is derived by the chain rule:

$$\frac{\partial}{\partial \xi_i} = \sum_j \frac{\partial}{\partial x_j} \frac{\partial x_j}{\partial \xi_i} \tag{5.23}$$

The Jacobi matrix is obtained by writing the last equation in the matrix form:

$$\frac{\partial}{\partial \boldsymbol{\xi}} = \boldsymbol{J}(\boldsymbol{\xi}) \frac{\partial}{\partial \boldsymbol{x}}. \tag{5.24}$$

The derivative $\frac{\partial}{\partial \boldsymbol{x}}$ can be replaced by the derivatives $\frac{\partial}{\partial \boldsymbol{\xi}}$ by using the reverse of the last equation:

$$\frac{\partial}{\partial \boldsymbol{x}} = \boldsymbol{J}^{-1}(\boldsymbol{\xi}) \frac{\partial}{\partial \boldsymbol{\xi}}. \tag{5.25}$$

The infinitesimal element $d\Omega$ can be calculated as

$$d\Omega = dx_1 dx_2 dx_3 = |\boldsymbol{J}|\, d\xi_1 d\xi_2 d\xi_3. \tag{5.26}$$

This equations are also same for the two dimensional space.

The integrals in (5.20) are calculated over each element using numerical integration techniques. As an example, if g is a function to be integrated over a two dimensional element Ω_e, it can be calculated numerically in natural coordinates as

$$\int_{-1}^{1}\int_{-1}^{1} g(\xi_1,\xi_2)d\xi_1 d\xi_2 = \sum_{i=1}^{n}\sum_{j=1}^{n} \alpha_i \alpha_j g(\xi_i,\xi_j). \tag{5.27}$$

$[-1,1]$ is the range of coordinate in each axis in natural coordinates. Here, ξ represents Gauss points, whereas α represents the corresponding weight factor.

5.1.2 Weak Formulation of the Elastic Equation

As in the weak formulation of the acoustic equation, the whole domain Ω consists of the domain of interest Ω_{doi} and absorbing domain Ω_{pml}. The borders of the domain in the absorbing region is denoted as Γ_{pml} where we apply Neumann boundary condition with no external stress on the surface because it is not realistic to have external stress on the surface which does not exist physically. We name the borders as in the acoustic case. First of all, we write down the equation with all boundary conditions

$$\begin{cases} -\rho\omega^2 \varepsilon_x \varepsilon_y \varepsilon_z \mathbf{u} - \nabla\cdot\boldsymbol{\sigma} = 0 & \forall\, \boldsymbol{x} \in \Omega \\ \boldsymbol{\sigma}\cdot\tilde{\boldsymbol{n}} - f = 0 & \forall\, \boldsymbol{x} \in \Gamma_{\text{pml}} \\ \boldsymbol{\sigma}\cdot\boldsymbol{n} - \boldsymbol{t}^* = 0 & \forall\, \boldsymbol{x} \in \Gamma_{\sigma} \\ \boldsymbol{u} = 0 & \forall\, \boldsymbol{x} \in \Gamma_{u}. \end{cases} \tag{5.28}$$

A complex-valued vector test function $\boldsymbol{w}$ is chosen which has the following properties:

- $\boldsymbol{w}$ satisfies the geometrical boundary conditions $\boldsymbol{w} = \mathbf{0}\ \forall\ \boldsymbol{x} \in \Gamma_u$
- $\boldsymbol{w}$ is infinitesimal
- $\boldsymbol{w}$ is arbitrary

The scalar product of the partial differential equation is taken with $\boldsymbol{w}$ and is integrated over the whole domain

$$-\int_{\Omega} \rho\omega^2 \varepsilon_x \varepsilon_y \varepsilon_z \mathbf{w}\cdot\mathbf{u} d\Omega - \int_{\Omega} \boldsymbol{w}\cdot[\nabla\cdot\boldsymbol{\sigma}]\, d\Omega = 0. \tag{5.29}$$

To simplify the equation, we use the product rule

$$\nabla\cdot(\boldsymbol{w}\cdot\boldsymbol{\sigma}) = \boldsymbol{w}\cdot(\nabla\cdot\boldsymbol{\sigma}) + \nabla\boldsymbol{w} : \boldsymbol{\sigma}. \tag{5.30}$$

$$\boldsymbol{w}\cdot(\nabla\cdot\boldsymbol{\sigma}) = \nabla\cdot(\boldsymbol{w}\cdot\boldsymbol{\sigma}) - \nabla\boldsymbol{w} : \boldsymbol{\sigma} \tag{5.31}$$

To convert the volume integral to a boundary integral, Gauss theorem is used

$$\int_{\Omega} \nabla \cdot (\boldsymbol{w} \cdot \boldsymbol{\sigma}) d\Omega = \int_{\Gamma} \boldsymbol{w} \cdot \boldsymbol{\sigma} \cdot \boldsymbol{n} d\Gamma = \int_{\Gamma_\sigma} \boldsymbol{w} \cdot \boldsymbol{\sigma} \cdot \boldsymbol{n} d\Gamma + \int_{\Gamma_{\mathrm{pml}}} \boldsymbol{w} \cdot \boldsymbol{\sigma} \cdot \tilde{\boldsymbol{n}} d\Gamma. \tag{5.32}$$

To simplify the weak form further, we use Neumann boundary conditions in (5.28) for Γ_σ

$$\int_{\Gamma_\sigma} \boldsymbol{w} \cdot \boldsymbol{\sigma} \cdot \boldsymbol{n} d\Gamma = \int_{\Gamma_\sigma} \boldsymbol{w} \cdot \boldsymbol{t}^* d\Gamma, \tag{5.33}$$

and for Γ_{pml}

$$\int_{\Gamma_{\mathrm{pml}}} \boldsymbol{w} \cdot \boldsymbol{\sigma} \cdot \tilde{\boldsymbol{n}} d\Gamma = 0. \tag{5.34}$$

Inserting (5.31), (5.32), (5.33) and (5.34) in equation (5.29), we obtain the weak formulation as

$$-\int_{\Omega} \rho\omega^2 \varepsilon_x \varepsilon_y \varepsilon_z \mathbf{w} \cdot \mathbf{u} d\Omega - \int_{\Omega} \boldsymbol{w} \cdot \boldsymbol{t}^* d\Gamma + \int_{\Omega} \nabla \boldsymbol{w} : \boldsymbol{\sigma} d\Omega = 0. \tag{5.35}$$

Since $\boldsymbol{w}$ and $\boldsymbol{u}$ are vectors, their components are discretized separately; they are again approximated as linear combination of shape functions $N(\mathbf{x})$

$$\boldsymbol{w}(\mathbf{x}) = w_i(\mathbf{x}) \boldsymbol{e}_i \approx \sum_{j=1}^{NS} N_i(\mathbf{x}) w_{ij} \tag{5.36}$$

$$\boldsymbol{u}(\mathbf{x}) = u_i(\mathbf{x}) \boldsymbol{e}_i \approx \sum_{j=1}^{NS} N_i(\mathbf{x}) u_{ij}, \tag{5.37}$$

where NS is the size of the basis. By substituting discretized functions in equation (5.14), we can write the equation in matrix and vector form as

$$\boldsymbol{K}\boldsymbol{u} + \omega^2 \boldsymbol{M}\boldsymbol{u} = \boldsymbol{f}, \tag{5.38}$$

where the matrices **K**, **M** and vector **f** stiffness matrix, mass matrix and external force vector, respectively.

5.1.3 Shape Functions

Selection of the shape functions is one of the important points at FE analysis. Hierarchical shape functions are used throughout this study. As degree of the basis increase, the basis is not changed completely, but only some new functions are added to the basis. This can ease the calculation of matrices tremendously once we have matrices for lower basis degree; only new entries are added to the matrices with lower basis degree to construct matrices for higher

degrees. We use Lagrange shape functions as a reference to compare hierarchical functions to. Lagrange functions are constructed with the formula

$$\varphi_i^{\text{lag}}(\xi) = \prod_{\substack{k=1 \\ k \neq i}}^{p+1} \frac{\xi - \xi_k}{\xi_i - \xi_k}. \tag{5.39}$$

where ξ_k^1 is the natural coordinate of ξ^1 at node k. The idea behind these shape functions is that every shape function is 1 at the node it is assigned to and zero at the rest of points to which shape functions are assigned. This relation can be shown mathematically as

$$\varphi_i^{\text{lag}}(\xi_k) = \delta_{ik}. \tag{5.40}$$

Hierarchical shape functions are constructed as

$$\varphi_1^{\text{hier}}(\xi) = \frac{1}{2}(1 - \xi) \tag{5.41}$$

$$\varphi_2^{\text{hier}}(\xi) = \frac{1}{2}(1 + \xi) \tag{5.42}$$

$$\varphi_i^{\text{hier}}(\xi) = \phi_{i-1}(\xi), \;\; i = 3, 4, ..., p + 1. \tag{5.43}$$

N_1 and N_2 are linear shape functions which is the same as linear Lagrange functions. N_i, for $i > 2$, is constructed by polynomial ϕ_{i-1} which is obtained by integrating Legendre polynomials

$$\phi_j(\xi) = \sqrt{\frac{2j-1}{2}} \int_{-1}^{\xi} L_{j-1}(x)\, dx = \frac{1}{\sqrt{4j-2}}(L_j(\xi) - L_{j-2}(\xi)), \;\; j = 2, 3, ... \tag{5.44}$$

where

$$L_n(x) = \frac{1}{2^n n!\, dx^n}(x^2 - 1)^n, \;\; x \in (-1, 1), \;\; n = 0, 1, 2, ... \tag{5.45}$$

Legendre polynomials are orthogonal

$$\int_{-1}^{1} L_n(x) L_m(x)\, dx = \begin{cases} \frac{2}{2n+1} & \text{if } n = m \\ 0 & \text{otherwise.} \end{cases} \tag{5.46}$$

In contrast to Lagrange polynomials, high order hierarchical polynomials are not equal to zero at the same point (see Figure 5.1). Furthermore, Lagrange polynomials change completely as

basis degree changes, whereas only new higher order polynomials are added in hierarchical basis as its degree increases. This fact can ease computational pain of this work. A lower basis degree is needed for lower frequencies than for higher frequencies. As we go up from low to high frequencies, we do not need to change the basis and matrices completely, but we just need to add new functions to the basis and add new entries to mass and stiffness matrices in order to carry out precise calculations for higher frequency.

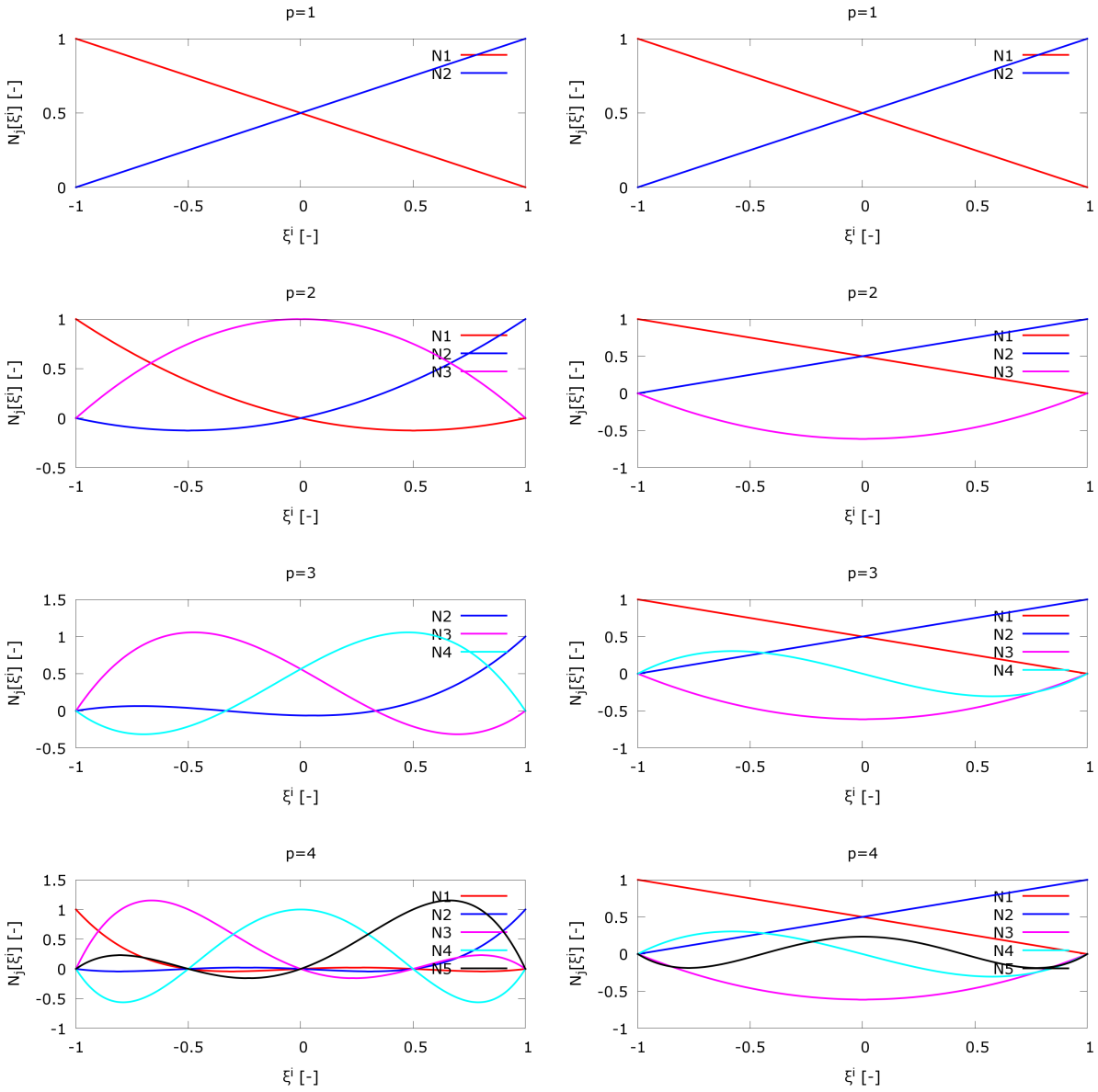

Figure 5.1: Lagrange (left column) and Hierarchical (right column) shape functions

6 Seismic inversion

Prediction of geological changes, such as caverns, fault zones, weakened zones, etc., ahead of the tunnel is crucial for the safety of the tunnel and the structures above the surface. Enough number of boreholes can give an understanding of the geological structure below the surface. However, too many of boreholes, which is very costly in terms of both time and money, are usually needed to scan the geological structure of the ground. To avoid the high cost, scanning ahead of a tunnel is usually done by carrying out a seismic survey. Sources are excited at certain points and the seismograms are read at geophones located at receiver points. The locations of the sources and receivers, the type of the source used to excite the waves determine the type of imaging approach used to predict the geological structure ahead of the tunnel.

Since the cutting wheel is not reachable during the boring process, placing source and receiver points at reachable locations makes their maintenance possible in case they fail.
[Petronio and Poletto, 2002], [Petronio et al., 2003], [Petronio et al., 2007], [Ashida, 2001], and [Brückl et al., 2008] use the energy of the cutting wheel as the source of the excitation of the seismic waves. Placing the receivers well behind the cutting wheel eases the maintenance of the system if necessary. The reflected P- and S-waves are used to detect the anomalies ahead of the tunnel.

Choosing both source and receiver points well behind the boring machine makes them reachable during the construction. In some of such applications, the source is excited by small explosions in boreholes well behind the front tunnel face, e.g. [Ashida, 2001], [Sattel et al., 1992]. [Sattel et al., 1992] and [Brückl et al., 2001] used vertical seismic profiling (VSP) technique, whereas [Inazaki et al., 1999] used horizontal seismic profiling technique for tunnel exploration purpose. Tunnel seismic prediction system, [Sattel et al., 1996], [Dickmann and Sander, 1996], is another compact commercial package, developed by Amberg Technologies, with measurement instrumentation and interpretation software together.

Seismic imaging system [Borm et al., 2003], tunnel reflector tracing [Neil et al., 1999],
[Yamamoto et al., 2011], true reflection tomography (TRT) [Otto et al., 2002], true reflection underground seismic technique (TRUST) [Benecke et al., 2008], tunnel seismic tomography (TST) [Zhao et al., 2006], and tunnel geological prediction (TGP) [Jiao et al., 2015] are other systems to predict geological structure of a tunnel.

[Kneib et al., 2000] and [Gehrig et al., 2010] propose Seismic Softground Probing (SSP) where all source and receiver points are located on the cutting wheel of the tunnel boring machine. SSP is designed for tunneling in soft soils by earth pressure balance machines (EPBMs). In case the source and receivers are failed, the maintenance is not possible during the boring process because the cutting wheel is not reachable. Migration is carried out over the reflected P-waves to scan ahead of the tunnel.

The systems mentioned till now mostly take advantage of first arrivals of body waves and seismic migration to interpret the reflection data. However, surface waves are also generated when small explosive are blasted in boreholes well behind the front tunnel face. It was figured out by

[Bohlen et al., 2007] and [Jetschny et al., 2010] that the surface waves propagating at the tunnel side walls are converted to body waves when they hit the front tunnel face. The reverse is also true when the body waves are reflected from the geological boundaries and hit the front tunnel face. Taking advantage of this finding, they use surface waves to explore the geological structure ahead of a tunnel.

More recently, [Tzavaras et al., 2012] applied 3D Kirchhoff prestack migration, Fresnel volume migration, and reflection image spectroscopy, and [Cheng et al., 2014] applied 2D reverse time migration to explore the reflectors ahead of tunnel.

6.1 Full waveform inversion (FWI)

It is possible to use only wave traveltimes of some waves and reconstruct the velocity field to some precision. However, waveforms contain more information than only traveltimes of some waves. This is the idea of full waveform inversion which aims to find such an optimal velocity field that fits the waveforms the best. All types of waves (body and surface waves) are superposed in a single seismogram. Goal of FWI is not only to fit first arrivals of some waves, but arrivals and amplitudes of all waves. Trying to fit full seismograms decreases the ambiguity level of the inverse problem. In other words, it reduces number of possible models which suit the real data. However, full seismogram contains a lot of information including all kinds of incident and reflected body and surface waves. This, in turn, makes the problem highly non-linear, which can be overcome with a very close initial model. The nonlinearity can also be partly subsided by using low frequency components of the seismogram first and use the resultant model as an initial model for the higher frequency components. Although it can be done in both time and frequency domains, the frequency domain provides more flexibility to handle any single frequency separately in a given frequency range. This fact is the motivation to carry out the numerical experiments of this study in the frequency domain.

Researchers have been applying FWI in geophysical exploration problems since early 1980s, [Bamberger et al., 1982], [Crase et al., 1990], [Pratt et al., 1998], [Pratt, 1999a], [Pratt, 1999b], [Virieux et al., 2009]. FWI is computationally expensive, which made it not practical to use. However, with the exponential growth of computer technologies, researchers apply FWI more often in a variety of exploration problems; e.g., continental scale problems are addressed by using FWI, [Fichtner et al., 2008], [Fichtner et al., 2009a], [Fichtner et al., 2009b].

6.1.1 Definition of the inverse problem in the frequency domain

In this section, we describe how we mathematically define our inverse problem in the frequency domain. We assume that our source function has a frequency range $[\omega_{min}, \omega_{max}]$. A set of discrete frequencies

$$F = \{\omega_1, \omega_2, ..., \omega_N\}, \text{ where } \omega_i \in [\omega_{min}, \omega_{max}]\,. \tag{6.1}$$

is chosen and collected in groups . We define K frequency groups where each group is a non-empty subset of F

$$G_k = \{\omega_{k_1}, \omega_{k_2}, ..., \omega_{k_{M_k}}\} \subset F, k = 1, ..., K, \tag{6.2}$$

where M_k is the number of frequencies in set k. The selection of these frequency groups plays a very crucial role in the inversion process. Too few frequencies may not be a good representation of the real problem so that the inversion process ends up with an unreasonable result. At the same time, a large number of frequencies tremendously increase the computation time. The importance of the frequency groups is highlighted in the results section.

The model is inverted over each frequency group separately and, for this reason, we solve K inverse problems in one FWI process. We define K inverse problems

$$P_i : \min_{c_i} \chi_i(c_i), i = 1, ..., K. \tag{6.3}$$

and denote the result of each problem as c_i^{res}. Here, $\chi(c)$ is the misfit functional and we define it as

$$\chi_i(c_i) = \sum_{j=1}^{M_i} \frac{1}{2} \sum_{l=1}^{n_s} \triangle \mathbf{p}_{\omega_{ij}}^l \cdot (\triangle \mathbf{p}_{\omega_{ij}}^l)^* = \frac{1}{2} \sum_{j=1}^{M_i} \sum_{l=1}^{n_s} |\triangle \mathbf{p}_{\omega_{ij}}^l|^2. \tag{6.4}$$

For each problem P_i which takes the frequency group G_i into account. $s_1, s_2, ..., s_{n_s}$ represent source points, whereas $r_1, r_2, ..., r_{n_r}$ represent receiver points. Here, n_s is the number of source points and $\triangle \mathbf{p}_{\omega_{ij}}^l(c_i)$ is the difference of the pressure values at the receiver points between the real and computer models when the source is fired at the sender point s_l

$$\triangle \mathbf{p}_{\omega_{ij}}^l = \mathbf{p}_{\omega_{ij}}^l - (\mathbf{p}_{obs})_{\omega_{ij}}^l. \tag{6.5}$$

Here, $\mathbf{p}_{\omega_{ij}}^l$ and $(\mathbf{p}_{obs})_{\omega_{ij}}^l$ are vectors of pressure values read at the receiver points when the source is fired at the sender point s_l in the computer and real models, respectively. $(\triangle \mathbf{p}_{\omega_{ij}}^l)^*$ is the conjugate of the complex vector $\triangle \mathbf{p}_{\omega_{ij}}^l$.

In the frequency domain, the misfit functional is minimized over a set of discrete frequencies. The lower frequencies are tackled first, and the result of the lower frequencies becomes the initial model of the next higher frequencies. As mentioned before, the misfit functional can be highly nonlinear in FWI. Tackling lower and higher frequencies separately helps to decrease the nonlinearity of the misfit functional, [Ajo-Franklin, 2005]. An initial model is very important for each problem P_i and we denote it as c_i^{init}. We can write each inversion process as

$$c_i^{init} \Longrightarrow P_i \Longrightarrow c_i^{res}, i = 1, ..., K, \tag{6.6}$$

which means that we use the initial model c_i^{init} as an input to the inverse problem P_i to obtain the desired c_i^{res}. Since the optimization method we use is a gradient-based method, the initial model should be close enough to the real model so that it is not stuck at a local minimum point. c_1^{init} depends on intuition or on previous experimental results, if there are any. For P_i $i = 2, ..., K$, the initial model is the result of the previous velocity field, which can be expressed mathematically as

$$c_i^{init} = c_{i-1}^{res}, i = 2, ..., K. \tag{6.7}$$

This work compares two inversion approaches - discrete and continuous. In the discrete approach, the velocity field is discretized beforehand such that a vector of design variables represents the velocity field. This problem can be solved by conventional optimization methods. In the continuous approach, the velocity function itself is sought in order to minimize the misfit function. In this case, there is no need to discretize the velocity field beforehand since the gradient

of the misfit is a functional gradient that is derived by taking the derivative of the misfit function with respect to the velocity function by means of functional derivations. In this work, the discrete approach is applied to both acoustic and elastic wave equations, whereas the continuous approach is applied only to the acoustic wave equation.

As already mentioned, a gradient-based optimization method is used to minimize the misfit functional and to find an optimal velocity field. More precisely, the conjugate-gradient (CG) method is applied to solve inverse problems. In the following sections, the algorithm of CG and the ways it is applied to both discrete and continuous approaches are described in detail.

6.1.2 Discrete approach and discrete adjoint method

We apply the discrete approach to both acoustic and elastic equations in a trivial manner. In this approach, the velocity field is approximated by a linear combination of adequately chosen basis functions $\varphi_i : \Omega \to \mathbb{R}$ and scalar valued model parameters $m_i \in \mathbb{R}$, $i = 1, 2, ..., n$ as

$$c_h(\mathbf{x}) = \sum_{e=1}^{n} \varphi_e(\mathbf{x}) m_e. \tag{6.8}$$

We use two different discretizations in this work: A piecewise linear approach where there are no jumps in the function and a piecewise constant function in which m_e is a velocity value on the element e. A comparison is given in the result section. Piecewise linear functions can be good to approximate a function that has no jumps and is changing smoothly. On the other hand, a piecewise constant function can be good to detect jumps and approximate rapidly changing functions. After discretization, the velocity field can be represented with a vector of model parameters

$$\mathbf{m} = (m_1, m_2, ..., m_n)^T. \tag{6.9}$$

Using a finite-element approximation, the acoustic wave equation in the frequency domain (2.25) can be reduced to

$$-\omega^2 \mathbf{M}(\mathbf{m})\mathbf{p}_\omega + \mathbf{K}\mathbf{p}_\omega = \mathbf{f}_\omega \tag{6.10}$$

where $\mathbf{M}, \mathbf{K}$, and $\mathbf{p}$ are the mass matrix, the stiffness matrix, and the discrete version of the pressure field, respectively. If a matrix $\mathbf{L}$ is defined such that $\mathbf{L} = -\omega^2 \mathbf{M}(\mathbf{m}) + \mathbf{K}$, equation (6.10) reduces to a system of linear equations

$$\mathbf{L}(\mathbf{m})\mathbf{p}_\omega = \mathbf{f}_\omega. \tag{6.11}$$

The gradient of the misfit functional $\chi(\mathbf{m})$ is calculated using the discrete adjoint method (see [Fichtner, 2011]). By applying the chain rule, the partial derivative of the misfit functional with respect to a model parameter m_i is

$$\frac{\partial \chi}{\partial m_i} = \nabla_{\mathbf{p}} \chi \cdot \frac{\partial \mathbf{p}_\omega}{\partial m_i} \tag{6.12}$$

where $\nabla_{\mathbf{p}} = \frac{\partial}{\partial \mathbf{p}_\omega}$. In order to derive the partial derivatives of the discrete pressure coefficients with respect to the model parameters, equation (6.11) is differentiated with respect to m_i

$$\frac{\partial \mathbf{L}}{\partial m_i} \cdot \mathbf{p}_\omega + \mathbf{L} \cdot \frac{\partial \mathbf{p}_\omega}{\partial m_i} = \mathbf{0}, \tag{6.13}$$

and thus

$$\frac{\partial \mathbf{p}_\omega}{\partial m_i} = -\mathbf{L}^{-1} \cdot \frac{\partial \mathbf{L}}{\partial m_i} \cdot \mathbf{p}_\omega. \tag{6.14}$$

By substituting the partial derivatives of the discrete pressure values with respect to the model parameters m_i into (6.12), the gradient of the misfit functional becomes

$$\frac{\partial \chi}{\partial m_i} = -\nabla_{\mathbf{p}}\chi \cdot \left(\mathbf{L}^{-1} \cdot \frac{\partial \mathbf{L}}{\partial m_i}\right) \cdot \mathbf{p}_\omega = -\mathbf{p}_\omega \cdot \left(\frac{\partial \mathbf{L}^T}{\partial m_i} \cdot \mathbf{L}^{-T}\right) \cdot \nabla_{\mathbf{p}}\chi. \tag{6.15}$$

In our case, $\boldsymbol{L}$ is a symmetric matrix. This allows us to replace $\boldsymbol{L}^T$ with $\boldsymbol{L}$. The discrete adjoint wave field $\mathbf{p}^\dagger_\omega$ is defined as the solution of the adjoint equation

$$\mathbf{L}^T \mathbf{p}^\dagger_\omega = -\nabla_{\mathbf{p}}\chi \quad \Rightarrow \quad \mathbf{p}^\dagger_\omega = -\mathbf{L}^{-T}\nabla_{\mathbf{p}}\chi. \tag{6.16}$$

This simplifies the calculation of the gradient of the misfit functional in (6.15)

$$\frac{\partial \chi}{\partial m_i} = \mathbf{p}^\dagger_\omega \cdot \frac{\partial \mathbf{L}}{\partial m_i} \cdot \mathbf{p}_\omega. \tag{6.17}$$

This equation significantly reduces the computational effort for calculating the gradient of the misfit functional: For every source point, the system of linear equations is solved only twice. If direct solvers are used, they need more time for the decomposition than for solving backward. This makes direct solvers advantageous in this case; decomposition is performed only once, and in the following calculations, only the backward solve is performed. Compared to a finite-difference approach, in which a linear system is to be solved for each model parameter m_i, this is a major improvement. Moreover, derivatives are computed exactly and the stepsize dilemma is avoided.

6.1.3 Continuous approach and functional gradient

We apply this approach only to the acoustic wave equation. Before the continuous approach can be applied, the functional must be derived by using the variational approach. $\frac{1}{c^2(\mathbf{x})}$, $f(\mathbf{x}, \omega)$ in equation (2.25) are replaced by $d(\mathbf{x})$, and $\delta(\mathbf{x} - \mathbf{s})$, respectively, to give

$$\triangle p_\omega + \omega^2 d(\mathbf{x}) p_\omega = \delta(\mathbf{x} - \mathbf{s}). \tag{6.18}$$

For the sake of simplicity, the equations are given here for only one frequency and one source point. In the end, the final formulations are only summation over the frequencies and the source points. The variation of the misfit functional (6.4) is

$$\delta\chi = \triangle(\mathbf{p}_\omega)^* \cdot \delta\mathbf{p}_\omega = \sum_{i=1}^{n_r} (p_\omega(\mathbf{r}_i) - p_{obs,\omega}(\mathbf{r}_i))^* \delta p_\omega(\mathbf{r}_i) \tag{6.19}$$

where n_r is the number of receiver points, and $p_\omega(\mathbf{r}_i)$ and $p_{obs,\omega}(\mathbf{r}_i)$ are the pressure values at the receiver point r_i in the computer and real models, respectively. We define $\triangle p^i_\omega$ to represent

$$\triangle p^i_\omega = p_\omega(\mathbf{r}_i) - p_{obs,\omega}(\mathbf{r}_i). \tag{6.20}$$

The variation of (6.18) is used to derive $\delta p(\mathbf{r}_i)$ and it takes the form

$$\triangle \delta p_\omega + \omega^2 d(\mathbf{x}) \delta p_\omega = -\omega^2 \delta d(\mathbf{x}) p_\omega. \tag{6.21}$$

Once (6.18) is solved, the solution of (6.21) can be constructed using Green's function as

$$\delta p^i_\omega(\mathbf{x}) = -\omega^2 \int_\Omega G_\omega(\mathbf{y}-\mathbf{x}) \delta d(\mathbf{y}) p^i_\omega(\mathbf{y}) d\mathbf{y}. \tag{6.22}$$

It is taken into account that $p(\mathbf{y})$ is the Green function of (6.18). $\delta p(\mathbf{r}_i)$ is substituted in (6.19) to obtain the equation

$$\delta\chi = -\int_\Omega \omega^2 \sum_{i=1}^{n_r} \left((\triangle p^i_\omega)^* G_\omega(\mathbf{y}-\mathbf{r}_i) G_\omega(\mathbf{y}-\mathbf{s}) \right) \delta d(\mathbf{y}) d\mathbf{y}. \tag{6.23}$$

Using the equation $\delta\chi = -\int_\Omega \nabla\chi \delta d(\mathbf{x}) d\Omega$ gives the functional gradient as

$$\nabla\chi = \omega^2 \sum_{i=1}^{n_r} \left((\triangle p^i_\omega)^* G_\omega(\mathbf{y}-\mathbf{r}_i) G_\omega(\mathbf{y}-\mathbf{s}) \right), \tag{6.24}$$

where $\nabla\chi = \frac{\partial\chi}{\partial d}$ as in [Sirgue and Pratt, 2004] and [Ajo-Franklin, 2005]. The functional gradient is the direction of the maximum rate of change. According to equation (6.24), the functional gradient can be constructed with Green functions, which are linear combinations of finite element basis. In our case, this means that discretization of the velocity field is directly dependent on the finite element basis.

6.1.4 Relation between discrete and continuous gradients

We aim to compare the discrete and continuous approaches in the acoustic wave equation and the mathematical relation between these two approaches are shown before doing this. In practice, before running any simulations, it is possible to see advantages and disadvantages of both approaches. The continuous approach does not require discretization of the velocity field before the simulation starts, and it provides a more precise gradient of the misfit functional. However, in the discrete approach, we can discretize the velocity field as we wish. This may be an advantage if we know what kind of medium we are trying to scan and, in such a case, we can discretize the velocity field accordingly. We compare the results of both approaches and discuss them in the result section. To show the mathematical correlation between the approaches, we analyze the relation between discrete and functional gradients. The derivative of (6.18) with respect to a model parameter m_k is used to derive $\frac{\partial p(\mathbf{r}_i)}{\partial m_k}$ and it takes the form

$$\triangle \frac{\partial p}{\partial m_k} + \omega^2 d(\mathbf{x}) \frac{\partial p}{\partial m_k} = -\omega^2 \frac{\partial d(\mathbf{x})}{\partial m_k} p. \tag{6.25}$$

Once (6.18) is solved, the solution of (6.25) can be constructed as

$$\frac{\partial p(\mathbf{x})}{\partial m_k} = -\omega^2 \int_\Omega G(\mathbf{y}-\mathbf{x}) \frac{\partial d(\mathbf{y})}{\partial m_k} p(\mathbf{y}) d\mathbf{y}. \tag{6.26}$$

The derivative of the misfit functional with respect to a model parameter m_k is

$$\frac{\partial\chi}{\partial m_k} = \sum \left(p(\mathbf{r}_i) - p_{obs}(\mathbf{r}_i) \right)^* \frac{\partial p(\mathbf{r}_i)}{\partial m_k}. \tag{6.27}$$

Substituting (6.26) in equation (6.27) gives

$$\frac{\partial \chi}{\partial m_k} = -\int_\Omega \omega^2 \sum \left(\triangle (p^i)^* G(\mathbf{y} - \mathbf{r}_i) G(\mathbf{y} - \mathbf{s}) \right) \frac{\partial d(\mathbf{y})}{\partial m_k} d\mathbf{y}. \tag{6.28}$$

Using equation (6.24) in (6.28), the relation between the continuous and discrete gradients is obtained as

$$\frac{\partial \chi}{\partial m_k} = -\int_\Omega \frac{\partial \chi}{\partial d} \frac{\partial d}{\partial m_k} d\mathbf{y} = - < \nabla \chi, \frac{\partial d}{\partial m_k} > \tag{6.29}$$

where the $<,>$ operator denotes the inner product. In this study, discretization is performed according to equation (6.8). If this equation is taken into account, the equation $\frac{\partial \chi}{\partial m_k} = - < \nabla \chi, \varphi_i >$ is obtained. In the end, the discrete gradient is related to the inner product of the continuous gradient, and shape functions are used to discretize the velocity field function.

6.1.5 Comparison of the discrete and continuous gradients

The idea of the functional gradient is that it calculates the gradient of the misfit functional with respect to the velocity field without discretizing it. If analytical solutions are known, the gradient could also be calculated analytically with equation (6.24) using the functional derivation. In this section, an example that has analytical solution for the acoustic equation is investigated to calculate the analytical gradient. We also calculate the gradient with the discrete adjoint and compare them. An infinite box is taken as an example. Only one single source point and one single receiver point are chosen in the model (see Figure 6.1a). It is assumed that the sought velocity field and the initial velocity field are homogeneous. The initial and sought velocity values are 2000 m/s and 1630 m/s, respectively. In this case, the analytical solutions of the acoustic equation (2.25) for both of the velocity fields are known. The analytical gradient is constructed as functional gradient (6.24) (see Figure 6.1c). Figure 6.1a and 6.1b are the gradient plots obtained by the adjoint method by discretizing the velocity with a basis of degrees 1 and 3, respectively. Unfortunately, Figure 6.1b looks numerically unreasonable because the picture is not pixel-wise very smooth. However, if we overlook this error, we will see that as the basis degree becomes higher the gradient converges to the functional gradient which is the analytical gradient of the example.

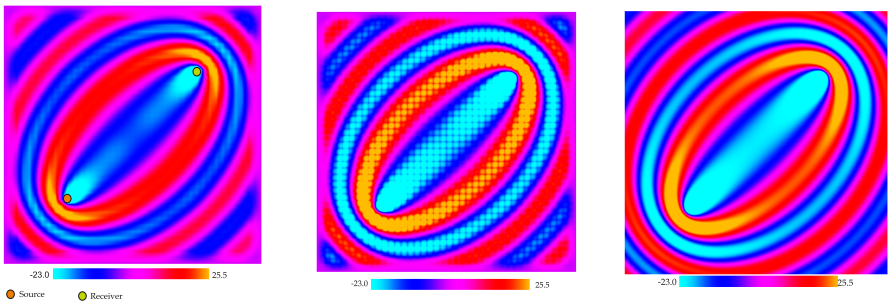

(a) adjoint p=1 (b) adjoint p=3 (c) functional

Figure 6.1: Gradients with the adjoint and functional approaches.

Scaled plots

6.2 Important concepts of an inverse problem

Our aim is to find such an optimal geological model $\boldsymbol{m}$ for the tunnel domain such that the misfit functional $\chi(\boldsymbol{m})$ is minimum. There are a few mathematical concepts which have to be understood well in order to have a good insight of the inverse problem we are trying to solve: global and local minima, non-uniqueness, and convexity. The search space for the geological model $\boldsymbol{m}$ is high-dimensional. It renders stochastic minimization methods not well applicable to FWI problems. We aim to use deterministic minimization methods which are dependent of the gradient of the misfit functional χ. Although the stochastic methods can avoid becoming stuck in a local minimum, gradient-based methods tend to take the way to the closest minimum point which can be local minimum. Figure 6.2a illustrates a function which has strict global and strict local minima. With a gradient-based method, it is required to have an initial earth model close enough to the global minimum not to let the method take the path to the local minimum. Being a strict global minimum means that there is only one point $\boldsymbol{m}_{\text{global}}$ that corresponds to the minimum value of the misfit functional χ. In other words,

$$\chi(\boldsymbol{m}_{\text{global}}) < \chi(\boldsymbol{m}) \text{ for all } \boldsymbol{m} \neq \boldsymbol{m}_{\text{global}} \tag{6.30}$$

It also means that m_{global} is unique. However, geophysical inverse problems do not usually have a unique solution and there are more than one global minimum:

$$\chi(\boldsymbol{m}_{\text{global}}) \leq \chi(\boldsymbol{m}) \text{ for all } \boldsymbol{m} \neq \boldsymbol{m}_{\text{global}} \tag{6.31}$$

Figure 6.2b shows an example of such global and local minima. Inverse problems which have only one global minimum without any local minima with a unique solution are the most convenient to handle. However, geophysical inverse problems, on which non-uniqueness of the solution and many local minima impose a big challenge, are the opposite.

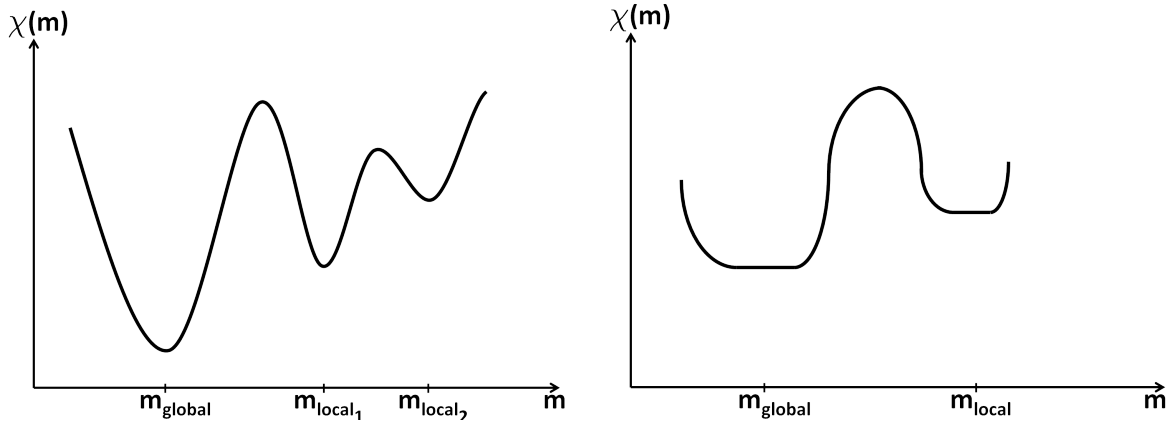

(a) Unique global minimum m_{global}, unique local minima m_{local_1} and m_{local_2}

(b) Non-unique global minimum m_{global}, non-unique local minimum m_{local}

Figure 6.2: Global and local minima

Convexity is a mathematical concept on which both the uniqueness and local or global nature of the minimum of the misfit function depend. The misfit functional $\chi(\boldsymbol{m})$ is a convex function if the relation

$$\chi[(1-\epsilon)\boldsymbol{m}_1 + \epsilon\boldsymbol{m}_2] \leq (1-\epsilon)\chi(\boldsymbol{m}_1) + \epsilon\chi(\boldsymbol{m}_2) \tag{6.32}$$

is satisfied for any earth models $\boldsymbol{m}_1$ and $\boldsymbol{m}_2$ in the search space and for any $\epsilon \in [0,1]$. This inequality means that the line connecting any two points on the graph of the misfit function is above or on the graph. The misfit function is called strictly convex when the line connecting two points on the graph is above the graph:

$$\chi[(1-\epsilon)\boldsymbol{m}_1 + \epsilon\boldsymbol{m}_2] < (1-\epsilon)\chi(\boldsymbol{m}_1) + \epsilon\chi(\boldsymbol{m}_2) \forall \epsilon \in [0,1]. \tag{6.33}$$

A convex function has no local minima, but one global minimum. However, the global minimum point is not unique and there are infinitely many of them. Strictly convex functions have unique global minimum and no local minima. In an ideal case, we would like to have a strictly convex function in order to have only one unique global minimum. We would be sure that the gradient-based method searches for the global minimum, but does not converge to a local minimum. Unfortunately, real world problems impose much more difficulties than an ideal case. To prove that a convex function have no local minima, but only global minimum, we assume that $\boldsymbol{m}_{\text{local}}$ is a local minimum and $\boldsymbol{m}_{\text{global}}$ is the global minimum. For the earth models $\boldsymbol{m}$ in the close vicinity of $\boldsymbol{m}_{\text{local}}$, the following relation

$$\chi(\boldsymbol{m}_{\text{local}}) \leq \chi(\boldsymbol{m}) \tag{6.34}$$

must satisfy. We choose an earth model $\boldsymbol{m}_1$ as

$$\boldsymbol{m}_1 = (1-\epsilon_0)\boldsymbol{m}_{\text{local}} + \epsilon_0\boldsymbol{m}_{\text{global}} = \boldsymbol{m}_l + \epsilon_0(\boldsymbol{m}_{\text{global}} - \boldsymbol{m}_{\text{local}}) \tag{6.35}$$

where ϵ_0 is chosen so close to zero that $\boldsymbol{m}_1$ is in the close vicinity of $\boldsymbol{m}_{\text{local}}$ to satisfy the relation

$$\chi(\boldsymbol{m}_{\text{local}}) \leq \chi(\boldsymbol{m}_1). \tag{6.36}$$

Using the convexity relation

$$\chi(\boldsymbol{m}_{\text{local}}) \leq \chi(\boldsymbol{m}_1) = \chi((1-\epsilon_0)\boldsymbol{m}_{\text{local}}+\epsilon_0\boldsymbol{m}_{\text{global}}) \leq (1-\epsilon_0)\chi(\boldsymbol{m}_{\text{local}})+\epsilon_0\chi(\boldsymbol{m}_{\text{global}}), \tag{6.37}$$

the relation

$$\chi(\boldsymbol{m}_{\text{local}}) \leq \chi(\boldsymbol{m}_{\text{global}}) \tag{6.38}$$

is obtained. Since $\boldsymbol{m}_{\text{global}}$ is the global minimum point, the inequality

$$\chi(\boldsymbol{m}_{\text{global}}) \leq \chi(\boldsymbol{m}_{\text{local}}) \tag{6.39}$$

must be right. The last two conditions must satisfy at the same time, which can only happen if

$$\chi(\boldsymbol{m}_{\text{global}}) = \chi(\boldsymbol{m}_{\text{local}}). \tag{6.40}$$

It means, if a function is convex and if it has a local minimum, the value of the misfit function at that point is equal to the value of the function at the global minimum. We choose any point $\boldsymbol{m}$ in between the local minimum $\boldsymbol{m}_{\text{local}}$ and the global minimum $\boldsymbol{m}_{\text{global}}$

$$\boldsymbol{m}_{\text{a}} = (1-\epsilon)\boldsymbol{m}_{\text{local}} + \epsilon\boldsymbol{m}_{\text{global}}. \tag{6.41}$$

Using the convexity condition,

$$\chi(\boldsymbol{m}_{\text{global}}) \leq \chi(\boldsymbol{m}_{\text{a}}) = \chi((1-\epsilon_{\text{a}})\boldsymbol{m}_{\text{local}}+\epsilon_{\text{a}}\boldsymbol{m}_{\text{global}}) \leq (1-\epsilon_{\text{a}})\chi(\boldsymbol{m}_{\text{local}})+\epsilon_{\text{a}}\chi(\boldsymbol{m}_{\text{global}}) = \chi(\boldsymbol{m}_{\text{global}})$$

(6.42)

is obtained. The inequalities can only be satisfied if

$$\chi(\boldsymbol{m}_{\text{global}}) = \chi(\boldsymbol{m}_{\text{a}}) \tag{6.43}$$

is satisfied, which means that value of the function at any point equals to the value of the function at the global minimum. This implies that $\boldsymbol{m}_{\text{local}}$ is not a local minimum, but one of infinitely many global minima. There can only be one global minimum region in a convex function. However, the minimum is not unique.

If we use strictly convex relation, and follow the same derivation as we applied for the convex functions, instead of equation (6.38), we obtain a strict inequality

$$\chi(\boldsymbol{m}_{\text{local}}) < \chi(\boldsymbol{m}_{\text{global}}) \tag{6.44}$$

which contradicts the relation (6.39) between the local minimum $\boldsymbol{m}_{\text{local}}$ and the global minimum $\boldsymbol{m}_{\text{global}}$. It is concluded that a strictly convex function has no local minima and it has only one unique global minimum.

The Hessian matrix $H_\chi(\boldsymbol{m})$ of a convex function χ, which equals $\frac{\partial^2 \chi}{\partial \boldsymbol{m} \partial \boldsymbol{m}}$, is positive semidefinite for any model $\boldsymbol{m}_2$:

$$\boldsymbol{m}_1 \cdot H_\chi(\boldsymbol{m}_2) \cdot \boldsymbol{m}_1 \geq 0 \tag{6.45}$$

for all earth models m_1 and m_2. In case of a strictly convex function χ, the Hessian matrix is positive definite for all m_2:

$$\boldsymbol{m}_1 \cdot H_\chi(\boldsymbol{m}_2) \cdot \boldsymbol{m}_1 > 0 \tag{6.46}$$

for all m_1 and m_2. One can refer to [Fichtner, 2011] for the derivation of (6.45) and (6.46) from the convexity condition. Since the model parameter m is too big in geophysical inverse problems, the calculation of Hessian matrix is computationally very expensive. However, it is easier to have some insight about the misfit function with the help of its Hessian relation than the convexity relation.

In tunneling problems, the sources and receivers geophones are usually placed inside the tunnel, either close to the tunnel face or side walls, due to time and budget restrictions. The response of the model can be measured only at certain points. It causes ambiguity in the misfit functional because not only one unique model has a similar approach. This is one reason of the non-uniqueness of the tunnel exploration problems. Another reason for non-uniqueness can be parameters which affect the wave propagation. The wave propagation sometimes depends on a parameter not directly, but it depends on some type of a relation between two parameters. For example, infinitely many Lamé parameters and density combination can give the same P- and S-wave speeds which can result in system behavior. Apart from uniqueness of the tunnel exploration problems, the misfit functional is a nonlinear function of parameters, such as wave speeds, density, etc., which define the mechanical properties of soil.

There are first-order and second order conditions to prove mathematically whether a point is a minimum point. Assume that $m_{\min}$ is a minimum point(either local or global). Then, the inequality

$$\chi(\boldsymbol{m}_{\min} + \epsilon_0 \boldsymbol{m}) \geq \chi(\boldsymbol{m}_{\min}) \tag{6.47}$$

holds for any model parameter $\boldsymbol{m}$ if ϵ_0 very close to zero. Taking all terms to the left side, dividing by ϵ, and taking limit for $\epsilon \to 0$, we obtain

$$\lim_{\epsilon \to 0} \frac{1}{\epsilon} \left(\chi(\boldsymbol{m}_{\min} + \epsilon_0 \boldsymbol{m}) - \chi(\boldsymbol{m}_{\min}) \right) = \boldsymbol{m} \cdot \nabla_m \chi(\boldsymbol{m}_{\min}) \geq 0 \tag{6.48}$$

which holds for any arbitrary model parameter $\boldsymbol{m}$. In other words, the inequality is true for both $\boldsymbol{m}$ and $-\boldsymbol{m}$, which can only be true if

$$\nabla_m \chi(\boldsymbol{m}_{\min}) = 0. \tag{6.49}$$

This equality, or the first-order necessary condition, is fulfilled if $\boldsymbol{m}_{\min}$ is a local or global minimum. However, the reverse of it is not true; if a point satisfies the equality (6.49), it can be a minimum, a maximum or a saddle point. Nevertheless, only the first order condition is used by minimization methods to find the minimum point. To derive the second order condition, Taylor expansion of χ is used:

$$\chi(\boldsymbol{m}_{\min} + \epsilon_0 \boldsymbol{m}) = \chi(\boldsymbol{m}_{\min}) + \epsilon_0 \boldsymbol{m} \cdot \nabla_m \chi(\boldsymbol{m}_{\min}) + \frac{1}{2} \epsilon^2 \boldsymbol{m} \cdot H_\chi(\boldsymbol{m}_{\min}) \cdot \boldsymbol{m} + \epsilon^3 \Theta(\boldsymbol{m}^3). \tag{6.50}$$

Rearranging the equation, considering the first order condition and that $\boldsymbol{m}_{min}$ is the minimum point,

$$\frac{1}{\epsilon^2} (\chi(\boldsymbol{m}_{\min} + \epsilon_0 \boldsymbol{m}) - \chi(\boldsymbol{m}_{\min})) = \frac{1}{2} \boldsymbol{m} \cdot H_\chi(\boldsymbol{m}_{\min}) \cdot \boldsymbol{m} + \epsilon_0 \Theta(\boldsymbol{m}^3) \geq 0 \tag{6.51}$$

is obtained. Here, ϵ_0 can be chosen so close to zero that, $\epsilon_0 \Theta(\boldsymbol{m}^3)$ term can be neglected with respect to $\frac{1}{2} \boldsymbol{m} \cdot H_\chi(\boldsymbol{m}_{\min}) \cdot \boldsymbol{m}$. It implies that

$$\frac{1}{2} \boldsymbol{m} \cdot H_\chi(\boldsymbol{m}_{\min}) \cdot \boldsymbol{m} \geq 0 \tag{6.52}$$

which is a second order necessary condition implying that Hessian matrix of χ at the minimum point $\boldsymbol{m}_{\min}$ is positive semi-definite, must hold.

6.3 Minimization methods

An appropriate minimization method is inevitable to solve the full waveform inversion problems. Figure 6.3 shows schematically how the minimization methods work. All non-linear iterative minimization methods, including stochastic methods, rely on updating the current parameter model $\boldsymbol{m}$:

$$\boldsymbol{m}_{i+1} = \boldsymbol{m}_i + \alpha_i \boldsymbol{s}_i \tag{6.53}$$

where α_i is step size and s_i is search direction at iteration i. The difference amongst minimization methods is the determination of the search direction. In FWI problems, where the model space is too big, determining the search direction with stochastic methods is almost impossible. This is the reason why we deploy gradient-based methods to minimize the misfit function. Once the search direction s_i is known, the next challenge is to determine the step size, which is done with the help of the first order condition:

$$\frac{d}{d\alpha_i} \chi(\boldsymbol{m}_i + \alpha_i \boldsymbol{s}_i) = \boldsymbol{s}_i \cdot \nabla_{\boldsymbol{m}} \chi(\boldsymbol{m}_i + \alpha_i \boldsymbol{s}_i) = 0. \tag{6.54}$$

With the quadratic approximation of $\chi(\boldsymbol{m}+\alpha\boldsymbol{s})$ with Taylor expansion around α

$$\chi(\boldsymbol{m}+\alpha\boldsymbol{s}) \approx \chi(\boldsymbol{m}) + \alpha\left[\frac{d}{d\alpha}\chi(\boldsymbol{m}+\alpha\boldsymbol{s})\right]_{\alpha=0} + \frac{\alpha^2}{2}\left[\frac{d^2}{d\alpha^2}\chi(\boldsymbol{m}+\alpha\boldsymbol{s})\right]_{\alpha=0}$$
$$= \chi(\boldsymbol{m}) + \alpha\boldsymbol{s}\cdot\nabla_{\boldsymbol{m}}\chi(\boldsymbol{m}) + \frac{\alpha^2}{2}\boldsymbol{s}\cdot\boldsymbol{H}_{\chi}(\boldsymbol{m})\cdot\boldsymbol{s}, \quad (6.55)$$

we obtain

$$0 \approx \frac{\chi(\boldsymbol{m}+\alpha\boldsymbol{s})-\chi(\boldsymbol{m})}{\alpha} \approx \boldsymbol{s}\cdot\nabla_{\boldsymbol{m}}\chi(\boldsymbol{m}) + \alpha\boldsymbol{s}\cdot\boldsymbol{H}_{\chi}(\boldsymbol{m})\cdot\boldsymbol{s}. \quad (6.56)$$

Solving the last equation, we obtain the step size α_i as

$$\alpha \approx -\frac{\boldsymbol{s}\cdot\nabla_{\boldsymbol{m}}\chi(\boldsymbol{m})}{\boldsymbol{s}\cdot\boldsymbol{H}_{\chi}(\boldsymbol{m})\cdot\boldsymbol{s}}. \quad (6.57)$$

The search for α is an iterative process. One possibility to avoid the calculation of the Hessian matrix is to use the Secant method to calculate $\frac{d^2\chi(\boldsymbol{m}+\alpha\boldsymbol{s})}{d\alpha^2}$ approximately :

$$\frac{d^2\chi(\boldsymbol{m}+\alpha\boldsymbol{s})}{d\alpha^2} \approx \frac{[\frac{d}{d\alpha}\chi(\boldsymbol{m}+\alpha\boldsymbol{s})]_{\alpha=\sigma} - [\frac{d}{d\alpha}\chi(\boldsymbol{m}+\alpha\boldsymbol{s})]_{\alpha=0}}{\sigma}$$
$$= \frac{\nabla_{\boldsymbol{m}}\chi(\boldsymbol{m}+\alpha\boldsymbol{s})\cdot s - \nabla_{\boldsymbol{m}}\chi(\boldsymbol{m})\cdot s}{\sigma}. \quad (6.58)$$

Substituting the Secant approximation in (6.55), we obtain

$$\alpha \approx -\sigma\frac{\boldsymbol{s}\cdot\nabla_{\boldsymbol{m}}\chi(\boldsymbol{m})}{\nabla_{\boldsymbol{m}}\chi(\boldsymbol{m}+\alpha\boldsymbol{s})\cdot s - \nabla_{\boldsymbol{m}}\chi(\boldsymbol{m})\cdot s} \quad (6.59)$$

which does not require calculation of the Hessian matrix.

Another possibility is to assume that the function $\chi(\alpha)$ is a quadratic function which is needs three points to be found. This process can be iteratively done around the minimum point of every iteration until the convergence criteria is satisfied.

There is one important thing about line search algorithms in case of FWI problems; the function $\chi(\alpha)$ can very easily be nonlinear. In this case, we try to find figure out the range of α in which the first minimum of $\chi(\alpha)$ locates and treat the function again as a quadratic function. This strategy is based on nothing else but trying to choose an initial point which is close enough to the solution.

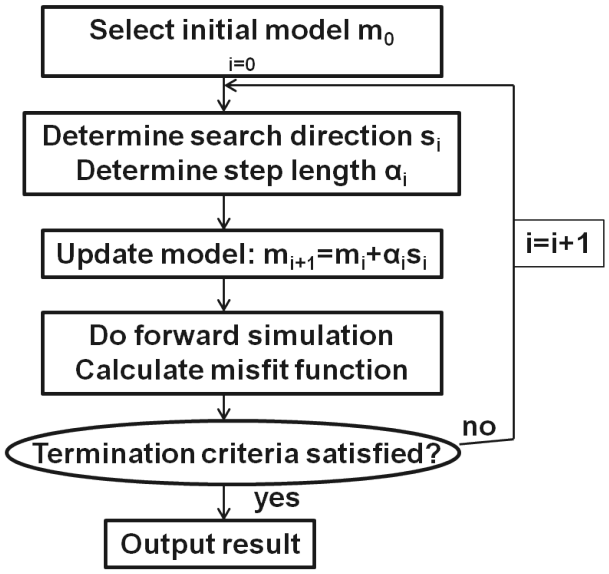

Figure 6.3: Minimization (optimization) process

6.3.1 Steepest descent method

The steepest descent (SD) method chooses the steepest descent direction as the search direction. The algorithm of SD is given in 1. Choosing the most rapid descent direction is effective locally. However, this strategy is not globally the most effective and it converges very slowly to the desired model in case of many non-linear inverse problems.

Algorithm 1 SD algorithm

Choose an initial model $\boldsymbol{m}_0$
$i = 0$
while convergence criteria not satisfied **do**
  calculate search direction $\boldsymbol{s}_i = -\nabla\chi(\boldsymbol{m}_i)$
  do line search(find α_i) $\boldsymbol{m}_{i+1} = \boldsymbol{m}_i + \alpha_i \boldsymbol{s}_i$
  update the model, $\boldsymbol{m}_{i+1}$
  $i = i + 1$
end while

6.3.2 Newton's method

The Newton's method is based on the first order necessary condition and linear Taylor expansion of the gradient $\nabla_{\boldsymbol{m}}\chi(\boldsymbol{m}_{min})$ around the minimum point $\boldsymbol{m}_{min}$:

$$0 = \nabla_{\boldsymbol{m}}\chi(\boldsymbol{m}_{min}) \approx \nabla_{\boldsymbol{m}}\chi(\boldsymbol{m}) + \boldsymbol{H}_{\chi}(\boldsymbol{m}_{min}) \cdot (\boldsymbol{m}_{min} - \boldsymbol{m}). \tag{6.60}$$

From the last equation, $\boldsymbol{m}_{min}$ is derived as

$$\boldsymbol{m}_{min} \approx \boldsymbol{m} - \boldsymbol{H}_{\chi}^{-1}(\boldsymbol{m}_{min}) \cdot \nabla_{\boldsymbol{m}}\chi(\boldsymbol{m}_{min}). \tag{6.61}$$

The algorithm of Newton's method is presented in algorithm 2. There is no need to perform a

Algorithm 2 Newton algorithm

Choose an initial model $\boldsymbol{m}_0$
$i = 0$
while convergence criteria not satisfied **do**
  calculate gradient $\nabla\chi(\boldsymbol{m}_i)$
  calculate Hessian matrix $\boldsymbol{H}_\chi(\boldsymbol{m}_i)$
  determine the search direction $\boldsymbol{s}_i = -\boldsymbol{H}_\chi^{-1}(\boldsymbol{m}_i) \cdot \nabla\chi(m_i)$
  update the model parameter $\boldsymbol{m}_{i+1} = \boldsymbol{m}_i + \boldsymbol{s}_i$, $(\alpha_i = 1)$
  $i = i + 1$
end while

line search calculation in case of the pure Newton method. Nevertheless, line search can also be performed to minimize $\chi(\boldsymbol{m}_{i+1})$ as much as possible. The advantage of the Newton's method is its quadratic convergence which is much faster than its counterparts. However, the calculation of the Hessian matrix is too expensive, especially in case of FWI problems. Moreover, the initial model has to be more appropriately chosen if Newton's method is to be used to solve a non-convex problem. If the initial model is far from the sought minimum point, the Hessian matrix may have negative eigenvalues or may be singular. In the best case, this can lead to very slow convergence, and in the worst case, the method can diverge from the minimum point.

There are several variants of Newton's method. One variant is regularized Newton method which circumvents inversion of singular Hessian matrix:

$$\boldsymbol{m}_{i+1} = \boldsymbol{m}_i - (\boldsymbol{H}_\chi(\boldsymbol{m}_i) + \beta\boldsymbol{I})^{-1} \cdot \nabla\chi(m_i). \tag{6.62}$$

Gauss-Newton method is another variant of Newton method. It accounts for reducing computational cost of the calculation of full Hessian matrix which is replaced by the approximate Hessian matrix. Gauss-Newton also has its regularized form which is called Levenberg method [Levenberg, 1944]. [Pratt et al., 1998] performs Gauss-Newton and full Newton methods in frequency-space seismic waveform inversion problems.

Another quasi-Newton method is BFGS, [Shanno, 1970], [Broyden, 1970], [Fletcher, 1970], which does not require the calculation of the Hessian matrix. [Yong and Dave, 2012] demonstrate BFGS on a full waveform inversion problem.

6.3.3 Generalized conjugate gradient method

The conjugate gradient method is widely used to solve linear systems and nonlinear optimization problems. The advantage of CG is that the search directions satisfy the orthogonality conditions. This fact guarantees the solution at most within n steps where n is the size of the model parameter $\boldsymbol{m}$. Unlike SD method, CG searches for the model in an orthogonal direction to the directions in the previous iterations. This means that the search direction in the current iteration does not have components in the previous search directions and thus, it does not search the model in the same direction over and over as SD does. For a detailed information about the CG method one can refer to [Shewchuk, 1994].

In this work, this method is used for both discrete and continuous approaches in which the objective χ is mapping from a linear space into real numbers. The linear space is equipped with

an inner product $<,>$ which is defined as

$$< \mathbf{u}, \mathbf{v} >= \mathbf{u} \cdot \mathbf{v} = \sum u_i v_i \tag{6.63}$$

for the discrete case and

$$< u, v >= \int uvd\Omega \tag{6.64}$$

for the continuous case.

Algorithm 3 CG algorithm

Choose an initial model m_0
$s_0 = r_0 = -\nabla\chi(m_0)$
do line search α_0, $m_1 = m_0 + \alpha_0 s_0$
update the model, m_1
$i = 1$
while convergence criteria not satisfied **do**
  calculate gradient $r_{i+1} = -\nabla\chi(m_{i+1})$
  calculate β_{i+1}
  calculate search direction $s_{i+1} = r_{i+1} + \beta_{i+1} s_i$
  do line search $m_{i+1} = \boldsymbol{m}_i + \alpha_i \boldsymbol{s}_i$
  update the model, m_{i+1}
  $i = i + 1$
end while

We use the Polak-Ribiere method [Polak and Ribiere, 1969] for β

$$\beta_{i+1} = \max\Big\{\frac{< r_{i+1}, r_{i+1} - r_i >}{< r_i, r_i >}, 0\Big\}. \tag{6.65}$$

Other possibilities are Fletcher-Reeves method[Fletcher and Reeves, 1964]

$$\beta_{i+1} = \frac{< r_{i+1}, r_{i+1} >}{< r_i, r_i >}, \tag{6.66}$$

and Hestenes-Stiefel method[Hestenes and Stiefel, 1952]

$$\beta_{i+1} = \frac{< r_{i+1}, r_{i+1} - r_i >}{< s_i, r_{i+1} - r_i >}. \tag{6.67}$$

6.3.4 Pre-conditioned conjugate gradient method

Pre-conditioned CG method can be used when we have prior information based on our experience or intuition about the inverse model. For example, the gradient of the misfit function is high at source and receiver points due to singularity at those points. One can suppress artificially high values at sources and receivers by using a pre-conditioning matrix $\boldsymbol{P}$. Or if we have information about the distribution of mechanical properties of some part from the whole domain, we can disregard or decrease the gradient with the help of $\boldsymbol{P}$ matrix. We can also use pre-conditioning as a form of regularization and force the method choose fastest directions to the minimum model using the information about the properties of the inverse problem. This can

happen when we have two or more variables such as λ, μ, and ρ. The gradient is sometimes sensitive with respect to one of parameters. In such a case, the inversion process will search for the solution mostly in the direction of the parameter with high sensitivity. Although CG guarantees solution in a finite number of iterations, to run the simulation for too many iterations is computationally too expensive. We can use the information about the sensitivity of the misfit function χ with respect to the parameters and build the pre-conditioning matrix $\boldsymbol{P}$ based on this knowledge.

Algorithm 4 Pre-conditioned CG algorithm

Choose pre-conditioning matrix $\boldsymbol{P}$
Choose an initial model $\boldsymbol{m}_0$
$\boldsymbol{m}_0^{'} = \boldsymbol{P}^{-1}\boldsymbol{m}_0$
$\boldsymbol{s}_0 = \boldsymbol{r}_0^{'} = -\boldsymbol{P} \cdot \nabla\chi(\boldsymbol{m}_0)$
calculate step size α_0 $\boldsymbol{m}_1^{'} = \boldsymbol{m}_0^{'} + \alpha_0 s_0$
update the model, $\boldsymbol{m}_1^{'}$
$\boldsymbol{m}_1 = \boldsymbol{P} \cdot \boldsymbol{m}_1^{'}$
$i = 0$
while convergence criteria not satisfied **do**

calculate gradient $\boldsymbol{r}_{i+1}^{'} = -\boldsymbol{P} \cdot \nabla\chi(m_{i+1})$
calculate β_{i+1} with $\boldsymbol{r}^{'}$
calculate search direction $\boldsymbol{s}_{i+1} = \boldsymbol{r}_{i+1}^{'} + \beta_{i+1}\boldsymbol{s}_i$
calculate step size $\boldsymbol{m}_{i+1}^{'} = \boldsymbol{m}_i^{'} + \alpha_i \boldsymbol{s}_i$
update the model $\boldsymbol{m}_{i+1}^{'}$
$\boldsymbol{m}_{i+1} = \boldsymbol{P} \cdot \boldsymbol{m}_{i+1}^{'}$
$i = i + 1$
end while

7 Forward modelling: Numerical experiments and verification

In this chapter, we are presenting forward wave propagation problems. As we use our own code to solve the wave equations, we need to verify our code. We do it by comparing the numerical results with analytical results. Moreover, we use Specfem software to prove that our program solves the wave equations precisely. Apart from the verification of the code, we present some forward simulation results to see the wave propagation behavior in the ground.

7.1 2D acoustic half-space

The first forward model we present is 2D acoustic half-space. The forward simulation is verified using a half-space example in which the analytical solution for a homogeneous velocity field is known. In two-dimensional infinite space, the analytical solution of the acoustic equation (2.25) for a constant velocity field and a point source $f_\omega(\mathbf{x}) = \delta(\mathbf{x} - \mathbf{s})$ is

$$p^{\mathbf{s}}_\omega = \frac{i}{4} H_0^{(1)}(k|\mathbf{x} - \mathbf{s}|), \tag{7.1}$$

where $H_0^{(1)}$ is the Hankel function of the first kind, $k = \frac{\omega}{c}$ is the wavenumber, and $p^{\mathbf{s}}_\omega$ is the pressure field when the source is fired at point $\mathbf{s}$. The analytical solution of the half-space problem is constructed using the solution of the infinite domain (7.1). If a source is fired at point $\mathbf{s}$ in a half-space, its analytical solution is $p(\mathbf{x}, \mathbf{s}, \omega) - p(\mathbf{x}, \mathbf{t}, \omega)$. The pressure fields $p(\mathbf{x}, \mathbf{s}, \omega)$ and $p(\mathbf{x}, \mathbf{t}, \omega)$ are calculated using (7.1). The line from point $\mathbf{s}$ to point $\mathbf{t}$ is bisected by and perpendicular to the free surface line (see Figure 7.1).

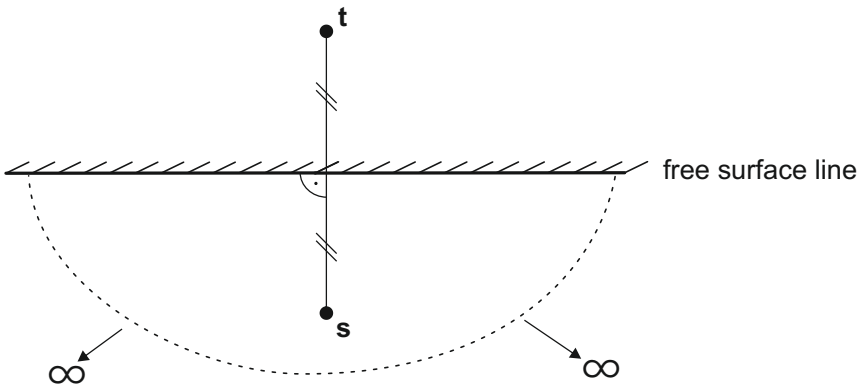

Figure 7.1: Acoustic half-space

Construction of the analytical solution

In this example, the acoustic equation is solved by the high-order finite elements method with hierarchical shape functions, [Szabó and Babuška, 2011], in a 90 m $\times$ 42.5 m domain with a mesh of 80×40 elements using a polynomial degree $p = 4$. To verify the code and the absorbing boundaries, the numerical result is compared to the analytical solution. The result in Figure 7.2 is the finite element solution of the Helmholtz equation with an angular frequency of 2000 Hz and a constant velocity field c=2000 m/s. The source is a Dirac delta distribution $f_\omega(\mathbf{x}) = \delta(\mathbf{x}-\mathbf{s})$ and the point $\mathbf{s}$ lies directly below the free surface.

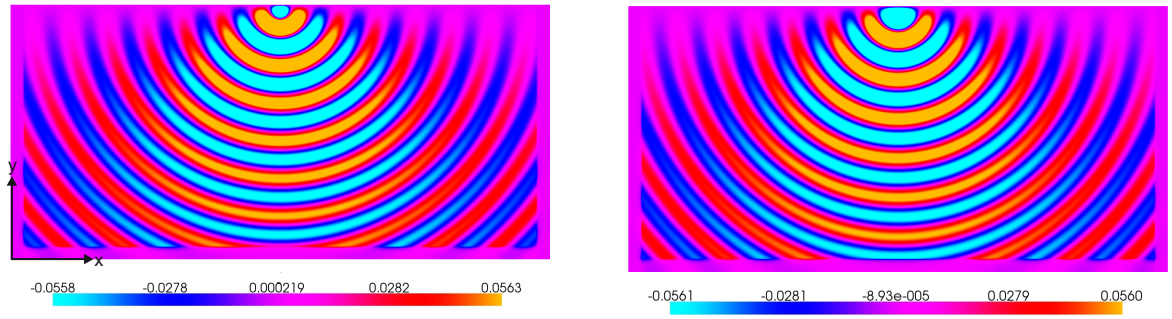

(a) Real part (b) Imaginary part

Figure 7.2: Wavefields in the acoustic half-space with FE

$\omega = 300$ Hz

In Figures 7.3 and 7.4, the analytical and FE solutions are compared over the horizontal line AB at about y=21.8 m and the vertical line CD at about y=44.4 m. A very good agreement is observed between the numerical and analytical results. In the numerical results, in the region close to the edges where there are PMLs, the solution is not correct since it is the part in which the PMLs are located and absorb the incoming waves. It is obvious that the norm of the pressure decay to zero in the PML region is very fast. In contrast to the FE result, the difference grows in PML regions. This is exactly what we expect from the PMLs. In Figure 7.3b, the difference function becomes larger in the region close to the free surface. However, this difference is negligible.

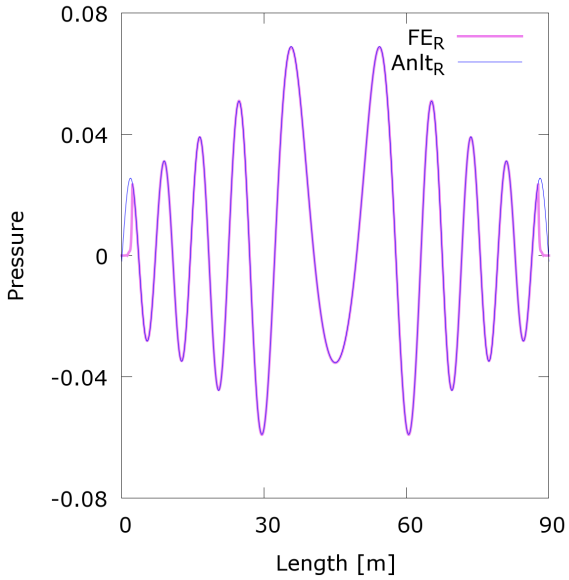

(a) Horizontal line AB, real part

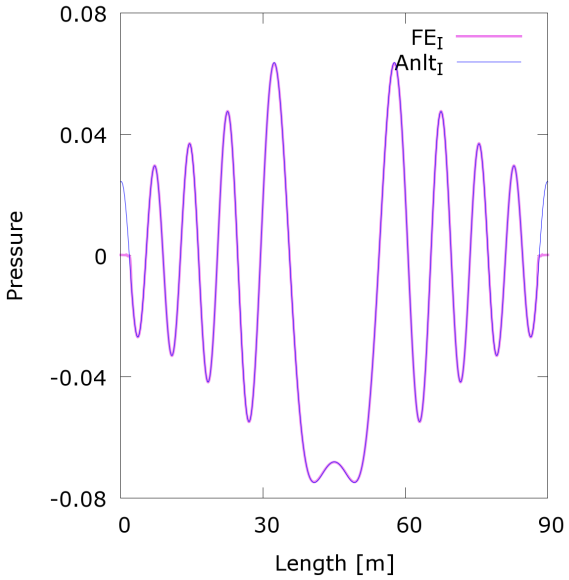

(b) Horizontal line AB, imaginary part

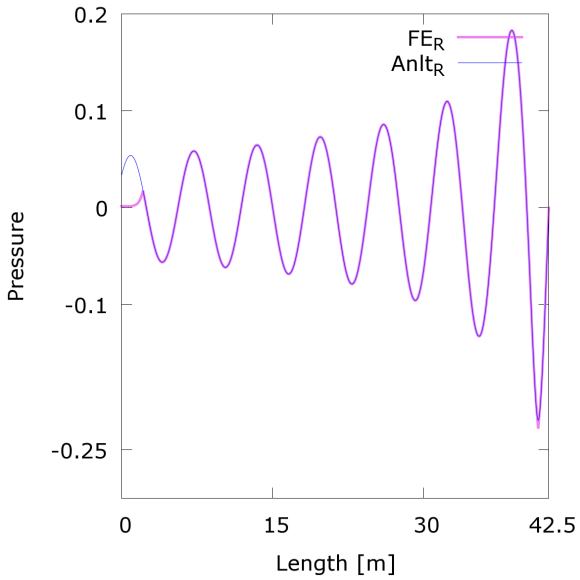

(c) Vertical line CD, real part

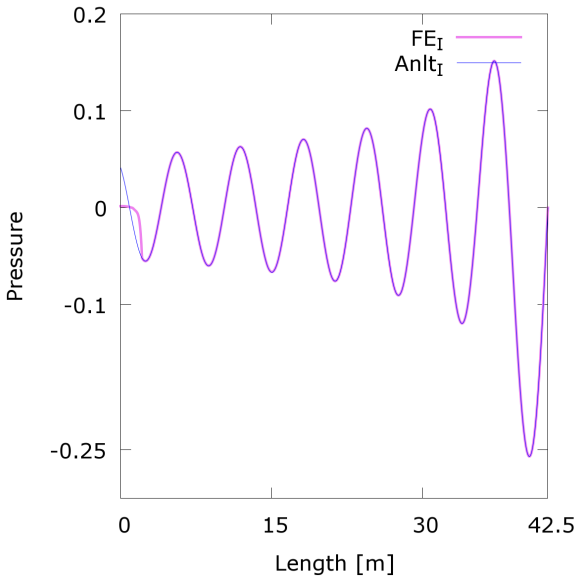

(d) Vertical line CD, imaginary part

Figure 7.3: Comparison of FE and analytical solutions over lines

$\omega = 2000\,\text{Hz}$

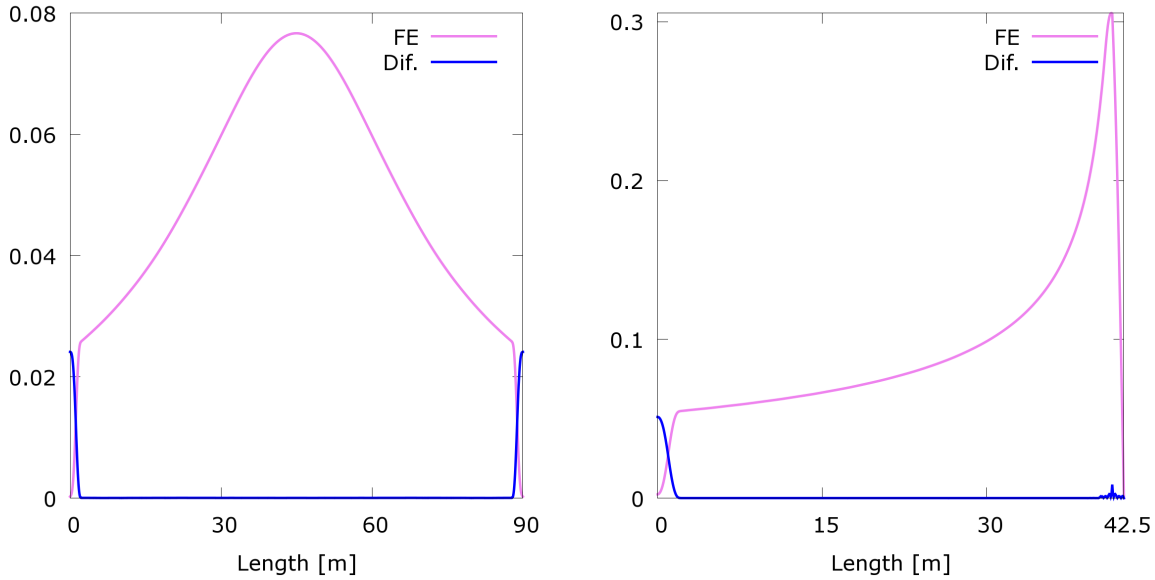

(a) Horizontal line AB (b) Vertical line CD

Figure 7.4: Norm of FE result and norm of the difference btw. FE and analytical results

$\omega = 2000\,\text{Hz}$

For a single frequency, it is seen that PML tackles the artificial boundaries perfectly. To see whether it performs well in a range rather than at a single frequency point, we read values at receiver points shown in Figure 7.2b for the angular frequency in the range 200-1200 Hz and compare the FE results to the analytical solution in Figure 7.5. Again, very good agreement is observed between FE solutions with PML and analytical solutions.

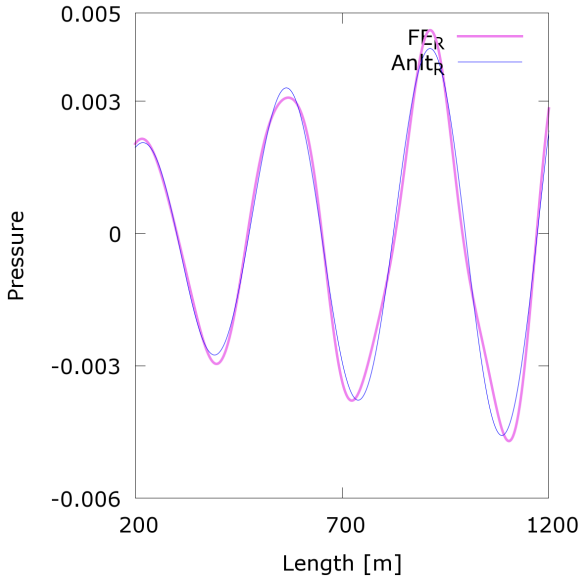

(a) Receiver $R1$ at $(9.0, 39.3125)$, real part

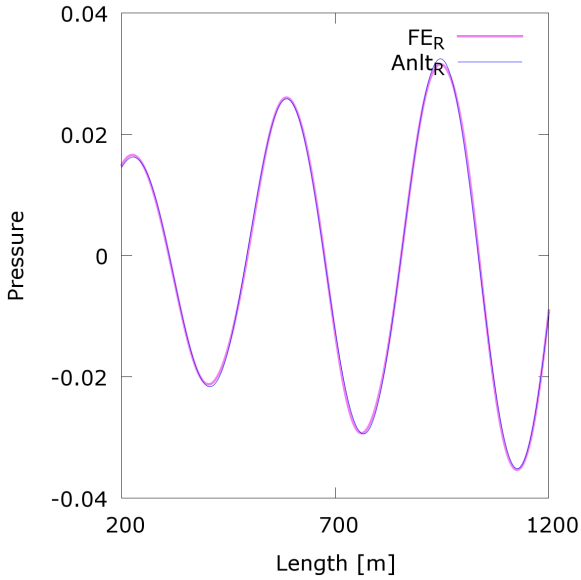

(b) Receiver $R2$ at $(19.125, 19.125)$, real part

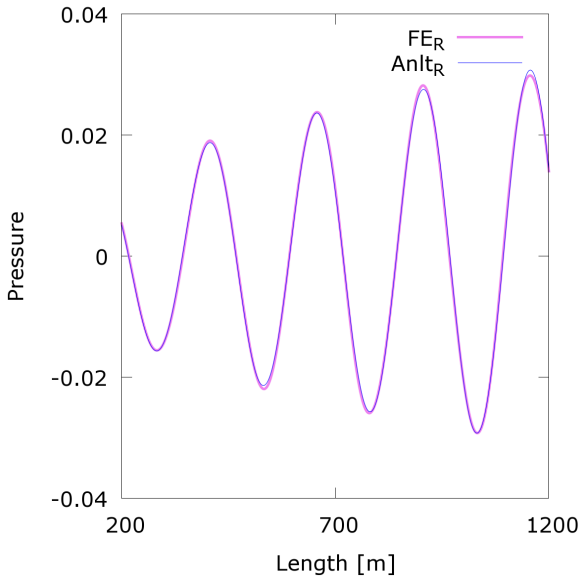

(c) Receiver $R3$ at $(9.0, 7.4375)$, real part

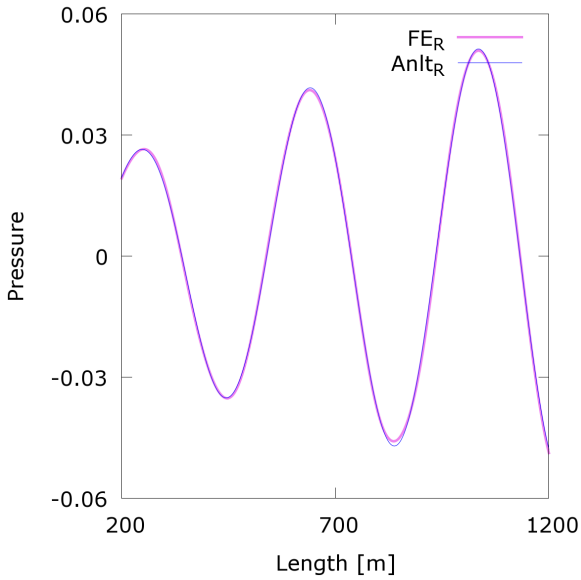

(d) Receiver $R4$ at $(45.0, 10.625)$, imaginary part

Figure 7.5: Comparison of FE and analytical solutions over a frequency range ω =200-1200 Hz

7.2 2D acoustic tunnel

Our numerical model is represented by the acoustic equation with no attenuation defined for a tunnel domain whose dimensions and boundary conditions are described in Figure 8.1. The air-soil interface is modelled with a free surface and artificial boundaries that do not exist in reality and are mimicked by PML layers. in the first step, a velocity field with a constant value c=2000 $\frac{m}{s}$ is considered, and simulations are run for the angular frequencies 1000 Hz and 2000 Hz. A Dirac delta function is applied just in front of the tunnel face. The results are shown in Figure 7.6.

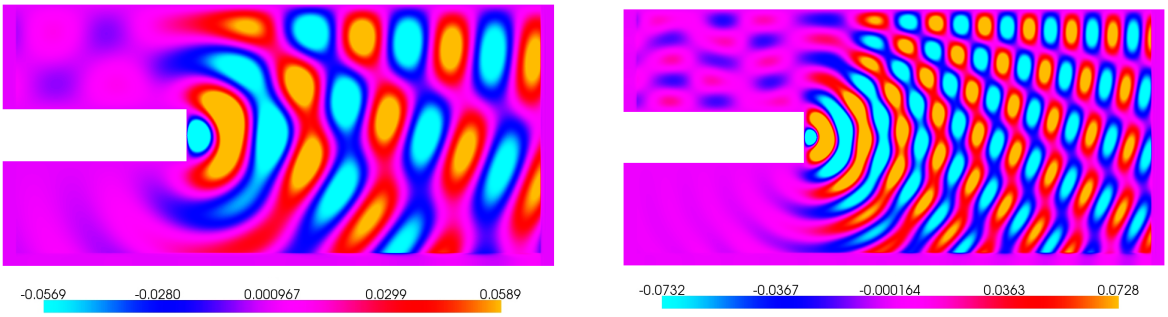

(a) Angular frequency 1000 Hz (b) Angular frequency 2000 Hz

Figure 7.6: Pressure wavefields in the tunnel by FE, homogeneous velocity field

Real part

Figure 7.6 shows that the pressure values are zero on the free surfaces. The waves are fully reflected back from the free surfaces, whereas the PML layers absorb the waves and act as though the artificial layers do not exist in the model. It is possible to see that the PML edges are perpendicular to the directions in which the waves are propagating and that the waves are efficiently absorbed by the PML layers. The precision of the absorption depends on coefficient c_{pml} and on damping function γ_x.

In the second step, an inhomogeneous velocity field is considered. The velocity field used for the next result is shown in Figure 8.1. The angular frequency is 2000 Hz, and the source is the same as in the previous example. The result of this simulation is given in Figure 7.7, which shows that the wavenumbers inside the circles are larger than outside the circles because the velocity value of the circles is smaller. When the waves hit the interface of the circles, reflection and refraction are observed.

7.2.1 Verification of the model with Specfem software

The next experiment is another important test for verification of our forward model. The aim is to simulate waves in time domain when a Ricker wavelet function is applied at a source point: this is achieved by solving the wave equation in the frequency domain over discrete frequencies and by transforming the data to the time domain with discrete Fourier transformation. At the same time, the same model is solved in the time domain by spectral element method in Specfem which is very well known in the community of geophysics. To have no reflections from the artificial boundaries in the time domain model, we make the numerical domain big enough such that we can stop the simulation before the reflected waves arrive at the stations. This gives

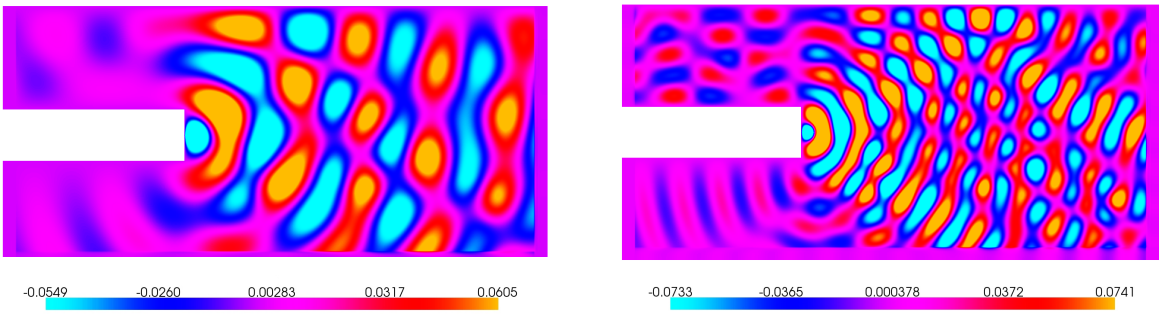

(a) Angular frequency 1000 Hz (b) Angular frequency 2000 Hz

Figure 7.7: Pressure wavefields in the tunnel by FE, homogeneous velocity field

Real parts

us opportunity to understand how effective the absorbing boundaries in the frequency domain model are.

We choose source and receiver points as illustrated in Figure 7.8. There are 31 receivers each of which is assigned a number. And there is only one single source point right ahead of tunnel face. The domain has a homogeneous velocity field of 3000 $\frac{m}{s}$. The source is a Ricker wavelet (Equation (4.15), (4.16)) with the peak frequency f_p =500 Hz and the temporal delay d_r =0 sec.

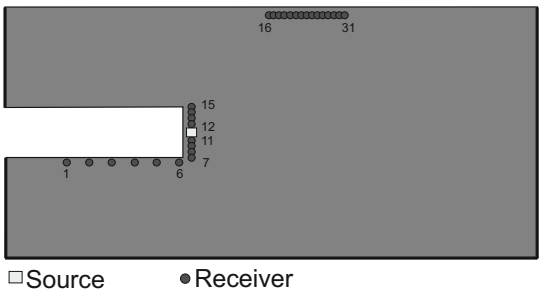

Figure 7.8: Source/receiver configuration

31 receivers, 1 source

We compare the seismograms from the time and frequency domain models in Figure (7.9). It is clearly observed that seismograms from frequency domain agree quite well with seismograms from the time domain model in which we avoided the reflected waves from the artificial layers. It means that the forward model in the frequency domain is precise enough with very robust absorbing boundaries. Nevertheless, there are some minor differences between the two wavefields. The differences can be due to different numerical approaches which are used to solve the problem, and different absorbing boundaries used for the models. In this case, the time domain model is chosen too big and the simulation is stopped before the reflections from the absorbing boundaries arrive at receivers. This lets us say that the error from the absorbing boundaries may only appear in the frequency domain model.

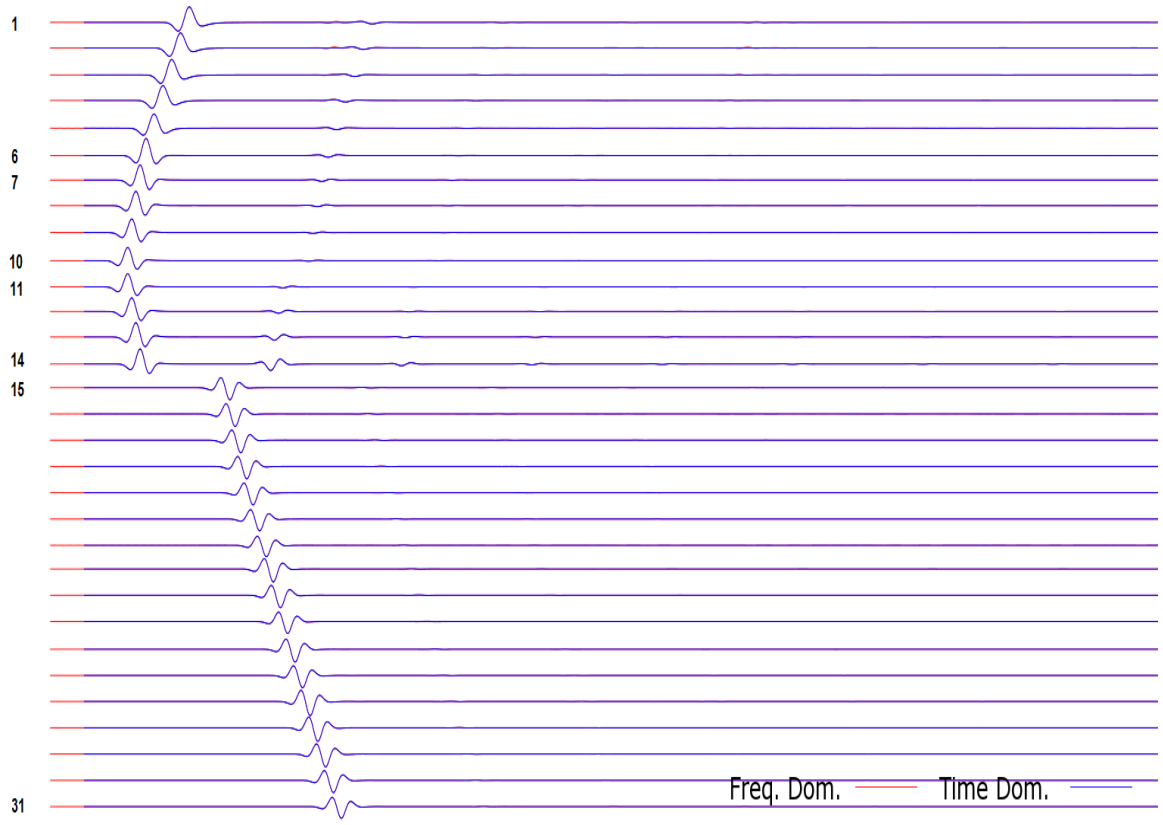

Figure 7.9: Comparison between the time and frequency domain models

Next, we choose an inhomogeneous velocity field (Figure 7.10) and compare it to the homogeneous case using the same source/receiver configuration in Figure 7.8. Doing so, we can distinguish the incident waves and reflections from the air-solid interfaces from the reflections from the geological change which has a circular boundary (Figure 7.11).

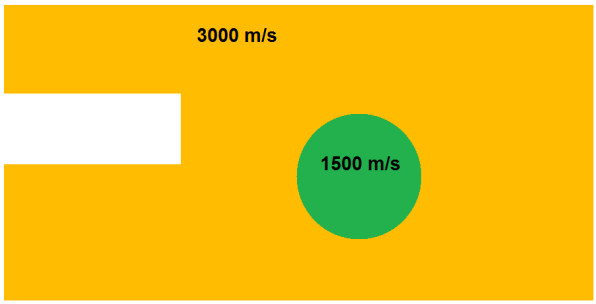

Figure 7.10: Inhomogeneous velocity field

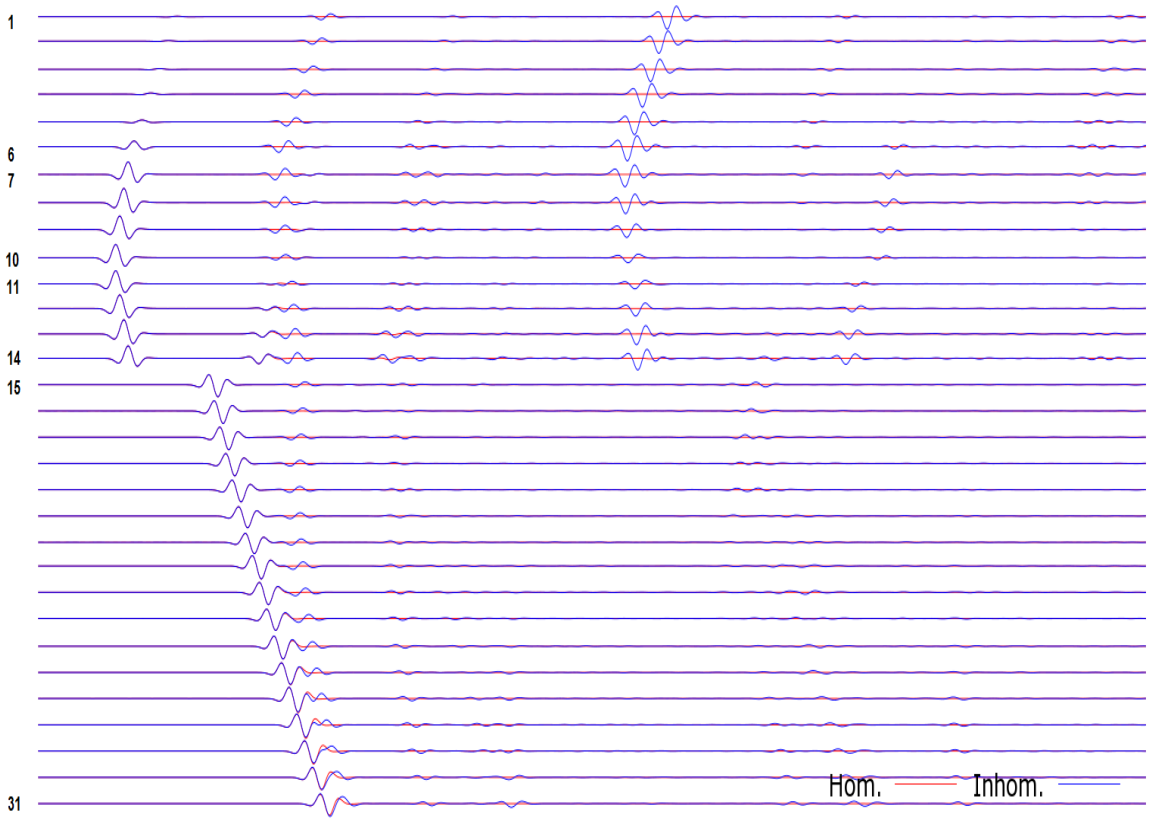

Figure 7.11: Wavefields from homogeneous and inhomogeneous models

7.3 2D viscoacoustic half-space

To have an insight of how attenuation influences the propagation of waves, we start with a half-space example. We use Kolsky-Futterman model, [Kolsky, 1956], [Futterman, 1962], to account for the viscosity in the domain. The parameter Q in eqn. (2.27) defines the attenuation. As $Q \longrightarrow \infty$, $\bar{c} \longrightarrow c$ and attenuation dissappears. In contrast, as $Q \longrightarrow 0$ attenuation affect increases. Figure 7.12 shows the intensity of attenuation as Q decreases. To see how the attenuation works for different frequencies, more numerical results for the pressure field with

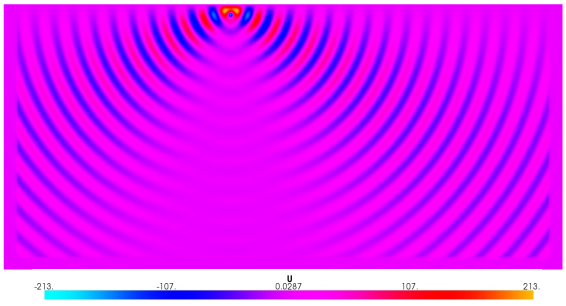

(a) $Q \longrightarrow \infty$

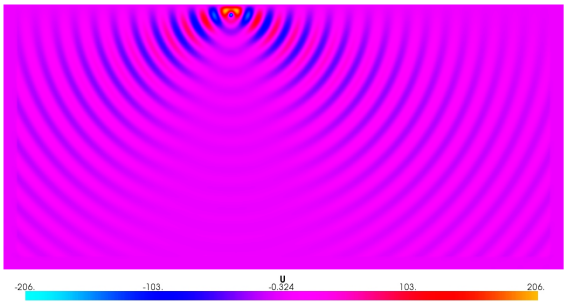

(b) Q=50

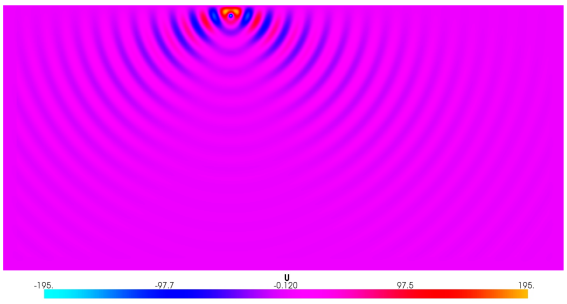

(c) Q=20

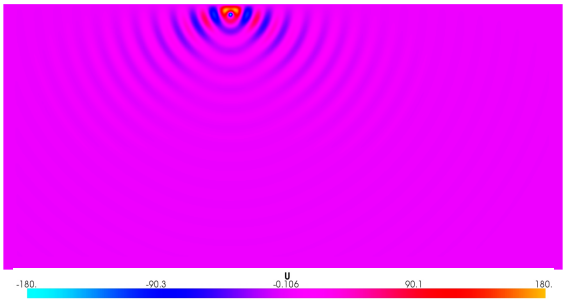

(d) Q=10

Figure 7.12: Attenuation in a half-space example

Real parts, ω = 1000Hz, domain 360m $\times$ 170m

$Q = 50$ is shown in Figure 7.13. The waves are attenuated to big extent till they reach the pml layers.

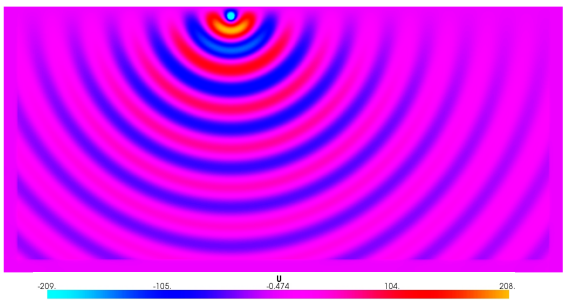

(a) ω =500Hz

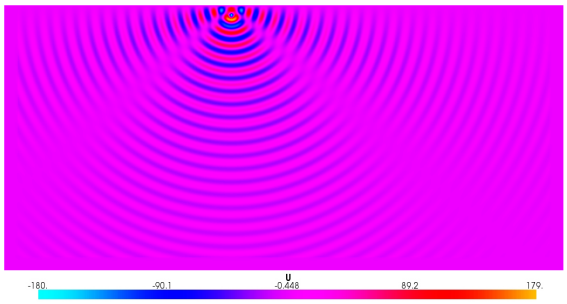

(b) ω =1500Hz

Figure 7.13: Viscoacoustic wavefields in half-space

To investigate the attenuation even closer, we choose 3 receiver points close to the surface and fire source at the source point which is located at the coordinate $(112.5, 167.875)$ as in the previous examples. This time, the simulation is carried out in the angular frequency range 100-1500Hz. As it is seen in Figure 7.14, the waves are attenuated as Q decreases. Especially in higher frequencies, the waves almost decay to zero with lower Q value.

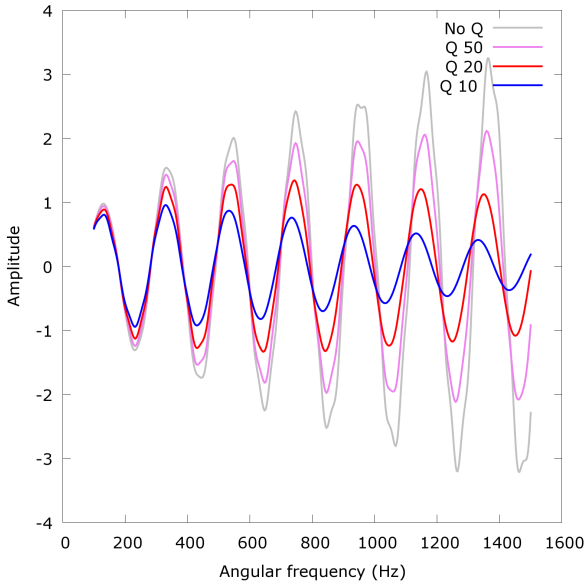

(a) Receiver 1 at (173.25, 167.875)

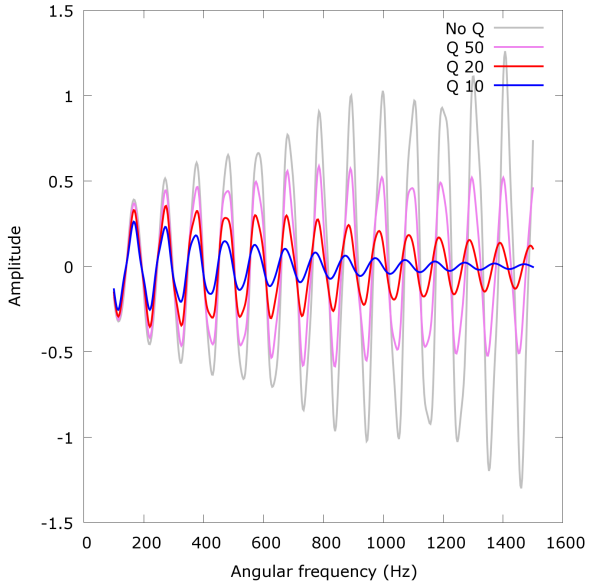

(b) Receiver 2 at (234.0, 167.875)

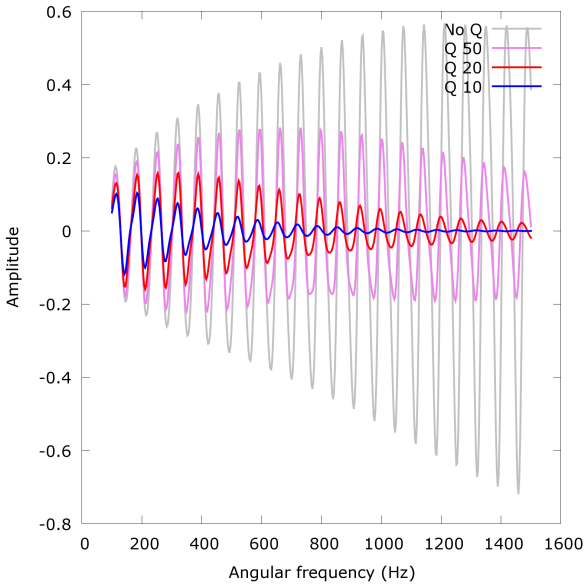

(c) Receiver 3 at (294.75, 167.875)

Figure 7.14: Attenuation at receivers over a frequency interval

Real parts, ω = 100-1500Hz

7.4 2D viscoacoustic tunnel

Next, we make a comparison between the tunnel model in Figure 7.10 and the same model with a homogeneous attenuation $Q = 60$. Figure 7.15 illustrates this comparison and it can be clearly seen in the amplitudes of wavefields that the energy is absorbed. The traveltimes of the incident and reflected waves do not change as we keep the velocity field the same in both cases.

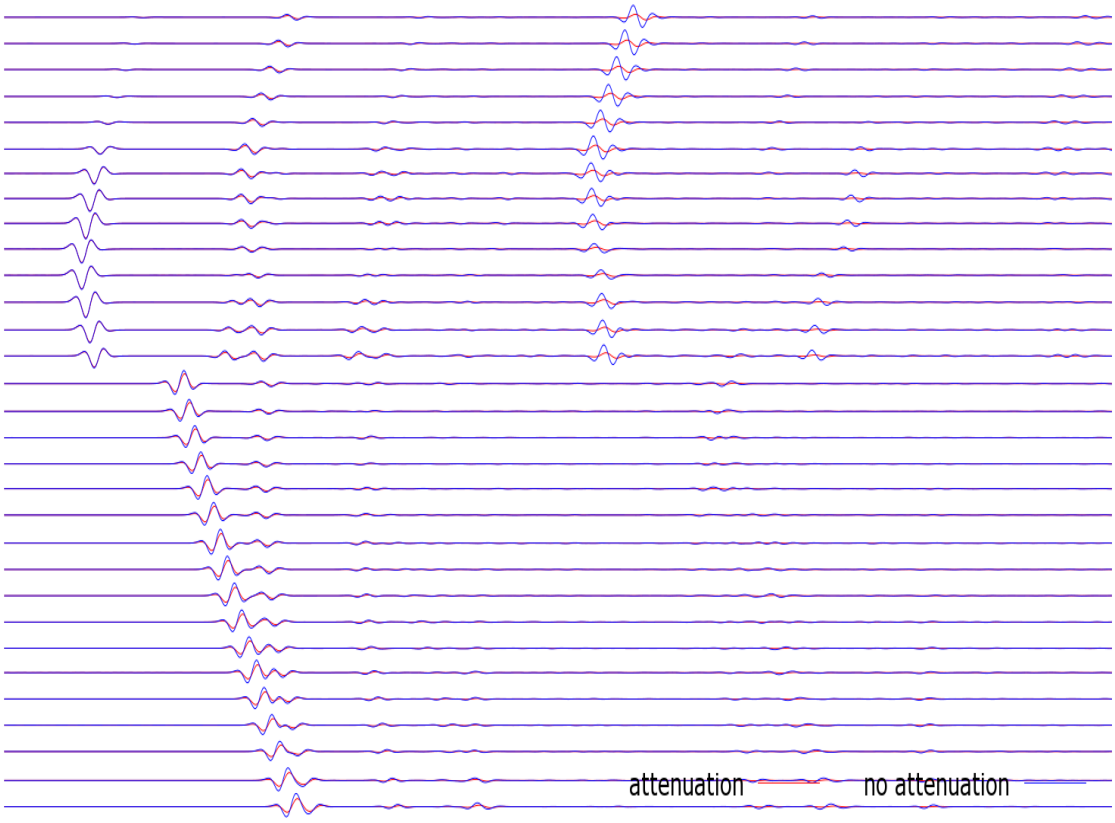

Figure 7.15: Viscosity influence on wavefields

In the following experiment, we add density inhomogeneity in the tunnel model. We choose the density as $1000\,{}^{kg}/_{m^3}$ everywhere outside the circle in Figure 7.10, where we choose it as $1500\,{}^{kg}/_{m^3}$. Again the traveltimes remain the same as seen in Figure 7.16. as expected, we observe that the amplitudes of incident waves are same. However, the amplitudes of the reflected waves are less in the case of the inhomogeneous density where we have higher value inside the geological obstacle.

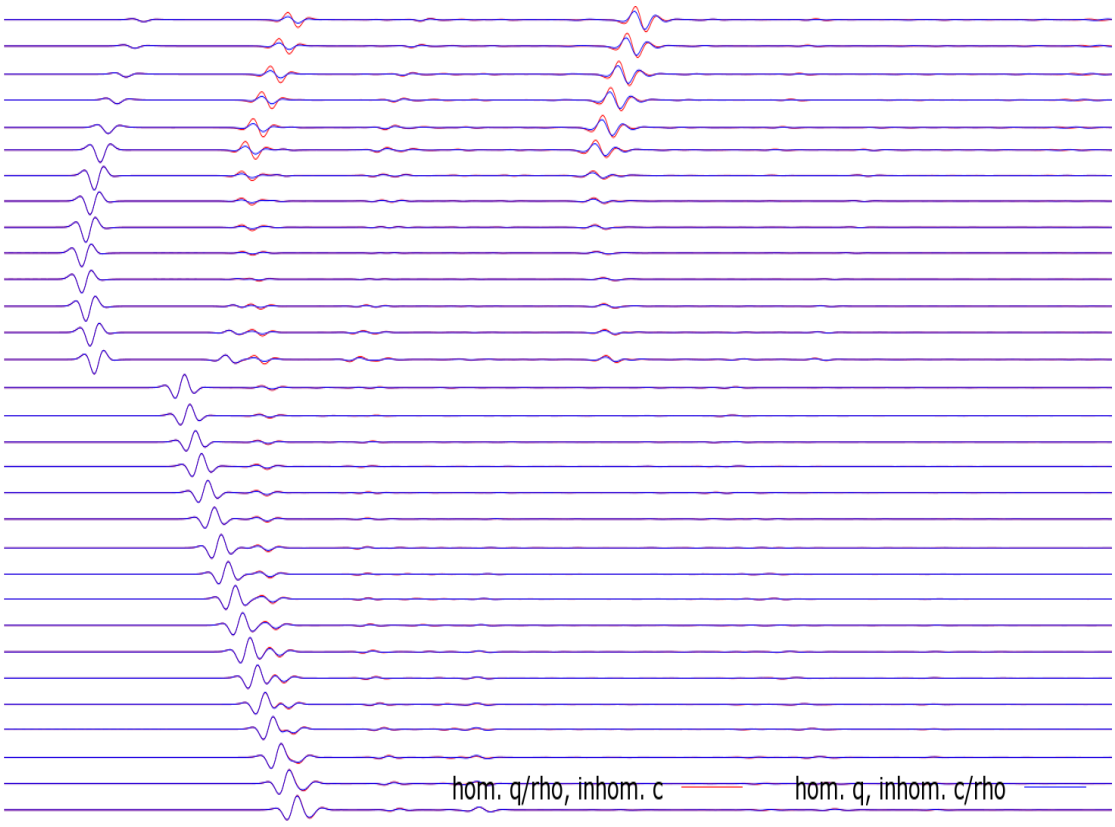

Figure 7.16: Influence of inhomogeneous density on wavefields

Finally, we consider the attenuation inhomogeneity in the model and try to observe the difference due to it. In Figure 7.17, we observe that the traveltimes and the amplitudes of the incident and first reflected waves remain the same. The density change caused amplitude change in all reflected waves. However, the attenuation change affected only the amplitudes of the reflected waves which arrive later than first reflected waves.

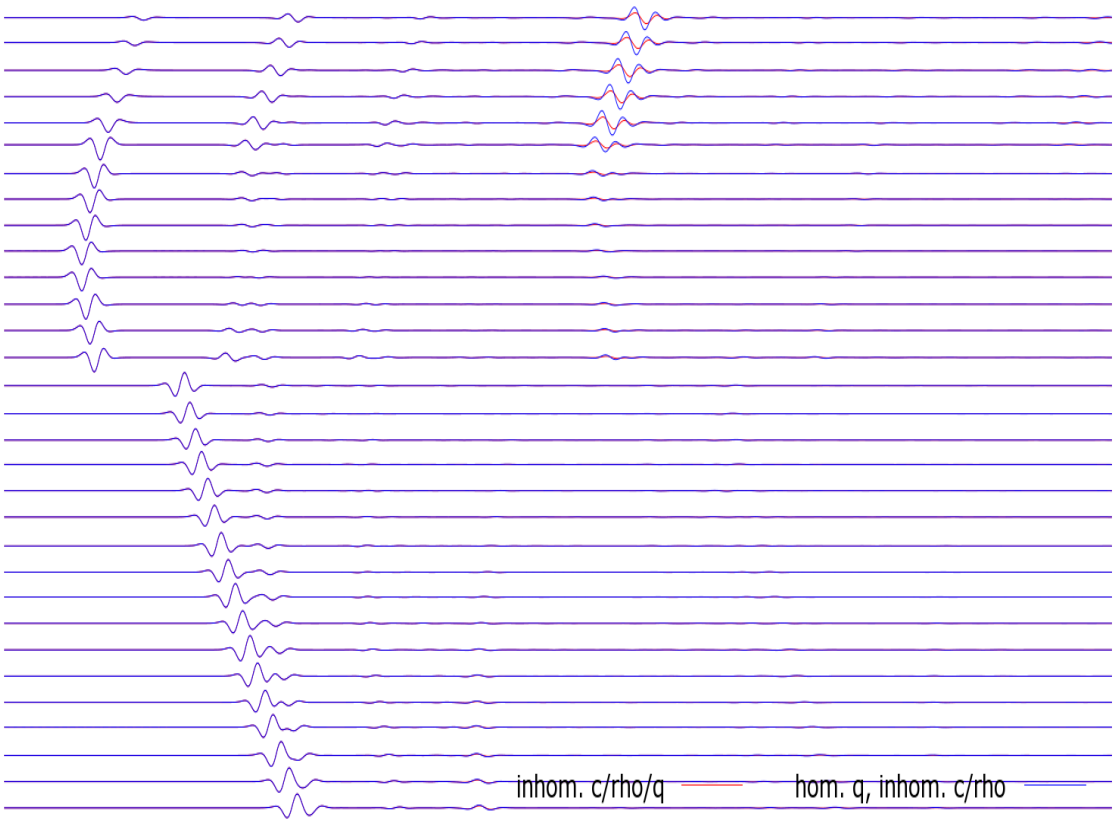

Figure 7.17: Influence of inhomogeneous attenuation on wavefields

7.5 3D acoustic forward simulation results

7.5.1 3D half-space and verification of the code with the analytical solution

In the three-dimensional infinite space, the analytical Green function of the acoustic equation (2.25) with a constant velocity field is

$$p(\mathbf{x}, \mathbf{s}, \omega) = \frac{e^{ik|\mathbf{x}-\mathbf{s}|}}{4\pi|\mathbf{x}-\mathbf{s}|}, \tag{7.2}$$

where $k = \frac{\omega}{c}$ is the wavenumber and $p(\mathbf{x}, \mathbf{s}, \omega)$ is the pressure field when the source is fired at point $\mathbf{s}$. First, the Helmholtz equation with homogeneous velocity field in an infinite domain is solved by FE method and the result is compared to the analytical solution (7.2) in Figure 7.18. Although there are some minor differences between the results, they overlap to a good extent.

(a) analytical result, real part

(b) analytical result, imaginary part

(c) numerical result, real part

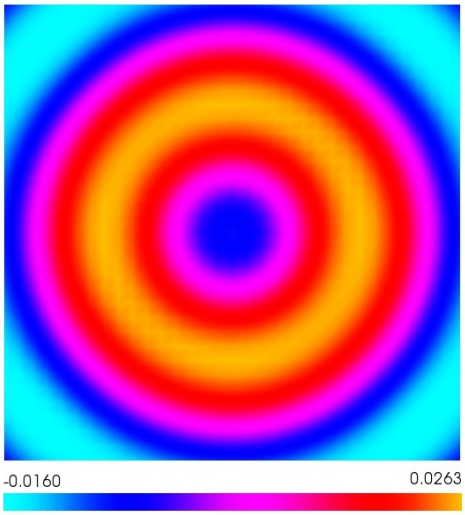

(d) numerical result, imaginary part

Figure 7.18: 3D full-space, pressure wavefields

$\omega = 3000$Hz, 8m $\times$ 8m $\times$ 8m, cut at 2m away from the source

Next, a half-space example is used to verify the forward model. The analytical solution of the half-space problem can be constructed by using the solution of the infinite domain in (7.2) as in the 2D acoustic half-space example (Figure 7.1). After solving the Helmholtz equation with FE method, the real and imaginary parts of the numerical results are compared to the analytical solutions in order to see whether the code solves the equation correctly in case of a half-space example, and whether the absorbing boundaries do what they are expected to do. The result in 7.19 is the solution of the Helmholtz equation with angular frequency 3000 Hz and constant velocity field 2000 $\frac{m}{s}$. The analytical result confirms the numerical result although there might be some minor numerical error which can mainly be caused by the coarse mesh. In this study, size of 3D numerical problems is kept relatively small as a result of the limited computer memory and time cost. To handle larger-sized problems, it is necessary to optimize and to parallelize the code. Another option is to run 3D simulations on computers with larger memories, where the time cost can still be high. Apart from the limited computer memory, numerical method itself brings in error too. It has to be considered that there is singularity at the source point and a numerical method has bigger error in the vicinity of the source point. This

error can be minimized by refining the mesh near the source point. Another source of the error can be the absorbing boundaries as every numerical method can produce errors. Although we try to keep the errors due to numerical methods minimum, they cannot be avoided fully.

(a) analytical result, real part

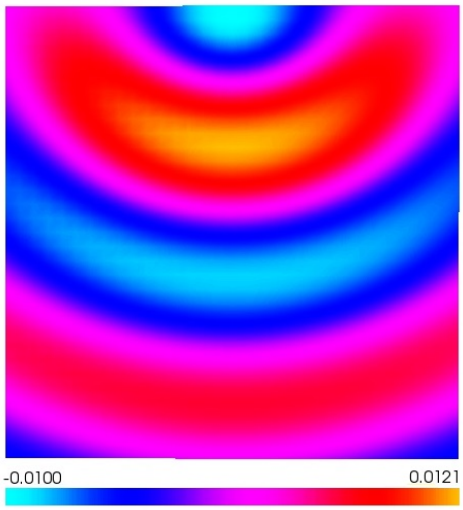

(b) analytical result, imaginary part

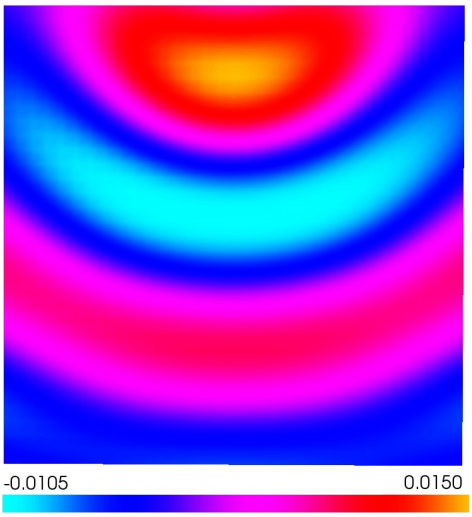

(c) numerical result, real part

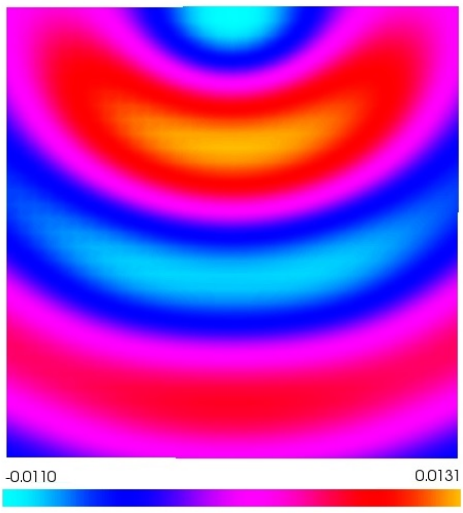

(d) numerical result, imaginary part

Figure 7.19: 3D half-space, pressure wavefields

$\omega = 3000$Hz, 8m $\times$ 8m $\times$ 8m

7.5.2 3D acoustic tunnel model

We consider a 3D tunnel model with a homogeneous velocity field of 2000 m/s and we run the simulations for the angular frequencies 1000 Hz and 2000 Hz. A Dirac delta function is applied right ahead the front tunnel face. The real parts of the complex wavefields are illustrated in Figure 7.20. From the figure 7.20, it can be seen that the pressure values are zero on the free surfaces. The waves are fully reflected back from the free surfaces, whereas the PML layers absorb the ways and act as though the artificial layers do not exist in the model.

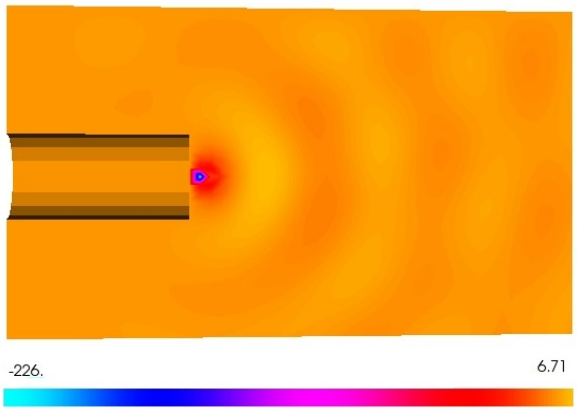

(a) Angular frequency 1200, real part

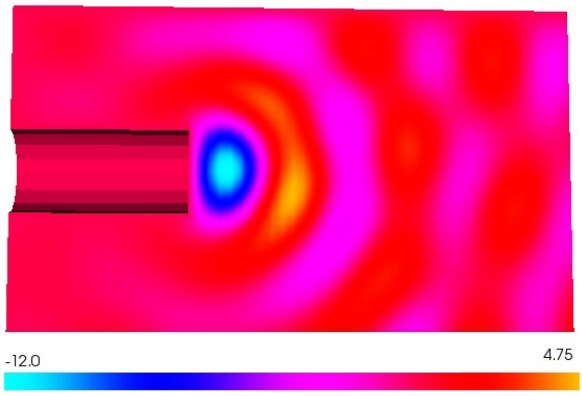

(b) Angular frequency 1200, imaginary part

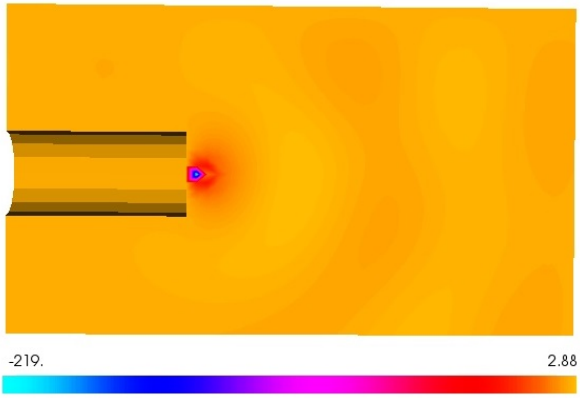

(c) Angular frequency 800, real part

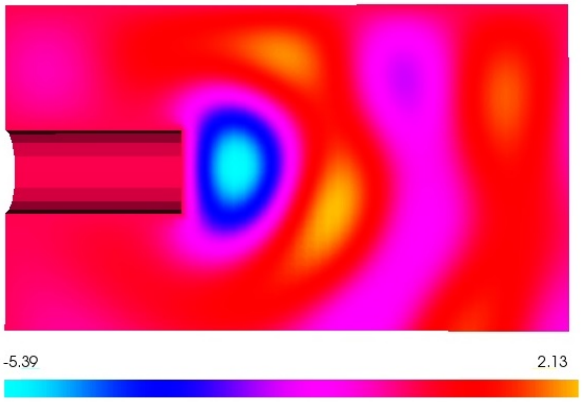

(d) Angular frequency 800, imaginary part

Figure 7.20: 3D tunnel, pressure wavefield

32m $\times$ 32m $\times$ 60m

7.6 2D elastic forward model

7.6.1 Verification of the 2D elastic tunnel model with Specfem software

To verify our 2D elastic tunnel model, we use a time domain model in Specfem software. We choose the domain big enough to avoid reflections from absorbing boundaries and we stop the calculations before the reflected waves arrive at receiver stations. In contrast to the acoustic waves, the reflected body waves from PMLs are not the only challenge encountered in an infinite

elastic model. Here, conversion of surface waves into body waves in PMLs parallel to the surface wave propagation direction is another challenge which occurs in case of low frequencies and shallow depth (Section 3.2). To cope with the body and surface waves at the same time, we use convolutional PML in elastic models.

The locations of the source and receiver points are shown in Figure 7.21, whereas the seismograms are presented in Figure 7.22 where seismograms from the time and frequency domain models are compared at each receiver point. The source function is the Ricker function with a peak frequency of 300 Hz and a temporal delay of 0 s. The seismograms confirm each other very well. However, this comparison is not very precise because it is not possible to see small differences. This is why we use single seismograms (Figure 7.23) to see differences between models. Figure 7.23 zooms in the displacement wavefields in both directions at one of the receivers to see the differences between the two models better. These differences are sometimes in the amplitude of body waves which can be caused by course mesh and lower FE basis degree which is 2 in our frequency domain model. Besides, the source of some part of the error can theoretically be absorbing layers. To carry out frequency domain analysis, the forward problem is solved over discrete frequencies and overall computational time of this process is high. Figure 4.2 is a clear example to see that the Ricker function approaches very fast to zero as the frequency goes farther from the peak frequency. We consider the frequency range till 1430 Hz to minimize the Fourier integration error as much as possible. Since the code is not parallelized, we try to keep the computational time low by using relatively course mesh and low polynomial degree 2. Although the model can still be improved by using finer mesh and higher FE degree basis, the model is already precise enough with some subtle errors and PML absorbing layers perform well in absorbing the incoming waves.

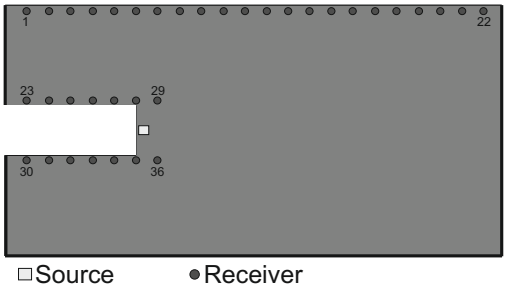

Figure 7.21: 2D elastic tunnel source/receiver configuration

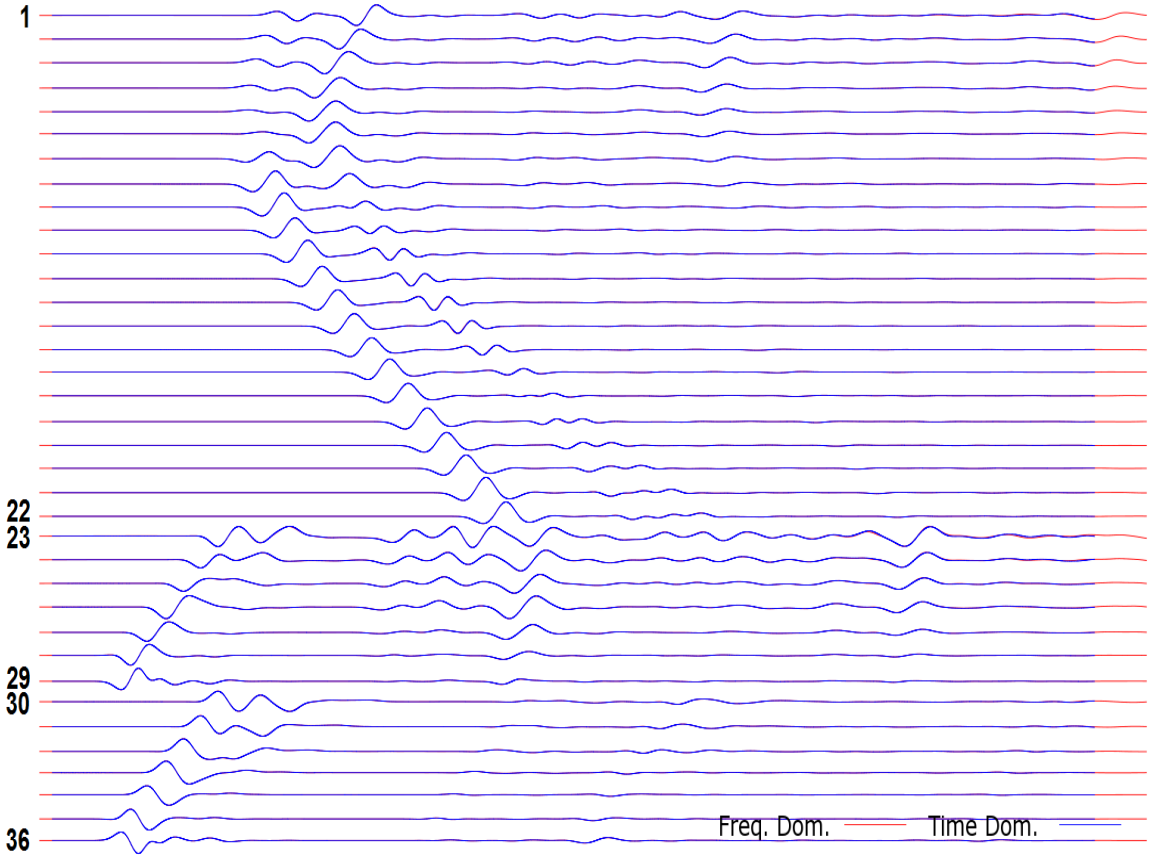

(a) Horizontal displacement u_x

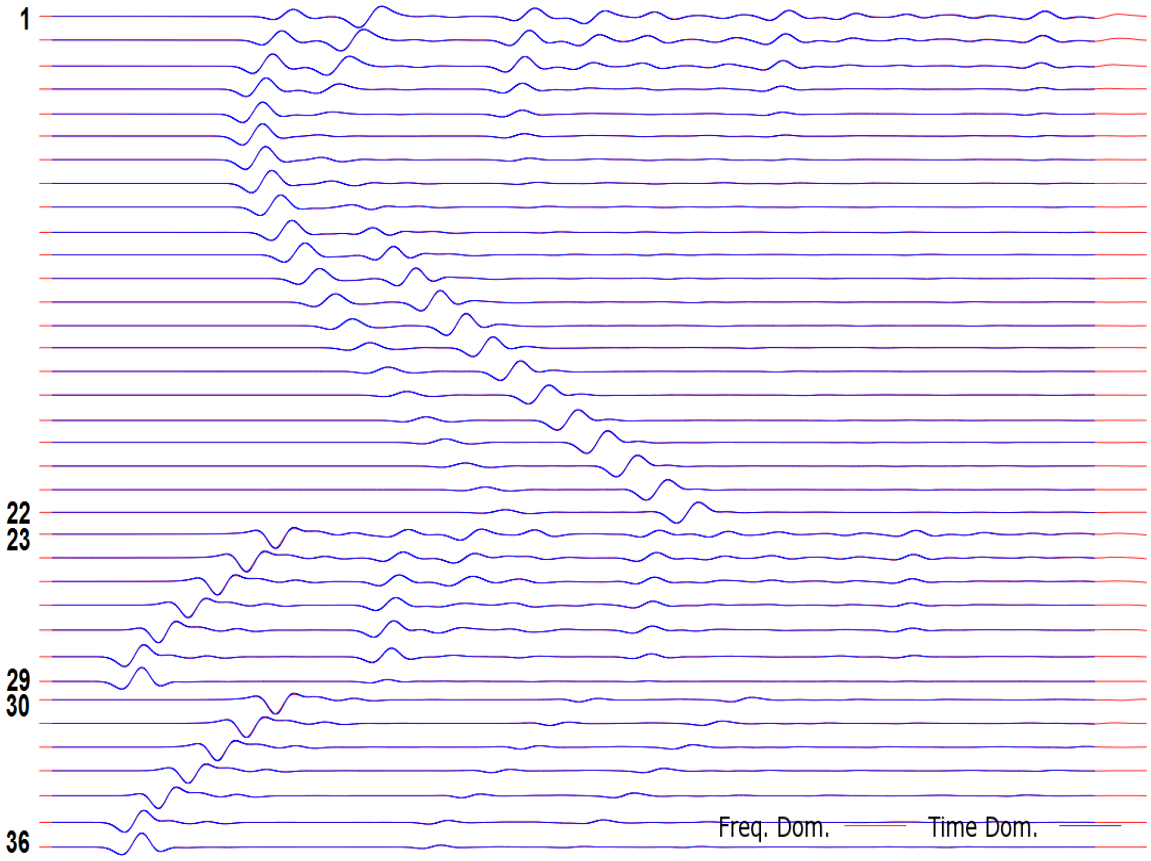

(b) Vertical displacement u_z

Figure 7.22: 2D elastic tunnel seismograms

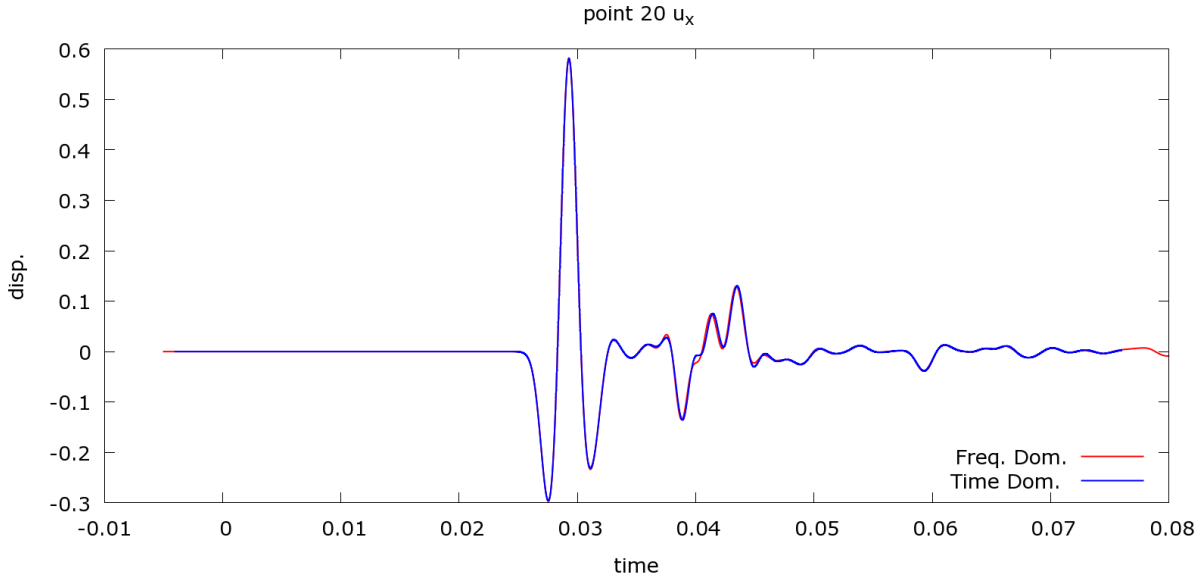

(a) u_x

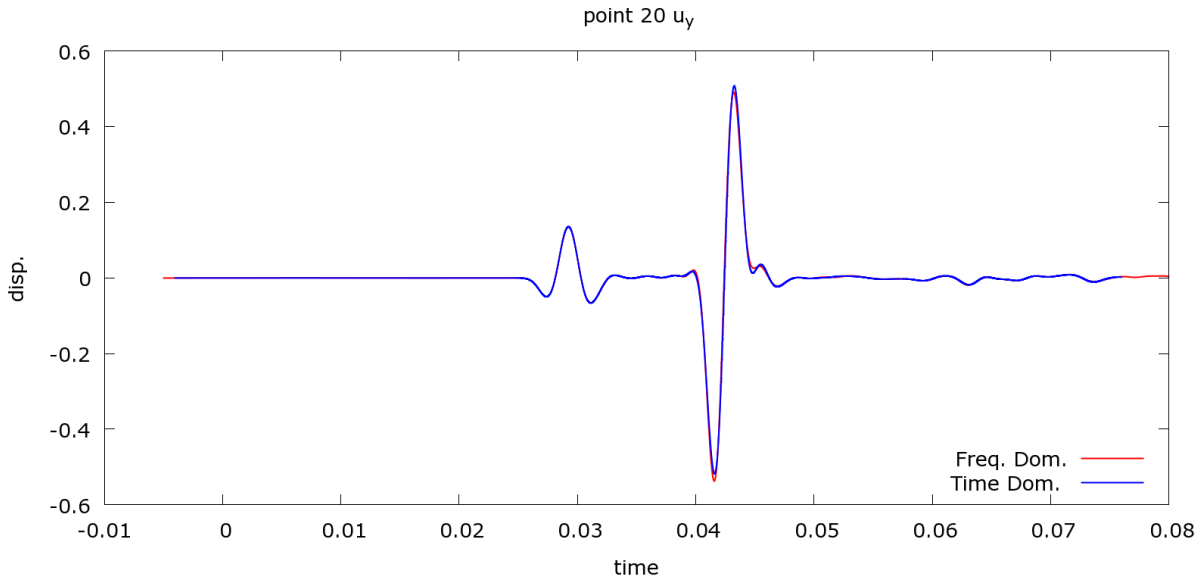

(b) u_y

Figure 7.23: Seismograms at point 20

8 Application of Full Waveform Inversion

8.1 Inversion of 2D acoustic waves

8.1.1 Scenario 1

In this section, we present the results of the inversion and discuss the influence of various parameters. The forward model (boundary conditions, dimensions, etc.) is shown in Figure 8.1). We use the higher-order finite elements method to solve the acoustic equation; the polynomial degree of the shape functions is 3, unless stated otherwise.

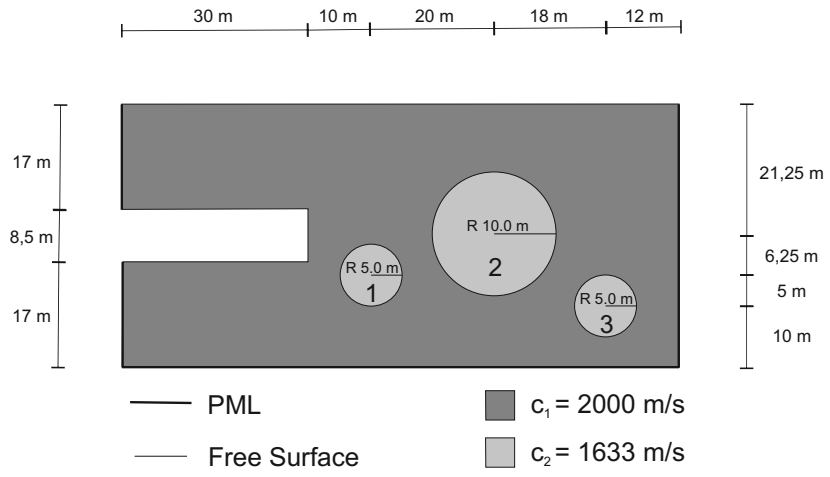

Figure 8.1: 2D acoustic tunnel forward model

Dimensions, boundaries and synthetic velocity field

The inversion results are verified with a synthetic model (see Figure 8.1), which is used to calculate the field data. There are three circles in the synthetic model where the velocity value is 1633 m/s. The velocity value in the rest of the domain is 2000 m/s. The initial model used in all the results illustrated in this paper is a constant velocity field with a value of 2000 m/s. The goal of the inversion is to detect the geometry, the locations, and the velocity values of the three circles.

Certain things must be carried out in order to have a well-posed inverse problem. This includes, in particular, the choice (position and number) of sender and receiver points. If these points are too few and the wrong locations are chosen, the inverse problem may become ill-posed because the data at the receiver points does not have enough information about the velocity field. Conversely, if there are too many senders and receivers, the computational cost greatly increases. The number of the source points, in particular, has a greater effect on the computational cost because the sources are fired one by one at every sender point. Bearing this in mind, we try to minimize the number of these points and to set them at reasonable locations. We use two different sender and receiver configurations in this work (see Figures 8.2a and 8.2b). In inverse

simulations, the configuration in Figure 8.2a is used, unless stated otherwise. The points of this configuration are more spread out over the domain, and include points on the front tunnel face and on the upper surface. The second configuration has points only on the front tunnel face and they are evenly distributed in the vertical direction, which is very similar to an actual industrial application, [Kneib et al., 2000].

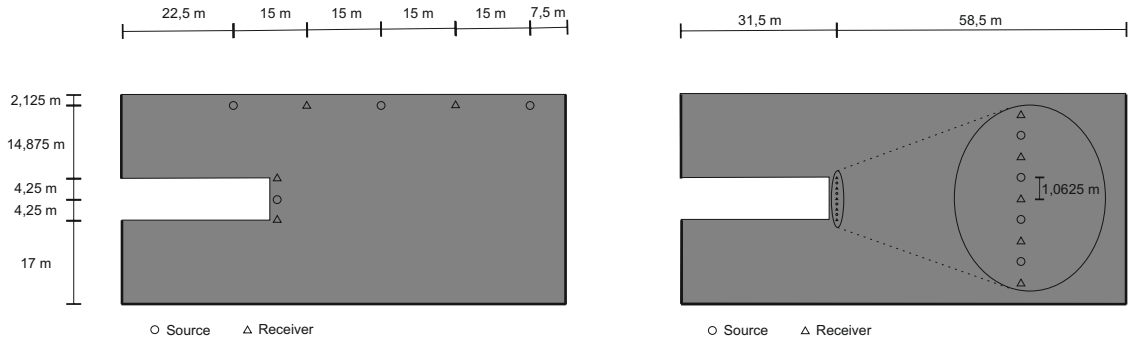

(a) Configuration A (b) Configuration B, points on the tunnel face

Figure 8.2: Source/receiver configurations

Another very important consideration is selection of the frequency set. The frequency set should be as small as possible to minimize computational costs. At the same time, it must be large enough to be able to reflect the real problem and not get stuck at a local minimum point. Two different angular frequency sets are used: the reduced set

$$G_R = \{50, 100, 150, ..., 1200\}, \tag{8.1}$$

and the full set

$$G_F = \{\{50\}, \{100\}, ..., \{600\}, \{600, 650\}, \{650, 700\}, \{700, 750\},$$

$$\{750, 800\}, \{750, 850\}, \{550, 900\}, \{950, 1000\}, \{1050\}, \{1100\}, \{1150, 1200, 900\}\}. \tag{8.2}$$

In the reduced set, there is only one frequency in every group. However, the second group is more mixed up, and some groups contain combinations of frequencies. The second frequency is always used, unless stated otherwise.

The results of discrete and continuous approaches are compared in Section 8.1.1. In all other sub-sections, only the discrete approach is used. In case of the discrete approach, we present results for both discretizations (piecewise linear combination and piecewise constant) of the velocity field, and compare them in Section 8.1.1.

To be able to see quantitative differences between the reference model and the results of the inversion, we define a relative error E_{rel} as

$$E_{rel} = \sqrt{\frac{\int_\Omega (c_{inv} - c_{syn})^2 d\Omega}{\int_\Omega c_{syn}^2 d\Omega}} \tag{8.3}$$

where c_{inv} and c_{syn} are the result of the inversion and the synthetic velocity field, respectively.

The Inversion results

Table 8.1 shows the relative errors for all the simulation results run in this study and is used to quantitatively compare the simulation results under different circumstances in the following sections. We distinguish between the simulations in 5 ways: inversion approach (discrete or continuous), sought function (c or $d = \frac{1}{c^2}$), discretization of the sought function, frequency set, and combination of senders and receivers.

#	Approach	Sought func.,deg.	Freq.	sender/rec.	Rel. Error %	w.r.t. best %
1	discrete	c,piecewise bilinear.	Full	A	2.543	100.0
2	discrete	c,piecewise const.	Full	A	6.818	268.1
3	discrete	c,piecewise comb.,deg.3	Full	A	2.783	109.4
4	discrete	c,piecewise comb.,deg.6	Full	A	2.787	109.6
5	discrete	c,piecewise bilinear	Reduced	A	2.874	113.0
6	discrete	c,piecewise bilinear	Full	B	3.722	146.4
7	discrete	d,piecewise bilinear	Full	A	3.208	126.2
8	discrete	d,piecewise comb.,deg.6	Full	A	3.254	128.0
9	continuous	d,FE degree 1	Full	A	3.080	121.1
10	continuous	d,FE degree 2	Full	A	4.422	173.9
11	continuous	d,FE degree 3	Full	A	4.856	191.0

Table 8.1: Relative errors in the results of the simulations

Next, we present the reconstructed velocity fields that we obtain from the inversion processes in Figures 8.3 and 8.4, where the inversion processes are based on the search for c and $\frac{1}{c^2}$, respectively. It is clearly observed that all inversion results are confirmed by the synthetic model. As expected, all of them have some errors involved in the reconstructed images. In general, we can see that the results obtained from the inverse simulations where c is searched look similar. The same thing can be said about the simulations based on the search of $\frac{1}{c^2}$. In the next sections, we discuss the differences amongst them and make conclusions about the influences of different parameters.

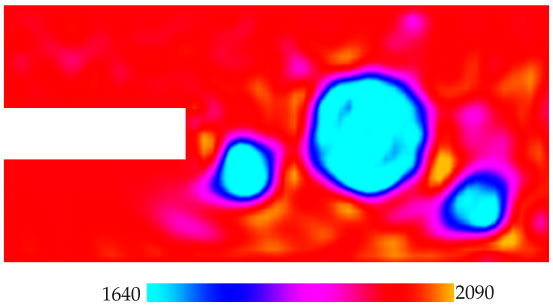

(a) #1

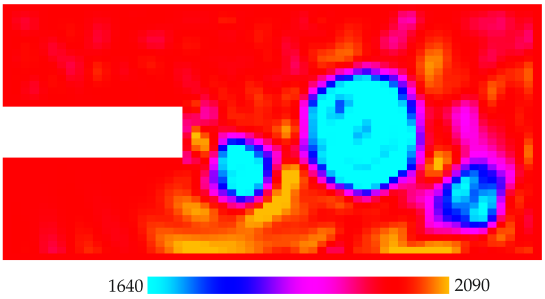

(b) #2, Piecewise constant vel. field

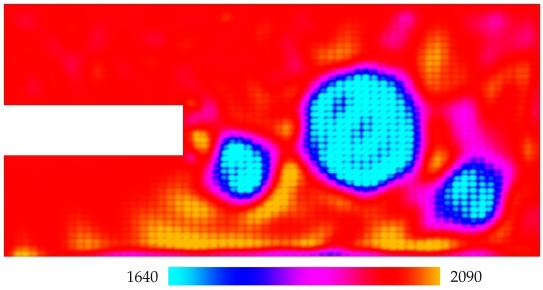

(c) #3, vel. field with polynomials of deg. 3

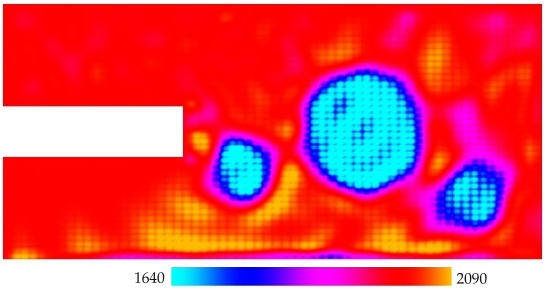

(d) #4, vel. field with polynomials of deg. 6

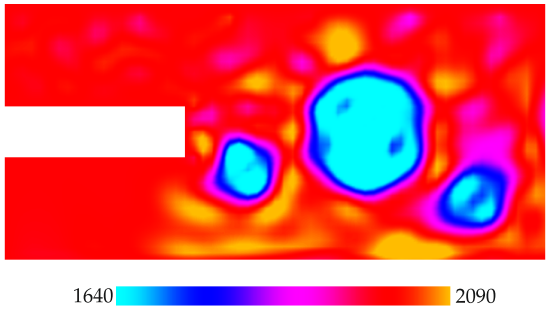

(e) #5, freq. set G_R,

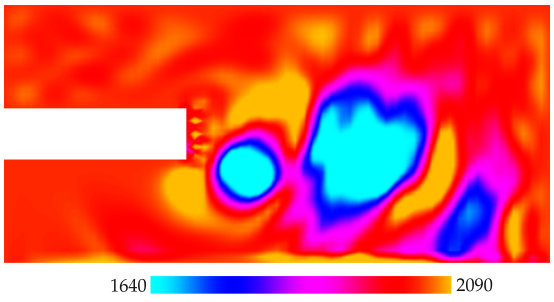

(f) #6, configuration B

Figure 8.3: Resultant velocity fields; search for c

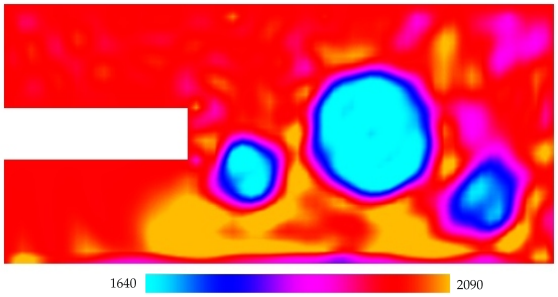

(a) #7, search for $d = \frac{1}{c^2}$ deg. 1

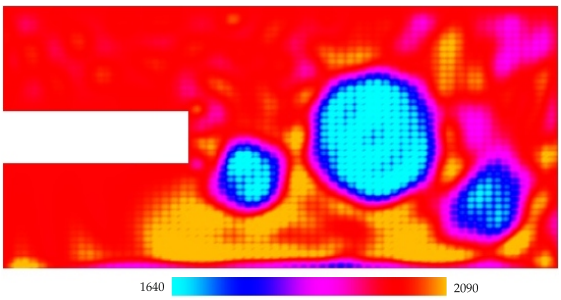

(b) #8, search for $d = \frac{1}{c^2}$ deg. 6

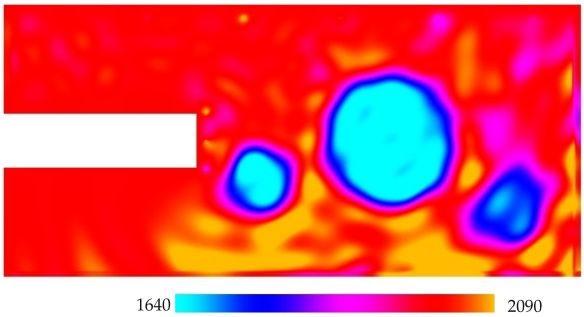

(c) #9, cont. approach, FE pol. deg. 1

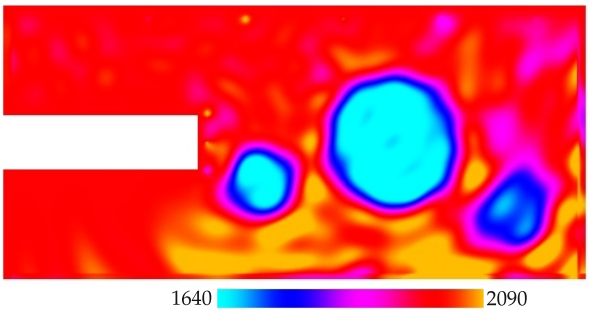

(d) #10, cont. approach, FE pol. deg. 2

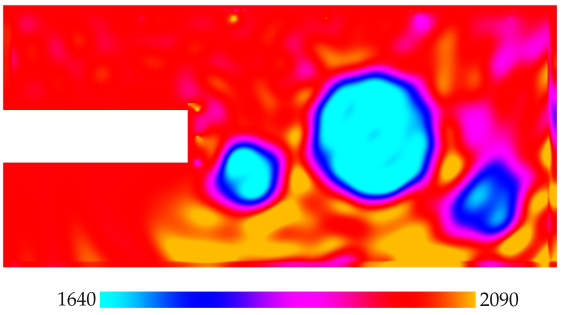

(e) #11, cont. approach, FE pol. deg. 3

Figure 8.4: Resultant velocity fields; search for $\frac{1}{c^2}$

In the end of this section, we highlight the result obtained using the discrete approach with configuration A in Figure 8.2a and frequency set G_F as defined in equation (8.2). To approximate the velocity field, the piecewise bilinear function is used. This simulation provides the best result amongst the results acquired from the other simulations performed in this work. The relative error E_{rel}, defined by (8.3), is 0.02543, which is the smallest error compared to the results of the other simulations (see Table 8.1). In an inversion simulation, it is interesting to see the convergences of the misfit function. Since there are 22 groups in set f_2, there are 22 inversion processes. Four representative frequency groups are shown in Figure 8.5.

At a local minimum point, the norm of the gradient is supposed to be zero. Since the inverse solver is numerical, the norm of the gradient is expected to converge to zero. The graphs in Figure 8.6 show how the norm of the gradient converges to zero.

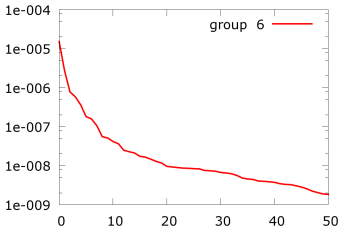

(a) Group 6

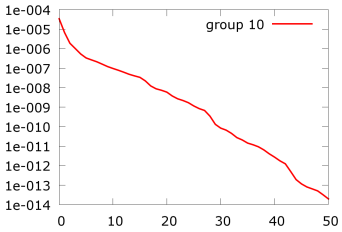

(b) Group 10

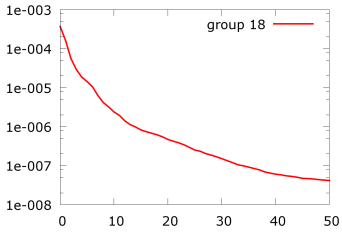

(c) Group 18

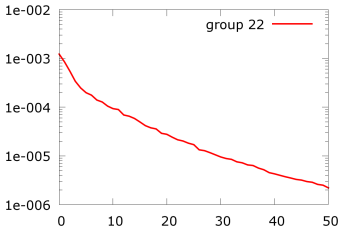

(d) Group 22

Figure 8.5: #1, misfit functional vs iteration, log scale

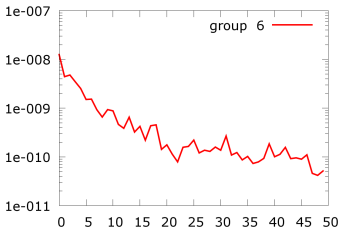

(a) Group 6

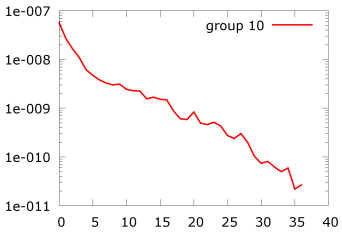

(b) Group 10

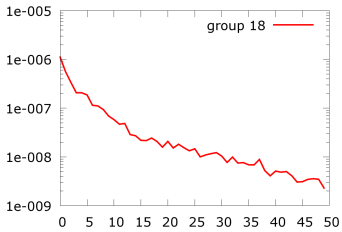

(c) Group 18

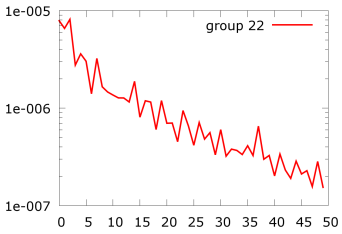

(d) Group 22

Figure 8.6: #1, norm of the gradient vs iteration, log scale

The final result is illustrated in Figure 8.3a and is in a very good agreement with the synthetic model in Figure 8.1. The geometry of the circles, their locations, and velocity values are detected to a good extent. Taking into account that the velocity field was discretized with piecewise bilinear functions and that the velocity field has no jumps over the domain, the edges of the circle could not have any severe jumps or drops. There are some fluctuations in the result that do not appear in the synthetic model. They reflect the error in the result. To see these fluctuations more clearly and to have a closer view of the result, the velocity field function is plotted against the vertical cuts passing through the center of each of the circles in Figure 8.7.

It is crucial to know how erroneous the result is in order to interpret the result correctly. The magnitudes of the fluctuations, which do not exist in the synthetic model, are very small compared to 370 m/s, which is the difference of the velocity value of the circles (1630 m/s) and the rest of the domain (2000 m/s). Thus, any fluctuation that is not far enough from 2000 m/s may be

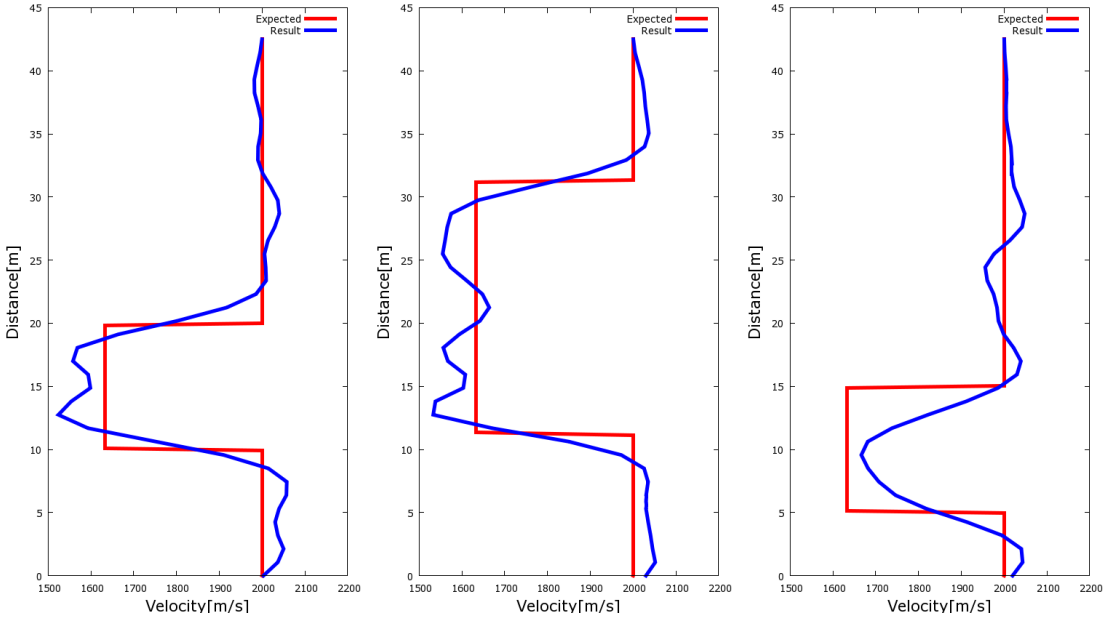

(a) Circle 1 (b) Circle 2 (c) Circle 3

Figure 8.7: #1, velocity distribution over the vertical cuts

Through the centers of the circles

a numerical error.

Investigation of the discretization of the velocity field

To investigate the influence of the higher-order basis on the result, the velocity field is discretized with basis degree 3 and 6, respectively. The relative errors are slightly larger than the error of simulation $\#1$, which uses bilinear polynomials to discretize the velocity field. When we look at the resultant velocity fields in Figures 8.3c and 8.3d, we observe stronger fluctuations compared to the result of $\#1$. The search space of higher-order basis is larger, and thus the inverse simulation may need more iterations to converge. The basis with degree 1 flattens out the spurious fluctuations in the velocity field that occur when the higher-order basis is utilized.

In the discrete approach, the velocity field can also be discretized with a piecewise constant function, as shown in equation (6.8). Since the synthetic velocity field has rapid changes in the interfaces with the circles, it is interesting to check whether this discretization better fits the result. The result illustrated in Figure 8.3b is obtained by using the same conditions as in Section 8.1.1. In general, the result successfully shows the locations and values of the circle. The spurious fluctuations overlap with those in its counterparts to a large extent. However its relative error is quite large when we compare it to other results.

The piecewise linear combination velocity field in Figure 8.3a turns out to be closer to the expected model than the piecewise constant function in terms of the resolution of the result and the precision of the geometry of the bodies with different velocity values. Furthermore, there are more artificial fluctuations in the piecewise constant velocity field. The piecewise bilinear function provides a smoother result owing to the fact that there cannot be rapid jumps and drops in this function.

Frequency set comparison

The frequency set G_R in equation (8.1) is chosen and the obtained result is compared to its counterpart with frequency set G_F. The result of the inversion of the model over the first frequency set G_R is shown in Figure 8.3e.

The relative error is slightly larger than the result obtained using the other frequency set. It is obvious that the G_F result is closer to the synthetic model in Figure 8.1 in terms of detecting the geometries of the circles. Furthermore, the result with G_F has less artificial fluctuations. As we go up to higher frequencies, the information about the minimum points of the lower frequencies is partially lost. For frequency set G_R, this loss is more than the loss for the frequency set G_F. In frequency set G_R, in every next step, only one higher frequency is considered. However, in frequency set G_F, higher angular frequencies are mixed up with lower ones. As we go up to higher numbers, in every step, the model is inverted over not only one, but few angular frequencies. By minimizing the misfit functional over lower frequencies at the same time with higher frequencies, we guarantee that we do not lose the information of the lower frequencies as we go to higher frequencies. Inversion over a few frequencies is more reliable than inversion only over one single frequency at a step.

Sender and receiver points on the front tunnel face

Configuration A in Figure 8.2a is enough to surpass ill-posedness in the inverse problem and to obtain reasonable results which can predict the geological changes. However, in the industrial application presented in [Kneib et al., 2000], the source and receiver points are placed on the front tunnel face only. This makes the inverse problem more challenging. In this section, to mimic the industrial application, the source and receiver points are located as in Figure 8.2b. The velocity field is sought in the set of piecewise bilinear functions, and the model is inverted over the frequency set G_F in (8.2) with a discrete approach. In this configuration, the sources and receivers are very close to each other. Since there are singularities in the pressure fields at the sender points, the vicinity of the source points must be refined in order to obtain precise values at the receiver points, which are very close to the sources in the configuration in Figure 8.2b. The result is shown in Figure 8.3f.

The result can be considered to be successful since it could roughly detect all three bodies with velocities close enough to the expected values. However, there are significant fluctuations that make the result deviate from the synthetic model. Furthermore, the geometries of two of the circles, 2 and 3, are not detected very precisely. For excavation purposes, this configuration could provide enough information about the mechanical properties of the domain in front of the tunnel boring machine if the result is interpreted correctly by taking its error into account. Two of the circles, circle 1 and 2, lay in the line of the tunnel. Circle 1 is very well detected. The velocity value and the location of the circle 2 are detected.

Configuration A in Figure 8.2a has source and receiver points spread over the domain. The receivers can catch the reflections from the boundaries of the circles much better. That is why the result obtained with this configuration can show the boundaries of the circles much better. However, for configuration B, this is not the case. The reflections from the edges of the circles in every direction cannot be caught well at the receivers, which are all on the front tunnel face. This becomes more correct as the circles lie further from the front tunnel face. This may be the

reason why the geometry of circle 3 is badly detected. Its top and bottom edges are not detected at all which may be due to the lack of information about the reflections from these edges.

Comparison of continuous and discrete approaches

If analytical green functions are given, the continuous approach can calculate the analytical gradient of the misfit function. However, the discrete approach uses the information to decide how the velocity field is discretized, and the gradient calculated by the discrete approach is expected to be less accurate than its counterpart. This is why the aim is to investigate whether the continuous approach is superior to its counterpart.

The tunnel model with configuration A is inverted over the frequency set G_F by using the continuous approach. According to equation (6.24), the velocity field in case of the continuous approach depends directly on the finite element basis; the velocity field is a piecewise linear combination whose basis degree is twice the degree of the finite element basis. If the degree of the finite element basis is 3, then the degree of the velocity field basis is 6. We run 3 simulations with FE basis degrees 1, 2, and 3. The mesh becomes finer as the FE basis degree becomes smaller.

To see whether the basis degree has an effect on the final result, the mesh is refined and the simulation is carried out with the continuous approach with $p = 1$, $p = 2$, and $p = 3$. The obtained results are illustrated in Figures 8.4c, 8.4d, and 8.4e: they look almost identical. The continuous approach successfully detects the circular disturbances inside the tunnel domain both geometrically and quantitatively up to some good precision. The relative errors are larger than their discrete counterparts. The error increases with increasing FE degree. This may be because the search space greatly increases as the FE degree increases.

A comparison of the continuous and discrete approaches shows that both of the approaches are successful with respect to detection of the geometry, the location, and the velocity values of the three circles. In both approaches, there are some fluctuations in the velocity field that do not exist in the synthetic model. However, it can clearly be seen that the result obtained with the continuous approach has fluctuations with larger amplitudes. It is because, in this case, it is not correct to compare these approaches because they are not solving the same mathematical problem. The continuous approach searches for the function $d = \frac{1}{c^2}$, whereas the discrete approach searches directly for c. The derivative of the misfit function χ with respect to d is

$$\frac{\partial \chi}{\partial d} = \frac{\partial \chi}{\partial c}\frac{\partial c}{\partial d} = \frac{-c^3}{2}\frac{\partial \chi}{\partial c}. \tag{8.4}$$

The factor c^3 may intensify the artificial fluctuations in the continuous result. To make the two approaches comparable, we search for $d = \frac{1}{c^2}$ with the discrete approach too. The velocity field is discretized with the basis degrees 1 and 6. The results are shown in Figures 8.4a and 8.4b.

Now that the two approaches solve exactly the same mathematical problem, it can be clearly seen that the results of both approaches look very similar. The differences are due to the different function sets used to discretize the velocity field. To have a closer look at both approaches, the convergences of the conjugate gradient method with both approaches are shown in Figures 8.8 and 8.9. The graphs illustrate how the misfit function and norm of the gradient go to zero

in each frequency group. All of them are quite close. In the continuous approach, $d = \frac{1}{c^2}$ is discretized with basis degree 6 since FE basis degree is 3. As already mentioned, as the degree of the basis of the velocity field increases, the discrete gradient converges to the continuous gradient. Convergences of the continuous approach and the discrete approach with basis 6 are usually slightly better than the discrete approach with basis degree 1. This may be because the gradient is more precisely calculated when the velocity field is discretized in a larger space. In general, none of them is dominant over the others, and a large difference is not observed in the convergence graphs and obtained velocity fields.

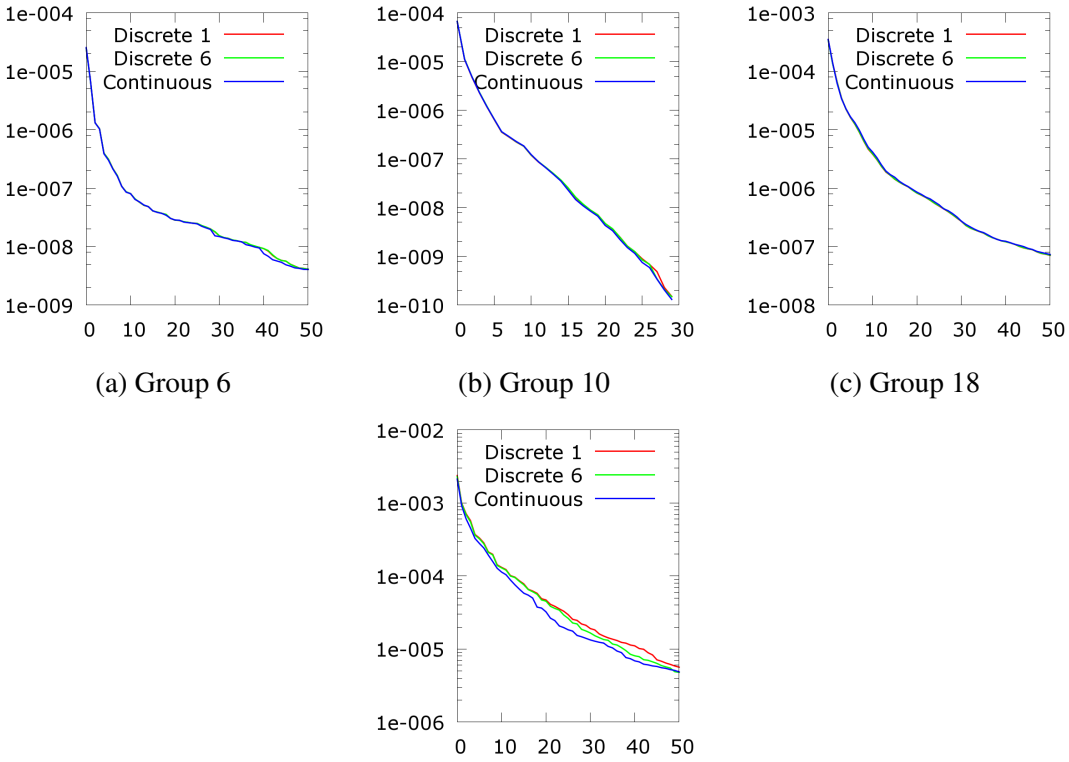

(a) Group 6

(b) Group 10

(c) Group 18

(d) Group 22

Figure 8.8: Comparison among experiments #7,#8, and #11, misfit function vs iteration

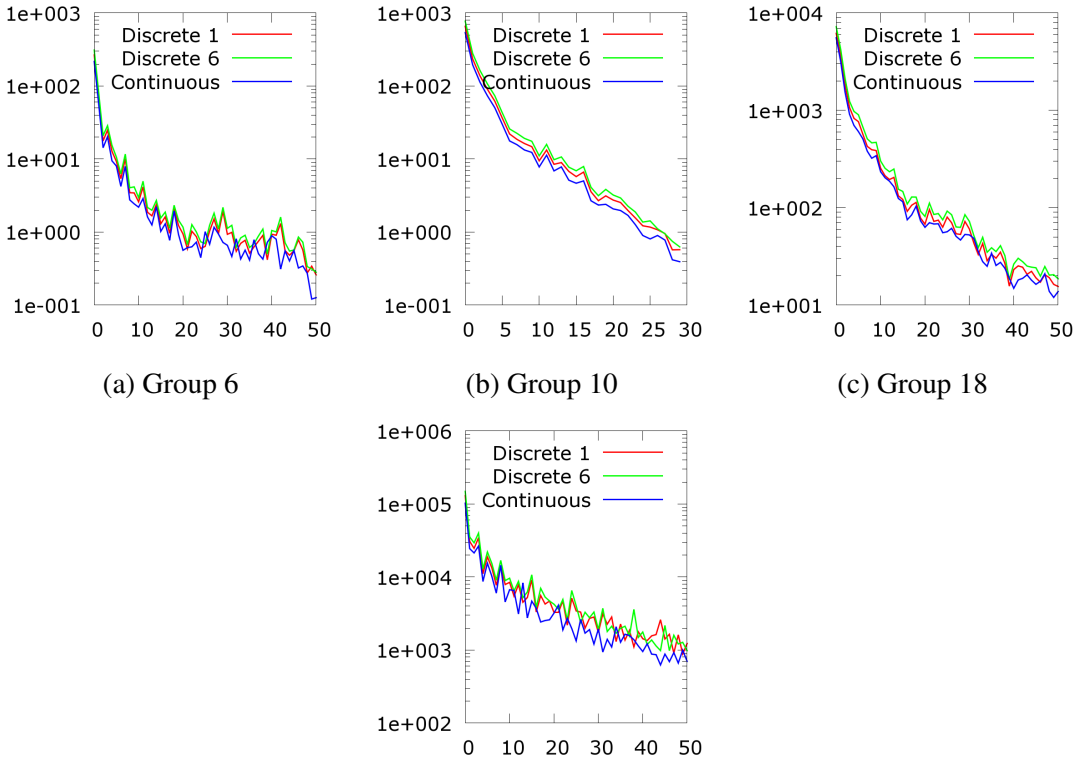

(a) Group 6

(b) Group 10

(c) Group 18

(d) Group 22

Figure 8.9: Comparison among experiments #7,#8, and #11, norm of gradient vs iteration

8.1.2 Scenario 2

Being able to detect geological bodies with different mechanical properties, a question arises whether we can detect geological layers along with bodies using FWI. The question is inspired by the Wehrhanlinie subway project in Düsseldorf in which there are different layers and a triangular shaped body. This question was answered by a civil engineering M.Sc program student Seyfettin Oezalp [Oezalp, 2015]. The synthetic model has a triangular geological body and two different layers (Figure 8.10). His research can be divided into parts: search for an optimal source/receiver points set up, affect of higher frequencies on inversion, relation between sought body size and highest frequency, and comparison of steepest descent and conjugate gradient method. In all cases, the starting model is a homogeneous velocity field of value 2000 $\frac{m}{s}$.

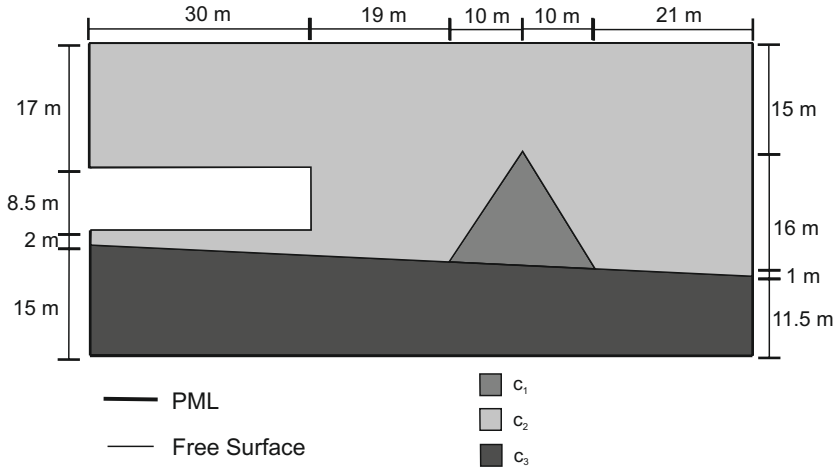

Figure 8.10: Scenario 2, synthetic velocity field

$c_1 = 1500\,\text{m/s}, c_2 = 2000\,\text{m/s}, c_3 = 2400\,\text{m/s}$

Optimizing source/receiver setup

First, different configurations are investigated to see what kind of advantages each individual setting has over others. The setting in Figure 8.11a has only one source point and keeps the computation cost minimum because source points directly influence the computation time. Despite the fact that the number of source points is only 5, they are placed roughly all around the obstacle. Applying FWI, the triangular object and the layer below it are detected (Figure 8.11b), but with low resolution. It is possible to scan geological structure ahead of tunnel with only one source point, but with lower resolution. The idea is to increase source points (Figure 8.11c) and obtain a better picture (Figure 8.11d). In this case, the triangular object and the inclined layer beneath it ahead of tunnel are very well detected. However, the layer beneath the tunnel is not detected. One more source and receiver points are added to the last configuration and the new setup is in Figure 8.11e with which the inversion ends up with the picture in Figure 8.11f. This result detects the layer well along with the triangular object. There are peaks around the source and receiver points beneath the tunnel which is theoretically expected due to the formulation of the gradient of the misfit functional. To reduce the number of source points we replace the source point beneath the tunnel by a receiver (Figure 8.11g) and the result in Figure 8.11h is a successful scan of the domain. Finally, again to mimic an industrial application as in the previous section, we place all points on the tunnel wall (Figure 8.11i). The resultant picture (Figure 8.11j) has roughly the triangular object in it and it can detect some part of the layer in the bottom of the domain. Although the picture is not very clean, in the excavation process it can give enough information about where the object is and what kind of geological structure it is.

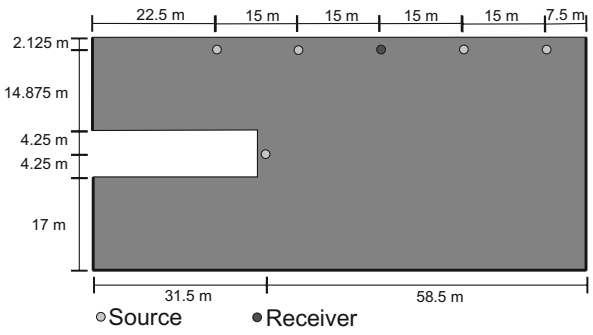

(a) #1 Configuration

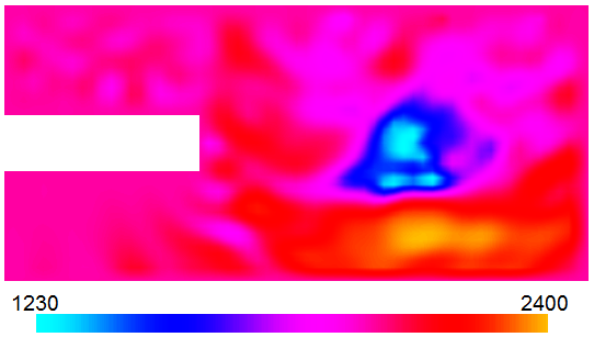

(b) #1 Result

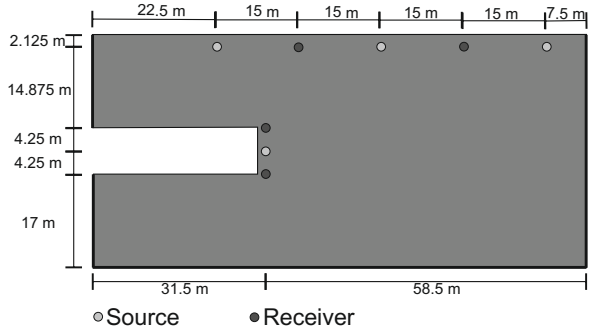

(c) #2 Configuration

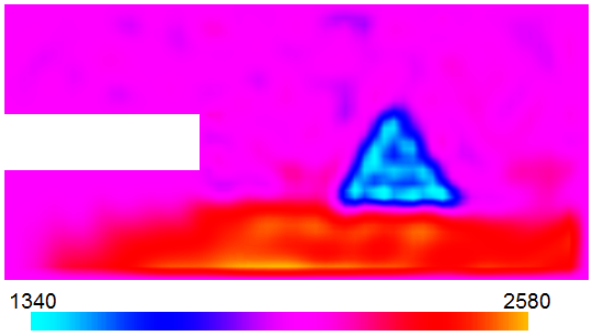

(d) #2 Result

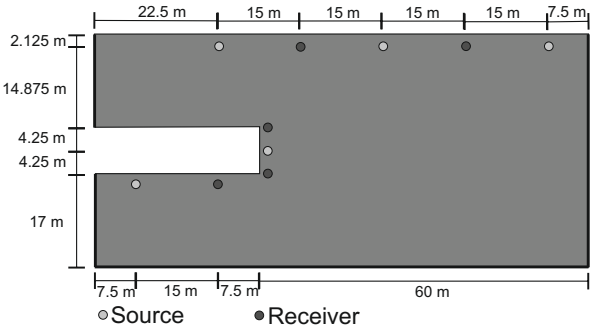

(e) #3 Configuration

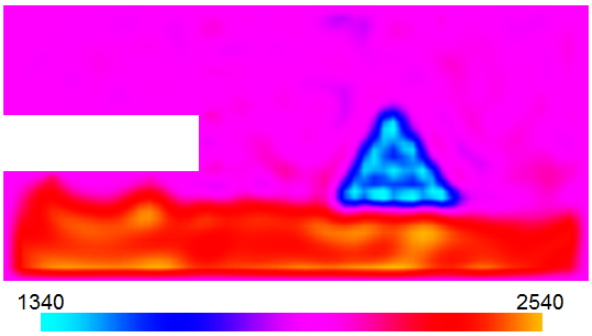

(f) #3 Result

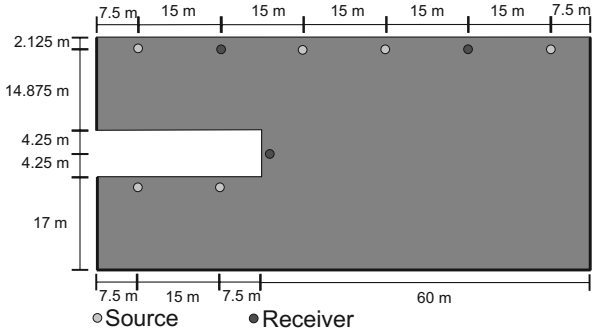

(g) #4 Configuration

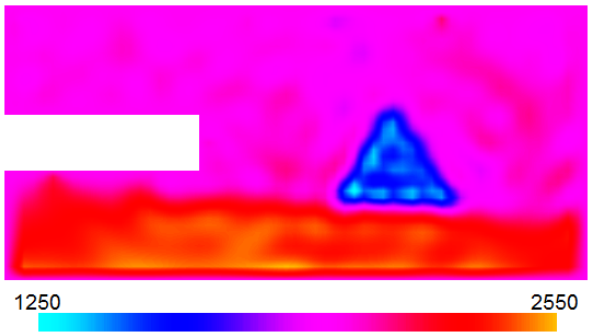

(h) #4 Result

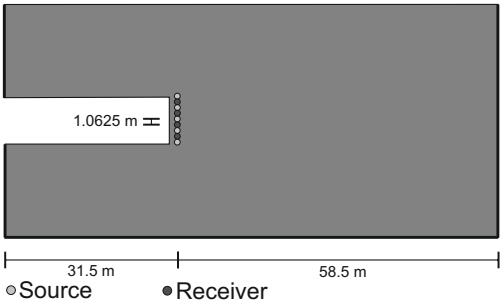

(i) #5 Configuration

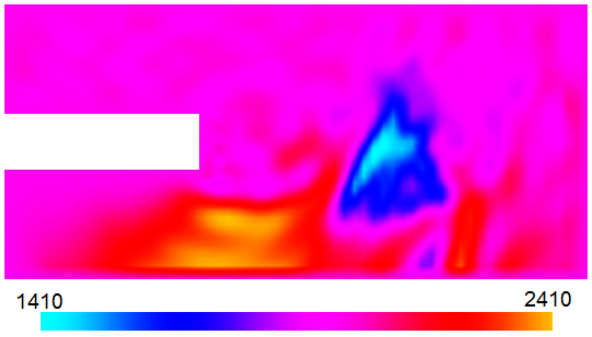

(j) #5 Result

Figure 8.11: Reconstructed velocity fields

Adding higher frequencies

In this part, we use the configuration in Figure 8.11e because it provides one of the best results amongst all configurations. The velocity field in Figure 8.11f is taken as the initial model to carry out inversion over higher frequencies. First, the model is inverted over the frequency set

$$f_2 = \{(1250), (1250, 1300), (1350), (1350, 1400), \\ (1450), (1450, 1500), (1550), (1550, 1600)\}. \quad (8.5)$$

Using its result (8.12a) as a starting model for the inversion over the frequency set

$$f_3 = \big\{(1650), (1650, 1700), (1750, 1800)\big\} \quad (8.6)$$

we obtain the result in Figure 8.12b.

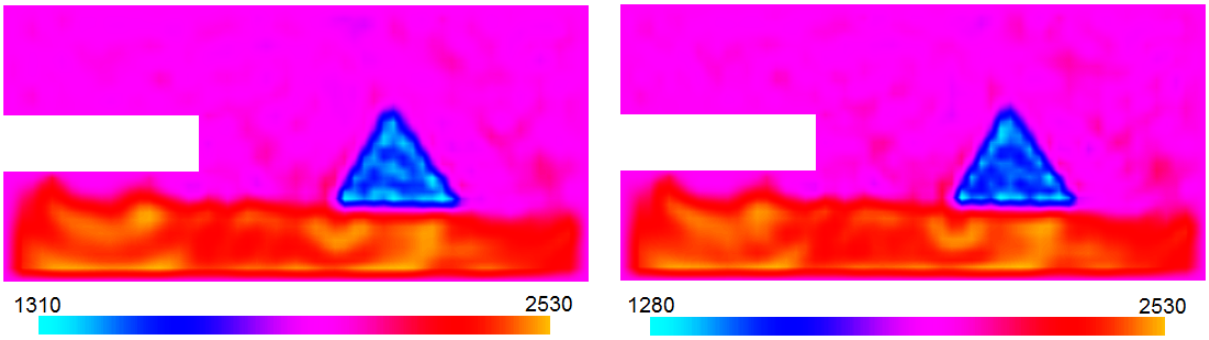

(a) Result using f_2 (b) Result using f_3

Figure 8.12: Resultant velocity fields using higher frequencies

The results by frequency sets with maximum frequencies 1200, 1600, and 1800 are all successful inversion results. It is difficult to see significant differences among them. However, it is clear that the corners and the edges of the triangle look sharper with higher frequencies. To see the difference more obviously, the resultant velocity fields are plotted over a vertical line passing through the triangle (Figure 8.13). The largest differences can be seen in the middle part of the plot which corresponds to the triangle. It is obvious that the plots of lower frequencies fluctuate with higher amplitudes; result of 1800 fluctuates the least and is closer to the expected line.

Steepest descent versus conjugate gradient

Search direction of steepest descent is the negative gradient direction. Conjugate gradient search direction is also related to the gradient. However, its constructed in such a way that search direction is orthogonal to search directions in previous iterations. It means that CG does search in a direction only ones and search directions in upcoming iterations have no components in previous search directions. This property makes the inversion faster with a new direction in each iteration which is orthagonal to the old search directions. In contrast to CG, SD search direction may have components in the search directions of previous and upcoming iterations. This may slow down the algorithm. To investigate how effective both methods are on FWI

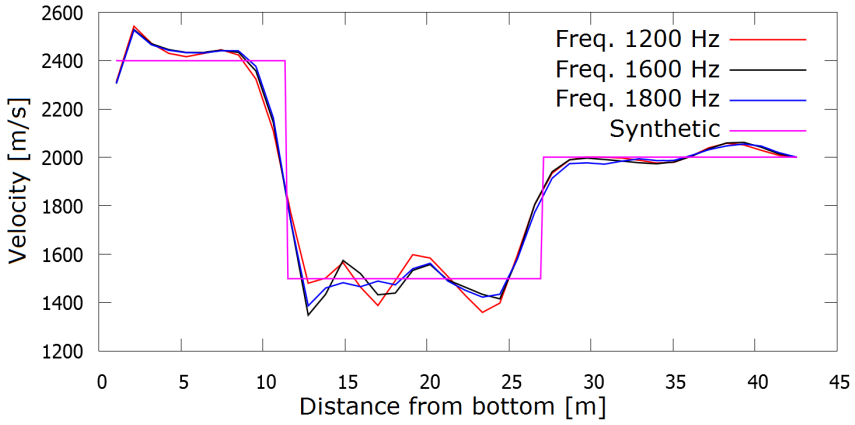

Figure 8.13: Velocity distribution over vertical line passing through the triangle

tunnel problems, we use the configuration in Figure 8.11e with maximum frequency of 1200. As an indicator of speed of convergence, we use misfit functional and norm of the gradient of the misfit functional which are supposed to approach zero. Figure 8.14 shows decline of misfit functional as iterations run with both SD and CG, whereas Figure 8.15 shows decline of the norm of the gradient. In both cases, it is obvious that CG has a significant advantage over SD.

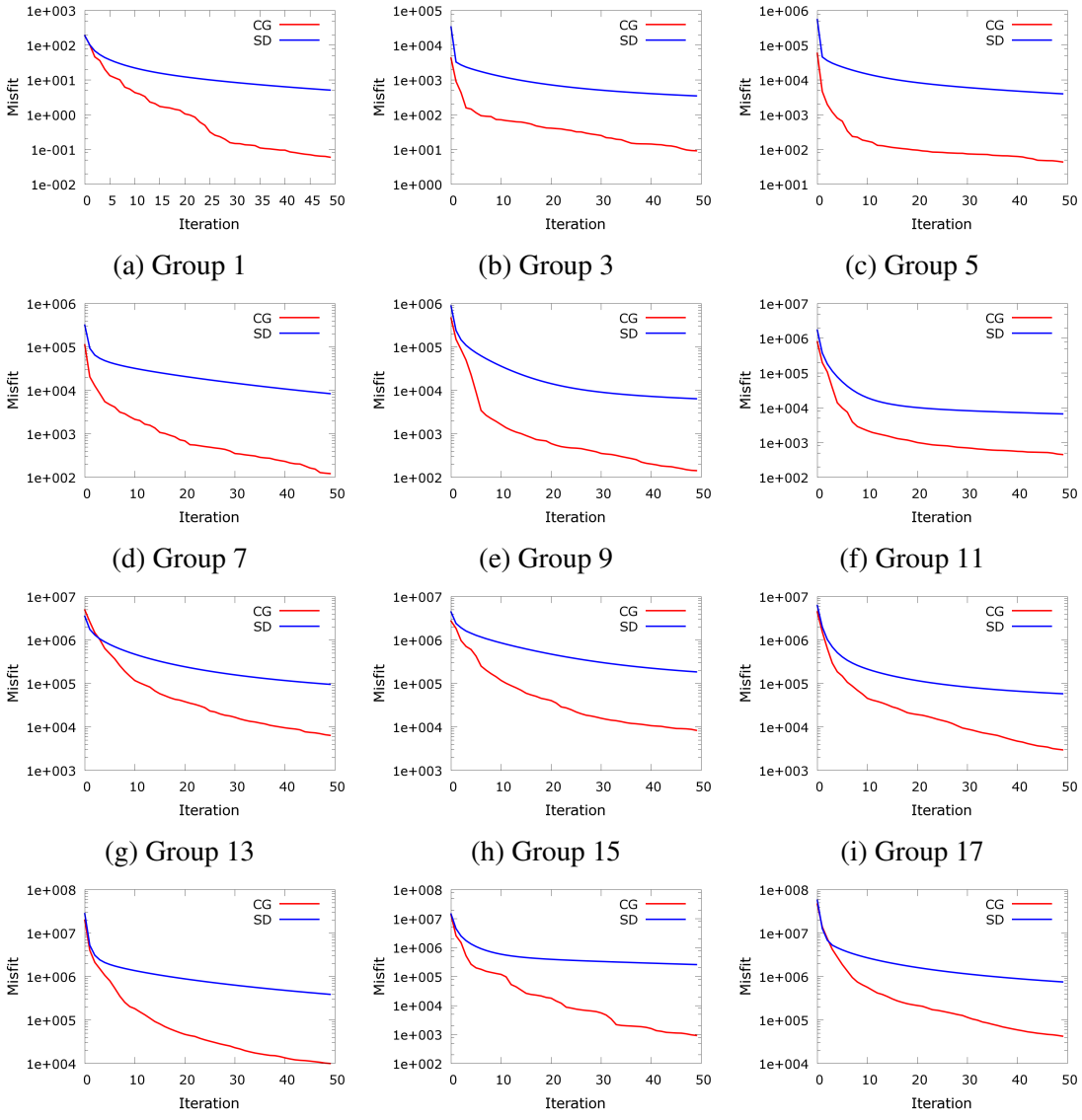

(a) Group 1 (b) Group 3 (c) Group 5

(d) Group 7 (e) Group 9 (f) Group 11

(g) Group 13 (h) Group 15 (i) Group 17

(j) Group 19 (k) Group 21 (l) Group 22

Figure 8.14: CG vs SD, misfit function vs iteration

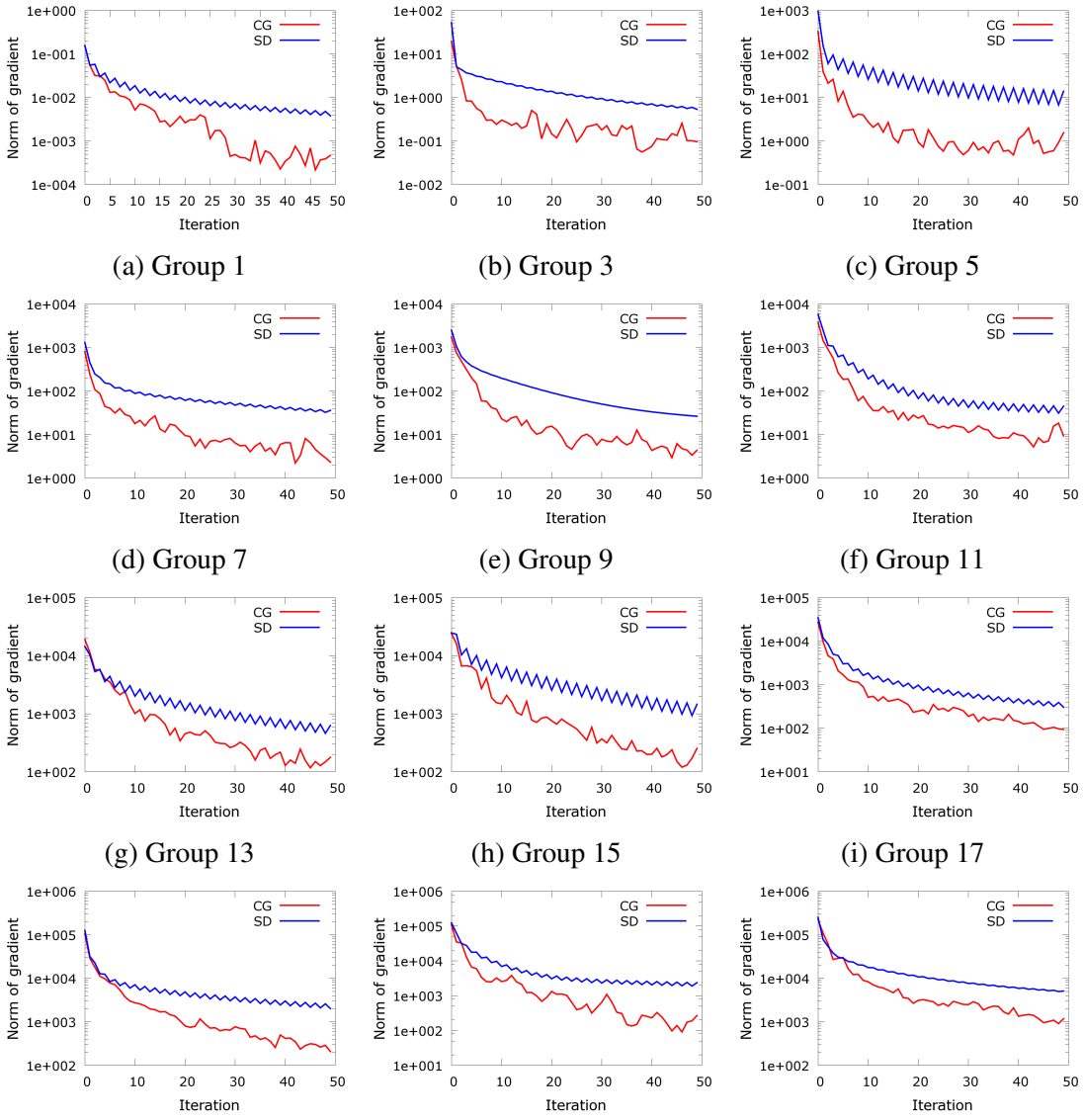

(a) Group 1 (b) Group 3 (c) Group 5

(d) Group 7 (e) Group 9 (f) Group 11

(g) Group 13 (h) Group 15 (i) Group 17

(j) Group 19 (k) Group 21 (l) Group 22

Figure 8.15: CG vs SD, norm of gradient vs iteration

Object size versus frequency

In this part, we try to show the relation between the size of the object to be detected and maximum frequency. We use a simple setup of points which basically surround the object (Figure 8.16). It is important to note than with a different setting the answers would be different. Another important issue is that the frequency may be not only dependent on the size of the object for a given source/receiver setup, but it may also be dependent on the velocity value of the object. However, in this investigation we use only one single velocity value and do not consider the affect of the velocity value of the object on the frequency size. To carry out the test, we use different sized objects with the same source/receiver setup. We need to define a criterion for the detection of the object because the answer becomes sharper and more precise with higher frequencies and it has to be stopped at some frequency which is accepted as minimum value for the maximum frequency. We use rule of thumb and decide on the frequency by looking at the resultant pictures (Figure 8.17): we say the frequency is the one which we need if its result more or less fulfill the borders of the object and the velocity value of it. Although this investigation is not very precise, the results let us say that as the size of the object get smaller, the frequency required to get a rough picture of the velocity field grows. This can be seen in Table 8.2. The object with radius 1 m could not be detected with the given source and receiver configuration. It is likely that we need more receiver points to catch the reflections from the borders of the object. It may become problematic to catch reflections from a small surface by very few receivers placed far from the object.

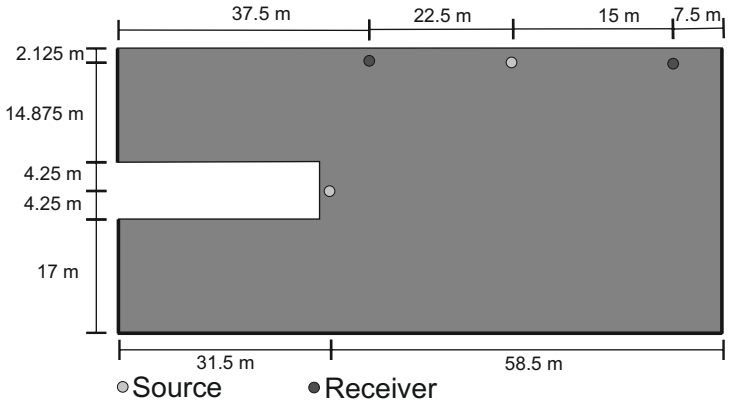

Figure 8.16: Source/receiver setup

Radius r [m]	**Frequency ω in [rad/s]**
13	100
10	200
7	300
4	400
1	not detected

Table 8.2: Radius r und and minimum required frequency ω to detect the object

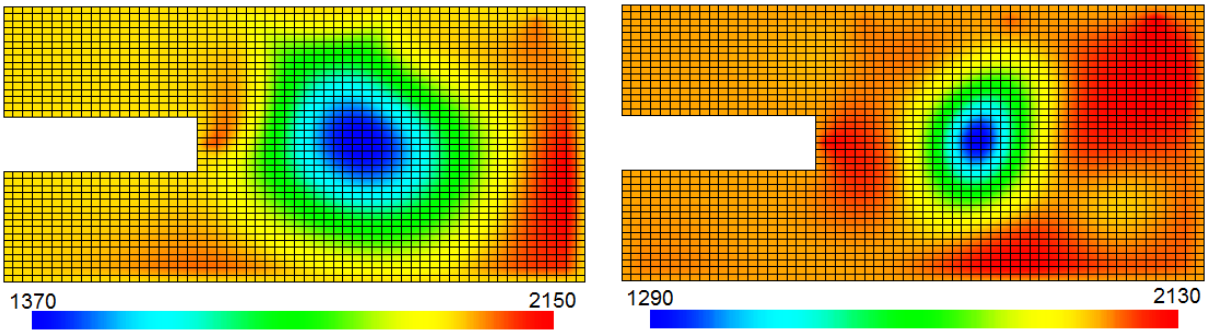

(a) $r = 13$ m, $\omega = 100$ Hz

(b) $r = 7$ m, $\omega = 200$ Hz

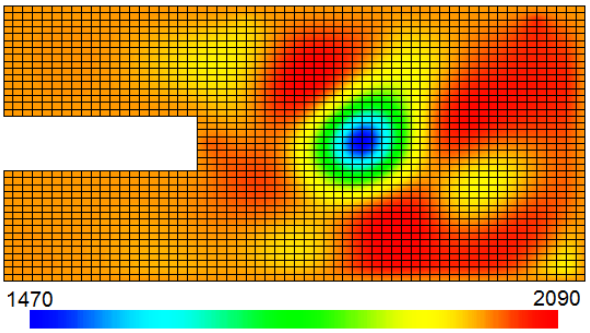

(c) $r = 4$ m, $\omega = 400$ Hz

Figure 8.17: Reconstructed velocity fields

8.2 Blind test on the 2D acoustic tunnel model

In the previous tests, we use synthetic model which imitate real models. They are defined exactly in the same way as the computer model. This causes same kind of errors in both synthetic and computer models. In the inversion process, the errors can be neutralized when the misfit functional is calculated based on the difference between the computer and synthetic data; this can happen because both models have the same sort of numerical errors and they can neutralize each other when the difference between the two models is calculated. To avoid this, and to have a more realistic scenario, we conduct a blind test in a tunnel environment. There are two parties in this test. The first party, Mr. Andre Lamert who is a coworker at the institute of geophysics in Ruhr-Universitaet Bochum, is responsible to make a precise synthetic model in the time domain in Specfem software and to read seismograms at the geophones located at certain locations, whereas we are the second party who is responsible of full waveform inversion and to try to predict the synthetic model without having completely no information about it except for the provided seismograms. The time domain model is defined on a very big domain to avoid any possible spurious reflections from the absorbing layers and the simulation is stopped before they reach the domain of interest. Apart from this, this model is solved with very fine mesh and higher order spectral element method to have precise seismograms. The frequency domain model is modelled in the Java-based program and it is solved by a different method which is a higher-order finite method based on hierarchical shape functions. This lets us to have different numerical errors in the models, which are not expected to neutralize each other when the misfit functional is calculated. It is very interesting to see whether the inversion process works when we have a synthetic model which is very precisely solved with a different numerical method. Furthermore, it is a provocative question whether the inversion scheme works in a blind test. The test is carried out absolutely blindly under 5 different scenarios each of which has a different

synthetic model.

8.2.1 Scenario 1

In Figure 8.18, we introduce the source/receiver configuration used in the first scenario. We try to choose them at accessible points such as the surface and the tunnel walls.

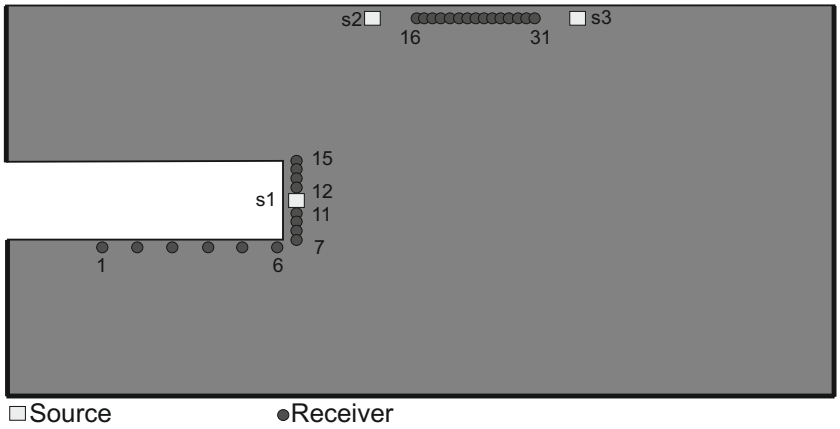

Figure 8.18: Blind test, source/receiver configuration (scenario 1)

The seismograms provided by the first party are illustrated in Figures 8.19,8.20, and 8.21 when sources are fired with Ricker wavelet with the peak frequency 500 Hz and the delay 0 s at points $s1$, $s2$, and $s3$, respectively.

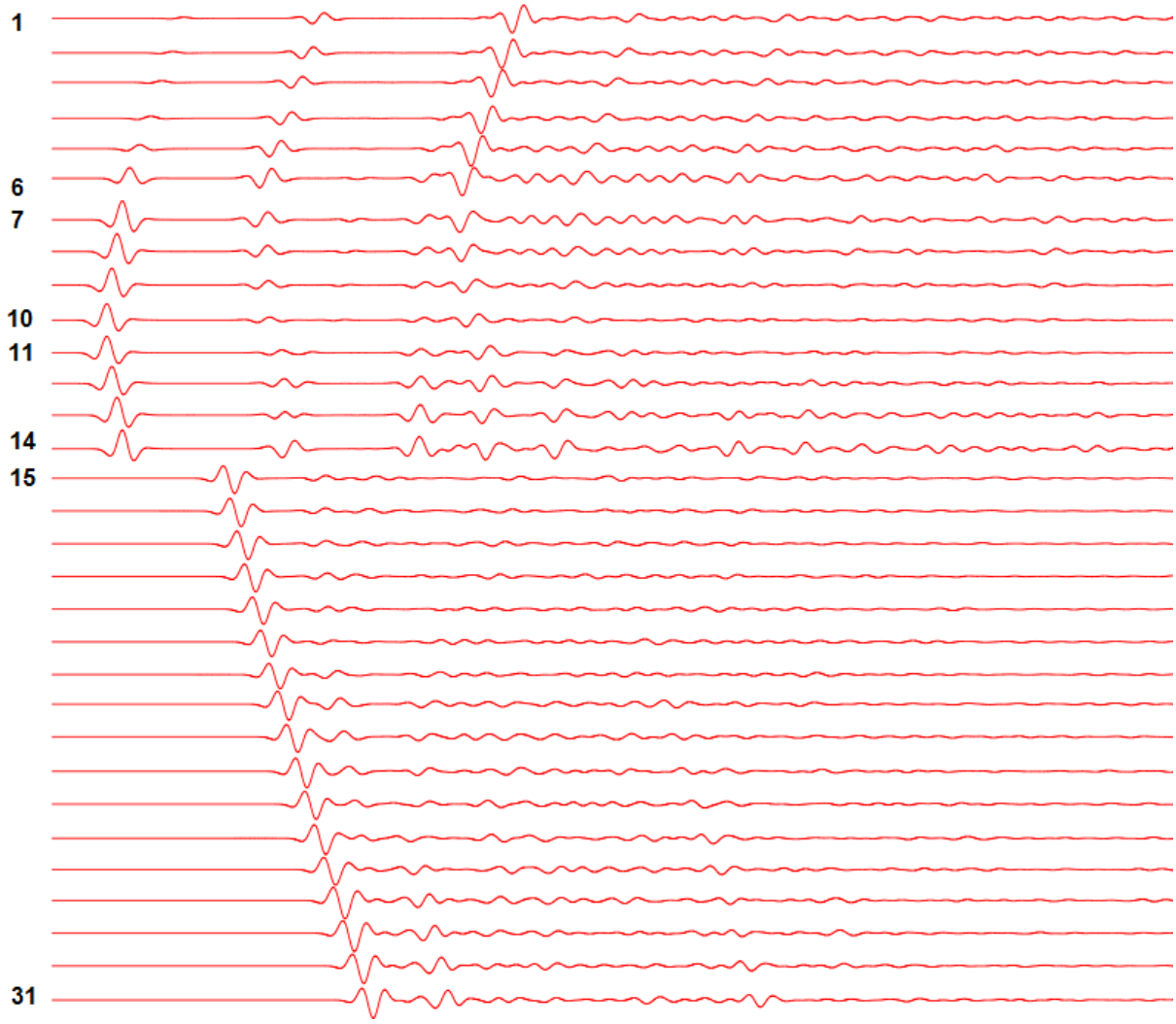

Figure 8.19: Wavefields at the receivers, source $s1$ (scenario 1)

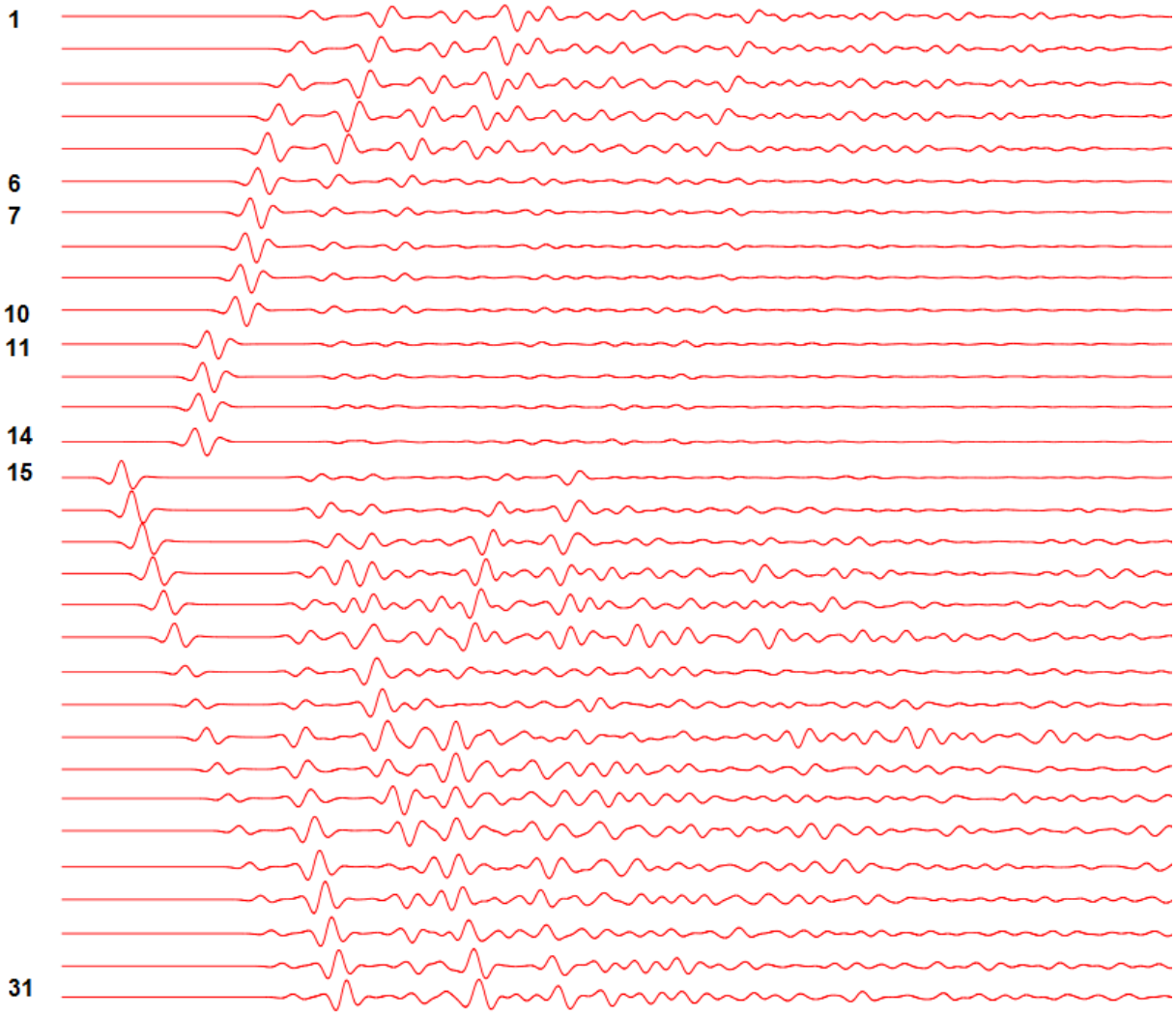

Figure 8.20: Wavefields at the receivers, source $s2$ (scenario 1)

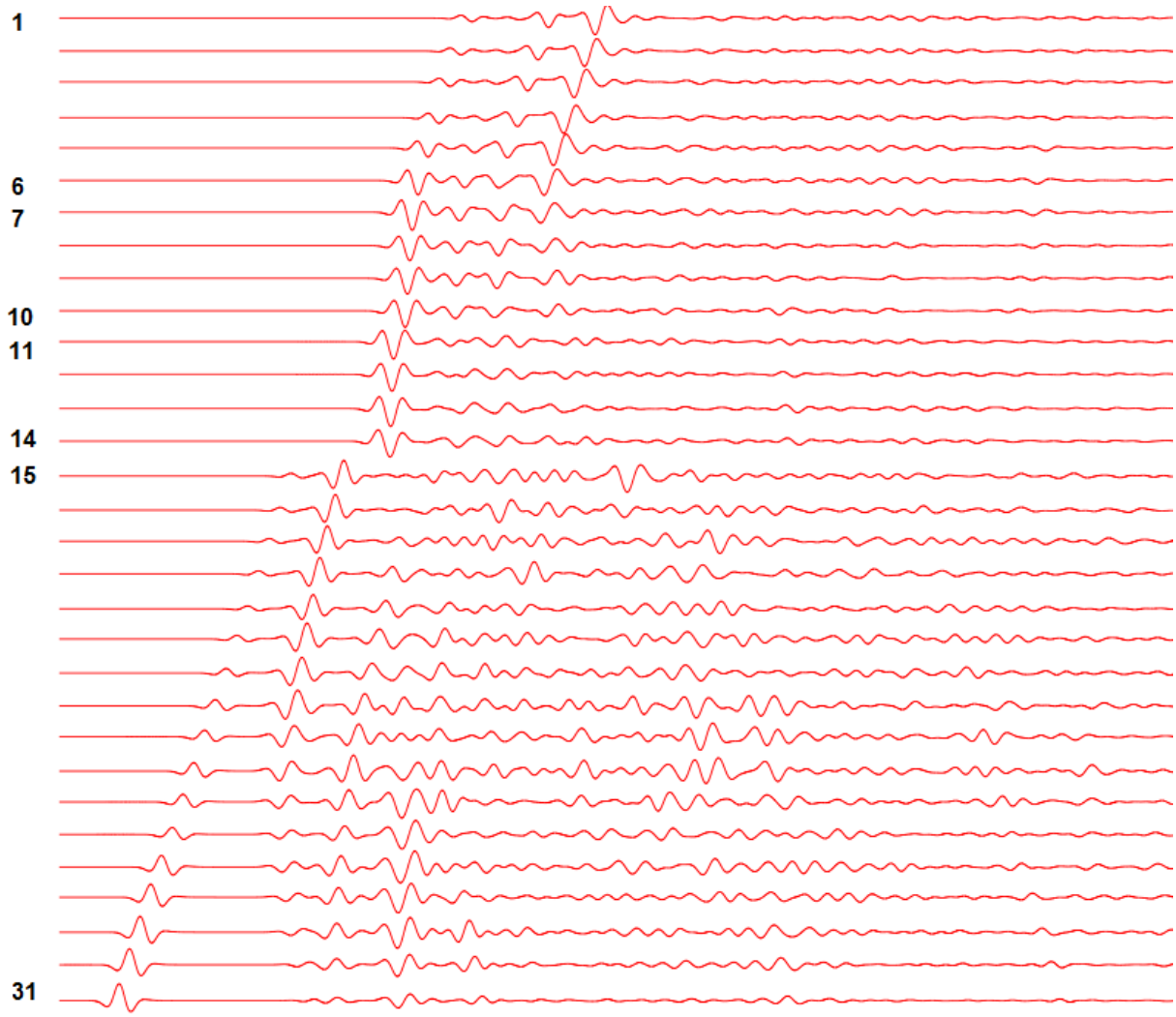

Figure 8.21: Wavefields at the receivers, source $s3$ (scenario 1)

Our starting model is a homogeneous velocity field of value 3000 m/s. From the theoretical point of view, the starting model has to be close enough to the minimum point because we are using the conjugate-gradient method, which is a gradient-based method, to minimize the misfit functional. In FWI problems, the misfit functional is defined by the difference between the field seismograms and computer model seismograms. For the source point $s1$, one can see the difference between the starting computer seismograms and the field seismograms by comparing Figures 8.19 and 7.9. We choose discrete angular frequencies between 400 Hz and 5000 Hz with 50 Hz increment. We do inversion over each single frequency from the low angular frequencies to the high angular frequencies. At the multiple of 500 Hz, we invert the model over few frequencies distributed evenly between 400 Hz and the current frequency. Doing so, we aim to remind the inversion about the smaller frequencies because some of the information about the lower frequency inversions can be lost as we proceed to the higher frequencies. In Figure 8.22, we present the results after some frequencies.

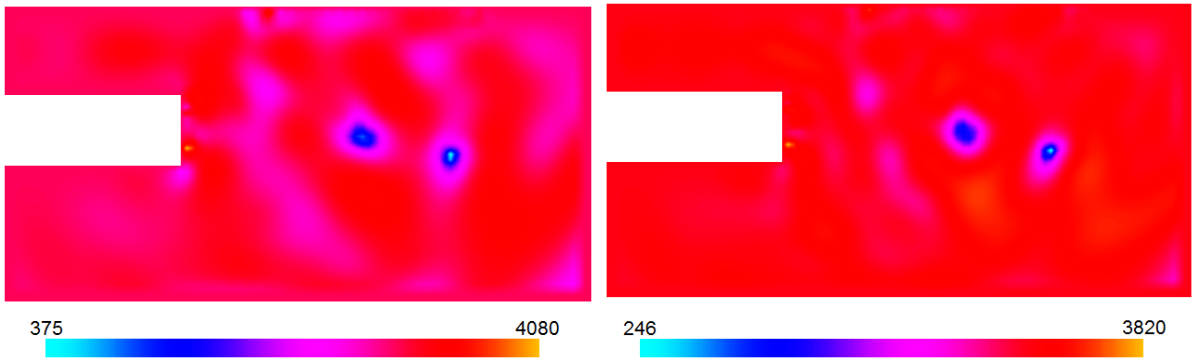

(a) Angular frequency 750 Hz

(b) Angular frequency 1000 Hz

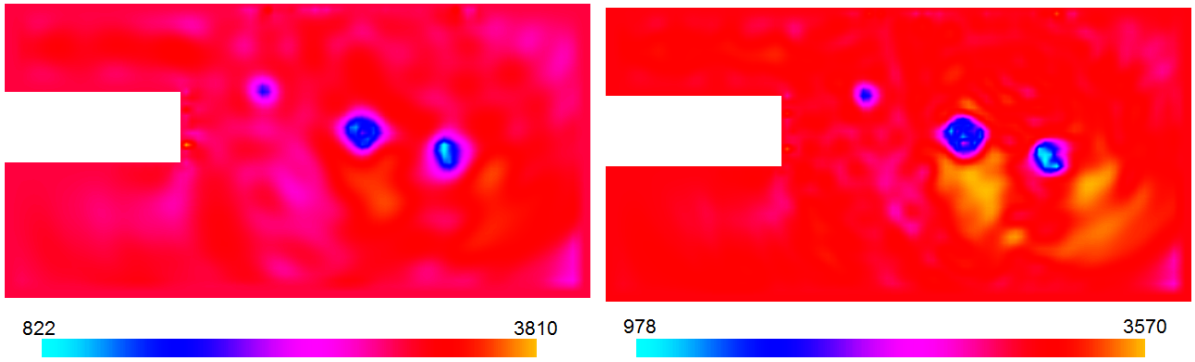

(c) Angular frequency 1500 Hz

(d) Angular frequency 2500 Hz

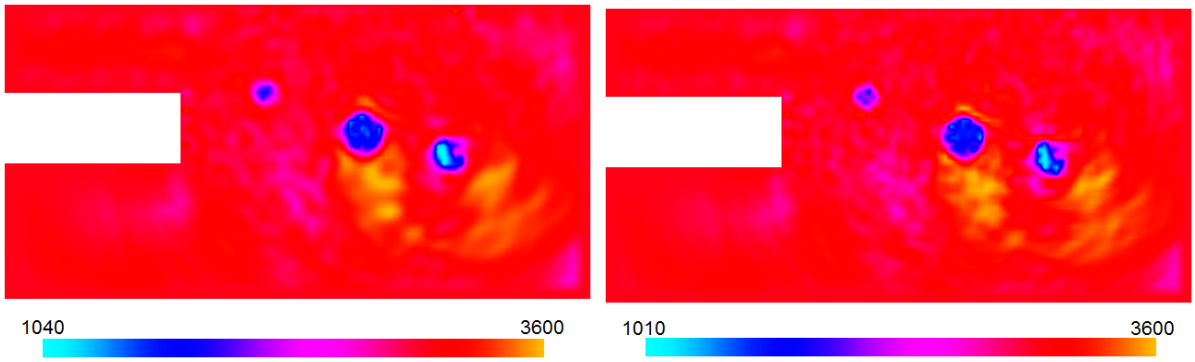

(e) Angular frequency 3000 Hz

(f) Angular frequency 4000 Hz

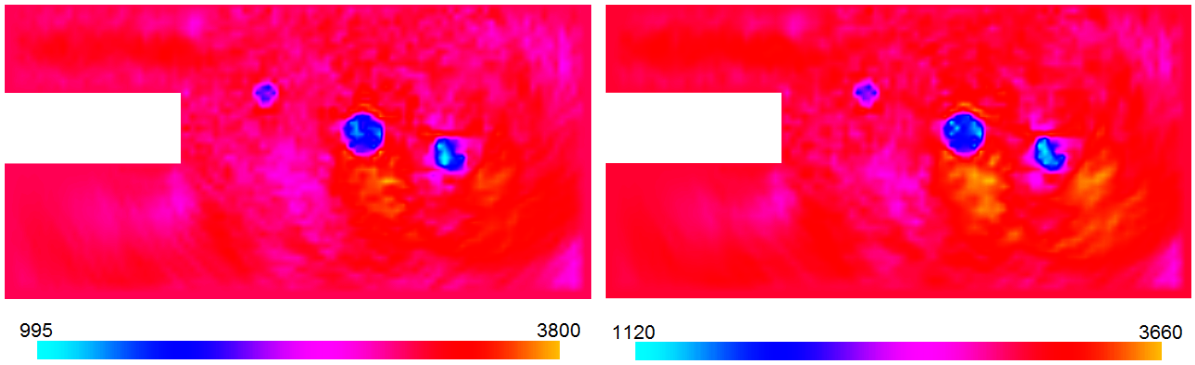

(g) Angular frequency 4500 Hz

(h) Angular frequency 5000 Hz

Figure 8.22: Reconstructed velocity fields after certain frequencies (scenario 1)

We see that even at the angular frequency 750 Hz two objects are emerging ahead of the tunnel. The smallest object appears in the reconstructed velocity field at 1500 Hz. As the inverse model is inverted over higher frequencies, the objects obtain clearer geometrical shapes. We, as a

second party who conducts the inverse simulation in this test, are shown the synthetic velocity field only after we obtain inversion results. At this point, we present the synthetic model which is made by the first party in Figure 8.23.

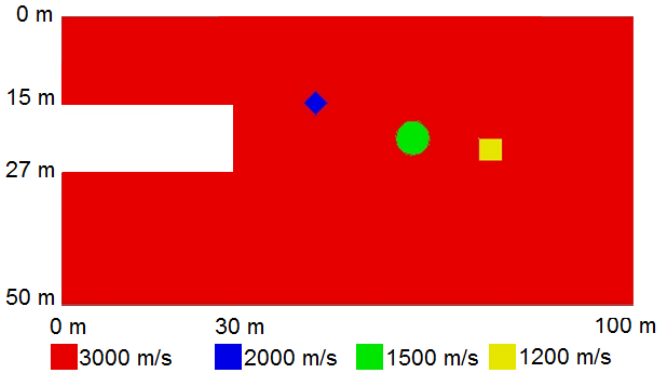

Figure 8.23: Blind test synthetic model (scenario 1)

It is observed that the objects ahead of the tunnel are detected successfully at right locations after the inversion process. The first two objects are more precisely detected in terms of their sizes and geometrical shapes. The first object is rotated by 45° in the synthetic model and only at higher frequencies we see a shape which looks like a small rotated rectangle. However, the third object is not well detected in terms of its size and shape. One reason can be the distance of the source/receiver points from the third object because the incidence angle becomes smaller. Another reason can be that the third object is in the shade of the other two objects. These two reasons do not allow much reflection information to reach the receiver points.

Apart from the locations, sizes, shapes of the objects, it is important to test whether the velocity values in the reconstructed images are confirmed by the synthetic model. In Figure 8.24, it is observed that the velocity values in the objects in the inversion results are very close to the expected values.

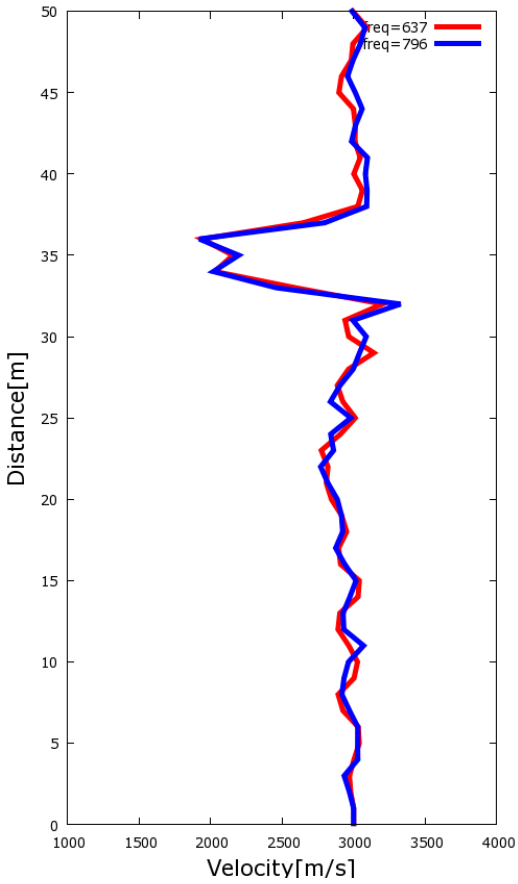

(a) Leftmost object (1), expected 2000 m/s

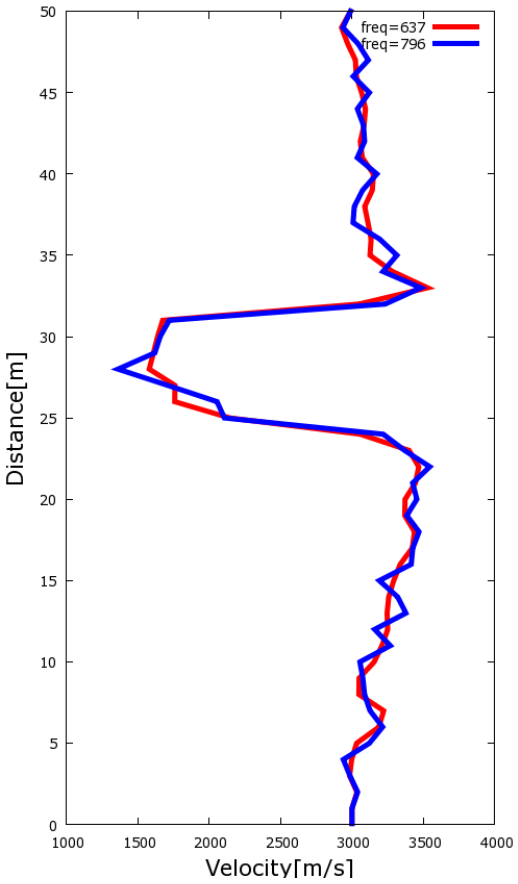

(b) Midmost object (2), expected 1500 m/s

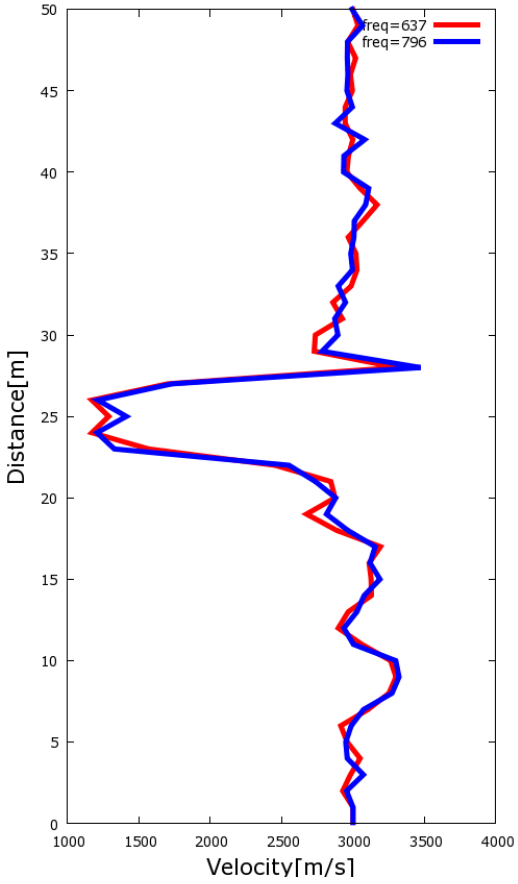

(c) Rightmost object (3), expected 1200 m/s

Figure 8.24: Vertical velocity distributions through the center of the objects (scenario 1)

We observe artificial fluctuation behind the second and third objects. Such pollution in the results is observed in the previous tests too. They appear in the shades of the objects from where the receivers do not obtain enough reflection data. This can force the inversion process to end up in a non-unique local minimum.

8.2.2 Scenario 2

This scenario differs from the first one with the source/receiver configuration and the synthetic model. The number of the source/receiver points is kept almost the same, although their locations were changed such that they cover more space especially at the surface and at the upper tunnel wall as shown in Figure 8.25.

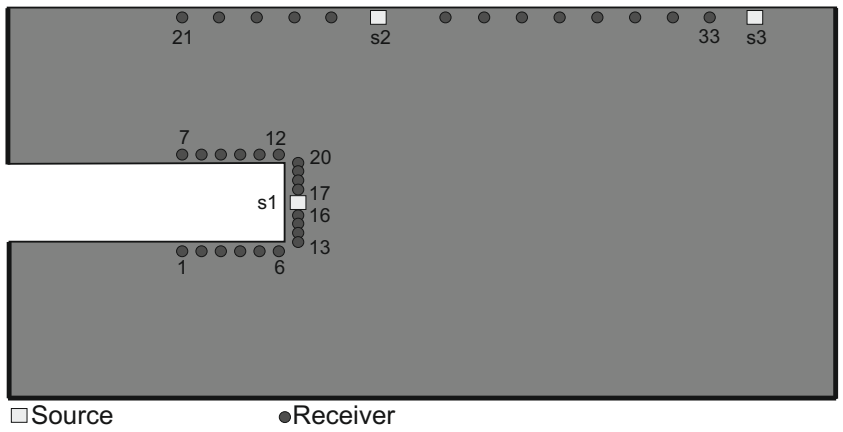

Figure 8.25: Blind test, source/receiver configuration (scenario 2)

The difference between the synthetic models of the first and second scenarios is only the velocity values inside the objects as one can see in Figure 8.26a. Apart from the mentioned differences, everything else is identical in both scenarios in the inversion process. The result of the inversion (Figure 8.26b) is a reasonable prediction of the synthetic model. The new source/receiver configuration is more spread over the surface and it can catch more of the reflecting waves from the objects in a wider range of angles. It leads to an improved result compared to the scenario one with the sharp detection of the geometries of the objects. However, artifacts remain at the shadow of the objects which are far from the tunnel.

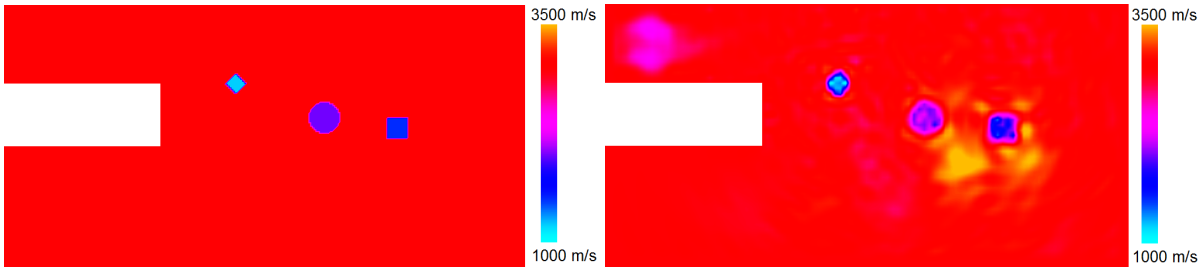

(a) Synthetic model (b) Reconstructed model

Figure 8.26: Scenario 2

8.2.3 Scenario 3

One question to be answered is whether we can detect faults ahead of a tunnel with FWI. Scenarios 3, 4, and 5 are dedicated to this question and we use the source/receiver configuration in Figure 8.25. Except for the synthetic models, everything else is kept identical. In scenario 3, the goal is to predict the synthetic model in Figure 8.27a which has a sudden change in the velocity field in the horizontal direction ahead of the tunnel. Since the reflective layer change is looking upwards where there are receivers, it can be expected that we gather enough information about the reflective layer thanks to the seismograms. The reconstructed model in Figure 8.27b successfully predicts the location of the fault and guesses the velocity value near the fault with some little error. However, some artificial peak values are observed on the left side of the fault. Apart from this, it cannot disclose much about the expected model on the right side of the fault. One possible reason is that seismograms do not carry information about the right side of the fault; the refracted waves are moving to infinity and do not bring back any information about the model on the right side of the fault.

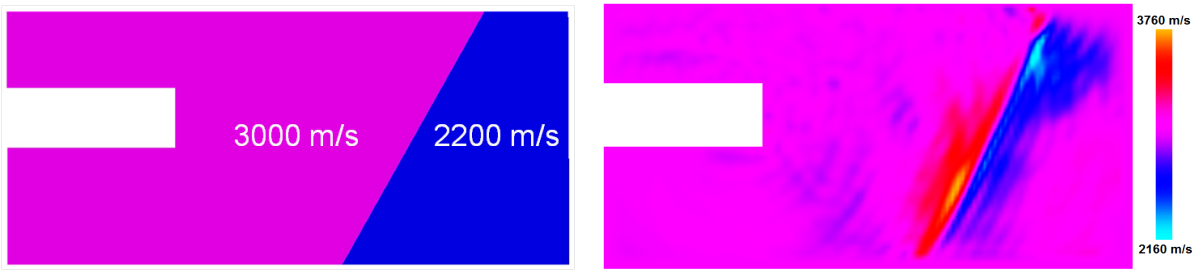

(a) Synthetic model (b) Reconstructed model

Figure 8.27: Scenario 3

8.2.4 Scenario 4

In scenario 3, the fault face is looking upwards and the reflections all along the fault can be well caught. An interesting question arises: What if the fault face looks downwards? The aim of this scenario is to try to answer this question with the synthetic model in Figure 8.28a. The reflections from the fault tend to move in the downward direction. However, there are some points around the tunnel and it is expected that the reflections from the upper part of the fault can still be well caught. The result in Figure 8.28b totally agrees with this expectation. Nevertheless, the reflections from the fault at greater depths are not received well at the receiver points. Thus, the reconstructed model can only tell us about the upper part of the fault.

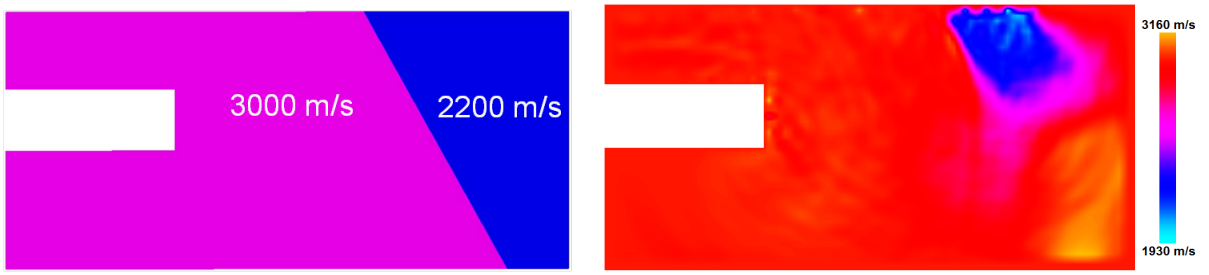

(a) Synthetic model (b) Reconstructed model

Figure 8.28: Scenario 4

8.2.5 Scenario 5

We have investigated the cases where we have a sudden change of the velocity in the horizontal direction. But what happens if the change of the velocity is smooth? To be able to answer this question, we try to predict the synthetic model in Figure 8.29a. The region in the middle is a smooth linear transition zone from 3000 m/s to v=2200 m/s. If enough reflections occur at the smooth transition zone, it will be possible to record them at the receivers since the face of the change zone looks upwards. Nevertheless, the reconstructed model in Figure 8.29b is not a good prediction of the expected model. The reconstructed model tells us a little bit about the face of the velocity change and that the velocity value is lower at the right side. The first thing which

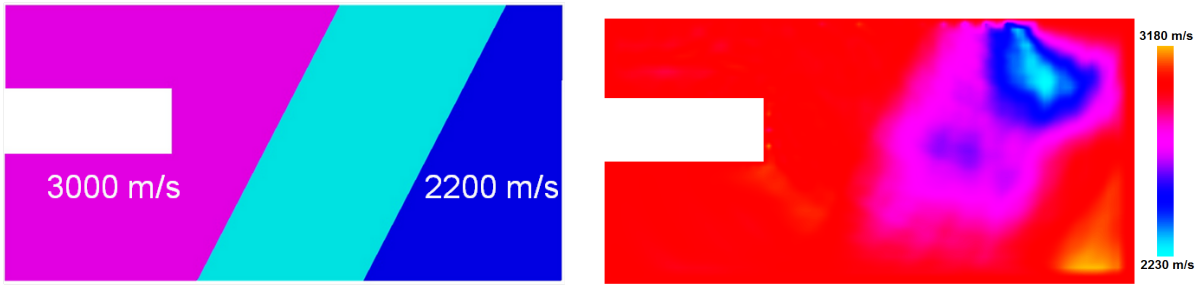

(a) Synthetic model (b) Reconstructed model

Figure 8.29: Scenario 5

comes to mind is to investigate the seismograms to see whether we are acquiring enough data about the smooth transition zone. Figures 8.30, 8.31, and 8.32 compare the seismograms of the model in Figure 8.29a with the seismograms of the homogeneous model with velocity value of 3000 m/s. The seismograms recorded when the source points $s1$ and $s2$ are fired differ very little from the seismograms of the homogeneous case. There are very little reflections only in the first few receivers. Last 3 receivers deviates much from the homogeneous case. The reason of this deviation is that the last 3 receiver points are lying in the region with lower velocity field, and thus the waves arrive a little later. The seismograms recorded when the source point $s3$ is fired differs from their homogeneous counterparts again with the amplitude and arrival time. The waves again arrive later than the homogeneous case. The only reason for the delay is that the source point $s3$ itself is lying in the region with lower velocity. To sum up, the most dominant information in the seismograms about the synthetic model belongs to the points in the lower velocity region, and we can predict the region around these points thanks to that information.

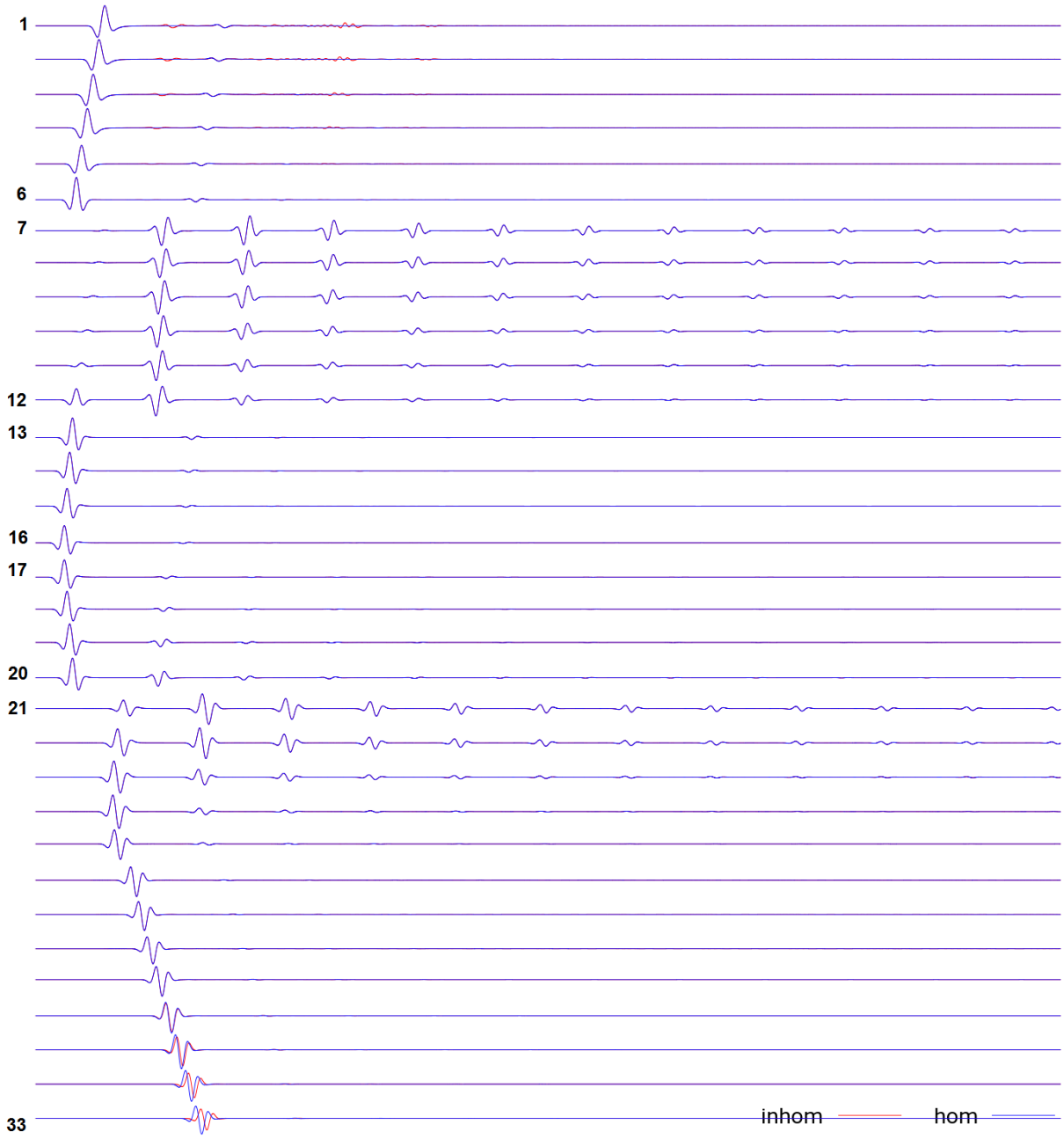

Figure 8.30: Wavefields at receivers, source $s1$ (scenario 5)

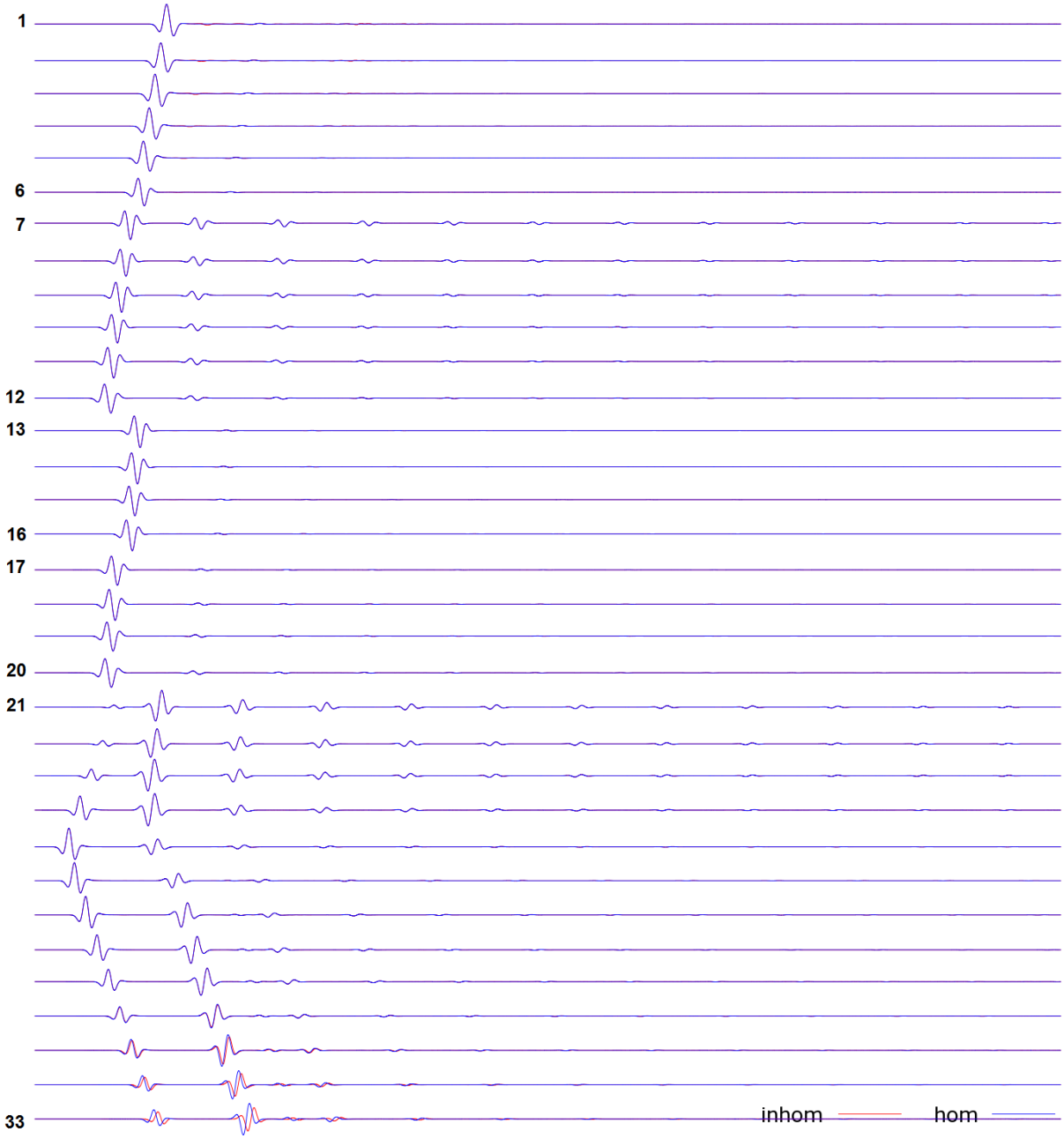

Figure 8.31: Scenario 5, wavefields at receivers, source $s2$ (scenario 5)

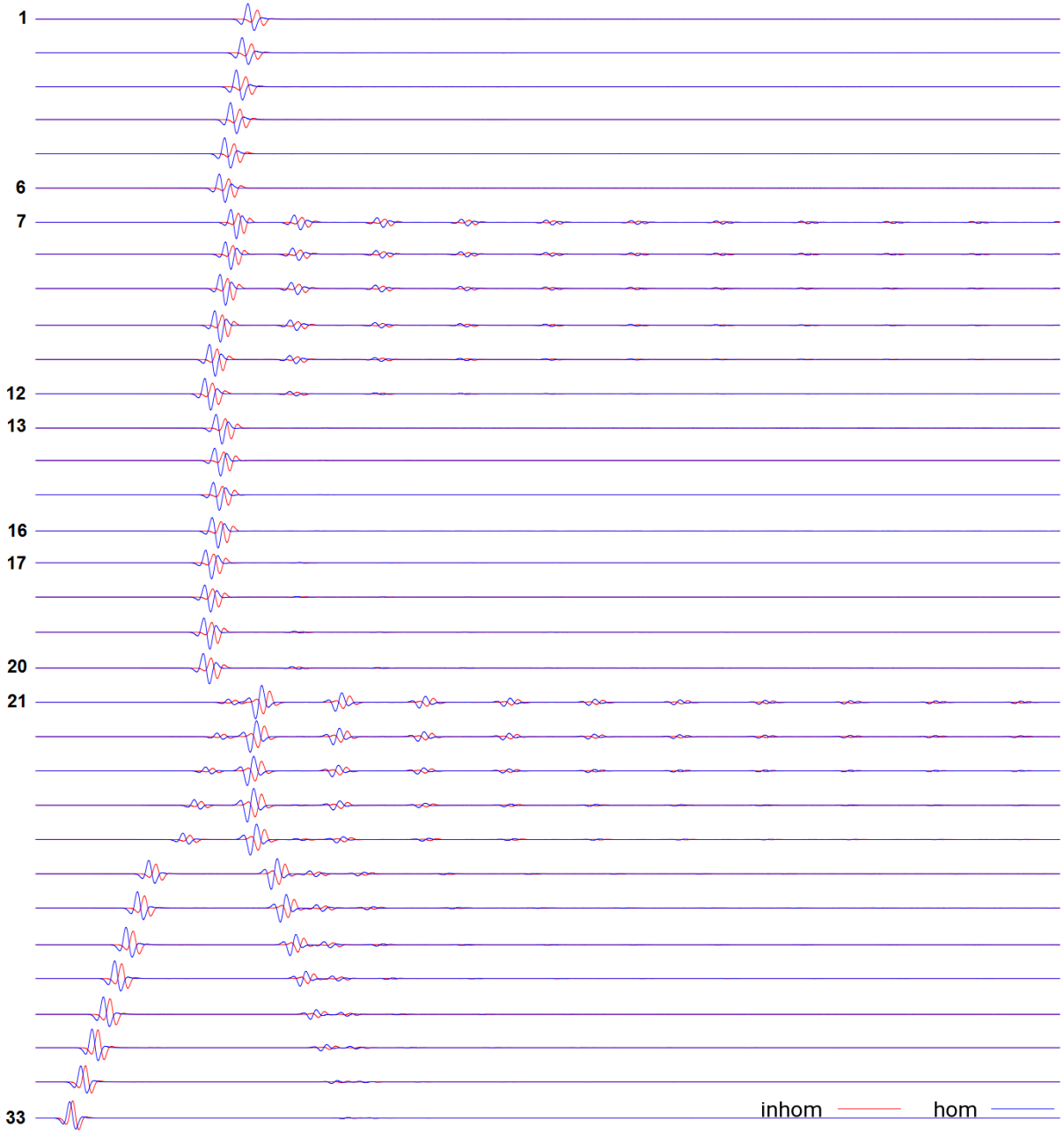

Figure 8.32: Scenario 5, wavefields at receivers, source $s3$ (scenario 5)

8.3 Inversion of 2D viscoacoustic waves

8.3.1 Experiment in a half-space

We start with a half-space example (360m $\times$ 170m) with a high attenuation profile $Q = 50$. In this case, the waves reflected from the reflectors decay very fast till they reach the receiver points. The farther the reflectors are from the sender points, the more the waves decay to zero. Such problems impose more challenge in inversion process because of scarcity of information about the reflectors. We use full waveform inversion to search for velocity and density fields. Searching for two fields brings more challenge and imposes more nonlinearity.

We consider synthetic model to imitate field data and to validate the inversion (see Fig. 8.33a). For synthetic density field, v=1000 kg/m^3, v_1=1300 kg/m^3, and v_2=700 kg/m^3, whereas for synthetic velocity field, v=2000 m/s, v_1=1600 m/s, and v_2=2400 m/s. The problem is investigated in angular frequency range 100-1500Hz. 3 Source and 3 receiver point are chosen right below the surface and distributed evenly in vertical direction over the layers.

After deploying conjugate gradient method, the misfit function is minimized and the resultant velocity and density fields are shown in Figures 8.33b and 8.33c. The layers are seen in the resultant velocity and density fields. However, the velocity field is closer to the synthetic field. There are some peak points close to the surface especially in the density field. These peaks arise near the sender and receiver points. The gradient is expected to have peaks near the sender and receiver points. The result can be improved by using a more optimal combination of source and receiver points. We used very few receiver points, and with the effect of high attenuation, the reflections cannot be caught at receivers good enough. Another key to better results is frequency. Adding even higher frequencies to the set can end up with better results.

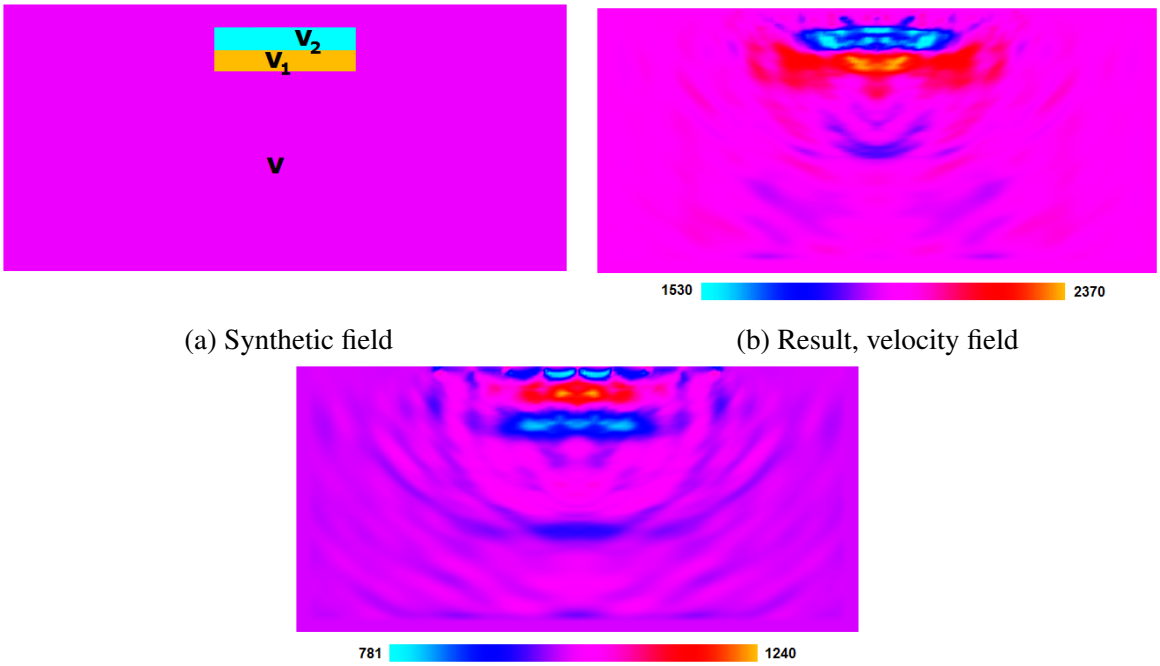

(a) Synthetic field

(b) Result, velocity field

(c) Result, density field

Figure 8.33: Inversion of viscoacoustic waves, half-space example

8.3.2 Experiment in a tunnel model

Next, we investigate a tunnel model (360m $\times$ 170m) with high attenuation profile (Q=50). The density field is constant and we search only for the velocity field. The synthetic model is shown in Figure 8.34a. There are 5 circles evenly distributed on the tunnel track. We use two source points on the front tunnel face and 23 receivers on the surface. With high attenuation, reflections from circles far from the tunnel face weaken a lot. Apart from this, reflection angle becomes smaller. By this example, we investigate how attenuation and distance from the tunnel face influences the result. We again use conjugate gradient method to minimize the misfit function over the angular frequency range 100-1200Hz and the resultant velocity is shown in Figures 8.34b. All five circles are successfully located. However, the shapes of circles farther from the front tunnel face are not well detected and they seem to be stretching in vertical direction. Since the waves start from the front tunnel face, they are attenuated as they move forward. The circles far from the tunnel face reflect weak waves to the receivers. Apart from this, the reflection angle also becomes too small. Circles seem to be stretching in vertical direction because of the small reflection angle. It is also obvious that spurious fluctuations are in the resultant figure. However, the fluctuations are weak compared to the detected objects.

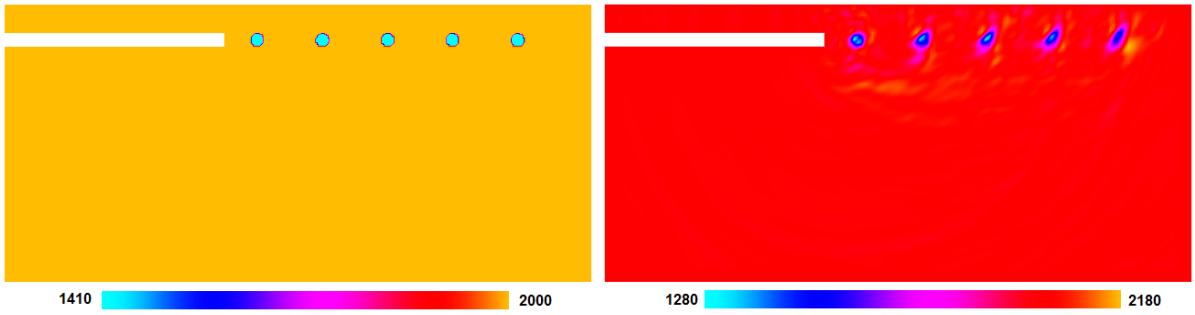

(a) Synthetic field (b) Result, velocity field

Figure 8.34: Inversion of viscoacoustic waves, tunnel model

8.4 Inversion of 3D acoustic waves

8.4.1 3D acoustic half-space experiment

A real-world problem can be reduced down to a 2-dimensional problem with some mathematical tricks. However, it is more realistic to carry out 3-dimensional experiments. The forward model is solved by FE and the pressure field is discretized with basis of degree 1. In one inverse simulation, considerably many forward simulations are run. And since the code is not optimized for very big problems, such simulations may take very long. For this reason, the size of the problems is restricted due to time constraint. This, in return, might have brought some numerical errors. In this section, the results of some 3-dimensional experiments are illustrated. In the first 3-dimensional experiment, a half-space model is examined. The synthetic velocity field has 3 different layers as shown in the figure 8.35. To mimic a half space, the surface is modelled as free surface and PML layers are put at the artificial boundaries. It means the domain is surrounded by absorbing boundaries except at the upper surface. Before running the inverse simulation, it is necessary to place source and receiver points in the domain. It is important to make the inverse problem well-posed. Too few these points may make the problem ill-posed and too many of them may increase the computation time. Number of source points is more crucial since gradient calculation needs to solve system of linear equations as many times as the number of source points. In this simulation, the points were chosen a bit far from the absorbing boundaries in order to reduce the numerical errors due reflected waves from PMLs which in reality would not exist. 7 source and 8 receiver points are evenly located near the surface. Another important issue here is to keep the receiver points far enough from the source points. Since FE basis degree is one and no mesh refinement is applied around the source points, the singularity near the source points brings numerical errors to the pressure value at the receivers if they are not far enough from sources. For inversion in frequency domain, it is important to choose discrete frequency set which, in this case, is chosen as $f_1 = \{50i\}, i = 2, \ldots, 13$. Conjugate gradient method does the inversion in each frequency group separately. The initial model for the first frequency is a constant velocity field with value 2000 m/s. The initial model for any other frequency is the result of the preceding frequency group. After running the inverse simulations, to see how CG method minimized the misfit function, the graphs 8.36 and 8.37 are plotted. These graphs show how the misfit function is minimized and the norm of the gradient go to zero in every frequency group, respectively. Misfit functions follow a strictly decreasing path towards zero. However, norm of gradients follow fluctuating path towards zero. In few frequency groups, such as group 6, the

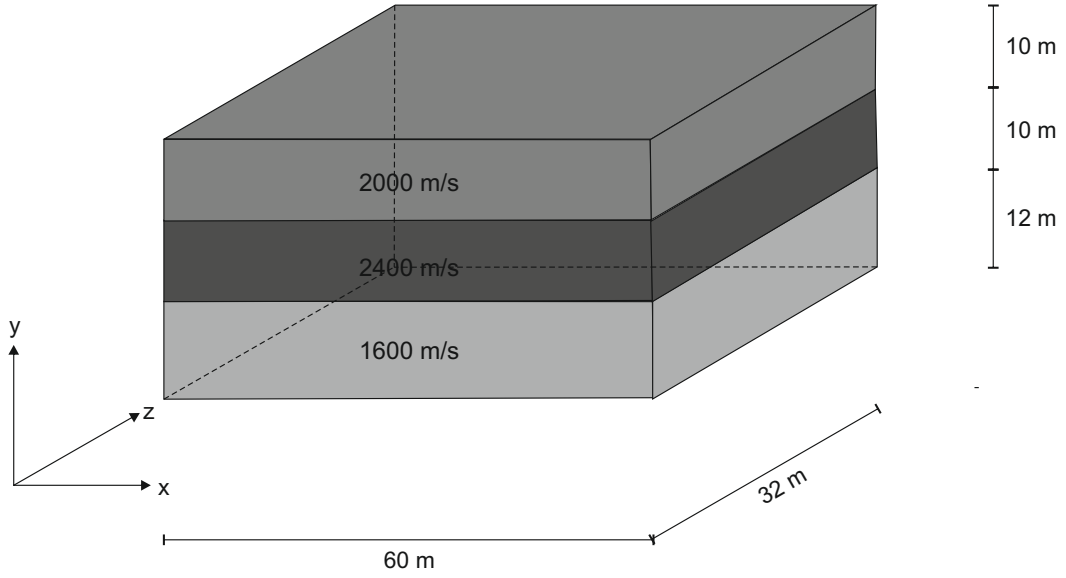

Figure 8.35: 3D half-space synthetic velocity field

norm of the gradient decreases very slightly and its consequence can be seen in misfit graph where the misfit function also decreases very little over many frequencies.

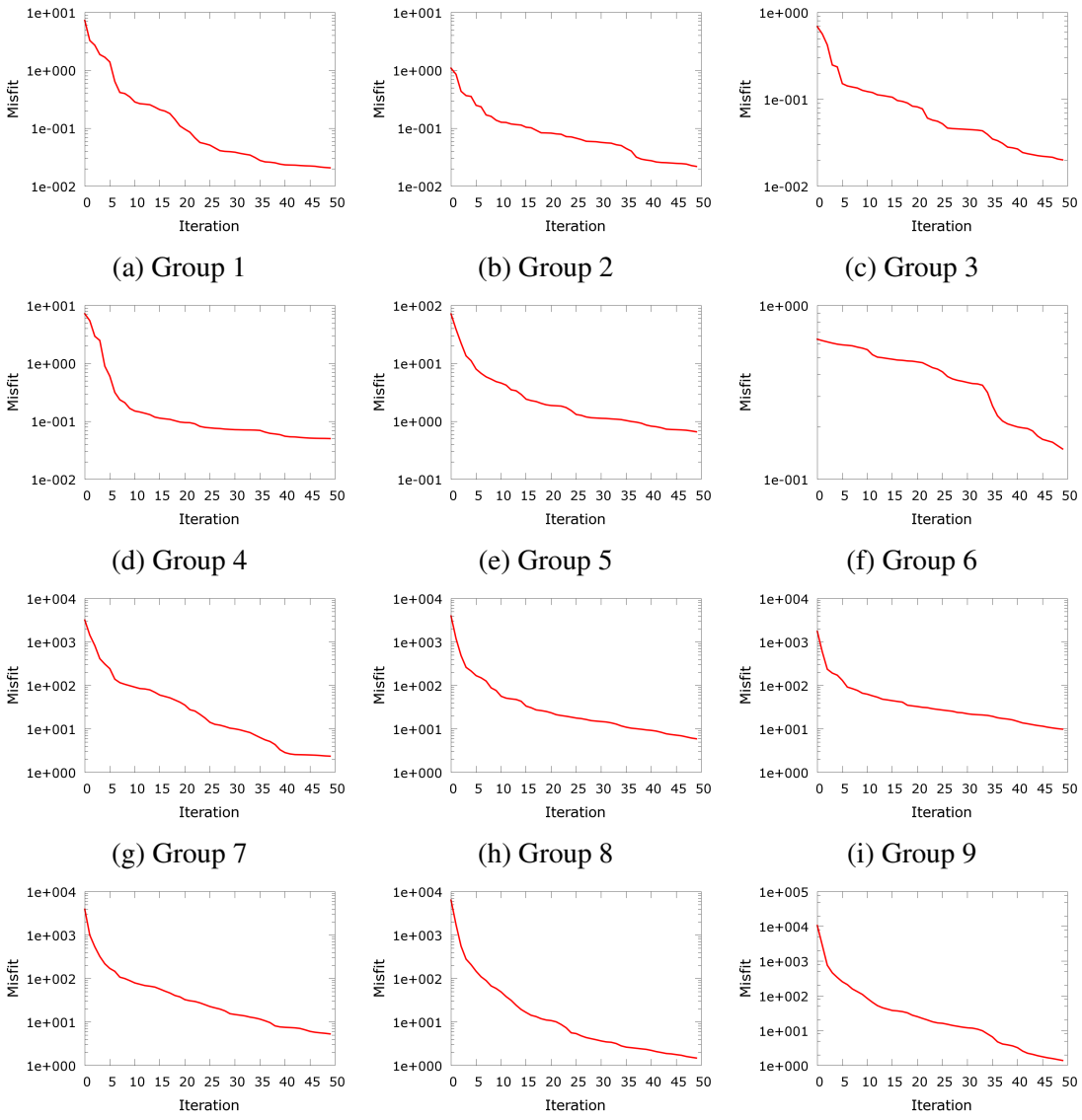

(a) Group 1 (b) Group 2 (c) Group 3

(d) Group 4 (e) Group 5 (f) Group 6

(g) Group 7 (h) Group 8 (i) Group 9

(j) Group 10 (k) Group 11 (l) Group 12

Figure 8.36: Misfit Function vs Iteration

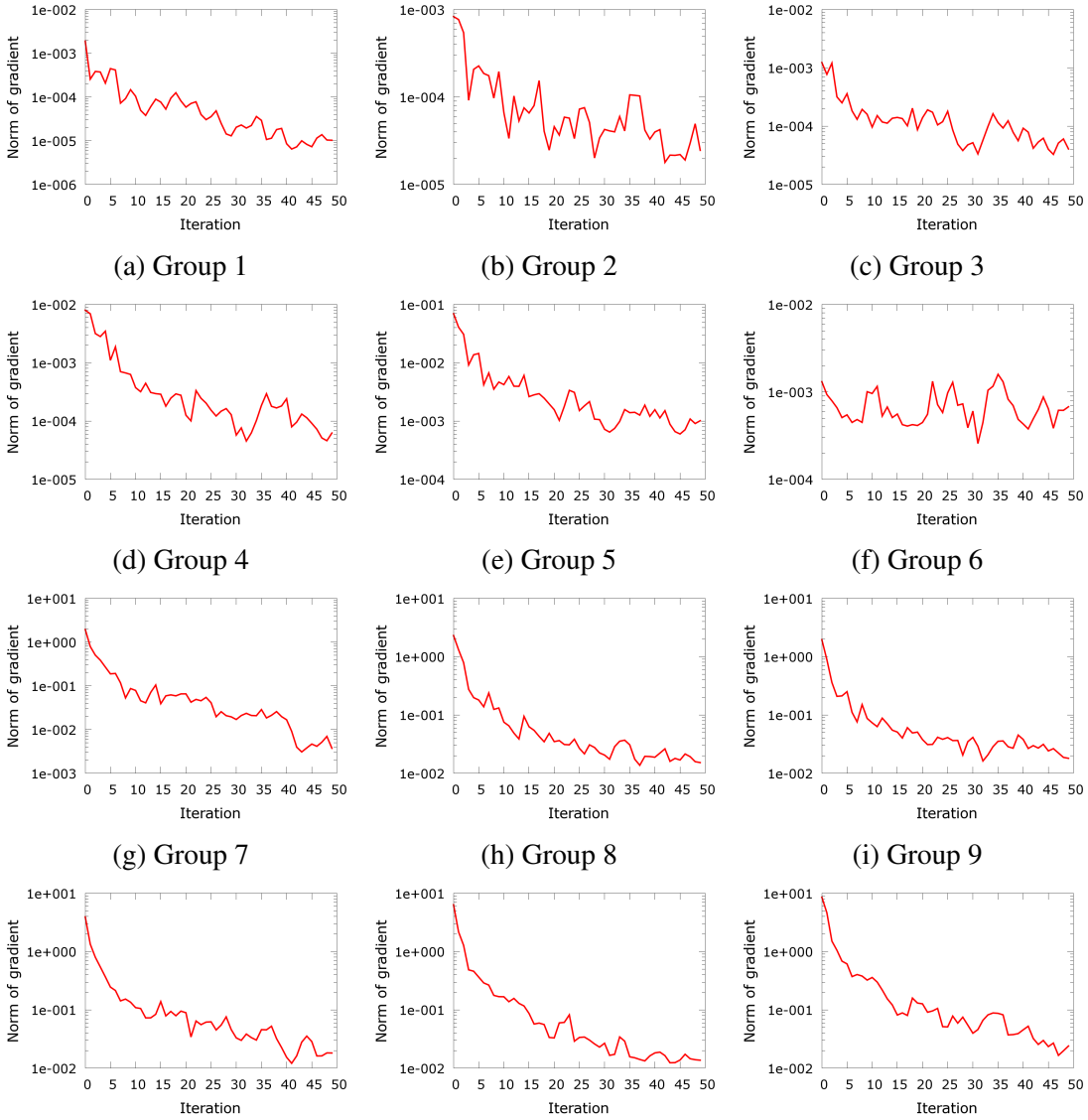

(a) Group 1 (b) Group 2 (c) Group 3

(d) Group 4 (e) Group 5 (f) Group 6

(g) Group 7 (h) Group 8 (i) Group 9

(j) Group 10 (k) Group 11 (l) Group 12

Figure 8.37: Norm of gradient vs iteration

The final velocity field obtained by the inverse simulation is illustrated in the figure 8.38. The velocity field is cut in x and z directions in order to have a better view of the vertical cross section of the domain. It can clearly be seen that the inversion method successfully detected the layers to some good extent. The velocity field has peak at the points where there are source and receiver points. This is due to the gradient calculation; according to (6.17), the gradient has singularities at the source and receiver points. Considering this theoretical information in the interpretation of the result, the peaks around the source and receiver points can be ignored. The inversion result can be improved by using higher frequencies, and mixing up frequency groups with higher and lower frequencies. As aforementioned, since it takes too much time and space with the current software, it was not further investigated. The forward model can be improved by solving the partial differential equation using higher-order FE basis and refining the mesh around the source points. To use higher frequencies, it is necessary to refine the mesh and use higher-order basis functions as well. However, this increases the inverse simulation time tremendously.

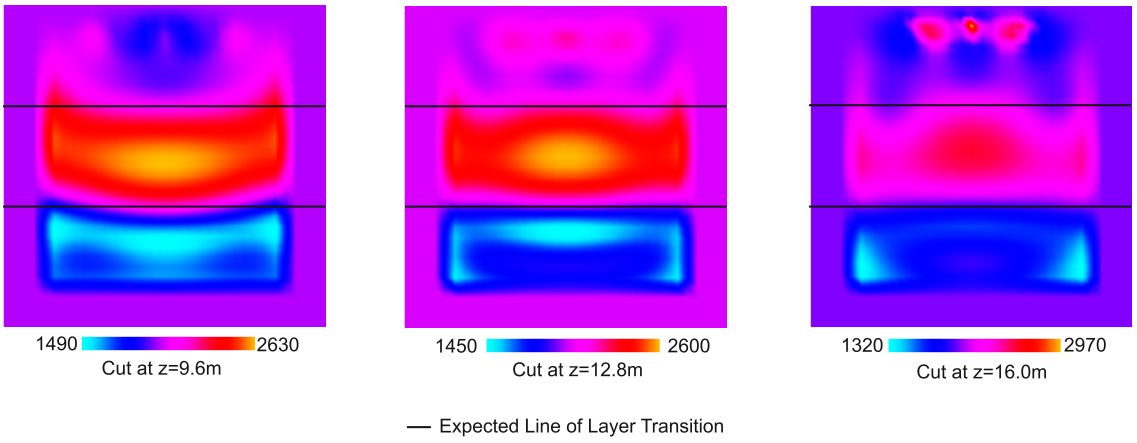

(a) Cut in z direction

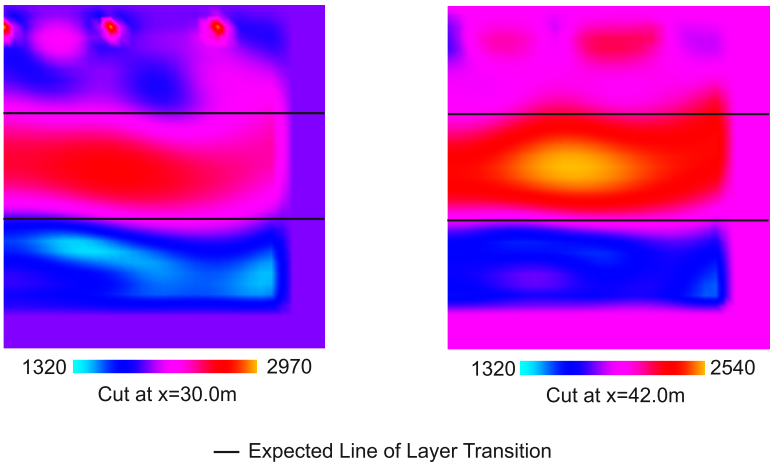

(b) Cut in x direction

Figure 8.38: Reconstructed velocity field

8.4.2 3D acoustic tunnel experiment

A 3D acoustic tunnel model is inverted over the velocity field of the domain. Source and receiver points are again chosen on the front tunnel face and on the upper edge of the domain which is ground in reality. There are 6 source and 9 receiver points on the upper edge, and 2 source and 2 receiver points on the front tunnel face. The angular frequency range is between 50 and 750. The synthetic model is chosen as constant everywhere except a disturbance in the tunnel track. There is a triangular disturbance which extends perpendicular to the tunnel track and parallel to the ground (Figure 8.39). The initial model is a homogeneous velocity field with value $c = 2000$ m/s everywhere. The dimension of the domain is $32 \times 32 \times 60$.

The results of the inversion are illustrated in the Figure 8.40. The disturbance in the velocity field can be seen in the result. It has a triangular shape (8.40a) and it is perpendicular to the tunnel extension (8.40b) as in the synthetic model.

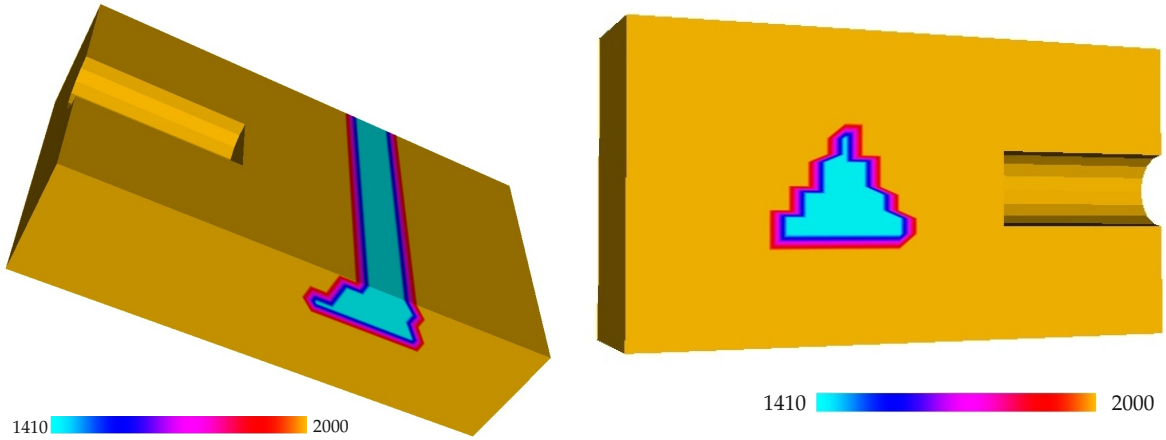

(a) Horizontal cut (b) Vertical cut

Figure 8.39: 3D acoustic tunnel, synthetic velocity field

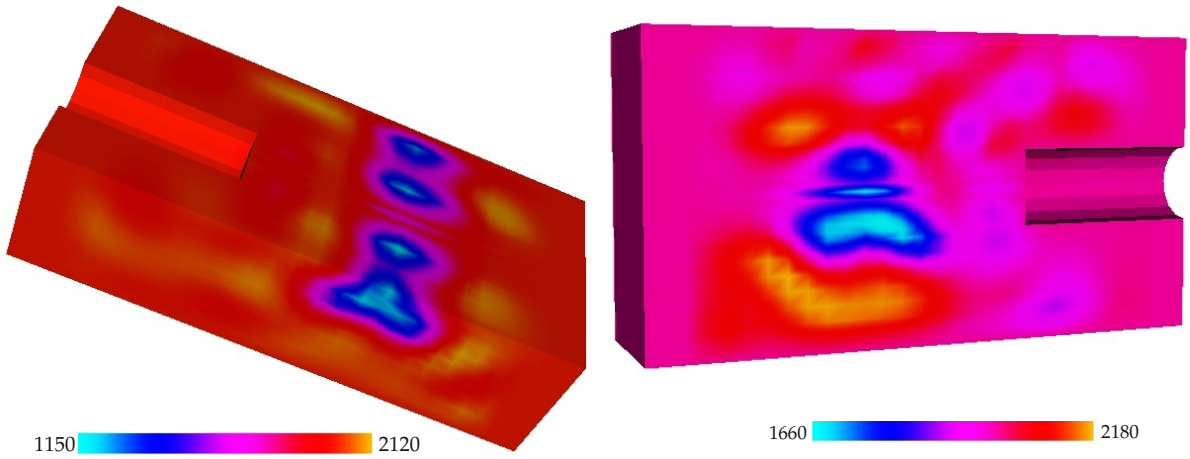

(a) Horizontal cut (b) Vertical cut

Figure 8.40: Reconstructed velocity field

8.5 Inversion of 2D elastic waves

Results from inversion of acoustic waves are presented till now. However, solids are not represented well enough with the acoustic model because it takes only pressure waves into considerations. In contrast to it, shear waves propagate in solids along with pressure waves. Besides this, body wave energy can be partly converted to surface waves at interfaces when the rest of the energy is reflected and refracted. Elastic wave model is capable to deal with pressure, shear, and surface waves. It is crucial to mention that it has been proven that in some application acoustic inversion can be used by separating pressure waves from the whole seismogram. As an example to this application, one can refer to [Fichtner, 2011]. In the first experiment, elastic parameter λ (synthetic model is in Figure 8.41) is sought where the μ and ρ are constant. The model is inverted over the frequency set

$$f_2 = \{(200), (300), (400), (500), (600), (700), (800), (900), (1000), (250, 550, 750, 1000)\}. \quad (8.7)$$

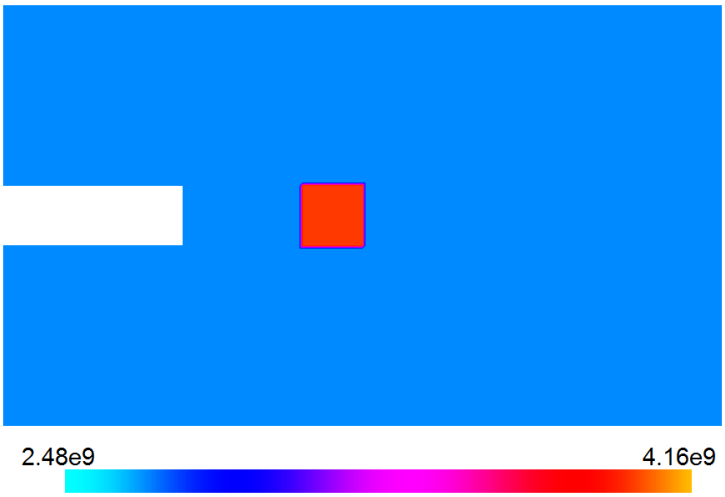

Figure 8.41: Synthetic λ model

The results after each frequency group (Figure 8.42) show how the object becomes clearer after each frequency group. In the end, the location of the object and its velocity value is fairly detected. However, the geometry of the object not precisely figured out. The fact that there is only one source point in front of the tunnel front face may be the reason why the geometry is not sharp enough. We turn two of the receivers near the surface into sources and run the inversion simulation after which we get the result in Figure 8.43. It is clear that the geometry of the object is better detected although we use 25 iterations per frequency whereas it is 40 iterations in the previous simulation.

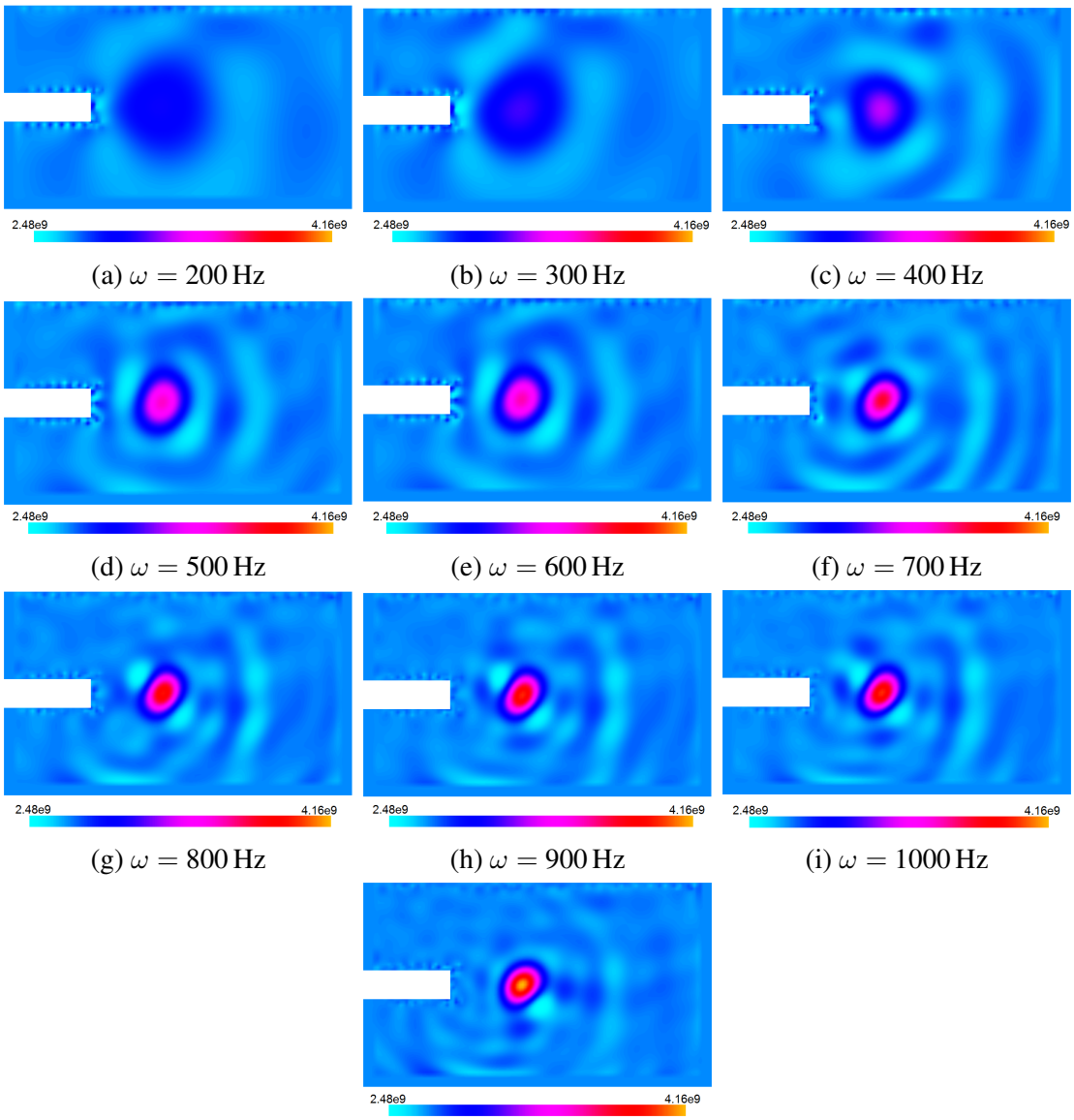

(a) $\omega = 200\,\text{Hz}$ (b) $\omega = 300\,\text{Hz}$ (c) $\omega = 400\,\text{Hz}$

(d) $\omega = 500\,\text{Hz}$ (e) $\omega = 600\,\text{Hz}$ (f) $\omega = 700\,\text{Hz}$

(g) $\omega = 800\,\text{Hz}$ (h) $\omega = 900\,\text{Hz}$ (i) $\omega = 1000\,\text{Hz}$

(j) $\omega = 250{,}550{,}750{,}1000\,\text{Hz}$

Figure 8.42: λ after inversion over each frequency group

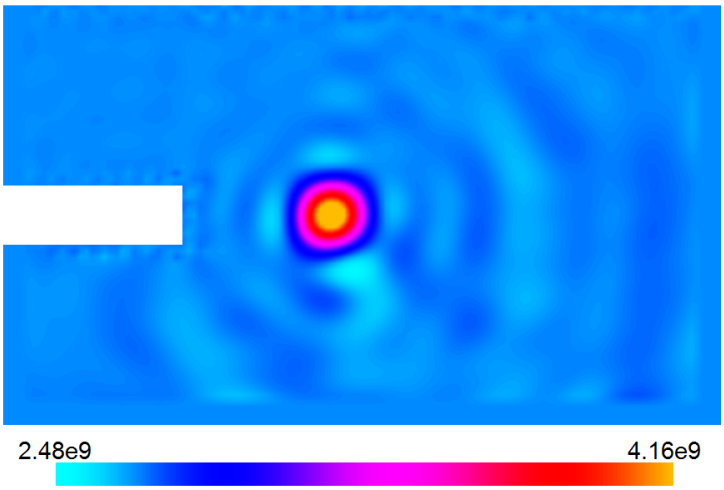

Figure 8.43: Reconstructed λ with the second configuration

In this test, we assume that parameters μ and ρ are constant and we search for only λ. However, searching for λ and μ simultaneously makes the inverse problem more realistic. In the next test, we search for λ, which is the same synthetic model as in the previous test, and μ, which is 1.5E10 N/m^2 inside the box and 1.08E10 N/m^2 elsewhere. The same frequency set and the second source/receiver setup of the previous test are used in this test too. After the last frequency group we obtain λ and μ which are shown in Figure 8.44. Although the object is well detected in both λ and μ, the square in μ is much clearer with edges and shape.

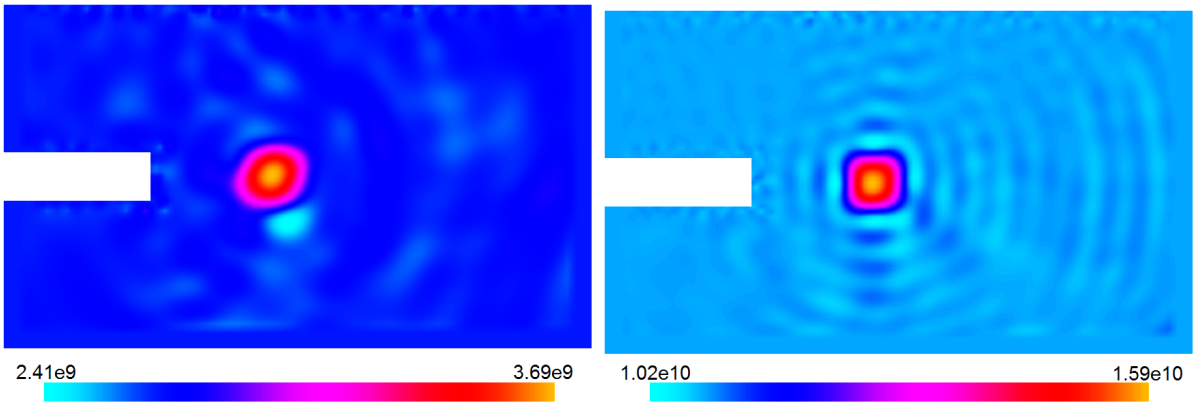

(a) λ (b) μ

Figure 8.44: Reconstructed λ and μ

However, this test is still not the most realistic test that can be carried out for elastic waves because density is never homogeneous in soil. Homogeneity effect of density can be neglected in a lot of cases. Nevertheless, in some special cases, e.g. when the density change is very sudden, the heterogeneity of the soil is not negligible. To investigate whether all three parameters λ, μ, and ρ can be detected at the same time, we carry out such an experiment where all parameters are heterogeneous and are sought. We use same synthetic models for λ and μ as in the previous test, whereas we choose ρ such that its value is 1700 inside the box and 2700 elsewhere. Applying same conditions to the experiment as in the previous experiments, after the last frequency group, it is observed that λ and μ did not deviate from their starting models. In contrast to ρ, λ and μ are not detected and surprisingly the inversion almost did not change initial λ and μ fields, which are homogeneous fields, at all. However, although the shape of the box is not perfect, ρ result

looks quite precise with value of the density in the box, its location and size (see Figure 8.45). To investigate why the other two parameters are not affected at all by the inversion, we have a look at the norm of gradients of the misfit functional with respect to the parameters. The range of the gradients with respect to the parameters are as follows: $\left|\frac{\partial \chi}{\partial \lambda}\right| \sim 10^{-11}$, $\left|\frac{\partial \chi}{\partial \mu}\right| \sim 10^{-10}$, and $\left|\frac{\partial \chi}{\partial \rho}\right| \sim 10^{-2}$. $\left|\frac{\partial \chi}{\partial \rho}\right|$ is too high compared to the others. On the other hand, ρ itself is in the range 10^3, whereas the others are in the range 10^{10}. In each iteration of the optimization, all three parameters are updated by the same steplength. Since ρ itself is much smaller than the others and at the same time, its sensitivity is much higher than the others, the change in ρ is enormously bigger than the change in other two parameters in each iteration. High sensitivity of ρ takes the solution probably to a local minimum by almost not considering the effects of λ and μ. This is the reason why λ and μ do not differ from its initial model, whereas the box is well detected in resultant ρ. Preconditioned conjugate-gradient method can help to equalize the sensitivities of the parameters. However, we do not include it within the context of this work.

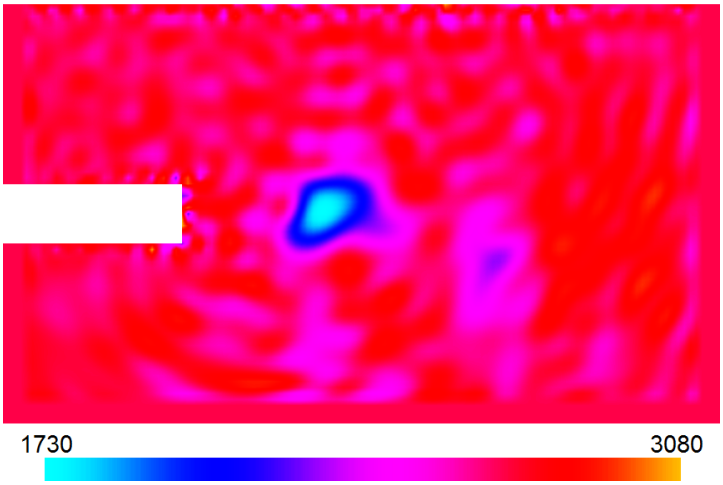

Figure 8.45: Search for λ, μ, and ρ; reconstructed ρ

9 Conclusions and Outlook

In a tunneling application, imaging the domain and detecting the irregularity of the structure of the domain are becoming very important in the excavation process. This information is useful because it can make the excavation process proceed more smoothly, more quickly, and with lower cost. Furthermore, the anomalies in the tunnel domain, depending on their geometry and mechanical properties, may lead to significantly large settlements on the surface after the tunnel has been excavated. If these anomalies are detected prior to excavation, preventative measures can be taken to avoid large settlements.

Main goal of this work is to investigate full waveform inversion approach in tunneling applications. For this reason, we address forward and inverse acoustic and elastic modelling of a tunnel. Furthermore, frequency domain is preferred because any single frequency can be investigated for both forward and inverse problems. However, frequency domain forward modelling is computationally cumbersome compared to the time domain. For the forward modelling, it is inevitable to implement certain boundary conditions that play a very crucial role in defining a realistic problem. These boundaries are the absorbing boundaries, which come into play from the fact that the domain is theoretically infinite, and the free surface, which mimics the air-soil interface. Perfectly-matched layers play a crucial role in completing the forward modelling part successfully.

Full waveform inversion is now becoming a very popular method used by geophysicists and earth scientists to explore the structure of the ground. However, it is not widely used in tunneling applications. In most cases, only the traveltime information of waves is used for the inversion. FWI provides more information about the model than the traveltimes. This is the motivation behind applying full waveform inversion to our inverse problems.

Moreover, we investigate the factors that influence the inversion result. The results with different frequency sets and different configurations of source and receiver points are compared. The source/receiver configuration is a crucial point in defining the inverse problem. The wrong configuration may lead to an ill-posed inverse problem. The size of the frequency set should be as small as possible to reduce the computation time, but it must not be too small at the same time. A very small frequency set size does not provide a good representation of the frequency range and the problem deviates from the real problem. It also becomes more difficult to find the global minimum of the misfit function. We conduct different experiments with different settings and investigate how each factor influence the final result.

Another aim of this work is to utilize the full acoustic waveform inversion technique using two similar, but different approaches: discrete and continuous approaches. The results obtained by both of them are compared and commented upon. We answer the question how the search for different functions, c and $\frac{1}{c^2}$, may end up with different results. It is concluded that a more appropriate discretization can decrease the relative error.

In general, we conduct successful numerical experiments which confirm that FWI can be used in tunneling applications. It is numerically more expensive than most of the migration tech-

niques. However, with an exponential growth of the computer technology, FWI may soon be a preferable technique to predict the geological structure ahead of a tunnel. Apart from two-dimensional problems, we extend the simulations to 3-dimensional cases to be closer to the realistic problems.

One of the biggest highlights of this work is blind test experiment. What makes it so interesting is the fact that we did not have any prior information about the synthetic model except for the seismograms. Furthermore, the synthetic model is very precisely modelled to have minimum possible numerical errors. This problem poses challenge for both forward and inverse models. We took the status of this work one step further by overcoming the challenge.

There are still many things that must be done in order to have better forward and inverse models. The plan is to have three-dimensional full elastic waves with attenuation and other factors, such as dispersion, if necessary. The code is already able to solve 3D problems. However, it has to be optimized and parallelized for big scale problems. At the same time, the lab experiments are being carried out for this project. It is a crucial step to have numerical models which can imitate the experiments in the lab. Moreover, the plan is to conduct inversion experiments with the laboratory data. The most important challenge would be to have data from a real tunnel construction site and apply FWI to that data. Such an experiment can be the ultimate aim of the project. FWI is applied to figure out the geological structure of the earth and some seismic companies are using the method in some cases. It looks very probable that FWI can provide some interesting result in tunneling as well.

References

[Achenbach, 1984] Achenbach, J. Wave propagation in elastic solids. NORTH-HOLLAND, Amsterdam-New York-Oxford, 1984.

[Ajo-Franklin, 2005] Ajo-Franklin, J. B. Frequency domain modeling techniques for the scalar wave equation : An introduction. Massachusetts Institute of Technology. Earth Resources Laboratory, 2005.

[Aki and Richards, 2011] Aki, K., Richards, P.. Quantitative Seismology. W. H. Freeman, New York, 1980.

[Alterman and Karal, 1968] Alterman, Z., Karal, F. C. Propagation of elastic waves in layered media by finite-difference methods. Bull. Seism. Soc. Am.. 58, 367-398, 1968.

[Ashida, 2001] Ashida, Y. Seismic imaging ahead of a tunnel face with three-component geophones. International Journal of Rock Mechanics and Mining Sciences. 38(6), 823-831, 2001.

[Bamberger et al., 1982] Bamberger, A., Chavent, G., Hemons, Ch., Lailly, P. Inversion of normal incidence seismograms. Geophysics 47(5), 757-770, 1982.

[Benecke et al., 2008] Benecke, N., Dombrowski, B. A., Lehmann, B. Trust–Exploration ahead of the tunnel face for reducing tunneling risks and supporting decision-making. In World Tunnel Congress, 1124-1129, 2008.

[Berenger, 1994] Berenger, J. P. A perfectly matched layer for the absorption of electromagnetic waves. J. Computational Physics. 114, 185-200, 1994.

[Bohlen et al., 2007] Bohlen, T., Lorang, U., Rabbel, W., Müller, C., Giese, R., Lüth, S., S., S., Jetschny Rayleigh-to-shear wave conversion at the tunnel face—From 3D-FD modeling to ahead-of-drill exploration. Geophysics. 72(6), 67-79, 2007.

[Borm et al., 2003] Borm, G., Giese, R., Klose, C., Mielitz, S., Otto, P., Bohlen, T. ISIS integrated seismic imaging system for the geological prediction ahead of underground construction. In the 65th Conference and Exhibition, EAGE, Extended Abstracts, 2003.

[Brossier et al., 2010] Brossier, R., Etienne, V, Operto, S., Virieux, J. Frequency-domain numerical modelling of visco-acoustic waves based on finite-difference and finite-element discontinuous Galerkin methods. SCIYO editions, 2010.

[Broyden, 1970] Broyden, C. G. The convergence of a class of double rank minimization algorithms. IMA Journal of Applied Mathematics 6, 222-231, 1970.

[Brückl et al., 2001] Brückl, E., Chwatal, W., Dölzlmüller, J., Jöbstl, W. A study of the application of VSP to exploration ahead of a tunnel. International Journal of Rock Mechanics and Mining Sciences. 38(6), 833-841, 2001.

[Brückl et al., 2008] Brückl, E., Chwatal, W., Mertl, S., Radinger, A. Exploration ahead of a tunnel face by TSWD–tunnel seismic while drilling. Geomechanics and Tunnelling 1(5), 460-465, 2008.

[Cerjan et al. 1985] Cerjan, C., Kosloff, D., Kosloff, R., Reshef, M. A nonreflecting boundary condition for discrete acoustic and elastic wave equations. Geophysics. 50, 705-708, 1985.

[Chaljub et al., 2007] Chaljub, E., Komatitsch, D., Vilotte, J. P., Capdeville, Y., Valette, B., Festa, G. Spectral element analysis in seismology. Advances in Geophysics. 48, 365–419, 2007.

[Cheng et al., 2014] Cheng, F., Liu, J., Qu, N., Mao, M., Zhou, L. Two-dimensional pre-stack reverse time imaging based on tunnel space. Journal of Applied Geophysics 104, 106-113, 2014.

[Chew and Weedon, 1994] Chew and Weedon. A 3D perfectly matched medium from modified Maxwell's equations with stretched coordinates. Microw. Opt. Technol. Lett. 7, 599-604, 1994.

[Chew and Liu, 1996] Chew, W. C., Liu, Q. H. Perfectly matched layers for elastodynamics: A new absorbing boundary condition. J. Comput. Acoust. 4, 341-359, 1996.

[Claerbout, 1979] Claerbout, J. F. Fundamentals of geophysical data processing. McGraw-Hill, New York, 1979.

[Clayton et al. 1980] Clayton, R. W., Engquist, B. Absorbing boundary conditions for wave-equation migration. Geophysics. 45, 895-904, 1980.

[Collina and Tsogka, 2001] Collina, F., Tsogka, C. Application of the perfectly matched absorbing layer model to the linear elastodynamic problem in anisotropic heteregeneous media. Geophysics 66, 294-307, 2001.

[Crase et al., 1990] Crase, E., Pica, A., Noble, M., McDonald, J., A. Tarantola Robust elastic nonlinear waveform inversion - Application to real data. Geophysics 55(5), 527-538, 1990.

[Dablain, 1986] Dablain, M. A. The application of high-order differencing to the scalar wave equation. Geophysics. 51, 54-66, 1986.

[Dickmann and Sander, 1996] Dickmann, T., Sander, B. Drivage concurrent tunnel seismic prediction. Felsbau-rock and Soil Engineering. 14(1), 406-411, 1996.

[Dongarra et al., 1988] Dongarra, J. J., DuCroz, J., Hammarling, S., Hanson, R. An extended set of fortran basic linear algebra subprograms. ACM Trans. on Math. Soft. 14, 1-32, 1988.

[Dongarra et al., 1989] Dongarra, J. J., Duff, I., DuCroz, J., Hammarling, S. A set of level 3 basic linear algebra subprograms. ACM Trans. on Math. Soft, 1989.

[Dumbser and Kaser, 2006] Dumbser, M., Kaser, M. An Arbitrary High Order Discontinuous Galerkin Method for ElasticWaves on Unstructured Meshes II: The Three-Dimensional Isotropic Case. Geophysical Journal International. 167(1), 319-336, 2006.

[Engquist and Majda, 1977] Engquist, B., Majda, A. Absorbing boundary conditions for the numerical simulation of waves. Mathematics of Computation. 31, 629-651, 1977.

[Emerman and Stephen, 1983] Emerman, S. H., Stephen, R. A. Comment on 'Absorbing boundary conditions for acoustic and elastic wave equations' by R. Clayton and B. Engquist. Bull. Seism. Soc. Am.. 73, 661-665, 1983.

[Festa and Nielsen, 2003] Festa, G., Nielsen, S. PML absorbing boundaries. Bull. Seismol. Soc. Am.. 93, 891-903, 2003.

[Festa et al. 2005] Festa, G., Delavaud, E., Vilotte, J. P. Interaction between surface waves and absorbing boundaries for wave propagation in geological basins: 2D numerical simulations. Geophys. Res. Lett. 32, 2005.

[Festa and Vilotte, 2005] Festa, G., Vilotte, J. P. The Newmark scheme as velocity-stress time-staggering: an efficient PML implementation for spectral element simulations for elastodynamics. Geophys. J. Int. 161, 789-812, 2005.

[Fichtner et al., 2008] Fichtner, A., Kenneth, B. L. N., Igel, h., Bunge, H. P. Theoretical background for continental- and global-scale full waveform inversion in the time-frequency domain. Geophys. J. Int. 175, 665-685, 2008.

[Fichtner et al., 2009a] Fichtner, A., Kenneth, B. L. N., Igel, h., Bunge, H. P. Spectral element simulation and inversion of seismic waves in a spherical section of the Earth. J. Numer. Anal. Ind. Appl. Math. 4, 11-22, 2009.

[Fichtner et al., 2009b] Fichtner, A., Kenneth, B. L. N., Igel, h., Bunge, H. P. Full seismic waveform tomography for upper-mantle structure in the Australasian region using adjoint methods. Geophys. J. Int. 179, 1703-1725, 2009.

[Fichtner, 2011] Fichtner, A. Full seismic waveform modelling and inversion. Springer, Berlin.Heidelberg, 2011.

[Fletcher and Reeves, 1964] Fletcher, R., Reeves, C. M. Function minimization by conjugate gradients. Comput. J. 7, 149-154, 1964.

[Fletcher, 1970] Fletcher, R. A new approach to variable metric algorithms. The Computer Journal 13, 317-322, 1970.

[Futterman, 1962] Futterman, W. I. Dispersive body waves. Journal of Geophysical Research. 67, 5279-5291, 1962.

[Gehrig et al., 2010] Gehrig, M., Kassel, A., Lorenz, K. Advance exploration accompanying the drive: mixshield with vision. In Tunnel, 14-29, 2010.

[Harari et al. 2000] Harari, I., Slavutin, M., Turkel, E. Analytical and numerical studies of a finite element PML for the Helmholtz equation. Journal of Computational Acoustics. 08, 121-137, 2000.

[Hastings et al., 1996] Hastings, F. D., Schneider, J. B., Broschat, S. L. Application of the perfectly matched layer(pml) absorbing boundary condition to elastic wave propagation. J. Acoust. Soc. Am. 100, 3061-3069, 1996.

[Hestenes and Stiefel, 1952] Hestenes, M. R., Stiefel, E. L. Methods of conjugate gradients for solving linear systems. J. Res. Natl. Bur. Stand. 49, 409-436, 1952.

[Higdon, 1990] Higdon, R. L. Radiation boundary conditions for elastic wave propagation. SIAM J. Numer. Anal. 27, 831-870, 1990.

[Higdon, 1991] Higdon, R. L. Absorbing boundary conditions for elastic waves. Geophysics. 56, 231-241, 1991.

[Inazaki et al., 1999] Inazaki, T., Isahai, H., Kawamura, S., Kurahashi, T., Hayashi, H. Stepwise application of horizontal seismic profiling for tunnel prediction ahead of the face. The Leading Edge. 18(12), 1429-1431, 1999.

[Jetschny, 2010] Jetschny, S. Seismic prediction and imaging of geological structures ahead of a tunnel using surface waves. Karlsruher Instituts fuer Technologie, Germany, 2010.

[Jetschny et al., 2010] Jetschny, S., Bohlen, T., De Nil, D. On the propagation characteristics of tunnel surface waves for seismic prediction. Geophysical Prospecting 58(2), 245–256, 2010.

[Jetschny et al., 2011] Jetschny, S., Bohlen, T., Kurzmann, A. Seismic prediction of geological structures ahead of the tunnel using tunnel surface waves. Geophysical Prospecting 59(5), 934-946, 2011.

[Jiao et al., 2015] Jiao, Y. Y., Tian, H. N., Liu, Y. Z., Mei, R. W., Li, H. B. Prediction of tunneling hazardous geological zones using the active seismic approach. Near Surface Geophysics. 13(4), 333-342, 2015.

[Keys, 1985] Keys, R. G. Absorbing boundary conditions for acoustic media. Geophysics. 50, 892-902, 1985.

[Kneib et al., 2000] Kneib and Kassel and Lorenz Automatic seismic prediction ahead of the tunnel boring machine. First Break. 18, 295-302, 2000.

[Kolsky, 1956] Kolsky, H. The propagation of stress pulses in viscoelastic solids. Philosophical Magazine. 1, 693-710, 1956.

[Komatitsch and Vilotte, 1998] Komatitsch, D., Vilotte, J. P. The spectral element method: an efficient tool to simulate the seismic response of 2D and 3D geological structures. Bull. Seismol. Soc. Am. 88, 368-392, 1998.

[Komatitsch and Tromp, 1999] Komatitsch, D., Tromp, J. Introduction to the spectral-element method for 3-D seismic wave propagation. Geophys. J. Int. 139(3), 806-822, 1999.

[Komatitsch and Tromp, 2003] Komatitsch, D., Tromp, J. A perfectly matched layer absorbing boundary condition for the second-order seismic wave equation. Geophys. J. Int. 154, 146-153, 2003.

[Komatitsch et al., 2004] Komatitsch, D., Liu, Q., Tromp, J., Suess, P., Stidham, C., Shaw, J. H. Simulations of ground motion in the Los Angeles basin based upon the spectral-element method. Bull. Seismol. Soc. Am. 94(1), 187-206, 2004.

[Kristek et al., 2002] Kristek, J., Moczo, P., Archuleta, R. J. Efficient methods to simulate pla-

nar free surface in the 3D 4th-order staggered-grid finite-difference schemes. Stud. Geophys. Geod. 46, 355-381, 2002.

[Kuzmin et al., 2013] Kuzmin, A., Luisier, M., Schenk, O. Fast methods for computing selected Elements of the Greens function in massively parallel nanoelectronic device simulations. Euro-Par 2013 Parallel Processing 8097, 533-544, 2013.

[Lambrecht and Friederich, 2013] Lambrecht, L., Friederich, W. Simulation of seismic wave propagation for reconnaissance in mechanized tunneling using spectral element and nodal discontinuous Galerkin method. EUROTUN 2013 Computational Methods in Tunneling and Subsurface Engineering, 769-777, 2013.

[LAPACK Users' Guide] Anderson, E., Bai, Z., Bischof, C., Blackford, S., Demmel, J., Dongarra, J., DuCroz, J., Greenbaum, A., Hammarling, S., McKenney, A.,Sorensen, D. LAPACK Users' Guide. Society for Industrial and Applied Mathematics. Philadelphia, PA, 1999.

[Lawson et al., 1979] Lawson, C., Hanson, R., Kincaid, D., Krogh, F. Basic linear algebra subprograms for fortran usage. ACM Trans. on Math. Soft. 5, 308-325, 1979.

[Lee et al., 2008] Lee, S. J., Chen, H. W., Liu, Q., Komatitsch, D., Huang, B. S., Tromp, J. Three-dimensional simulations of seismic wave propagation in the Taipei basin with realistic topography based upon the spectral-element method. Bull. Seismol. Soc. Am. 98(1), 253-264, 2008.

[Levenberg, 1944] Levenberg, K. A method for the solution of certain non-linear problems in least-squares. Q. Appl. Math. 2, 164-168, 1944.

[Liu and Tao, 199] Liu, Q., Tao, J. The perfectly matched layer (PML) for acoustic waves in absorptive media. Jour. Acoust. Soc. Am.. 102, 2072-2082, 199.

[Madariaga, 1967] Madariaga, R. Dynamics of an expanding circular fault. Bull. Seism. Soc. Am.. 67, 163-182, 1967.

[Mahrer, 1986] Mahrer, K. D. An empirical study of instability and improvement of absorbing boundary conditions for the elastic wave equation. Geophysics. 51, 1499-1501, 1986.

[Mahrer, 1990] Mahrer, K. D. Numerical time step instability and and Stacey's and Clayton-Engquist's absorbing boundary conditions. bull. Seism. Soc. Am.. 80, 213-217, 1990.

[Marsden and Hughes, 1983] Marsden, J. E., Hughes, T. J. R. Mathematical foundation of elasticity. Dover Publications, Berlin-Heidelberg, 1983.

[Miro, 2012] Borm, G., Giese, R., Klose, C., Mielitz, S., Otto, P., Bohlen, T. Scenario-driven system identification for the specification of ground models in mechanized tunneling. 14th International Conference on Computing in Civil and Building Engineering, 2012.

[Moczo et al., 2002] Moczo, P., Kristek, J., Vavrycuk, V., Archuleta, R. J., Halada, J. 3D heteregeneous staggered-grid finite-difference modelling of seismic motion with volume harmonic and arithmetic averaging of elastic moduli. Bull. Seism. Soc. Am. 92, 3042-3066, 2002.

[NAG1] The Numerical Algorithms Group(NAG). The NAG library. http://www.nag.com,

ACM Trans. Oxford, United Kingdom.

[NAG2] The Numerical Algorithms Group(NAG). The NAG fortran compiler. http://www.nag.com, ACM Trans. Oxford, United Kingdom.

[Neil et al., 1999] Neil, D. M., Haramy, K. Y., Descour, J., Hanson, D. Imaging ground conditions ahead of the face. World Tunneling. 12(9), 425-429, 1999.

[Nguyen, 2016] Nguyen, Luan T and Nestorović, T. Unscented hybrid simulated annealing for fast inversion of tunnel seismic waves. Computer Methods in Applied Mechanics and Engineering. 301, 281-299, 2016.

[Oezalp, 2015] Oezalp, S. Finite Elemente Analyse von akustischen Wellen und Full Waveform Inversion in einer 2D-Tunnelumbegung. Ruhr Universität Bochum, Germany, 2015.

[Otto et al., 2002] Otto, R., Button, E., Bretterebner, H., Schwab, P. The application of TRT – true reflection tomography – at the Unterwald Tunnel. Felsbau. 20(2), 51-56, 2002.

[Petronio and Poletto, 2002] Petronio, L., Poletto, F. Seismic-while-drilling by using tunnel boring machine noise. Geophysics. 67(6), 1798-1809, 2002.

[Petronio et al., 2003] Petronio, L., Poletto, F., Schleifer, A., Morino, A. Geology prediction ahead of the excavation front by Tunnel-Seismic-While-Drilling (TSWD) method. Society of Exploration Geophysicists, 73rd Annual International Meeting, Expanded Abstracts, 2003.

[Petronio et al., 2007] Petronio, L., Poletto, F., Schleifer, A. Interface prediction ahead of the excavation front by the tunnel-seismic-while-drilling (TSWD) method. Geophysics 72(4), 39-44, 2007.

[Pica et al., 1990] Pica, A., Diet, J. P., Tarantola, A. Nonlinear inversion of seismic reflection data in laterally invariant medium. Geophysics 55, 284-292, 1990.

[Polak and Ribiere, 1969] Polak, E., Ribiere, G. Note sur la convergence de la mèthode de directions conjugèes. Revue Fr. Inf. Rech. Oper. 16-R1, 35-43, 1969.

[Pratt et al., 1998] Pratt, R. G., Shin, C., Hick, G. J. Gauss–Newton and full Newton methods in frequency–space seismic waveform inversion. Geophysical Journal International. 133, 341-362, 1998.

[Pratt, 1999a] Pratt, R. G. Seismic waveform inversion in the frequency domain, Part 1: Theory and verification in a physical scale model. Geophysics 64, 888-901, 1999.

[Pratt, 1999b] Pratt, R. G. Seismic waveform inversion in the frequency domain, Part 2: fault delineation in sediments using crosshole data. Geophysics 64(3), 902-914, 1999.

[Priolo et al., 1994] Priolo, E., Carcione, J. M., Seriani, G. Numerical simulation of interface waves by high-order spectral modeling techniques. J. acoust. Soc. Am. 95, 681-693, 1994.

[Sacks et al., 1995] Sacks, Z. S., Kingsland, D. M., Lee, R., Lee, J. F. A perfectly matched anisotropic absorber for use as an absorbing boundary condition. IEEE Trans. Antennas Propag. 43, 1460-1463, 1995.

[Sattel et al., 1992] Sattel, G., Frey, P., Amberg, R. Prediction ahead of the tunnel face by seismic methods-pilot project in Centovalli Tunnel, Locarno, Switzerland. First Break. 10(1), 19-25, 1992.

[Sattel et al., 1996] Sattel, G., Sander, B. K., Amberg, F., Kashiwa, T., T Predicting ahead of the face-tunnel seismic prediction. Tunnels and Tunnelling. , 24-30, 1996.

[Schenk and Gaertner, 2004] Schenk, O., Gaertner, K. Solving unsymmetric sparse systems of linear equations with PARDISO. Journal of Future Generation Computer Systems. 20(3), 475-487, 2004.

[Seriani and Priolo, 1994] Seriani, G., Priolo, E. Spectral element method for acoustic wave simulation in heterogeneous media. Finite elements in analysis and design. 16, 337—348, 1994.

[Shewchuk, 1994] Shewchuk, J. R. An Introduction to the Conjugate Gradient Method Without the Agonizing Pain. Carnegie Mellon University, Pittsburgh, PA, USA, 1994.

[Shanno, 1970] Shanno, D. F. Conditioning of quasi-Newton methods for function minimization. Mathematics of Computation 111, 647-656, 1970.

[Simone and Hestmolm, 1998] Simone, A., Hestmolm, S. Instabilities in applying absorbing boundary conditions to high-order seismic modelling algorithms. Geophysics. 63, 1017-1023, 1998.

[Sirgue and Pratt, 2004] Sirgue, L., Pratt, R. G. Efficient waveform inversion and imaging: A strategy for selecting temporal frequencies. Geophysics. 69(1), 231-248, 2004.

[Szabó and Babuška, 2011] Szabó, B., Babuška, I. Introduction to Finite Element Analysis: Formulation, Verification and Validation. John Wiley and Sons, 2011.

[Tarantola, 1984] Tarantola, A. Inversion of seismic reflection data in the acoustic approximation. Geophysics 49, 1259-1266, 1984.

[Tarantola, 1987] Tarantola, A. Inverse problem theory. Methods for data fitting and model parameter estimation. Elsevier, Amsterdam, 1987.

[Tromp et al., 2008] Tromp, J., Komatitsch, D., Liu, Q. Spectral-element and adjoint methods in seismology. Communications in Computational Physics. 3(1), 1-32, 2008.

[Tzavaras et al., 2012] Tzavaras, J., Buske, S., Gross, K., Shapiro, S. Three-dimensional seismic imaging of tunnels. International Journal of Rock Mechanics and Mining Sciences 49, 12–20, 2012.

[Vai et al., 1999] Vai, R., Castillo-Covarrubias, J. M., Sánchez-Sesma, F. J., Komatitsch, D., Vilotte, J. P. Elastic wave propagation in an irregularly layered medium. Soil Dynamics and Earthquake Engineering. 18(1), 11-18, 1999.

[Virieux, 1984] Virieux, J. SH-wave propagation in heteregeneous media: Velocity-stress finite-difference method. Geophysics. 51, 1933-1957, 1984.

[Virieux et al., 2009] Virieux, J., Operto, S. An overview of full-waveform inversion in exploration geophysics. Geophysics 74(6), 1-26, 2009

[Wang et al., 2008] Wang, H. J., Igel, H., Gallovic, F., Cochard, A., Ewald, M. Source-related variations of ground motions in 3D media: application to the Newport-Inglewood fault, Los Angeles basin. Geophys. J. Int. 175, 202-214, 2008.

[Williams, 1999] Williams, E. G. Fourier Acoustics: Sound Radiation and Nearfield Acoustical Holography. Academic Press, 1999.

[Yamamoto et al., 2011] Yamamoto, T., Shirasagi, S., Yokota, Y., Koizumi, Y. Imaging geological conditions ahead of a tunnel face using Three-dimensional Seismic Reflector Tracing System. International Journal of the JCRM. 6(1), 23-31, 2011.

[Yong and Dave, 2012] Yong, M., Dave, H. Quasi-Newton full-waveform inversion with a projected Hessian matrix. Geophysics 77(5), , 2012.

[Zeng and Liu., 2001] Zeng, Y., Liu, Q. A staggered grid finite difference method with perfectly matched layers for poroelastic wave equations. Jour. Acoust. Soc. Am. 109, 2571-2580, 2001.

[Zeng et al., 2001] Zeng, Y., He, J. Q., Liu, Q. The application of the perfectly matched layer in numerical modeling of wave propagation in poroelastic media. Geophysics. 66, 1258-1266, 2001.

[Zhang, 1985] Zhang, G. Q. High-order approximation of one-way wave equations. J. Comput. Math. 3, 90-97, 1985.

[Zhao et al., 2006] Zhao, Y., Jiang, H., Zhao, X. Tunnel seismic tomography method for geological prediction and its application. Applied Geophysics. 3(2), 69-74, 2006.

[Zheng and Huang, 2002] Zheng, Y., Huang, X. Anisotropic perfectly matched layers for elastic waves in cartesian and curvilinear coordinates. Massachusetts Institute of Technology. Earth Resources Laboratory, Technical Report, 2002.